NASA CR 172324

BODY-FREEDOM FLUTTER OF A 1/2 SCALE FORWARD-SWEPT-WING MODEL, AN EXPERIMENTAL AND ANALYTICAL STUDY

Richard Chipman, Frank Rauch
Melvyn Rimer and Benigno Muñiz

Prepared for

NATIONAL AERONAUTICS AND SPACE ADMINISTRATION
LANGLEY RESEARCH CENTER

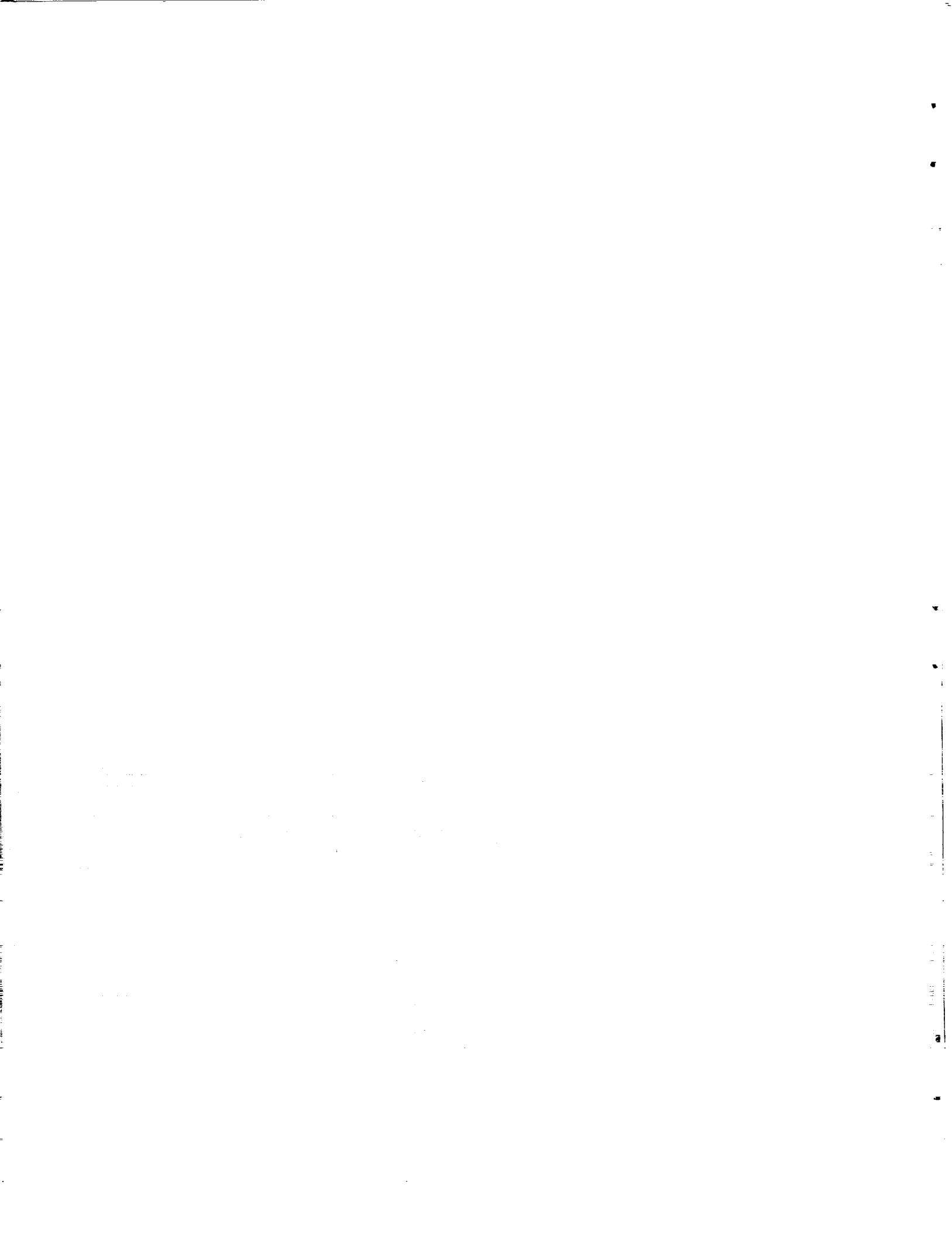Under Contract NAS1-17102

April 1984

By

GRUMMAN AEROSPACE CORPORATION
BETHPAGE, NEW YORK 11714

NASA

National Aeronautics and
Space Administration

Langley Research Center
Hampton, Virginia 23665

BODY-FREEDOM-FLUTTER OF A 1/2 SCALE
FORWARD-SWEPT-WING MODEL,
AN EXPERIMENTAL AND ANALYTICAL STUDY

by R. Chipman, F. Rauch, M. Rimer, and B. Muñiz

1.0 SUMMARY

A transonic wind-tunnel test program was conducted on a 1/2-scale model of a forward swept wing configuration with-and-without relaxed static stability. The test gathered dynamic data confirming the existence of body freedom flutter (BFF) and defining instability-speed boundaries for the phenomenon. BFF was found to occur at substantially lower speeds (10% - 24%) than did static aeroelastic wing divergence on the same model.

Because several of the configurations tested were statically unstable (negative static margin), a canard-based Stability Augmentation System (SAS) was incorporated in the model. To assist in the design of the SAS, a preliminary tunnel test was performed in which aerodynamic data were measured at various Mach numbers and dynamic pressures. These data included a set of flexible aerodynamic derivatives with respect to changes in angle of attack and canard incidence, which proved valuable in tuning the analysis and contributed to the accuracy of the BFF predictions.

Data from the configurations flown with the SAS indicate that BFF is not dependent on open-loop static margin but, rather, on the equivalent closed-loop dynamics provided by the SAS. Consequently, similar BFF boundaries were obtained on statically stable, marginally unstable and highly unstable configurations.

Servo-aeroelastic analyses of the model were performed using a state-variable formulation incorporated in a computer code known as SAEL. Correlation between test data and the analytically predicted onset of BFF was good (-3% to +6%) at subsonic speeds and acceptable, though consistently unconservative (+3% to +10%), at transonic speeds.

2.0 TABLE OF CONTENTS

3.0 INTRODUCTION

A fundamental elastic characteristic of forward swept wings (FSW) is that upward bending induces positive (leading edge up) twist. Known as wash-in, this behavior makes possible the occurrence of static aeroelastic divergence on a FSW clamped at its root. In a dynamic sense, this divergence tendency is manifested by the destiffening (decreasing frequency) of the primary wing bending mode with increasing airspeed or dynamic pressure. On a freely flying vehicle, this destiffening can lead to dynamic aeroelastic interactions. In particular, analyses (References 1 through 3) of forward swept wing vehicles have indicated that, at high dynamic pressures, adverse aeroelastic coupling can occur between the primary wing-bending mode and the symmetric rigid-body modes of the aircraft. This coupling has been shown analytically to cause degradations in anticipated flying qualities and, in severe cases, to lead to a low-frequency dynamic instability denoted, herein, as body freedom flutter (BFF). In designs with high relaxed static stability (RSS), this phenomenon is complicated by the presence of a high-authority longitudinal control system (Ref. 4). Furthermore, prior to the subject effort, it was unknown to what extent transonic unsteady aerodynamics might aggravate the problem. Consequently, the present study was undertaken to obtain experimental confirmation of the predicted phenomenon and to clarify these other aspects of the problem (RSS and transonics).

The primary objective of this contract (NASA Langley Contract Number NAS 1 - 17102) was the experimental study of BFF at transonic speeds on a model of a FSW aircraft (Figure 1) with and without RSS. To accomplish this, body-freedom-flutter boundaries were determined for three configurations: statically stable, marginally unstable and highly unstable. These boundaries were then compared to the wing divergence boundary. To enable the latter two configurations to fly, a canard-based Stability Augmentation System (SAS) was designed and built for the model. A secondary objective was the calibration of an analysis procedure used for predicting the servo-aero-elastic phenomenon, BFF, on a FSW vehicle with RSS. (SAEL, the analysis code evaluated, is

representative of modern linear state-variable analysis procedures for use in Servo Aero Elastic calculations.)

To accomplish these objectives, work was done on six major technical tasks. Figure 2 shows their interrelations. Two wind tunnel tests on a 1/2-scale semispan FSW dynamic model were conducted: (1) an aerodynamics test and (2) a dynamics (body-freedom-flutter) test. The first test took place in January 1983; the second in August 1983. For that first test, an existing model (Figure 3) was modified (Task I), checked and ground tested (Task V), and tunnel tested transonically in the NASA Langley Transonic Dynamics Tunnel (TDT) (Task VI) to produce a set of aerodynamic data. This flow of work is indicated by the dashed lines in Figure 2. Section 5 of the present report documents these efforts and the supporting analyses for the first tunnel entry. The flow of work leading to and culminating in the second test is indicated by the solid lines in Figure 2. The model was further modified (Task I); a canard actuation system was designed and built (Task II); control system electronic components were designed and built (Task III); the model and its control system were checked and ground tested (Task V); and control laws were updated (Task IV) using data from the ground test and the first tunnel test (aero test). With these tasks complete, the model was tested in the NASA-LaRC TDT (Task VI) to produce a set of dynamic (body-freedom-flutter) data which was then correlated with analytical predictions from the SAEL code. Section 6 of this report documents this work, discusses the analytical methods, presents the comparative experimental and analytical results, and states the conclusions drawn from the study. Finally, Section 7 presents recommendations for future investigations and for analysis of FSW aircraft in light of body-freedom flutter.

Many individuals at Grumman contributed to the successful completion of this study. The authors wish especially to acknowledge the efforts of the following individuals in their respective areas of responsibility: P. Manitt, design of the model modifications and support systems; R.Rowan, instrumentation and data acquisition; R. Zanella, control system electronics; J. Biercuk, control actuation

system; R. Alleva, implementation of the control laws; and E. Troglauer, model assembly and tunnel installation.

4.0 LIST OF SYMBOLS

$a_{11}, a_{12}, \ldots$	Individual terms in state matrix (Eq. 10)
b	Reference semichord, feet
c	Local chord length, inches
e	Error signal (Figure 33)
f	Frequency, Hertz
f_A and f_T	Analytic and test flutter frequencies, Hertz
$f_{RF}, f_{FF}, \ldots$	Aerodynamic correction factors (Eq. 14)
g	Acceleration of gravity, ft/sec^2
h	Normalized modal vertical deflection (Table 4)
i_c	Canard incidence, degrees
k	Reduced frequency (= $b\omega/V$)
ℓ	Aerodynamic lag state index
m	Mass of Model, slugs
p or p_ℓ	Aerodynamic lag
$\bar{p}$	Scaled aerodynamic lag (Eq. 5)
$\bar{q}$	Dynamic pressure (also, $\bar{Q}$), lb/ft^2
s	Laplace variable
$\bar{s}$	Scaled Laplace variable, = sb/V
t/c	Airfoil thickness to chord ratio
u	Control signal (Figure 33)

x_{REF}	Streamwise location of moment reference axis, inches
$\underline{x}$	Full state vector
$\underline{\dot{x}}$	Time derivative of state vector
$\underline{x_a}$	Partial state vector (Eq. B6 - B7)
$\underline{x_F}$	States related to flexible motion
z	Model vertical displacement relative to tunnel
$\dot{z}$	Vertical velocity relative to tunnel, ft/sec
A_{RF}, A_{FF}, ...	Submatrices of the state matrix (Eq. 14)
A	Full state matrix
$1/A$	Peak hold projection (Figures 68 through 75)
A_a, $\bar{A}_a$	Partial state matrix (Eq. B6 - B7)
A0, A1, ...	Aerodynamic stiffness, damping, etc. (Eq. 1)
$\bar{A}i$	Scaled aerodynamic terms (Eq. B2)
B	Control matrix
C_L	Lift coefficient, $= L/\bar{q}S_R$
C_M	Moment coefficient, $= PM/\bar{q}S_R b$
C_{L_0}, C_{M_0}	Lift and moment coefficients at zero angle of attack and zero canard incidence
C_{L_α}, C_{M_α}	Lift and moment coefficients per angle of attack
C_{L_δ}, C_{M_δ}	Lift and moment coefficients per canard incidence
D_Z	Gain matrix
E	Measurement matrix
$F(k)$	Real part of generalized aerodynamic force (Eq. 3)
F_W, F_Q, ...	Aerodynamic forces due to motion (Eq. B1)
F_R, F_F	Static aerodynamic forces (Eq. 14)
$G(k)$	Imaginary part of aerodynamic force (Eq. 4)

G_W, G_Q, ...	Aerodynamic forces due to control motion (Eq. B1)
$\overline{G}$, $\overline{G}_\ell$, G, G_ℓ	Control and control lag aerodynamic force matrices (Eq. B6 - B7)
I	Identity matrix
I_c or IC	Canard incidence, degrees
I_{yy}	Model pitch moment of inertia, slug-ft^2
K	Spring constant, lb/ft
$K_{\xi\xi}$	Modal stiffness matrix
K_F, K_I, K_L, K_{NZ}, K_Q, K_α	Gains (Figure 33)
L	Lift, lb
M	Mach number
M_x	Moment about x-axis through balance, positive wing-tip up, ft-lb
M_y	Moment about y-axis through balance, positive nose up, ft-lb
M_z	Moment about z-axis through balance, positive nose right, ft-lb
$M_{\xi\xi}$	Generalized mass matrix
M_a	Combined inertial or "left-hand-side" matrix
M_B	Swept wing bending moment about inboard strain gage
N_{z_c}	Vertical acceleration, g's
N_z	Commanded vertical acceleration, g's
P	Diagonal matrix of lags (Eq. B3)
P_R	Hydraulic return from actuator
P_S	Hydraulic supply to actuator
P_x	Load in x-direction, positive aft, lb

P_y	Load in y-direction, positive outboard, lb
P_z	Load in z-direction, positive down, lb
PM	Pitching moment about balance (FS 220.6), ft-lb
Q	Pitch rate, rad/sec
$\dot{Q}$	Pitch acceleration, rad/sec²
$\overline{Q}$	Dynamic pressure (also, $\overline{q}$) lb/ft²
$\overline{Q}_A$ and $\overline{Q}_T$	Analytic and test dynamic pressures at flutter, lb/ft²
RM	Rolling moment about balance (BL-2.5), ft-lb
S_R	Reference area, ft²
V or V_o	Freestream velocity, ft/sec
W	Vertical velocity in body axis system, ft/sec
$\dot{W}$	Vertical acceleration in body axis system, ft/sec²
Z	Measurement vector (Eq. B12)
α	Angle of attack, rad or deg as specified
δ	Canard displacement or incidence, rad or deg as specified
δ_C	Canard command (Figure 33), rad
δ_{CDM}	Canard trim command (Figure 29), rad
δ_I	Integral command (Figure 33), rad
δ_ℓ	Canard lag state
ΔT_F	Change in cable tension, lb
θ	Pitch angle relative to wind tunnel, rad
$\dot{\theta}$	Pitch rate (=Q), rad/sec
ξ	Model displacement generalized coordinate
ρ	Density of fluid (freon in tunnel), slugs/ft³
τ	Time constant in actuator model, sec
ω	Frequency, rad/sec

5.0 AERODYNAMIC TEST

5.1 WIND-TUNNEL MODEL

The model used in this test was a slightly modified version of one tested previously in the experimental wing divergence program described in Reference 5.

5.1.1 Original Model Review

The model, as originally designed, is a 1/2-scale reflection plane model of a Forward Swept Wing Aircraft. The general arrangement may be seen in Figure 4. The model is comprised of three major components, an aeroelastically scaled wing, a rigid non-dynamic fuselage, and a remotely positioned rigid canard surface. The original design was for installation on the east wall turntable of the NASA Langley Research Center's 16 ft. transonic dynamics tunnel.

To properly scale the wing structure, special uni-directional graphite/epoxy tape having a nominal thickness of .00137 inches was developed. Covers made from this tape are bonded to a substructure constructed of full depth honeycomb with fiberglass forward and aft spars. Both the covers and spars are bonded to an aluminum wing root fitting at the fuselage side. To complete the aerodynamic simulation, leading and trailing edges made from fiberglass covered foam are bonded to the structural box. Instrumentation is installed on the wing to monitor loads during various test phases.

The non-dynamic fuselage is constructed of a profiled solid aluminum backplate with a central built-up structural member to accommodate the aerodynamic loading and the attachment of fiberglass-covered wooden aerodynamic fairings. A 28-volt DC motor is located in the forward section of the fuselage to provide power to remotely position the non-dynamic canard surface. The model scale factors are presented in Table 1.

5.1.2 Modifications and Additions

The model was to be mounted on a force balance; and aerodynamic forces were to be measured for various component build-ups, i.e., fuselage alone, fuselage/wing, fuselage/canard and fuselage/wing/canard. To enable this to be done, the following modifications and additions to the model (see Figure 5) were made:

o   <u>Fuselage</u> - The turntable mount fitting was removed, and a bolt-hole pattern was located on the fuselage structure (profile plate and built-up structure) to attach the balance adapter. The location was 9.75 inches above where the turntable bolt pattern was originally located. Additionally, a wood fairing was made to replace the wing in the wing-off configurations.

o   <u>Balanced Mount</u> - Since the configuration of the NASA TDT balance is such that the upstream face is the interface with the model, a balance adapter fitting was required. The design of the fitting minimized the amount of model-induced rolling moment by placing the model and balance within close proximity. Stand-off of the model from the tunnel wall (to achieve adequate flow quality) was accomplished by using a spacer block between the turntable and balance.

o   <u>Model Splitter Plate & Windscreen</u> - In order to insure proper flow over the model and shield the balance from the air flow, a splitter plate and windscreen were designed and fabricated. (The device is called a Splitter plate because it effectively splits off low-energy boundary-layer flow and directs that flow behind the plate, away from the model.) The splitter plate assembly consisted of a 1/2-inch thick core of balsa, faced with aluminum sheets and mounted to a series of four streamwise trusses. For the aerodynamic test, the splitter plate was located approximately 8 inches from the tunnel wall to provide easy access during installation. A hole in the splitter plate (lined up with the

turntable) allowed the spacer, balance and balance adapter assembly
to be accessible from the outboard side of the splitter plate.

A three-piece windscreen acted to shield the balance and
associated active parts of the support system from the airstream.
The windscreen assembly consisted of two wooden outer
airfoil-shaped fairings and an aluminum inner 'racetrack'-shaped
covering. Rubber seals were provided to attach to the surfaces
that contact the model and the tunnel wall. When assembled, the
items attached directly to the splitter plate. The inner
'racetrack' passed through the splitter plate, and the rubber seal
at the outboard end contacted the inboard face of the model profile
plate. Since the gap between the model and splitter plate that
would occur on the body-freedom model was simulated on this aero
model, an optional wooden airfoil fairing was required between the
model and splitter plate to cover the protruding 'racetrack' cover.

5.1.3   Model Properties

A detailed discussion of the model properties is given in Reference
6. The key data are repeated here. Model inertia data are given in
Table 2, original design loads in Table 3, original model mode shapes in
Table 4, modal frequencies in Table 5, and the mode shape grid in Figure
6.

5.1.4   Model Loads and Strength Analyses

Load critical points on the model were determined for each of the
four model configurations to be tested. Aerodynamic forces were derived
by scaling down the analytical loads used in the original model's stress
analysis to the maximum levels obtained during the previous tunnel tests
at a dynamic pressure of 150 PSF. These loads were then applied to the
simplified NASTRAN model (Figure 7) along with weights of the various
model components to determine loads at the balance adapter bolts and
balance centerline.

o   Loads at Model-To-Balance Adapter - A summary of loads for the various test configurations may be found in Table 6. As may be seen, the highest combined shear load (308 lbs.) appears at bolt 1005 for the fuselage/wing aero case. Since the ultimate shear load for a 1/2-13 bolt is 10,140 lbs, a safety factor of 33 is obtained. For tension, bolt 1002 is subjected to a max load of 587 lbs in the fuselage/wing/canard configuration. This load will result in a safety factor of 29.

o   Loads at Balance Centerline - A summary of loads at the balance centerline for the test configuration may be found in Table 7. A series of NASTRAN runs was made with and without aerodynamic loads and model weight for the configurations to be tested. These runs were made to determine if ballast would be necessary to pre-load the balance and, if so, the amount and location required. From a review of the summary table, it appeared that only one case (Fuselage/Wing) required ballast. Twenty pounds located 50 inches aft of the balance reduced the pitching moment by 1000 in lbs, thereby permitting adequate margins in this configuration.

5.1.5   Model Stability Analyses

Predictions were made of the static and dynamic aeroelastic stability of the model for the test. Using a combination of analysis and measured data from the previous divergence test effort, calculations were performed that indicated the model would not encounter any aeroelastic instability within the tunnel operating envelope (dynamic pressure less than 150 PSF) prescribed for the test.

For the analyses, a set of modes, frequencies and generalized masses were computed by coupling the cantilevered wing modes previously measured on the model with calculated rigid-model/tunnel-balance modes (i.e., model plunge, pitch and roll about the balance). Figures 7 and 8 (from Ref. 5) show the grid on which the cantilevered wing modes were measured and plots of those mode shapes. In Table 4, the modal deflections and frequencies are recorded. Figure 6 is a sketch of the NASTRAN

idealization of the model connected to the balance by springs representative of the balance flexibilities. Because the purpose of this idealization was to obtain "rigid" modes, the wing and canard were represented as lumped masses rigidly connected to a simplified model of the fuselage. The fuselage is itself very rigid; consequently, the primary modes obtained were those of a lumped mass (total model) offset from the end of plunge, pitch and roll springs. Table 8 lists the NASA supplied balance flexibilities used in the analysis. The plunge and pitch flexibilities were measured values; whereas, for roll, two calculated values were run for the two sets of flexibilities. Table 8 also records the modal frequencies obtained. Figure 9 shows the weights grid and the inertial breakdown used to compute the generalized mass matrix that couples the cantilever and rigid modes.

The steady and unsteady aerodynamics for the various modes were obtained from the doublet lattice program at M = 0.9. Calculations were run for both test configurations in which the wing was present, i.e. wing/fuselage and wing/fuselage/canard. Additionally, another set of calculations was run eliminating the fuselage aerodynamic modelling and simply end-plating the wing and canard at their roots.

Using the results of the above dynamic and aerodynamic calculations, flutter analyses were run using the traditional k-method. Three principle instability mechanisms were looked for: wing divergence, pitch/wing bending coupling (body freedom flutter), and pitch/roll coupling (rigid body flutter). Because the pitch mode was stiffer than wing bending, body freedom flutter did not occur; however, a slight coupling between the two modes at low speeds leading to a very lightly damped region was predicted. Assuming modest amounts (1/2%) of structural damping eliminated this problem. Because the roll mode was very stiff and well separated from the pitch mode, rigid-body flutter did not occur. Wing divergence was predicted to be the critical instability, occurring at 205 KEAS. This is virtually identical to the speed at which divergence is predicted when the rigid modes are not included; thus, the effect of the balance flexibilities is negligible. Similar

results were obtained for all cases run. Although 205 KEAS translates to a dynamic pressure of 143 psf, no instability was expected in the test at pressures below 160 psf. This conclusion was reached based on the fact that the previous divergence test showed that the divergence speed predicted using measured modes was conservative. The lowest divergence point determined in that test was at 160 psf, M = 0.95. At M = 0.90, the lowest divergence point was 177 psf.

5.1.6   Ground Tests and Checkouts

Prior to the tunnel test a series of checks was performed on the original model and the modified model installation. The following paragraphs describe the results obtained during these checks.

o   <u>Pre-Modification Inspection</u> - Visual inspections of the components of the original existing 1/2-scale model revealed acceptable model condition with the following two exceptions: (1) Exterior finish on the forward fuselage fairing was chipped and peeling. Repainting was necessary. Also, some minor touch-up was desirable on the remaining fairings. (2) Some areas of the leading and trailing edges of wing number 1 were rough due to minor on-site repairs made during the previous tunnel test. Sanding was required to smooth the surface. The indicated repair work was done to correct these two sets of deficiencies.

To determine whether the dynamic characteristics of the model had changed since the previous tunnel entry, a cursory vibration survey (frequency and node lines) was made with the model rigidly supported in a manner similar to that used for the original survey. The measured first four modal frequencies are recorded in Table 5. These results showed good agreement (within 5%) between the two surveys and indicated that the wing essentially was dynamically unchanged from its original condition. The slight decrease in all frequencies falls within the repeatability range of the test itself.

16

The existing instrumentation of the wing consists of 3 bending-moment circuits, 3 torsion circuits, 8 laminate strain gages, and a wing-tip accelerometer. These circuits were tested and determined to be operational. Furthermore, the various cables and bridge-completion circuits used in the previous tunnel entry were also checked out.

o   Model Parts Compatibility Check - Prior to shipping the model to the test site, a trial assembly was made with the turntable plate, spacer, dummy balance, balance adapter and fuselage structure. Included in the assembly were the truss and splitter plate. During initial assembly, openings in the splitter plate required for snubber attachments and wire bundle routings were established and cut through. Arcs describing maximum angle travel of the fuselage where checked on the splitter plate and areas requiring clearances were modified.

o   On-Site Pre-Entry Checks - Upon arrival at the test site, the model wing was mounted on the calibration lab backstop. A cursory vibration survey was performed that verified the modal frequencies were unchanged. A series of prescribed static load checks were made to verify the calibration of the wing strain gage circuits.

o   Post-Installation Checks - After the model was installed in the wind tunnel, the wing frequency checks and static-load calibrations were repeated. Wing frequency checks were also repeated at each tunnel entry during testing. (Table 5 records the frequencies at one point during the test.)

o   Force-Balance Checks - During the wing static-load checks, it was discovered that the force balance did not give correct readings for the low loading levels checked. The wing was removed and a simple rugged loading fixture attached to the fuselage, so that large loads could be applied without risk to the wing. A series of large-load calibrations was then made to assure the basic fidelity of the balance for the range of loads of interest.

Finally, a post-test recalibration of the balance was performed and the aero test data reprocessed accordingly.

5.1.7   Instrumentation

During this test phase, the prime objective was to measure aerodynamic properties of the model in various configurations. Since these data were to be acquired at dynamic pressures below the previously tested divergence envelope, it was necessary to monitor the model instrumentation only as a precautionary measure. As such, model load monitoring was confined to the inboard bending moment and torsion measurements only. For completeness, information pertaining to all model instrumentation has been included in this report. Table 9 lists the model instrumentation and type. Figure 10 indicates the location of the various wing instrumentation. A list of gage sensitivity factors is provided in Table 10.

The data acquired during this test may be separated into two main categories: Data pertaining to the safe operation of the model within the tunnel envelope, and aerodynamic data to be used in analyses of the body-freedom model. (See Figure 11, block diagram.) Data acquired for safety of operation were data pertaining to: 1) static loading of model and/or balance and 2) aeroelastic instabilities (divergence) of the model system. To meet the first requirement, real time displays on both digital displays and brush recorders were used to ascertain when limit loads were being approached. To monitor aeroelastic divergence, a predictor technique was used; i.e., data acquired at prior conditions were used to determine if a safe margin existed to proceed to the next point.

Aerodynamic data were acquired directly from the NASA balance and processed on line to derive corrected forces and moments and coefficient-type data. These data were also stored on magnetic tape and subsequently reprocessed using recalibrated balance coefficients to

improve the quality of the final data. In addition to being processed, raw lift, rolling moment and pitching moment measurements were displayed in real time on monitoring equipment, as part of the operation safety information.

5.2 WIND-TUNNEL TEST

The Langley Transonic Dynamics Tunnel (TDT) is a closed-circuit continuous-flow tunnel which has a 16 foot square test section with cropped corners and slots in all four walls. Mach number and dynamic pressure can be varied simultaneously, or independently, with either air or Freon used as a test medium. For the present test, Freon-12 was used. As shown in Table 11, four configurations were tested: fuselage alone, fuselage/wing, fuselage/canard, and fuselage/wing/canard. Data were gathered for each configuration at three Mach numbers and a variety of dynamic pressures.

5.2.1   Test Procedures

The general operating procedure used during the tunnel tests was as follows: Where possible, the tunnel operated along a constant total pressure line. As dynamic pressure was increased, the model angle of attack was "trimmed" to minimize model loads; the canard remained at zero incidence; and the model and balance loads were monitored for safety. When a desired operating point was reached, the model angle of attack was slowly increased until either 4.0 degrees was attained or some load (model or balance) reached its allowable limit. The angle of attack was then decreased in moderate steps back thru the "trim" point until either -1.0 degrees or a load limit was reached. At each step, force data were gathered and stored by the data acquisition computer. At the end of the alpha-sweep, the angle of attack was returned to a value approximately mid-way between the positive and negative limits of the sweep. The data were then inspected using the on-line graphical display unit (GDU) of the data acquisition system. Force vs. angle of

attack plots were viewed, erratic points deleted from the data base, and automatic least-squared sloping performed to obtain derivative data. (Typically, the highest positive-alpha point was deleted; the associated data were erratic due to back-lash effects in the tunnel turn-table on which the model/balance mounted.)

For the two configurations with canard, a sweep of canard incidence (delta) was next performed. The sweep followed the same format as the alpha-sweep but within a delta range of 4.0 to -2.0 degrees. At the completion of the sweep, the canard incidence was returned to zero. The tunnel was then changed to the next desired operating point.

5.2.2   Data Reduction Procedures and Test Results

For each data point not deleted from the alpha and delta sweeps, three cards of data were punched for post-test reduction. These cards (numbers 1 to 3 of Table 12) contained information specifying the tunnel conditions and force data. For each set of points corresponding to an alpha-sweep, a fourth card was punched containing the sloped alpha-derivatives for the five balance forces and moments. The set of all such punched output comprised the basic reduced balance data. As mentioned in Section 5.1.6, these data were revised to reflect the post-test recalibration of the force balance. This revision was easily accomplished because all raw data gathered during the test was stored on magnetic tape.

Subsequent to the test, detailed reduction of the preliminary aero data was undertaken using the punched data as input. For each configuration/Mach-number/dynamic-pressure combination, plots were generated of lift, pitching moment, and rolling moment coefficients as functions of angle of attack for a fixed canard incidence and as function of canard incidence for fixed angle of attack. (See Figures 12 and 13 for representative plots.) Spurious points were deleted and the data were fit to determine C_{L_0}, C_{L_α}, C_{L_δ}, etc. (Note that this procedure was a repeat of that used on-line for the alpha-sweep data.) These

coefficients/derivatives are presented in Table 11. Next, these data were plotted as functions of dynamic pressure for each configuration/ Mach-number combination. (See Figures 14 and 15 for representative plots.) These final plots constitute the aerodynamic data with which the model SAS was to be designed for the flutter test.

Further processing of these data was required for estimating loads to design new structure for the flutter test. In particular, component loads were determined; e.g., wing loads were obtained by differencing loads on the full-up configuration (fuselage/wing/canard) with loads on the fuselage/canard configuration. Plots such as Figures 16 and 17 were generated of these component loads. Section 6.1.3 describes the use of these loads in the design.

5.3 ANALYSIS AND CORRELATION

Analyses were run prior to the test to obtain estimates of the model flexible aerodynamic derivatives; i.e., C_{L_α}, C_{M_α}, C_{L_δ}, C_{M_δ} as functions of dynamic pressure. In these analyses, the rigid portions of the aerodynamics were taken from a separate experimental source; analysis was relied on essentially for the flexibilization. Subsequent to the test, emphasis was placed on tuning the mathematical idealization such that the predicted rigid aerodynamics came more in-line with the test results. This was done to generate an idealization that could be used with improved reliability for computations related to the flutter test.

5.3.1 Analysis Methods and Math Idealizations

For the pre-test analyses, aerodynamics were generated by Grumman programs that are roughly equivalent to the Woodward code (Reference 7). In the subsonic speed regime', the code is identical to the steady-state portion of the doublet lattice program (Reference 8) that was used in the subsequent flutter calculations. Figure 18 shows the panelling used in these subsonic (M = 0.9) computations. Figure 19 presents the

panelling used in the supersonic (M = 1.2) counterparts. The codes
computed flexible effects based on structural influence coefficients
available from Reference 5.

5.3.2   Tuning of the Math Model

The subsonic math model or idealization was tuned using the M = 0.9
rigid data, obtained by extrapolating the experimental aerodynamic
derivatives to zero dynamic pressure. Table 13 records these data. The
tuning was done on a component build-up basis, and changes were made
such that the idealization remained reasonably faithful to the basic
physical geometry of the model. Also recorded in Table 13 are the
analytical derivatives before and after tuning. As can be seen, the
tuning improved the ability of the analysis to reproduce the measured
derivatives in all configurations with the possible exception of
fuselage alone. (Actually, the fuselage revisions were made prior to the
availability of the revised force-balance data and reproduced the
original test data exactly. The fuselage tuning was not repeated to
match the final data since the agreement was felt to be close enough.)
The changes to the idealization were as follows:

o   <u>Fuselage Alone</u> - The idealization consists of a axial distribution
     of slender-body elements, whose strengths are dependent on the
     varying fuselage cross section, a cylinder of interference panels
     extending most of the way along the fuselage, and a small lifting
     surface representative of the model nacelle protuberance. The
     actual fuselage grows in cross section from zero at the nose to a
     maximum in the vicinity of the cockpit/nacelle/canard area; it
     diminishes in size from that point aft but does not close to zero
     again. The original slender body model followed this true
     distribution. The first revision consisted of holding the cross
     section constant aft of fuselage station 230. This point
     corresponds to an actual observable steepening in the rate at which
     the cross-section diminishes. Hypothetically, the flow may be
     separated aft of this point on the physical model. The second

revision consisted of reducing the span of the nacelle panel to 60% of its physical size. This was to account for the fact that the physical nacelle on the model is not a thin lifing surface; instead, it has a squarish cross-section, no flow-thru and, thus, would generate little lift. (See Figure 20 for a picture of these modelling details)

o Fuselage/Canard - The idealization consists of a lifting surface, representing the canard, attached to the above-mentioned math model. The revisions consisted of (1) the above, (2) a correction to an error in the original model leading and trailing edge sweep, and (3) an arbitrary 5% reduction in the canard span.

o Fuselage/Wing/Canard - The idealization consists of a lifting surface, representing the wing, attached to the preceding math model. The revisions consisted of the above mentioned revisions and alignment of the wing panelling to be consistent.

5.3.3   Correlation

It was planned that test data be gathered at both the subsonic and supersonic analysis points, i.e., M = 0.9 and 1.2. However, the highest Mach number attainable for the full-up configuration of this model in the TDT was found to be 1.05. Consequently, the correlation presented is direct only at M = 0.9. For the other Mach number, M = 1.05, analytical predictions were generated by combining the M = 0.9 and M = 1.2 results with the knowledge of how rigid aero derivatives behaved at intermediate (transonic) Mach numbers in a prior test of an 1/8th scale model of a similar FSW configuration (Reference 9).

Figures 21 through 24 show the test/analysis correlation. For the M = 0.9 analyses, the revised panelling has been used. The trends in lift curve slope ($C_{L\alpha}$) seem to be predicted reasonably well; but the levels are too high and the amplification with increasing dynamic

23

pressure (flexible effect) is clearly over-predicted. The C_{M_α} predictions are good. C_{L_δ} is computed accurately at low-dynamic pressures but its amplification is under-predicted. Finally, C_{M_δ} is slightly over-predicted and the absence of a significant flexibility effect is properly predicted. Considering that the wing and canard are closely coupled aerodynamically on this configuration, the correlation is rather remarkable.

6.0 FLUTTER TEST

6.1   WIND-TUNNEL MODEL

6.1.1   Structure and Support System

Figure 25 shows an exploded view of the main structural components of the model as modified for the present test. The principal new components were (1) a light-weight fuselage, (2) light-weight wing attachment fittings, (3) a canard attachment fitting with an actuator and linkages, (4) a model support system including roll rods and lift, drag, and snubber cables, (5) a splitter plate and truss work to attach the plate to the tunnel wall, and (6) ballast weights to vary the model center of gravity. The existing fuselage fairings were routed on the inside to reduce weight. Also, sensors (accelerometer and pitch rate gyro) and various hydraulic and electronic components were provided; these are discussed in a later section.

o   Light Weight Fuselage - It was apparent at the outset that the weight and pitching moment of inertia of the original fuselage were much too high (relative to the wing inertial properties) to be representative of a realistic airplane design. Accordingly a light-weight but relatively rigid fuselage was designed and fabricated. This was accomplished by using semi-circular honeycomb torque tubes (backed up by a honeycomb profile plate) as the primary longitudinal structural members. Solid aluminum machined bulkheads were added at the wing and canard attachment points. Additionally, material was removed from the inside of the existing fairings and all new parts were kept as light as practical consistent with a conservative approach to strength.

o   Light Weight Wing Attachment Fittings - The wing was originally attached to the fuselage by a heavy, full-chord fitting. In the redesign the center portion of the fitting was removed and the remaining forward and aft fittings were attached directly to the two aft major fuselage bulkheads. The bulkhead locations coincide

with the support linkages thereby providing direct, efficient load paths from the wing root to the tunnel wall.

o Canard Attachment - Although the original canard surface was retained, the attachment and drive system were reconfigured such that the surface was driven (via appropriate linkages) by a highly responsive hydraulic actuator in lieu of the original electric motor. The actuator was mounted vertically on a fitting that attached to the most-forward fuselage bulkhead. This bulkhead location also coincided with a support linkage to provide a direct load path to the tunnel wall.

o Model Support System - Whereas the original model was rigidly attached to the tunnel wall turntable, yielding a cantilevered wing condition, in this test the model was supported in a manner approximating free flight in the symmetric degrees of freedom. Vertical and pitch degrees of freedom as well as roll, yaw and lateral restraints were accomplished by a pair (one forward, one aft) of classical four-bar linkage systems oriented vertically in the inboard-outboard plane. The inboard vertical leg of the system was the tunnel wall and the outboard leg the model itself (see Figure 25). The horizontal legs ("roll bars") were fitted to the model and tunnel wall through universal joints which accommodated limited differential vertical motion (pitch) of the two linkage systems. The length of these rods was chosen so that moderate pitch (±4°) could be obtained without excessive lateral motion of the model. The total stand-off (model to tunnel-wall) was 26 inches. Drag loads were partially reacted by a fore-aft diagonal member attached to the model at the lower rear bulkhead and to the tunnel wall at the aft lower rod attachment point. That portion of the model weight not supported by aerodynamic lift was supported by a cable attached to low-rate lift springs. Snubber cable attachment points were located on the roll-rod attachment points at the fuselage. Additionally, a drag cable attachment assembly attached to the back side of the fuselage profile plate.

26

o   Splitter Plate and Mounting Truss - The model support system
    described above projected through a large splitter plate which
    defined the reflection plane of the semi-span model. The splitter
    plate, in turn, was mounted off the tunnel wall through five
    commercial-construction-type trusses, thus, providing a simple,
    strong reflection plane. Incorporated in the splitter plate and
    attached to the truss were adjustable stops which, by contacting
    the model roll rods, restrained the model from excessive travel.

o   Ballast Weights - The fuselage of the model was fitted with
    forward, center and aft ballast weights, segments of which were
    removable in order to allow testing at any one of three center-
    of-gravity positions. This range of c.g.'s corresponded to a range
    of static stability levels - stable, moderately unstable, highly
    unstable.

6.1.2   Model Properties

    Details of the model properties are given in Ref. 10. The signi-
ficant data are repeated herein. Table 14 gives the model weight and
pitch moment of inertia for each of the three c.g. locations tested.
Table 15 presents the locations and weights of the ballast needed for
each center of gravity. (In each case, the total ballast is 33.2 lbs
and this amount is included in the total model weight to 324 lbs.) Table
16 records the flexibilities of the canard assembly in pitch (with
hydraulics active and inactive) and in roll. Also recorded is the
static load required to overcome the actuator spring stiffness when the
hydraulics are inactive.

6.1.3   Model Loads & Strength Analyses

o   Design and Working Load Limits - Design loads for the wing and
    canard were established during the original model design effort
    (Ref. 5). Also during that effort, a proof load test was conducted
    on the wing. The maximum applied shear load in that test was only

768 lbs. For added conservatism, the working shear load on the wing was limited to 768 lbs for the present test. Since no pitching moment limit was established for the canard in the original design effort, a limit of 500 in-lb about the pivot was chosen for the present test. This corresponds to a center of pressure that is 2.4 inches ahead of the pivot axis - a reasonable value, based on aerodynamic analyses of the model. The present working load limits are presented in Table 17.

No additional proof load tests were done on the wing or canard under the present contract. However, a test of the canard actuator and back-up structure was done as part of the proof test on the new fuselage (see Section 6.2.5).

o   Angle-of-Attack and Canard-Incidence Limits - To avoid excessive loading on the wing and canard during the present test, limits were established on the angle of attack and canard incidence. At each Mach number for various dynamic pressures, curves (straight lines, actually) were generated relating angle of attack to canard incidence for each component load limit (i.e., maximum wing pitching moment, minimum wing pitching moment, maximum canard lift, etc.). This was done using the aerodynamic coefficients of Section 5.2.2 and the load limits of Table 17. Figure 26 shows a representative plot. The intersections of the various lines define a polygon, which is an envelope of angle of attack and canard incidence within which no component load is exceeded. A rectangle inscribed within this envelope represents a safe set of upper and lower limits for α and i_c at that dynamic pressure. Figures 27 and 28 show plots of these limits as functions of dynamic pressure. (In Figure 27, a ± 4 degree absolute limit on angle of attack is additionally imposed due to geometric constraints of the model support system.) The angle of attack limits were updated during the flutter test, using a procedure described in Section 6.3.2.1.

o   <u>Stress Calculations</u> - Load critical points on the model and the support system were determined. Using the design applied loads above, stress calculations were performed. Table 18 summarizes the safety factors determined.

6.1.4   Model Divergence Analyses

o   <u>Canard</u> - Analyses were done to assure that aeroelastic divergence would not occur within the test envelope. Torsional (pitching) and bending (rolling) divergence were considered. By balancing the aerodynamic moment against the structural restoring moment, the dynamic pressures at divergence were computed. The aerodynamic moments were determined using the largest experimental lift curve slope of the canard (aero test data, Section 5.2.2) and the most forward, most outboard center of pressure form analysis. (Test data were considered inaccurate for canard c.p. determination.) The structural restoring moments were determined using the measured flexibilities of Section 6.1.2. Results showed safety factors of 6.4 on torsion and 11.5 on bending (dynamic pressure at divergence divided by 150 psf).

o   <u>Wing</u> - A correction factor was developed to scale the divergence boundary measured in Reference 5 to an appropriate level for this test. The differences between the stiffness of the back-up structure (fuselage) in each test and the changes in the wing (minor repairs subsequent to the divergence test) necessitated this correction. The factor was based on measured first wing bending frequencies and vibration analyses of the model in each test. Applying this factor, the model was expected to diverge at a 10% lower dynamic pressure; thus, the critical $\bar{Q}$ was expected to be 143 psf at M = 0.97.

6.1.5 Model Control System

6.1.5.1 Components - A schematic of the control system is shown in Figure 29. The components are:

o   Sensors - Sensor requirements were established by various control system analyses, including time histories of model responses to a step change in angle of attack scaled to represent an estimated maximum vertical velocity induced by tunnel turbulence. Band widths were chosen to be greater than that of the actuator. Thus, the gyro requirements were as follows: range to equal or exceed ±10 deg/sec and bandwidth to exceed 20 Hz. The accelerometer requirements were as follows: range to equal or exceed ± 2 g's and bandwidth to exceed 20 Hz.

     The gyro chosen was Hamilton Standard 10-05435-158 single-axis rate gyro. The accelerometer was the Schaevitz LSBP-2 unit.

o   Actuator & Hydraulics - Actuator requirements were established by a number of considerations. Control system studies determined that the acceptable bandwidth should be greater than 50 rad/sec. Because we planned to excite the model during the tunnel test via a noise spectrum from 1.0 to 20 Hz, we wanted actuator rates to be high enough to excite first wing bending (approximately 60 rad/sec); consequently, a maximum rate of 60 deg/sec was required. Based on trim analysis, the maximum canard hinge moment was estimated to be 500 in-lbs. (The critical condition actually occurs at low dynamic pressures, where the canard would have to be deflected approximately -45 degrees to trim the model; but, in the test, the model was to be snubbed in this range.) The maximum actuator throw was determined to be -10 to +5 degrees by considering trim, stabilization, and excitation signals over the tunnel operating range for which the model was to be unsnubbed.

Based on these requirements and geometric constraints, the actuator selected was one half of an F-14 Series Input Servo Actuator, manufactured by National Waterlift Company, part number 3281000-5.

o   EIB - The Electronic Interface Box (EIB), PN90SKAE111-1 (Reference 11), consists of a single channel electro-hydraulic servo controller (MTS Systems Corp # 406.11) for positioning of the canard, along with circuits for conditioning signals from the fuselage accelerometer and rate gyro. The unit operates on 115 V, 60 Hz power; all other required voltages, including 26 V, 400 Hz, are derived within the unit. Accelerometer and gyro signals fed to the analog computer are scaled for a maximum of ± 10 V. Capability is provided for attenuating the random noise signal and for enabling a notch filter (tunable from 0.2 to 200 hz). The AC output of the LVDT is passed through a phase sensitive demodulator and a gain stage prior to entering the servo amp. The actuator assembly also contains a solenoid valve powered via a switch in the EIB.

o   Analog - The control laws were implemented on the G.F.E. EAI 580 Hybrid Analog Computer. The interfaces between the analog and both the sensor signals and the actuator commands were via the EIB. The scalings for the sensor interfaces were as follows: ± 10 V equals ± 2 g and ± 50 deg/sec respectively. An actuator command of ± 10 V was equivalent to ± 10°. The structure of the control laws is shown in Figure 30.

6.1.5.2   Control Laws -   A pitch rate gyro and an Nz accelerometer sense model motions; and the actuator is driven by a combination of proportional plus integral compensation. Additionally, for trimming the model, a position command (due to pilot stick) is added. The design technique chooses the loop gains so as to locate the closed-loop short-period mode in the left-hand plane at a desired frequency and damping. To make the model test configurations relevant to current FSW aircraft development, short-period frequency and damping were chosen to equal those expected of the real aircraft at tunnel flight conditions corresponding to points within the atmosphere. For tunnel points outside this

31

envelope (points corresponding to below sea level in the atmosphere), sea-level aircraft dynamics were chosen as the design goal. These goals were mid-range of level-one flying qualities, i.e. CAP equal to 1.2 and damping ratio between 0.6 and 0.9.

Initial control law design was based on analytic data. These control laws were revised to reflect the aerodynamic test results; and, following the final evaluation of the model properties, a final set was generated (Table 19). At the test site some further control law tuning was required to account for the addition of a feedback loop from canard position command to vertical acceleration command (Fig. 30). This loop was implemented because, in the tunnel environment, the combination of model drift and narrow angle of attack limits (required for structural loads restrictions) made testing without the loop practically impossible. During the tests the overall loop gain was adjusted (via analog potentiometers) such that, with this added loop in place, the drift fell within acceptable limitations. In subsequent post-test analyses, these heuristically established pot settings were converted to proper equivalent control loop gains (Table 20).

6.1.6   Model Instrumentation

Wing inboard bending moment and torsion measurements were utilized for aeroelastic stability predictions and model load monitoring. A wing tip accelerometer was provided to help predict potential flutter. In the event of a circuit failure, other backup circuits could have been utilized. Table 21 lists the complete model instrumentation required to support the body freedom flutter test. The devices added for this test are items 12 to 20.

A fuselage pitch rate gyro and Nz accelerometer were installed in the fuselage to determine model motions for the SAS. Mounting provisions were made to easily move this package to any one of 3 C.G. locations. A linear voltage differential transformer, built into the

canard servo-actuator, provided position feedback. Load cells were installed in the lift, drag, and snubber cables. Fouling lights were mounted on the face of the splitter plate and wired to indicate contact between the roll rods on the model and the stop blocks on the splitter plate truss.

6.2 GROUND TESTS

In preparing the model and its control system for tunnel testing, a series of checks and ground tests was performed. The following paragraphs describe the results obtained.

6.2.1   Component Tests

o   Actuator-Bench Test - Frequency response functions were measured for the actuator with various input levels. Figure 31 is a representative plot of results: amplitude ratio and phase as functions of frequency. A 75 radian/sec bandwidth was determined to be an appropriate model of the actuator performance over the intended range of commands and rates. Subsequent tests with the servo controller to be used during the tunnel test indicated a 70 radian/sec bandwidth.

o   Sensor Calibrations - The accelerometers and gyros to be used in the model (primary and back-up) were calibrated. The sensitivities of the accelerometers were 0.4002 g's/volt; their zero offsets were -0.0029 to -0.0037 g's. The sensitivities of the gyros were 9.813 deg/sec/volt to 9.968 deg/sec/volt; their zero offsets were -0.124 to +0.055 deg/sec.

o   Analog Computer - A simple second-order unstable math model (representative of the unstable aircraft configuration) was programmed on the analog together with one of the designed control laws. The control law was verified to stabilize the math model and to produce the expected system dynamics.

o   Canard Assembly - The canard/actuator/linkages/mounting-structure
    was assembled and adjusted to minimize free-play. The pitch
    flexibility of the assembly was measured with hydraulics on and
    off. These data are presented in Table 16.

o   Sensor/EIB Checkout - The sensor/EIB interface was checked out (See
    Figure 32) as follows: The sensors (accelerometer and rate gyro)
    were mounted on a flexible cantilevered beam, the length of which
    could be varied by moving the "root" clamp. The beam was vibrated
    by a mechanical shaker driven by a tunable electrical oscillator.
    After peaking-in resonance, the oscillator signal was compared
    (using a dual channel analyzer) to the sensor outputs directly and
    to the sensor outputs as passed thru the EIB. This procedure was
    repeated for various beam lengths (i.e., resonant frequencies).
    The results showed the sensor outputs to have the correct phasing
    in relation to each other and to beam motion. Additionally, the
    outputs of the sensors as passed through the EIB were found to have
    no significant phase lag up to 10 hertz. The signal magnitudes
    were properly amplified to yield ± 10 volts input to the analog.

o   EIB/Analog Checkout - Using a pseudo-random electrical input to the
    EIB (in place of a sensor signal), the frequency response function
    (gain and phase) was determined across the EIB/Analog-Computer by
    means of the dual channel analyzer (See Figure 32). These results
    properly reflected the transfer function programmed on the analog.
    To eliminate integrator drift in the control law programmed on the
    analog, a feedback loop was added to the system for this test
    (Figure 33). This technique was subsequently used in the tunnel
    test to eliminate drift (see Section 6.1.5.2).

o   Actuator/Servo/EIB Checkout - The actuator/servo/EIB interface was
    checked as follows: The canard actuator was mounted on its attach-
    ment bracket and the appropriate electrical, hydraulic, and '
    mechanical connections were made. The canard itself was then
    mounted. With the hydraulic and electrical systems powered, a

static trim command was given using the pilot stick box; and the canard rotation was determined as a function of this command. Results were linear and correct within the allowable limits of canard travel. Next, for various trim settings, the dynamic characteristics of the system were determined using the dual channel analyzer. This was done by comparing the LVDT output from the actuator to pseudo-random-noise input injected at the summing junction of the EIB (see Figure 34). The frequency response function of the system (Figure 35) was acceptable over the 0 to 20 Hz range and compared well in phase to the bench-test results of the actuator alone. The test was repeated with-and-without the physical canard, and with-and-without an 80 lbs distributed load on the canard. In general, the results were similar, but scatter in the data was less in the loaded and deflected canard cases.

To measure the canard rotation more directly and to, thereby, account for the flexibility in the actuation linkages, the above test was repeated using as outputs the signals from the rate gyro and accelerometer (which were temporarily clamped onto the canard root for this purpose). No significant additional phase lag was found.

o   **End-to-End Checkout** - End-to-end measurements were made by injecting pseudo random noise into the N_z and Q input channels of the EIB and comparing these signals to the LVDT output. Therefore, this configuration included the following: EIB, Analog, EIB, servo, actuator, linkages and canard (See Figure 36). Transfer functions were recorded and found to agree with predictions based on the results of the previous tests.

6.2.2   System Acceptance Test

An acceptance test of the complete control system installed on the model while the model was suspended from the roll rods and lift spring was conducted. This test checked and calibrated the various command channels, i.e., pilot stick input, analog computer input, random noise

35

channel input. It also verified the solenoid-off return to neutral and qualitatively checked the closed loop performance; i.e., a nose-up pitch results in a leading-edge down canard motion and a positive acceleration also results in a leading-edge down canard motion. The acceptance test procedure and results are given in Reference 11.

6.2.3   Open & Closed Loop Ground Tests

Open-and-closed-loop Frequency Response Functions (FRF) were measured for the entire system and across various portions of the loop. Figure 37 shows the test set up. The model was suspended by the roll rods and lift cable. To excite the system, pseudo random noise was injected at the summing junction of the EIB in the same way it would be during the tunnel test. (Note that the feedback loop of Figure 33 was present in these tests.)

Data were gathered for the following: (1) input equal to the random noise, output equal to the LVDT, and the loop open (Figure 38); (2) input equal to the servo command, output equal to the LVDT, and loop closed (Figure 39); (3) input equal to the random noise, output equal to gyro pitch rate, and the loop open (Figure 40); (4) input equal to the servo command, output equal to the gyro pitch rate, and the loop closed (Figure 41); (4) input equal to the servo command, output from the accelerometer, and the loop closed (Figure 42); (6) input equal to the servo command , output equal to the analog computer output, and the loop closed (Figure 43); and (7) input equal to the random noise, output equal to the analog computer output, and the loop closed (Figure 44). Items (6) and (7) represent the open-loop and closed-loop transfer functions of the entire system, respectively. All data were consistent with the component transfer function of Section 6.2.1.

Based on the system open-loop transfer function (Figure 43) a gain margin for the air-off system was predicted to be 20 dB (i.e., a factor of 10) - well in excess of the 6 dB gain margin usually required of such a system in a wind-off condition. To partially verify this margin, the

measurement was repeated with increased loop gain. Figure 45 shows the result for the system with the loop gain set at twice its nominal value. The gain margin is roughly 14 dB; the decrease equals the expected factor of two (6 dB). As expected the system was stable at loop gains in excess of four times nominal (12 dB). An attempt to obtain positive confirmation of the entire 20-dB predicted margin was not made.

6.2.4   Ground Vibration Survey, or GVT

o   <u>Model Support</u> - For the vibration tests the model was mounted on a simulated tunnel mount. Because it was necessary to suspend the model to achieve the body degrees of freedom, certain compromises were required between the way the model was mounted for the GVS and the way it was later mounted in the tunnel. To achieve a level attitude (without air load to trim) a temporary bracket was installed on the lift cable pickup assembly. This bracket permitted the model to be supported at its C.G., thus hanging with the Fuselage Reference Line (FRL) level. The other compromise was to carry the total model weight on the lift springs.

o   <u>Instrumentation</u> - A block diagram indicating the equipment used during the tests may be seen in Figure 46.

o   <u>Procedure</u> - Once the model was suspended, an electro-magnetic shaker was attached to the rear lower snubber attachment. A low frequency sweep (0.1 to 2.0 Hz) was made to determine the rigid body pitch and heave frequencies. Output of the integral pitch rate gyro and Nz accelerometer were used to assist in locating these frequencies.

After the rigid body modes were found, a series of frequency sweeps from 1 to 100 Hz was made to locate any model structural modes. During these sweeps, output from accelerometers was monitored and plots of response vs. frequency were generated. These plots were then examined and major responses were chosen for further investigation.

At each of the chosen responses, a mode shape was determined by
moving the probe to each of the measurement grid points and
recording the amplitude and phase (relative to the reference
accelerometer). In addition to the mode shape, a time history of a
decaying response (resulting from a force cutoff) was recorded for
each response. Damping for each mode was determined from this
decay record using the log decrement method.

o   Results - Appendix A summarizes the frequencies and damping
     coefficients, mode shapes, and generalized masses.

6.2.5   Proof Load Tests

o   Drag Cable Restraint - The drag cable restraint was proof loaded in
     tension to 600 lbs without yielding. This corresponds to four
     times the expected drag load limit, based on the aerodynamic test
     of January, 1983.

o   Fuselage Structure and Model Support System - In Section 6.1.3, the
     design loads were discussed. The proof load test requirement for
     support systems was 1.2 times the highest expected loads in the
     tunnel. Since the highest dynamic pressure to be run was 130 psf
     and this was less than the 150 psf associated with the design
     loads, the loads data were re-examined to determine appropriate
     values at 130 psf. The critical loads for this case are listed in
     Table 22. A loading rig was made to use in place of the wing for
     the proof test, so that the wing would not be unnecessarily endan-
     gered. Figure 47 shows the set-up for the test. Based on the
     x-direction moment arm of the rig, a 1030-lbs load was required to
     obtain the desired pitching moment. This load was higher than the
     760 lbs required and yielded a higher rolling moment than required.
     This means that the test was more conservative than it needed to
     be. Table 22 also lists these loads and their proof-load counter-
     parts, i.e., scaled up by a factor of 1.2. Additionally, the

scaled applied canard loads are also listed. The test successfully applied these combined wing and canard loads to the model without failure of the fuselage structure or model support system.

6.3 WIND-TUNNEL TEST

As shown in Table 23, three configurations were tested: statically stable, moderately unstable and highly unstable. Each was flown and data gathered at three Mach numbers : 0.6, 0.80, 0.85. The highly unstable case was also tested at higher Mach numbers (up to 0.94). For the statically unstable configurations, various SAS control laws were tested as indicated in the table.

6.3.1   Wind-Off Checks

Checks and calibrations, discussed in 5.1.6, of the model instrumentation were repeated prior to this tunnel entry. After the model was installed, frequency checks were made by exciting the model via canard motion; i.e., random noise was input as a canard command. The wing-bending moment circuit and the fuselage pitch rate gyro outputs then were analyzed to determine the model modal frequencies. The wing measurement was used to assess model integrity. These checks were repeated before each wind-on test. Results are presented in Table 24. With the exception of the final run, which was made with ballast added to the wing tip , the wing frequencies remained fairly constant indicating no deterioration in model condition. To assess the control system integrity, portions of the acceptance test procedure of Reference 1 were repeated at each tunnel opening.

6.3.2   Test Procedures

6.3.2.1   Stops and Limiter Selection - As discussed in Section 6.1.3, excessive angle of attack and canard incidence at certain flight conditions might give rise to aerodynamic loads large enough to cause

structural failure of the model. Figures 27 and 28 showed the limits recommended to avoid such an occurrence, based on analysis and the aero test data. The canard incidence limitation was actually based on worst-case scenario in which the hydraulic supply was assumed to have failed and only the actuator's mechanical spring remained to resist canard rotation. Thus, the limit was simply not to exceed the static-release moment shown in Table 16. However, even if this limit were exceeded and the canard deflected full throw, no structural failure would occur if the angle of attack were constrained to within the limits of Figure 27. Thus, the canard limits were redundant in a safety sense; whereas, the angle of attack limits were absolute - that is,exceedance might cause structural failures, regardless of canard incidence. With this distinction in mind, a simple electrical limiter was designed for the canard; whereas, the structural stops described in Section 6.1.1 were attached to the splitter-plate truss to physically restrict the angle of attack. Furthermore, a boot-strap procedure was employed during testing to update and adjust the angle of attack limits based on direct load measurements from the present test.

o   Canard Incidence Limiter - An electrical limiting circuit was added
    to the EIB to restrict commanded canard incidence. Separate
    tunable upper and lower limits were provided. The limiter worked
    such that, if the total position command (trim, excitation, and
    feedback) were in excess of the limit, the command would be trun-
    cated to the limit. Below the limit, the system would behave
    linearly. Figure 48 shows the calibration curves for this circuit
    as measured prior to the first tunnel run. With the limits pro-
    perly set according to Figure 28, an hydraulic failure would leave
    the canard incidence at a position where the structural spring in
    the actuator could not be overpowered by the aerodynamic moment.

o   Angle of Attack Stops - The mechanical stops restricted the
    model angle of attack by limiting the vertical travel of each of
    the four roll rods. Each stop was separately adjustable, but such
    adjustments could only be made between runs when the tunnel was

open. The boot-strap procedure relied on wing-load measurements made during each run. Each time a tab point was recorded, measurements of wing bending moment, wing torsion, angle of attack, canard incidence, and tunnel condition were also recorded. After each run, the data were examined, sorted by flight condition and then combined with data from prior runs. For each flight condition, the loads were plotted versus angle of attack, as in Figure 49, and linearly curve fit. At each Mach-number/dynamic-pressure these data were used, together with limit working loads, to define angle of attack limits. The limit loads selected were ±3000 in-lb for wing-root swept torsion and ±16,000 in-lb for wing-root swept bending moment. The torsion limit corresponds to the limit design loads (Table 17) but the bending limit corresponds to only 70% of the design loads. This lower number was chosen for added conservatism, since in prior tunnel entries the model had not been loaded beyond this limit. As data were gathered for several dynamic pressures at a given Mach number, curves of alpha-limit versus dynamic pressure were generated and extrapolated to higher q's (see Figure 50). Prior to each tunnel run, the stops were reset (if desired) to account for the latest alpha-limit estimates. Because the model was difficult to fly within narrow stop settings, the stops were set only as small as required to reach the highest dynamic pressure attempted in a particular run.

6.3.2.2 Wind-On Procedures - After the tunnel was closed and sealed, the control system hydraulics were turned on and the lift cable tension set to its nominal value. On the EIB, the limiter in the servo was adjusted to establish the canard incidence limits and the analog computer channel was switched off. The pilot stick was moved to the zero position. The tunnel was brought slowly up to the first operating point. Along the way, a continuous evaluation of the model based on wing loads, snubber loads, angle of attack, and model motion was made to assure safety.

When an operating point was reached, the pilot adjusted the trim so that the snubber cable loads balanced out. Then an attempt was made to unsnub and fly the model. If the configuration was statically unstable, an appropriate SAS control law, programmed on the analog, was switched on as the model was being unsnubbed. If the control law were switched on prior to unsnubbing, a control instabililty typically resulted, because the canard was frustrated in its attempt to "fly" the restrained model. If the model were unsnubbed prior to switching on the SAS, the entire model would go unstable because of negative static margin. Hence, a simultaneous unsnub/switch-on-analog technique was used.

If the trim setting made before unsnubbing were not accurate enough, the model would drift into the upper or lower alpha-stops. In these cases, the pilot would move the canard in order to fly the model off the stop, and then retrim before it drifted into another stop. As in actual flying, practice makes perfect, i.e., practice led to smooth take offs.

Similarly, to "land" the model, snubbing was gradually applied and the SAS simultaneously turned off. Again, practice produced smoother landings. In the case of BFF encounters, the rapidity of the actions - rather than the specific order - was appreciated.

With the model flying unsnubbed, data were ready to be gathered. Plots of system frequency response were generated by turning on the random-noise input to the canard and using the dual channel analyzer to process two signals, the dynamic servo command signal (input) and the analog command signal (output). Also peak-hold and randomdec (Ref. 12) data were gathered to give estimates of the proximity to a dynamic instability. When data collection was complete, the random-noise input was turned off; and, if another control law were to be evaluated at that flight condition, the model was snubbed ("landed"). By resetting dial potentiometers on the analog computer, the next control law was readied for use. When all control laws were tested at a given test condition, typically the model would be flown to the next operating point without resnubbing.

When an instabililty was encountered at a given test condition, the model was snubbed. The next control law then would be tested anyway, because different control laws could and did have different instability speeds. If no control laws were found to be stable, a higher dynamic pressure would not be attempted at that Mach number.

6.3.3   Data Reduction Procedures and Test Results - The data acquired during this test may be separated into three main categories: data pertaining to the safe operation of the model within the tunnel envelope, control law implementation and flutter/divergence detection. A block diagram (Figure 51) indicates model instrumentation tunnel interface, conditioning, and data acquisition equipment that supported the body freedom flutter test. Table 25 indicates the applicable category each parameter pertains to and the type of monitoring required for safety, control law implementation, and flutter/divergence detection. In addition to the use of alpha-stops, real time displays on both digital displays and brush recorders were used for safety to indicate when limit loads were being approached. Control law implementation data were acquired using signals available at the output of the electronic interface box. A two-channel spectrum analyzer (Digital Equipment Corporation Model 6000) was used to monitor system performance. Flutter detection was monitored on brush recorders using wing bending, wing torsion, wing tip accelerometer, fuselage accelerometer, fuselage pitch rate gyro and canard position signals.

The data were reduced and evaluated in various ways to extract basically three types of information: (1) divergence boundary, (2) SAS performance, and (3) flutter boundary

6.3.3.1   Divergence Boundary - The procedure for obtaining this boundary includes some of the steps in the procedure for obtaining angle-of-attack limits (Section 6.3.2.1). For clarity, the discussion of those steps is repeated in the following description:

Because the model had been structurally modified for this project, the divergence boundary measured in 1979 was no longer representative of the model. Thus, to ascertain a new wing-divergence boundary, wing-root bending moment data were examined. These data were gathered for various flying (unsnubbed, trimmed) and restrained (model unsnubbed and bearing against the stops, or model snubbed and not bearing against stops) conditions. These measurements obviously reflect wing-root flexibility due to the new fuselage and back-up structure and, thus, constitute a suitable base-line against which the flutter-boundaries should be compared. The data were sorted by Mach number ($\pm$ 0.1) and dynamic pressure ($\pm$ 1.0 psf). The angle of attack (α), canard incidence (i_c) and bending moment (M_B) were noted. Because of trim requirements for the flying conditions, only a very small variation in α was obtained for a particular condition ($\bar{q}$, M, CG). Hence, at a given ($\bar{q}$, M) point, significant variations of α in the data were generally associated with (1) variations in CG and , hence, i_c or (2) snubbing. Consequently, the data were insufficient to determine the dependence of M_B on i_c and α independently. Assuming that the dependence of wing loads on i_c is secondary to the dependence on alpha, bending-moment slopes ($\Delta M_B / \Delta \alpha$) were obtained from the data. Figure 49 shows a representative plot and gives an indication of the amount of scatter in the data and the associated variation in slope. For each Mach number, these slopes were plotted versus the slopes per dynamic pressure (Southwell method of Reference 13) , and projections of divergence were made (see Figure 52). Similarly, the Divergence Index Method (Reference 13) was employed to obtain divergence projections (see Figure 53). Figure 54 shows the resultant divergence boundary and the 1979 clamped-wing boundary for comparison. As can be seen a large amount of uncertainty exists in the present boundary. It is clear, however, that the boundary is 10% to 20% lower than in the original test. This trend is consistent with the presence of additional wing-root-flexibility in the new model. (In subsequent comparative plots in this report, the 10% to 20% curves will be used to represent the divergence results.) The large uncertainty obtained in the present test was not characteristic of the 1979 test reported in Reference 5. Three factors are responsible for this: (1) Because the present model had to fly, it was not mounted

on a turntable; consequently, angle of attack could not be varied directly or precisely. (2) For the same reason, canard incidence and angle of attack could not be varied independently. (3) The model was not tested at dynamic pressures close to divergence, because BFF precluded this.

6.3.3.2   SAS Performance - A two-channel signal analyzer was used to generate system frequency response functions (FRF) during the test. First, the model was excited by injecting a pseudo-random noise signal into the canard command summing junction indicated in Figure 37. Two pseudo random noise signals were used - one band-limited to 20 Hz, the other to 10 Hz. Each was obtained by playing a pre-recorded digitally generated cassette tape. For the frequency range of interest in the test (less than 10 Hz), acceptable results were obtained with each. Then to obtain the FRF between any two points in the SAS, the signals at both points were selected at the EIB and fed into the analyzer as input and output channels. The analyzer digitally sampled these signals and by Fast Fourier analysis Techniques (FFT) computed the FRF, which was then displayed as plots of gain and phase versus frequency (Bode plots). Of most interest was the SAS open-loop FRF. This was obtained while the SAS was operating (closed-loop) by choosing the summing junction output (signal into the actuator servo) to be the input channel and choosing the analog computer output to be the output channel of the analyzer. (See Figure 37.)

By comparing a series of test-generated Bode plots at increasing dynamic pressures to a similar series obtained by pre-test analysis, an indication of SAS performance was obtained. In particular, the onset of BFF could be anticipated. A typical sequence of test plots is shown in Figures 55, 56 and 57. The test configuration was CG 231 (high static instability) at M = 0.8, using SAS control law C2-4. The dynamic pressures associated with the three figures are 77, 90 and 100 psf. (As is typical in experimental FRF's of this type, the gain curve is much more reliable than that of phase; therefore, discussion will be limited

to those curves.) Three trends are apparent in Figure 55: (1) The
dynamics of the "rigid body" and the cable system combine in the low
frequency range (0 to 2 Hz) delaying the expected roll-off and, hence,
maintaining the gain at 0 dB. (Note, in these gain plots, the vertical
scale is actually semi-dB, i.e. ten times log-base-ten, not twenty times
log-base-ten.) (2) Beyond 2 Hz, a characteristic roll-off is observed
to about 8 Hz. (3) Between 8 to 10 Hz, the roll-off is again
delayed due to the effect of the first wing bending mode. As the
dynamic pressure is increased, the wing bending mode can be expected to
drop in frequency (destiffen). This trend is clearly evident in Figure
56, where the roll-off is delayed at frequencies near 6 Hz due to the
wing mode. As this destiffening progresses, the wing bending mode
approaches the short-period (or rigid-body) frequency range and BFF
should result. Figure 57 shows the type of FRF obtained at a condition
of imminent BFF. Both the FRF plots and the analyzer input and output
channel time histories are displayed. At this flight condition, the
aeroelastic coupling has caused the short period mode to become almost
neutrally stable. Thus, the random noise and tunnel turbulence cause
the model to respond at essentially a single frequency. This is
apparent in the input/output time histories, which appear nearly
harmonic with little overtones. Because the energy content at this
frequency far outweighs that at any other frequency, the FFT can no
longer extract a meaningful FRF. It does, however tend to give a flat
o-dB/o-phase region around the frequency of the instabiltiy.

Two additional checks and demonstrations of the SAS performance
were made during the test. The first was a direct verification of its
ability to stabilize an otherwise unstable configuration; the second was
an attempt to estmate the damping of the system with the SAS engaged at
a point well below BFF. These are discussed in the next paragraphs.

The brush recordings in Figure 58 document the SAS verification.
Three traces are shown: fuselage Nz acceleration, fuselage pitch rate,
and canard command. The test configuration is the moderately unstable
static margin case (CG 225); the flight condition is M = 0.86, $\bar{q}$ = 58

psf; and the SAS control law is Cl-1. As the trace begins, the model is trimmed and flying. At the point indicated, the SAS is turned off. Within one second, the model can be seen to oscillate; within two seconds the motion was rapidly diverging. At three and a half seconds, the SAS was re-engaged and, as seen, the oscillations quickly subsided. (It should be explained that, although on a freely flying aircraft departure would have occurred when the SAS was turned off, on the wind tunnel model the oscillatory behavior observed was to be expected. This difference is due to the influence of the cable-support system.)

The next investigation was attempted to estimate short period damping. The randomdec procedure of Ref. 12 was initially used for this purpose and for obtaining flutter-speed projections. Its reliability was questioned, however, because the damping estimates were consistently lower than reasonable and did not always converge to a zero-damping point. Subsequently, the peak-hold technique was used to obtain flutter-speed projections, as described in Section 6.3.3.3. The following estimate of damping was attempted for one condition/configuration: With the model trimmed and flying (CG231, C2-4, M = 0.85 and $\bar{q}$ = 90), a series of short pulses was electrically injected into the canard command channel and the transient response of the model was observed. Figure 59. shows the strip chart recording of this test. The three traces are fuselage accelerometer, fuselage pitch-rate gyro, and the canard pulse. The model response to the pulses is most clearly visible in the pitch rate trace. Prior to pulsing, the background gyro signal is ± 0.25 deg/sec. This is the response to tunnel turbulence. The response to the pulse peaks between 1.0 and 1.5 deg/sec and settles down to the background level within one to two cycles. The damping ratio estimate is approximately 0.15. (For comparison, the randomdec estimate for this point was less than 0.1.) This damping verifies that the SAS successfully fulfills its function (supplying damping to an otherwise unstable configuration) at flight conditions sufficiently below BFF.

47

6.3.3.3 <u>Flutter Boundaries</u> - Two types of related dynamic instabili-
ties were actually encountered in the test: (1) body-freedom-flutter
(BFF), characterized by a dynamic coupling between wing bending and a/c
pitching motions and (2) basic a/c short-period instability (SPI),
occurring on the statically unstable configurations when the control
system loop-gain was insufficient to stabilize the model. Attempts to
distinguish between them will be discussed below. The methods used to
identify an occurrence of either type were essentially the same.

o   <u>Procedures</u> - First, visual observations made and recorded during
     the test were consulted to identify probable instances of instabi-
     lity. A corresponding set of tab points was compiled from the run
     log. Next brush records and video tapes (where available) were
     examined in detail for those tab points. Figures 60, 61 and 62
     show excerpts from the brush records for three of those points. In
     incidences like those of Figures 60, and 61 the neutrally damped or
     negatively damped harmonic motion is readily apparent and, without
     question, an instability can be said to exist. In incidences like
     that of Figure 62, the absence of a clear trend makes such pro-
     nouncements difficult. Based on these evaluations, each point was
     proclaimed either stable, unstable, or lightly damped ("close" to
     unstable).

     Next, because in many cases no instability was observed to the
     highest dynamic pressures tested (e.g., configuration c.g. 225),
     the peak-hold spectra and randomdec data gathered during the test
     at subcritical points were analyzed. In general, the randomdec did
     not produce useful projections (too much scatter/did not converge
     to zero damping, as in Figure 63) while the peak-hold data did
     (albeit, with considerable uncertainty bands for certain configura-
     tions). Figure 64 shows a representative plot of a peak-hold
     spectrum obtained using the pitch-rate gyro data for one tab point.
     From such plots, the amplitudes of the resonant peaks of the
     flutter mode were read. The inverses of these peak amplitudes were
     then plotted as functions of dynamic pressure, as in Figure 65, and

extropolated to determine the instability point, i.e. the dynamic pressure at which 1/A would become zero. Finally, as described in Section 6.3.3.2, the Bode plots generated on-line during the test were examined to detect trends of approaching instability with increasing dynamic pressure.

Using all of the various techniques discussed above, instability boundaries were generated. Before these are discussed in detail, a slight digression is necessary.

o   SPI and BFF - As mentioned previously, two types of dynamic instabilities were possible, body-freedom flutter (BFF) and the aircraft short-period instability (SPI). How can they be distinguished? SPI involves only the short-period dynamics; it can occur even on rigid configurations. Consequently, it can be characterized by the absence of dynamic coupling between rigid and flexible motions and, hence, the absence of phase difference between such motions. On the present model, this means that nose-up pitching motion should be in phase with tip-up wing bending; thus, the pitch rate should lead the wing-bending moment by roughly 90 degrees. Figure 66 shows the brush records of an instability that demonstrated this characteristic during the test. This was an instance of SPI. On the other hand, an occurrence of BFF involves the dynamic aeroelastic coupling of two modes of motion, the short-period and the primary wing-bending modes. Thus, it is characterized by a phase difference between these two motions. In a severe instance, pitching motion might lead wing bending by 90 degrees; thus, pitch rate would be 180 degrees out of phase with wing bending moment. For the configurations tested on the present model, analysis indicates that 130 degrees phase difference is to be expected. Figure 67 shows the brush records of such an instance (phase difference of approximately 100 to 120 degrees) of BFF. Unfortunately, not all cases were as distinct as these two. Typically, the phase differences lay somewhere between 90 and 130 degrees and could not be determined to an accuracy

better than 20 degrees. Furthermore, from a practical viewpoint, there is always some dynamic coupling between wing bending and aircraft pitch, even at low dynamic pressures. Thus, the theoretical distinction between SPI and BFF is hard to draw. Consequently, the following indirect method of discriminating between BFF and SPI was used:

From the analytical studies of Reference 4, it is known that the present canard-based SAS cannot suppress BFF to a significant degree, because it can only weakly observe (thru fuselage mounted sensors) and weakly control (thru canard/wing aerodynamic inter- action) the destiffening of the wing-bending mode. Thus, changes in SAS control-law should have little effect on BFF but a large effect on SPI. In reviewing the instability boundaries, several were found to fall almost on top of one another. Being independent of control law, these boundaries were identified as BFF. The other instabilities were called SPI. The SPI points and boundaries occur at lower dynamic pressures than do the instances of BFF.

o   Results - Figures 68 through 76 are the boundaries generated. Cross hatching indicates a band of uncertainty in identifying the critical dynamic pressures from the test. Those cases, such as CG213 (Figure 68), for which boundaries are defined over a range of Mach numbers, exhibit a transonic dip appearing as early as M = 0.70. (This behavior has been observed in other flutter tests of wings with supercritical airfoil sections.) The lower limit of the uncertainty band for those cases that are identified as BFF is shown in Figure 77. The definite occurrences of SPI are as follows: C1-4 at 82 psf, M = 0.85 and C2-1 at 84 psf, M = 0.85. These fall well below the composite boundary of Figure 77. Cases that are somewhat below the boundary but that possibly could be thought of as BFF anyway are as follows: all of C2-3 and C2-4; C1-1 at 100 psf, M = 0.85; and C1-3 at 104 psf, M = 0.85.

Determination of flutter frequencies was made from inspection of
the brush records, peak hold spectra and FRF's. Plots of these
results are shown in Figures 78 through 86. As can be judged by
the scatter, the accuracy of these data is poor.

6.3.4. Comparative Results and Discussion

Examining Figures 68 through 75, we see that the BFF boundaries are
similar for all configurations. Table 26 summarizes comparative results
at M = 0.60 and 0.85. Virtually the same results were obtained for the
statically stable CG (CG213), one of the moderately unstable configura-
tions (CG 225, C1-3), and one of the highly unstable configurations
(CG231, C2-4A). This is consistent with the fact that the SAS system
was designed to make the unstable configurations behave as if they were
stable. In other words, it is not the open-loop static margin but,
rather, the closed-loop dynamics that influence the occurrence of BFF.
Table 26 also shows that variations in the control law (e.g., C2-4,
C2-3, and C1-3) can lower the BFF speed somewhat. However, very low
instability speeds (such as for C2-1 and C1-4) are actually an indica-
tion of SPI and, as such, can be alleviated by a simple increase in the
SAS overall loop gain. (This contention was verified in the test by
increasing the loop gain by 50% for configuration C1-4 after
encountering an instability at 81 psf, M = 0.85. Thereafter, the model
was able to fly at that condition successfully with no indication
whatsoever of instability.)

From observations of the model's behavior during testing, it can be
concluded that the onset of BFF is mild or gradual. This in undoubtedly
a reflection of the low frequency (2 to 4 Hz) of the instability. Also
the model flies well (motions are reasonably damped) to within 10% of
the flutter speed. This implies that longitudinal flying qualities are
not compromised until BFF is imminent.

Examination of the BFF boundaries shows the transonic dip is not abrupt but rather gradual, occurring over an interval of 0.2 in Mach number. Referring to Figure 77, the minimum transonic flutter speed occurs near M = 0.85. The minimum flutter speed divided by the estimated subsonic (M = 0.6) flutter speed is between 0.92 to 0.86; i.e., the dip is 8% to 14% in speed. These effects and the early onset of the dip (approximately, M = 0.70) are attributed to the supercritical airfoil on the model wing and are judged not to be a property of BFF in-and-of itself, because similar behavior has been observed in flutter tests of other wings with supercritical airfoils.

Figure 76 shows the test results for a special case. The configuration with highest negative static margin (CG231) was re-tested after a modification. Ballast, in the form of two lbs of lead weight, was added within the wing tip-cap. Such a small mass at that location did not noticeably change the model c.g. (or static margin) but did affect the wing bending frequency, lowering it to 7.6 Hz (a -34% change). Had the drop in frequency been caused by a decrease in structural stiffness, one would expect the wing divergence speed to be less and, hence, would expect the aircraft to encounter BFF at a lower $\bar{q}$. Because the drop in frequency was caused by the addition of mass, very little change in BFF should be expected. A comparison of the flutter point in Figure 76 with that of Figure 75 (also C2-4A control law), shows that the flutter speed was unchanged.

By comparing Figures 54 and 77, we see that BFF is (as expected) more critical than aeroelastic wing divergence. Although the large uncertainty band in the test data (particularly, the divergence data) make it difficult to quantify precisely, it is clear that BFF occurs much before divergence - at least 20% lower in dynamic pressure, perhaps as much as 42% lower. This translates to a flutter speed that is 10% to 24% lower than divergence speed. This comparative result is summarized in Figure 87.

6.4 ANALYSIS AND CORRELATION

The wind tunnel article tested was a 1/2-scale, flexible semispan model, "flying" at transonic speeds while supported by an elaborate combination of cables, pulleys, springs and rods. In addition, the model relied on a SAS control system to supply static stability for various configurations tested. While no comprehensive analysis was practical that would account for all the complexities of this unique arrangement, a great deal of effort was expended to represent analytically the major elements of the system. In particular, the aerodynamics (steady and unsteady) were represented by a state-of-the-art linear panel method (Reference 8); the vibrational characteristics were represented using mode shapes measured in the ground vibration survey; the control system was modeled with a linear state-variable procedure, using the transfer function measured for the actuator installed on the model during ground tests; and the cable support system was modelled in an approximate fashion, using a combination of measured and estimated data. The following sections describe the analytical methods used to predict the dynamic behavior of the model, the BFF boundaries obtained by these analyses and the correlation of these predictions with the test data.

6.4.1 Math Models

6.4.1.1 Aerodynamic Idealization - Figures 18 and 20 show the aerodynamic panelling used to represent the model. As described in Section 5.3.2, the idealization was tuned to better reflect the data measured in the January tunnel entry. The panelling essentially conforms to the actual geometry with the following exceptions: (1) The slender body model maintains a constant radius aft of fuselage station 230 to account for the probable flow separation or boundary layer thickening. (2) The nacelle span is reduced to 60% of its true value to reduce its effectiveness in carrying lift. (3) The canard span is reduced 5%. (4) The wing span is reduced 1.4% to account for the portion of its root that is masked by the nacelle/forward-fuselage.

6.4.1.2 Vibrational Idealization - As an aid in model and control system design, a set of preliminary analyses was performed using free-free modes, frequencies and generalized masses computed by mass coupling the measured cantilevered-wing modes of Reference 5 to the assumed rigid fuselage/canard. Design target mass and moment of inertias were used for the fuselage/canard (FC). By shifting the FC mass, the appropriate three c.g.'s were modelled. Examination of the FC motion, generalized mass and generalized frequencies in the flexible modes (Table 27) showed that the FC motion was negligible and that its contribution to generalized mass was less than 3%. This indicated that measurement of a single set of free-free modes (i.e., a single CG) would suffice for the GVS.

The modes measured in the final GVS (Section 6.2.4) were used in the final analyses presented below. Because the fuselage and canard motions were negligible in the flexible modes used, they were set to zero. The modes selected for the analyses were aircraft pitch and heave, wing first bending, wing second bending, wing first torsion, and wing second torsion/third bending.

6.4.1.3 Control System Idealization - The block diagram is presented in Figure 30. The actuator was represented by a first-order system with a break frequency of 70 rad/sec. The dynamics of the accelerometer and pitch rate gyro were not modelled. The integral compensation was represented as a pure integrator, and the feedback paths and gains were modelled in a straight-forward manner.

6.4.1.4 Cable Support System Idealization - The cable support system was modelled as shown in Figure 88. The particular values of the various elements (springs, etc.) are given in Table 28.

6.4.2 Analysis Methods

6.4.2.1 GRUMCABLE - The GRUMCABLE code (Reference 14) analyzes the behavior of a rigid, full-span, cable-mounted, wind tunnel model. Trim and rigid-body stability are determined. For use on our configuration,

54

the code was modified to represent the elements of the SAS and their interconnections. This included the feedback to the canard of both vertical acceleration and pitch rate and the integral plus proportional compensation. Additionally, the pitch stiffness introduced by the roll rods was included. The structure of the equations in the modified code is given in Table 29. The code was used to help design the model support system and, as discussed below (Section 6.4.2.3), results were incorporated in the SAEL analyses.

6.4.2.2   SAEL - The SAEL code (Reference 1) is used to analyze the stability and dynamic behavior of a freely flying flexible aircraft with or without active controls. A modal representation of the aircraft and unsteady harmonic aerodynamics is employed. The equations of motion are transformed into state variable form and the appropriate eigenvalue problem is solved at user specified flight conditions. Both discrete (digital) and continuous systems may be analyzed. For the present study, only the continuous-system capabilities were necessary.

In SAEL, the equations of motion are formulated in a body-fixed-axes system for perturbations in motion about trimmed flight. The generalized coordinates appropriate to the present application are aircraft vertical velocity, aircraft pitch rate, canard rotation, and the modal coordinates for displacement in the first four flexible wing modes. The generalized aerodynamic forces acting on the aircraft are functions of the generalized coordinates, their derivatives and their lags. This relationship is more easily appreciated when the Laplace transformation of the forces is written. For example, in Laplace notation, the functional relationship for lift due to displacement in a flexible mode is:

$$\bar{q} \; [A0_{W\xi} \cdot \xi + A1_{W\xi} \cdot \bar{s} \cdot \xi + A2_{W\xi} \cdot \bar{s}^2 \cdot \xi + \sum_{\ell=3}^{L} A\ell_{W\xi} \cdot \xi_\ell], \tag{1}$$

where

$$\bar{s} \cdot \xi_\ell + p_\ell \xi_\ell = \bar{s}\xi, \; \text{for} \; \ell = 3, \; L. \tag{2}$$

55

The four terms in Equation (1) may be thought of as aerodynamic stiffness, damping, inertia and lag forces.

One of the first tasks performed by SAEL is the determination of the coefficients, A0 to AL, in the expansion of each generalized force term. This is done by numerically fitting Equation (1) to a table of unsteady harmonic generalized aerodynamic forces computed for a chosen set of reduced frequencies using the aerodynamic math model. For the present study, six reduced frequencies were used: 0, 0.01, 0.025, 0.05, 0.10, 0.20. Separating the real and imaginary parts of each harmonic force and substituting Vk/b for s, Equation (1) becomes (omitting the W subscripts)

$$F(k) \cdot \xi = \bar{q} \left[A0 - A2 \cdot k^2 + \sum_{\ell=3}^{L} A\ell \frac{k^2}{k^2 + \bar{p}^2} \right] \xi \qquad (3)$$

$$G(k) \cdot \xi = \bar{q} \left[A1 \cdot k + \sum_{\ell=3}^{L} A\ell \frac{\bar{p}}{k^2 + \bar{p}^2} \right] \xi \qquad (4)$$

$$\bar{p} = V \cdot p/b \qquad (5)$$

for each k chosen. The SAEL code chooses A0 to match F at k=0 and determines the remaining L coefficients by a least square fit to both F-A0 and G simultaneously. Obviously, the number of non-zero reduced frequencies and the number of lag terms must be chosen such that the number of equations (twice the number of frequencies) equals or exceeds the number of unknowns (L). The locations of the poles (p_ℓ) in the lag equations are somewhat arbitrary but influence the accuracy of the functional fit, as do the number of lags and the number and values of the reduced frequencies. Numerical experimentation is typically used to obtain reasonable fits with as few lag terms as practical. Two lags were chosen with poles 0.1 and 0.2 for the present study. Figures 89 and 90 show representative fits from the present study.

Once the aerodynamic functional representation is computed, SAEL forms the rigid and modal equations of motions. Equations representing the control system dynamics and feedback structure are appended to

56

these. (Details are given in Appendix B.) Included in these equations for the present study are the particulars of the control system model discussed in Section 6.4.1.3. The complete system of equations written in standard form as

$$\dot{\underline{x}} = [A] \cdot \underline{x} + [B] \cdot u, \tag{6}$$

$$u = [D_z] \cdot \underline{Z}, \tag{7}$$

$$\underline{Z} = [E] \cdot \underline{x}. \tag{8}$$

where the state vector $\underline{x}$ includes aircraft vertical velocity and pitch rate, modal displacements and rates, aerodynamic lags, canard displacement and the integral command. The open loop system is obtained by setting $U = 0$ in Equation (6); and the closed-loop system is obtained by combining Equations (6) - (8) to give

$$\dot{\underline{x}} = [A + BD_z E] \cdot \underline{x} \tag{9}$$

6.4.2.3 **CABSAEL** - This code is simply the SAEL code with two additional variables and equations added to approximately model the cable support system. The added terms are obtained by transforming the equations of motion formed in the GRUMCABLE code. These equations are the force balance in x and z directions, the moment balance in pitch and the constraint equation arising from cable geometry. The equations were recast in state variable form, manipulated to eliminate algebraically dependent variables, and transformed to the body-axis system used in SAEL. The resulting equations can be written symbolically as

$$\begin{bmatrix} \dot{W} \\ \dot{Q} \\ \dot{z} \\ \dot{\theta} \end{bmatrix} = \begin{bmatrix} a_{11} & a_{12} & a_{13} & a_{14} & a_{15} \\ a_{21} & a_{22} & a_{23} & a_{24} & a_{25} \\ 1 & 0 & 0 & 0 & -V \\ 0 & 1 & 0 & 0 & 0 \end{bmatrix} \cdot \begin{bmatrix} W \\ Q \\ \delta \\ z \\ \theta \end{bmatrix} \tag{10}$$

where Vo is the free stream velocity. The values of a_{11} to a_{13} and a_{21} to a_{23} computed by and present in SAEL were left alone. Only the cable coupling terms (a_{14}, a_{15}, a_{24} and a_{25}) and the last two equations above were added to produce "CABSAEL". Because the SAS system on the model feeds back a vertical acceleration measurement and vertical acceleration is dependent on $\dot{w}$, the cable coupling terms also must be present in the CABSAEL control system equations. In particular, the following terms were added in the z and θ columns of the actuator, the integral command and the actuator lag equations:

$$\dot{\delta} = \cdots - K_1 \cdot a_{14} \cdot z - K_1 \cdot a_{15} \cdot \theta$$

$$\dot{\delta}_I = \cdots - K_2 \cdot a_{14} \cdot z - K_2 \cdot a_{15} \cdot \theta$$

$$\dot{\delta}_\ell = \cdots - K_1 \cdot a_{14} \cdot z - K_1 \cdot a_{15} \cdot \theta \qquad (11)$$

where

$$K_1 = \frac{K_{NZ}}{g} \left(\frac{K_F \cdot K_L}{\tau(1 + K_F \cdot K_\alpha)} \right) \qquad K_2 = \frac{\tau \cdot K_I}{K_F} \qquad (12)$$

Similarly, because the aero lag equations associated with W involve $\dot{w}$, terms a_{14} and a_{15} also were added to the z and θ columns of these equations to give

$$\dot{W}_\ell = \cdots + a_{14} \cdot z + a_{15} \cdot \theta \qquad (13)$$

for each of the two W-lag equations.

6.4.2.4 <u>Aerodynamic (Aero) Corrections</u> - Although the aerodynamic math model was tuned to better represent the rigid data inferred from the January aerodynamic test, this adjustment by itself cannot guarantee that the aerodynamic forces computed at non-zero dynamic pressures will agree with the flexible aero data-base generated in that same test. SAEL, however, enables the user to make further corrections to assure this compatability. It does this thru the use of input multiplicative factors on the various aerodynamic force terms. These factors can be scheduled for each separate condition (configuration, Mach number and

dynamic pressure) analyzed. This procedure was followed in the analyses to be presented.

To illustrate the procedure, we will write the static rigid and flexible forces needed for equilibrium as

$$
\begin{bmatrix} F_R \\ F_F \end{bmatrix} = \begin{bmatrix} f_{R\alpha} \cdot A_{R\alpha} & f_{RF} \cdot A_{RF} & f_{R\delta} \cdot A_{R\delta} \\ f_{F\alpha} \cdot A_{F\alpha} & (f_{FF} \cdot A_{FF} - K_{\xi\xi}) & f_{F\delta} \cdot A_{F\delta} \end{bmatrix} \cdot \begin{bmatrix} \alpha \\ \underline{x}_F \\ \delta \end{bmatrix} \tag{14}
$$

where the f's are matrices of multiplicative factors.

Typically - as in the January aerodynamic test - only total forces (lift and moment) are available from test data. In the present study, only $f_{R\alpha}$ and $f_{R\delta}$, are used i.e., factors on the rigid components of lift and pitching moment due to angle of attack and canard incidence. Thus,

$$
\begin{bmatrix} F_R \\ F_F \end{bmatrix} = \begin{bmatrix} f_{R\alpha} \cdot A_{R\alpha} & A_{RF} & f_{R\delta} \cdot A_{R\delta} \\ A_{F\alpha} & (A_{FF} - K_{\xi\xi}) & A_{F\delta} \end{bmatrix} \cdot \begin{bmatrix} \alpha \\ \underline{x}_F \\ \delta \end{bmatrix} \tag{15}
$$

To compute these factors, the flexible forces are set to zero and the lower equation is solved for the flexible displacements, $\underline{x}_F$. These are then substituted back in the top equation,

$$
[F_R] = ([f_{R\alpha} \cdot A_{R\alpha} \quad f_{R\delta} \cdot A_{R\delta}] - [A_{RF}] \cdot [A_{FF} - K_{\xi\xi}]^{-1} \cdot [A_{F\alpha} \quad A_{F\delta}]) \cdot \begin{bmatrix} \alpha \\ \delta \end{bmatrix}
$$

$$
\tag{16}
$$

The two resulting terms are the rigid and modal contributions to the total forces. SAEL computes and prints each component and the total;

thus, it is a simple manner to calculate (for each condition) the factors f_{R_α} and f_{R_δ} required to make the total forces equal the corresponding values in the experimental data base.

6.4.3   Results and Correlations

6.4.3.1   Preliminary Predictions - Prior to the August flutter test, various series of GRUMCABLE, SAEL and CABSAEL analyses were conducted to help design the model and its control system and to predict the dynamic behavior of the model in the tunnel. The data in these analyses changed as the design evolved. Because these calculations are rather unconservative when compared to the experimental results, a brief review is presented to identify the source of this unconservatism.

First, some typical results of the GRUMCABLE analyses are discussed. Figures 91 shows the root loci (with increasing dynamic pressure) for the statically stable configuration at M = 0.9. A similar plot is shown in Figure 92 for the highly unstable configuration with the pre-test version of SAS control law C2-3. In each figure, two roots appear. These correspond to the short period mode and a cable-related plunge mode. In Figure 91, the cable mode is relatively unaffected by dynamic pressure; whereas, in Figure 92, the presence of the SAS causes this mode to change as $\bar{q}$ is varied. Notice that in neither case does an instability occur in either the short period or cable mode. Earlier GRUMCABLE analyses indicated the presence of a cable-mode instability; the cable support system was tuned to eliminate this problem. This tuning consisted of increasing the rear-cable tension, moving the lift-cable atttachment point farther aft and moving the drag-cable attachment point farther forward. The absence of a short-period mode instability is to be expected because (1) the SAS is designed to prevent an occurrence of SPI and (2) no BFF can be predicted without the presence of flexible modes in the analysis.

Next, some basic SAEL results are presented. Figures 93 and 94 correspond to the two cases discussed above. These SAEL analyses do not include any modelling of the cable support system; thus, the cable-root

is not present in the loci. On the other hand, the flexible modes are included (though, only the lowest such mode is shown in the figures). The presence of the first wing bending, in particular, makes BFF now possible; and its occurrence can be seen clearly as the short-period mode curves unstable with increasing dynamic pressure.

Finally, the corresponding pre-test CABSAEL analyses (Figures 95 and 96) are presented. The loci are a combination of the GRUMCABLE/SAEL results. The cable root is present in the CABSAEL results and behaves in a manner similar to that predicted by GRUMCABLE. The flexible wing roots behave as in SAEL. The short-period root, however, follows the GRUMCABLE trend at low dynamic pressure and the SAEL trend (toward instability) at high $\bar{q}$'s. On Figure 97, which is an overlay of Figures 92, 94 and 96, these trends can be more clearly seen.

Table 30 compares pre-test predictions, post-test analyses, and test data for one particular configuration. It also identifies the principal differences between the various analyses. The pre-test SAEL and CABSAEL predictions of BFF speed are seen to be quite unconservative - 18% and 14%, respectively - whereas the final CABSAEL results are only slightly (5%) unconservative. As documented in the table, the most significant factor contributing (6%) to the extra 9% conservatism in the original CABSAEL analysis is the absence of $\bar{q}$-scheduled aero corrections in the pre-test analyses. Thus, the procedure of Section 6.4.2.4 is shown to significantly improve the accuracy of the analyses.

The necessity of using the correction factor procedure deserves some comment. Without these corrections, the analysis relies on a truncated set of modes to account for the flexibility of the structure. It is a well-known fact that the truncated mode approach is inaccurate for predicting static aeroelastic effects, such as divergence. (See Reference 6 for sample comparisons.) Because BFF is a low-frequency phenomenon, accurate representation of the static aeroelastics of the problem undoubtedly is critical to predicting BFF also. Although the data-base used to derive the static corrections for the present study was derived from test data, an analytical flexibilization of rigid

experimental derivatives using structural influence coefficients probably would have provided acceptable results. Subject to availability, the use of flexible test data is, of course, preferable.

6.4.3.2 Final Analyses - For final correlations, CABSAEL analyses were conducted at three Mach numbers (M=0.6, 0.8 and 0.9) for all configurations/ control-laws tested. Root loci were generated over a range of dynamic pressure sufficient to define the point of instability in each case. These final analyses used the tuned aerodynamic math model, the aerodynamic correction procedure, the measured GVS modes, the control system math model of the SAS as tested, and cable support system data as measured on site. Appendix C presents the root loci for all cases. Illustrative samples at Mach= 0.90 are extracted as Figures 98 through 100.

Figure 98 shows the results for the statically stable configuration. The trends are similar to those of the pre-test analysis (Figure 95), but the short-period mode is more lightly damped and goes unstable at a lower dynamic pressure. Figure 99 is the counterpart of Figure 96. In this case (C2-3), the behavior of the cable mode is somewhat different that seen in the pre-test analyses. As dynamic pressure is increased, the mode first becomes critically damped, then combines with an aerodynamic lag root and loses damping. The short-period mode is lightly damped at all speeds and abruptly goes unstable at 113 psf. Figure 100 shows a case (C1-4) which analysis predicts to be unstable at a very low dynamic pressures (40 psf); however, the configuration was successfully flown at 54 psf in the test. The root locus shows the amount of negative damping (i.e., the predicted level of instability) to be quite small at low pressures. Thus, a reassessment was made of the analysis results by assuming the existence of a small amount of structural damping (5% - equivalent to a damping ratio of .025). For C1-4, this change led to a predicted instability occurring at 60 psf, which more accurately reflects the test data. In the correlations presented below, the existence of this level of damping was assumed in all cases.

Figure 101 presents the analytical flutter boundaries for the three configurations and the various control laws tested. The predicted effect of compressibility is seen to be a lowering of flutter speed by about 7% to 8% (14% to 16% in $\bar{q}$) in each case. This is less than the true transonic flutter dip encountered in the test (8% to 14% in speed). Such a discrepancy is typically encountered in conventional flutter testing and is caused by deficiencies in the linear aerodynamic theories. Figure 101 shows that analysis predicts three major trends borne out by the test: (1) a relative insensitivity of flutter speed to configuration (open-loop static margin); (2) a relative insensitivity of flutter speed to control law variations; and (3) instances of SPI occurring when the control is too weak (e.g., C1-4 and C2-1).

Figures 102 through 107 show comparisons of the analytical and experimental flutter boundaries for the six cases in which enough test data exist to define a boundary, i.e., CG213 open loop, C1-1, C1-3, C2-3, C2-4 and C2-4A. Comparisons for the other cases (C1-2, C1-4, C1-4A, C2-1 and C2-2) are limited to analytical boundaries and isolated test points. They are presented in Figures 108 to 112. As might be expected, the best correlation is obtained for the configuration without SAS. As Figure 102 shows, the analytical flutter speed predictions are. slightly conservative in the subsonic regime (-3% at M = 0.6) and slightly unconservative in the transonic regime (+3% at M = 0.85). Most of the SAS configurations show the same trend - slightly conservative subsonically, slightly unconservative transonically - but there are two instances (C2-3 and C2-4) where analysis is also somewhat unconservative at subsonic speeds. Table 26 summarizes the flutter speed correlations at M = 0.6 and M = 0.85. At M = 0.6, the correlation is generally excellent, -3% to + 6%. At M = 0.85, correlation is not quite as good, +3% to +10%, and analysis is consistently unconservative.

Also listed in the table are results for the cases with limited test data, i.e. C1-2, C1-4, C1-4A, C2-1 and C2-2. Here the correlation is less definitive and requires some explanation. C1-2 was flown at 55 and 81 psf but there were insufficient data for projecting the

BFF speed. Analysis agreed that the case flown would be stable. C1-4 was stable in the tunnel at 54 but not at 81 psf. Analysis (at M = 0.9) predicted the onset of an instability (SPI) between these points (60 psf). As predicted by analysis, a 50% increase in loop gain (C1-4A) stabilized this case at 81 psf. C2-1 was stable at 65 psf in the tunnel and unstable at 84 psf. The analysis root locus for this case (M = 0.9) shows a small region of stable flight at about 90 psf and predicts instability at both higher and lower dynamic pressures. This analytical result, however, is very dependent on the assumed level of structural damping. It would appear that good correlation for such a marginally stable case is not possible. Finally, C2-2 was stable in the tunnel at both 65 and 84 psf, but there were insufficient data for a projection of BFF speed. The analysis also predicted stability for this case at the conditions tested. For all of these cases, with the possible exception of C2-1, analysis agreed qualitatively with the test data.

6.4.3.3 Instability Frequencies - Figure 113 shows the instability frequencies for each configuration as predicted by analysis. In each case, the frequencies fall between 1.0 and 2.0 Hz. They decrease about 0.25 to 0.5 Hz as Mach number increases from 0.6 to 0.9. Comparisons of these results with the test data of Figures 78 through 86 show the test frequencies to be approximately 1.5 Hz higher than predicted. Investigation of this discrepancy reveals the following: (1) At the lowest dynamic pressures tested, spectral data show two model/cable rigid-body modes - one at 0.5 Hz and one at 2.0 to 2.5 Hz. (2) Wind-off data, however, show frequencies of 0.5 and 1.0 Hz. (3) The GRUMCABLE and CABSAEL analyses predict the low-$\bar{q}$ or wind-off frequencies to be 0.5 and 1.0 Hz. It is concluded that additional structural stiffness arises when the wind is turned on and that the absence of these terms in the analyses causes the discrepancy in frequency correlation. A possible physical source of this extra stiffness might be the "relaxed" snubber cables, which are stretched taut when the wind is turned on. Similar wind effects might also impact the other cables (lift and drag) but to a lesser extent because they are pre-loaded in tension.

To prove that an additional structural spring would change the flutter frequency but not the flutter speed, CABSAEL runs of configuration C2-4A were made arbitrarily increasing various cable spring terms. Figures 114 through 116 show representative results. In Figure 114, term a_{14} of Equations (10) through (13) was increased; in Figure 115, term a_{25} was increased. These changes represent basically independent variations in the springs resisting lift and pitch. In Figure 116, all of the cable terms (a_{14}, a_{15} a_{24} and a_{25}) were varied simultaneously to model an additional spring located at a distance from the model c.g. equal to that at which the snubbers were attached during the test. In all of these three cases, the flutter frequency was significantly increased by (0.5 to 2.0 Hz) but the flutter speed remained relatively unchanged (± 1%). (Of course, there is a limit to this. One would not be able to raise the frequency by 5 Hz, for example, without expecting drastically different results.) This finding is consistent with the hypothesis, put forward above, that the frequency discrepancy could be attributed to missing structural stiffness terms in the analysis and gives reassurance that the absence of these terms does not invalidate the flutter speed correlation.

6.4.3.4   Frequency Response Functions - The SAEL code has the capability of generating open-loop frequency response functions (Bode plots) for the system. This was done for one of the configurations tested in the wind tunnel, i.e. CG 225 C1-1 at M - 0.80, so that comparisons could be made with Bode plots measured on-line during the test. Because the SAEL Bode plot capability has not been extended to include the cable system dynamics added in CABSAEL, an exact correlation is not possible. The absence of the cable dynamics primarily affects the trends obtained in the low (0 to 1.5 Hz) range. Figures 117 through 119 present the SAEL Bode plots and the corresponding test data. The test data was measured only up to 10 Hz (62.8 radians per second.) Note that different scales are used in the upper and lower plots of each figure. In the upper plots, the ordinate scale is in dB's, and the abscissa scale is logarithmic in rad/sec. In the lower plots, the ordinate scale is in semi-dB's (i.e., dB/2) and the abscissa scale is linear in Hz.

In each figure, various fundamental characteristics of the system are apparent in the SAEL results. Inspecting the gain curves, one can see an initial 20 dB/decade roll off. This is due to the integrator in the SAS control system. In four frequency ranges (30 to 60, 190 to 210, 290 to 320 and 430 to 460 radians per second), characteristic second-order-system dynamics are present. The gain curve levels off or actually increases at each natural frequency and, thereafter, rolls off at an increased (40 dB/decade) rate. This behavior is caused by the flexible wing modes in the system. The four frequencies in question are the frequencies of these modes at the flight conditions analyzed and, thus, vary somewhat between Figures 117 and 119. In particular, the first wing bending mode can be seen to drop from about 52 radians per second at 65 psf (Figure 117) to 35 at 110 psf. (This is consistent with the SAEL root locus for this case.) The test data overlaid on these figures correlates well with the analytical trends over the 10-to-60 rad/sec range. As mentioned previously, the cable dynamics present in the test data strongly affect the results below this range and no data was gathered above this range.

7.0   CONCLUSIONS

As discussed in the Introduction, the study had two sets of objectives: the primary set related to obtaining, through experiment, a more complete understanding of body freedom flutter on FSW configurations with and without RSS. The secondary objective was to evaluate an analysis method for predicting the phenomenon. Conclusions relevant to the primary objective are:

o   BFF was experimentally verified to occur on a realistic FSW configuration, with and without RSS.

o   The flutter boundary exhibited a transonic dip of 8% - 14% (in speed) characteristic of classical flutter.

o   The transonic dip had an early onset (M = 0.7) and reached its minimum at a relatively low Mach number (0.85). This is characteristic of the supercritical airfoil section of the wing of the model.

o   BFF occurred 10% - 24% lower in speed than did static aeroelastic wing divergence.

o   The characteristic destiffening of the primary wing bending mode was traced to the onset of BFF, using frequency response functions generated on-line during the test, to confirm the frequency coalescence between that mode and the rigid-body (short-period) mode.

o   The model exhibited no degradation in longitudinal flying qualities until within 10% of the BFF speed.

o   The onset of BFF was relatively mild due to its low frequency and could be best tracked in the pitch rate signal.

Using a canard-based SAS, the model was successfully flown in configurations that had significant negative static margin (up to 25% unstable). The following conclusions pertain to this RSS aspect of the study:

o   When the SAS is properly implemented to give short period dynamics similar to those of the statically stable configuration, the BFF speed boundaries are essentially the same as that of the statically stable configuration.

o   When the SAS is designed to give inadequate short period damping, (degraded flying qualities) the static aeroelastic interaction between wing-bending and the short period mode causes instability at low speeds. This is SPI, not BFF, because dynamic interaction is not evident.

o   When the SAS is designed to give higher short period damping than the statically stable configuration, the BFF speed can actually be somewhat higher than that of the statically stable configuration.

o   BFF is not dependent on the open-loop static margin but rather on the equivalent closed-loop dynamics provided by the SAS.

o   The onset and appearance of BFF on the RSS configurations were similar to those of the statically stable configuration and could be best tracked on the pitch-rate and canard-position signals.

The major conclusions relative to the secondary objective are:

o   The SAEL code is a good tool for analyzing the servo-aeroelastic interactions characteristic of FSW configurations with RSS. (Only the continuous-system capabilities were verified in the present study.)

68

o   BFF speed predictions are very good (-3% to +6%) at subsonic
    conditions; they are acceptable but consistently unconserva-
    tive (+3% to +10%) in the transonic regime.

o   Although a 7% to 8% decrease in flutter speed was predicted
    between M = 0.6 and 0.9, the code does not accurately predict
    the transonic dip. This shortcoming is felt to be a limita-
    tion of the linear aerodynamic theory used.

o   The use of aero corrections factors to match static flexible
    aerodynamic derivatives contributed significantly to the
    accuracy of BFF speed predictions. In the present study, an
    experimental data-base of flexible derivatives was measured
    and, thus, was available for this purpose. Data derived from
    the analytical flexibilization of rigid test derivatives using
    structural influence coefficients would probably be an
    acceptable alternative.

8.0 RECOMMENDATIONS

Because BFF was found to have a profound effect on the stability of FSW configurations, a reliable predictive tool such as SAEL is considered essential in the design of such vehicles. Furthermore, because BFF was proved to occur at much lower equivalent air speeds than static aeroelastic wing divergence, and because configurations carrying external wing-mounted stores could exhibit even lower flutter speeds due to the aerodynamic effects of the stores, an active suppression system is a logical option to be considered on FSW vehicles with stores. Through gain scheduling, an active suppression system could provide the flexibility of protecting against BFF in various store loadings. Becausethe present test showed that only modest increases in BFF speed could be attained by varying the control laws commanding the canard and that these changes would directly affect the longitudinal flying qualities, a suppression system would have to rely on wing devices. The implementation of such a system on an actual aircraft would be deemed high risk; consequently, a proof-of-concept ground validation wind-tunnel test is strongly recommended. This test could be economically undertaken by further modifications to the existing 1/2-scale model used in the present study.

The inability of analysis to accurately predict the transonic dip associated with BFF identifies the need for reliable transonic unsteady aerodynamic prediction methods. Because the development and validation of these methods are still probably a decade away, transonic dynamic model tests are considered indispensible. Such tests would seem particularly necessary on configurations for which even the subsonic unsteady prediction tools are marginal, e.g. wing/stores configurations.

The present study was restricted to a continuous control system. For increased confidence in the reliability of codes such as SAEL when applied to modern digital fly-by-wire systems, a similar model test is recommended upgrading the SAS to a digital system.

70

Some of the experience gathered in performing this test is applicable to the flight testing of vehicles subject to BFF, i.e., FSW aircraft. It was observed that the build up of BFF was readily apparent in the pitch-rate signal, the canard position signal and (to a lesser extent) in the strain gage circuit monitoring wing bending moment. Control system frequency response functions also provided valuable information on the approach of BFF in the RSS configurations. Excitation of the aircraft over an appropriate frequency range (0 to 10 Hz) was conveniently accomplished using a pseudo random input to the canard; thus, the canard can serve as the flutter shaker for this phenomenon.

9.0 REFERENCES

1. Chipman, R., Zislin, A., and Waters, C., "Control of Aeroelastic Divergence", AIAA Paper No. 82-0684, SDM Conference Proceedings, May 1982.

2. Miller, G., Wykes, J., and Brosnan, M., "Rigid Body-Structural Mode Coupling on a Forward Wept Wing Aircraft", AIAA Paper No. 82-0683, SDM Conference Proceedings, May 1982.

3. Weisshaar, T., Zeiler, T., Hertz, T., and Shirk, M., "Flutter of Forward Swept Wings, Analysis and Test", AIAA Paper No. 82-0646, SDM Conference Proceedings, May 1982.

4. Rimer, M., Chipman, R., and Mercadante, R., "Divergence Suppression System for a Forward Swept Wing Configuration with Wing-Mounted Stores", AIAA Paper No. 83-2125, AFM Conference, August 1983.

5. Wilkinson, K., and Rauch, F., "Predicted and Measured Divergence Speeds of an Advanced Composite Forward Swept Wing Model", Air Force Report No. AFWAL-TR-80-3059, July 1980.

6. Chipman, R., "Aero Pre-Test and Model Properties Report for 1/2-Scale Forward-Swept-Wing", Grumman Report No. LD-901-171.1, December 1982.

7. Woodward, F. A., "Analysis and Design of Wing-Body Combinations at Subsonic and Supersonic Speeds", Journal of Aircraft, Vol. 5, No. 6, November-December 1968.

8. Giesing, J., Kalman, T., and Rodden, W., "Subsonic Unsteady Aerodynamics for General Configurations", Air Force Report No. AFFDL-TR-71-5, Part 1, February 1971.

9. Calandra, J., et al, "Forward Swept Wing Demonstrator Technology Integration & Evaluation Study", AFWAL-TR-80-3145, Vol II, December 1980.

10. Chipman, R., Rauch, F., Rimer, M., and Muniz, B., "Flutter Pre-Test and Model Properties Report for 1/2-Scale Forward-Swept-Wing", Grumman Report No. LD-10-171.1, August 1983.

11. Zanella, R., and Rowan, R., "Acceptance Test Procedure for 1/2-Scale FSW Flutter Model Control Electronics", Grumman Report No. LD-901-169.1, July 1983.

12. Ruhlin, C., Watson, J., Ricketts, R., and Doggett, R., "Evaluation of Four Subcritical Response Methods for On-Line Prediction of Flutter Onset in Wind-Tunnel Tests", AIAA Paper No. 82-0644CP, SDM Conference Proceedings, May 1982.

13. Ricketts, R., and Doggett, R., "Wind Tunnel Experiments on Divergence of Forward Swept Wings", NASA-TP-1685, August 1980.

14. Chin, J., and Barbero, P., "User's Guide for a Revised Computer Program to Analyze the LRC 16' Transonic Dynamics Tunnel Active Cable Mount System", NASA-CR-132692, July 1975.

TABLE 1 - SCALE FACTORS FOR 1/2 SCALE MODEL (MODEL/FULL SCALE).

(SCALED CONDITION, MACH 0.9, SEA LEVEL)	
LENGTH	0.5
DYNAMIC PRESSURE	0.069
MASS	0.0369
FLUID DENSITY	0.295
FREQUENCY	0.96
FORCE	0.0173
MOMENT	0.00862
INFLUENCE COEFFICIENT (SLOPE/$_{LOAD}$)	57.80
COVER THICKNESS	0.037
LONGITUDINAL PLY MODULUS (E_{11})	0.93

TABLE 2 - AERODYNAMIC MODEL INERTIAL DATA.

CONFIGURATION	WEIGHT (LB)	STREAMWISE CG (IN)	MOMENTS OF INERTIA (LB - IN^2)		
			STREAMWISE	SPANWISE	VERTICAL
FUSELAGE	499	124.6	1.05×10^4	0.94×10^6	3.70×10^5
FUSELAGE & CANARD	520	123.1	2.49×10^4	0.97×10^6	4.15×10^5
FUSELAGE, CANARD WING	568.1	125.7	5.06×10^4	1.02×10^6	4.84×10^5
FUSELAGE & WING	547.1	127.2	--	0.99×10^6	--

TABLE 3 - ORIGINAL MODEL DESIGN LOADS.

COMPONENT	REF. PT. (IN) FS	REF. PT. (IN) BL	LIFT (LBS)	PITCHING MOMENT (IN-LBS)	ROLLING MOMENT (IN-LBS)
WING	269.9	5.1	1280	44,000	49,350
CANARD	187.2	4.0	212	-	4235

TABLE 4 - ORIGINAL MODEL VIBRATION MODES.

MODE: WING BENDING
FREQUENCY: 10.4 Hz

NODE #	NORM. h	NODE #	NORM. h	NODE #	NORM. h	NODE #	NORM. h
1	.002	12	.001	22	.001	32	.001
2	.006	13	.004	23	.002	33	.002
3	.015	14	.022	24	.023	34	.002
4	.061	15	.073	25	.082	35	.021
5	.140	16	.147	26	.163	36	.079
6	.227	17	.252	27	.265	37	.159
7	.366	18	.383	28	.383	38	.258
8	.510	19	.530	29	.562	39	.401
9	.690	20	.718	30	.740	40	.573
10	.892	21	.939	31	.913	41	.755
11	1.000						

MODE: WING SECOND BENDING
FREQUENCY: 36.9 Hz

NODE #	NORM. h	NODE #	NORM. h	NODE #	NORM. h	NODE #	NORM. h
1	-.007	12	-.006	22	-.005	32	-.006
2	-.012	13	-.014	23	-.014	33	-.009
3	-.035	14	-.065	24	-.122	34	-.018
4	-.118	15	-.184	25	-.230	35	-.152
5	-.196	16	-.273	26	-.343	36	-.274
6	-.270	17	-.322	27	-.415	37	-.386
7	-.206	18	-.296	28	-.382	38	-.518
8	-.027	19	-.110	29	-.201	39	-.491
9	+.271	20	+.209	30	+.137	40	-.290
10	+.694	21	+.631	31	+.555	41	+.051
11	+1.000						

MODE: WING TORSION
FREQUENCY: 48.2 Hz

NODE #	NORM. h	NODE #	NORM. h	NODE #	NORM. h	NODE #	NORM. h
1	.011	12	-.011	22	-.011	32	+.010
2	.013	13	-.011	23	-.012	33	-.011
3	.058	14	+.012	24	-.039	34	-.016
4	.156	15	.040	25	-.079	35	-.113
5	.294	16	.082	26	-.101	36	-.194
6	.387	17	.112	27	-.140	37	-.266
7	.472	18	.093	28	-.261	38	-.348
8	.455	19	.013	29	-.412	39	-.531
9	.363	20	-.125	30	-.581	40	-.792
10	.176	21	-.313	31	-.736	41	-1.0
11	.034						

MODE: WING THIRD BENDING
FREQUENCY: 76.2 Hz

NODE #	NORM. h	NODE #	NORM. h	NODE #	NORM. h	NODE #	NORM. h
1	.039	12	.039	22	.039	32	.054
2	.043	13	.064	23	.077	33	.048
3	.065	14	.210	24	.403	34	.155
4	.089	15	.287	25	.541	35	.682
5	.044	16	.205	26	.460	36	.893
6	-.134	17	0	27	.162	37	.865
7	-.318	18	-.297	28	-.314	38	.353
8	-.345	19	-.447	29	-.620	39	-.347
9	-.040	20	-.185	30	-.421	40	-.823
10	.813	21	.556	31	.268	41	-.696
11	1.46						

TABLE 5 - COMPARISON OF MODAL FREQUENCIES (HZ).

Mode	1979 Survey	1983 Survey	Aerodynamic Test, Jan. 1984
1st Wing-Bending	10.4	10.1	10.5
2nd Wing-Bending	36.8	35.0	37.5
1st Wing-Torsion	48.2	47.9	47.7
3rd Wing-Bending	76.2	75.0	72.7

TABLE 6 - SUMMARY OF MODEL-TO-BALANCE-ADAPTER LOADS.

LOAD CONDITION CONFIGURATION	BOLT	WEIGHT ONLY			AEROLOAD & WEIGHT			AEROLOAD ONLY		
		P_X	P_Y	P_Z	P_X	P_Y	P_Z	P_X	P_Y	P_Z
FUSELAGE & WING & CANARD	1000	79.9	28.7	59.2	-9.4	-368.0	-38.0	-173.8	-397.3	-97.2
	1001	72.8	40.5	70.3	-91.7	-517.8	-32.1	-164.5	-558.3	-102.4
	1002	55.9	46.0	67.2	-86.9	-586.5	-14.6	-142.8	-632.5	-81.8
	1003	39.5	40.2	48.8	-83.8	-510.5	5.5	-123.3	-550.7	-43.3
	1004	-5.2	-19.2	-80.1	-56.6	234.4	185.0	-51.4	253.6	265.1
	1005	-100.4	-45.9	-42.3	82.1	573.1	206.9	182.5	619.0	249.2
	1006	-147.9	-63.5	178.4	206.3	817.1	-74.5	354.2	880.6	-252.9
	1007	-5.5	-26.7	246.6	24.8	358.8	-262.7	19.3	385.3	-509.3
FUSELAGE AND WING	1000	91.6	19.1	61.7	-122.8	-345.0	-44.4			
	1001	84.8	27.0	71.8	-121.6	-484.7	-35.8			
	1002	68.1	30.7	66.7	-117.1	-549.1	-13.6			
	1003	51.7	26.8	46.5	-113.8	478.1	10.8			
	1004	1.4	-12.8	-106.6	-72.0	220.0	250.1			
	1005	-113.8	-30.7	-74.3	116.0	537.2	235.5			
	1006	-180.8	-42.4	182.7	289.0	764.7	-85.7			
	1007	-2.8	-17.8	278.5	46.0	335.0	-341.9			
FUSELAGE & CANARD	1000	64.7	14.5	52.5	85.4	-18.6	46.0			
	1001	57.9	20.5	63.6	82.7	-26.0	54.0			
	1002	42.3	23.3	62.2	70.9	-29.3	51.0			
	1003	27.2	20.4	46.6	57.0	-25.4	36.4			
	1004	-9.7	-9.7	-53.9	-4.1	11.0	-116.4			
	1005	-82.4	-23.3	-14.9	-126.4	27.9	-100.2			
	1006	-111.3	-32.2	160.9	-211.4	41.4	146.6			
	1007	-11.3	-13.6	202.9	-32.5	19.1	257.0			
FUSELAGE	1000	76.4	5.0	55.1						
	1001	70.0	7.1	65.1						
	1002	54.5	8.0	61.7						
	1003	39.4	7.0	44.3						
	1004	-3.2	-3.4	-80.3						
	1005	-95.7	-8.0	-46.9						
	1006	-144.3	-11.1	165.3						
	1007	3.0	-4.7	234.8						

TABLE 7 - SUMMARY OF BALANCE LOADS.

CONFIGURATION	WEIGHT ONLY	(150 PSF) AERO + WEIGHT	(150 PSF) AERO, NO WEIGHT	LOADS AT BALANCE					
				P_X LBS	P_Y LBS	$-P_Z$ LBS	M_X FT-LBS	M_Y FT-LBS	M_Z FT-LBS
FUSE, WING CAN.	X	—	—	0	0	-548	-5861	+3046	0
	—	X	—	+100	0	+ 25	+19038	-4367	-922
	—	—	X	+100	0	+573	+24899	-7413	-922
FUSE, WING	X	—	—	0	0	-527	- 5202	+3716	0
	—	X	—	+ 96	0	- 25	+17440	-6040	-880
FUSE, CAN.	X	—	—	0	0	-520	- 4909	+2300	0
	—	X	—	+ 79	0	-374	- 2051	+4194	-642
FUSE	X	-	-	0	0	-499	- 4250	+2970	0
BALANCE WORKING LIMITS				-	-	±1500	±30000	±6000	-

76

TABLE 8 - PITCH BALANCE STIFFNESS & MODEL-ON-BALANCE FREQUENCIES.

PLUNGE		PITCH		ROLL			
				LOW		HIGH	
K LB/IN	f (HZ)	K (IN-LB/DEG)	f (HZ)	K (IN-LB/DEG)	f (HZ)	K (IN-LB/DEG)	f (HZ)
1.3×10^6	154	0.33×10^6	12.4	0.15×10^6	26.8	3.7×10^6	38.9

TABLE 9 - AERODYNAMIC TEST MODEL INSTRUMENTATION LIST.

ITEM	MEASUREMENT	DEVICE
1	Outboard bending moment	4 arm strain gage circuit
2	Outboard torsion	4 arm strain gage circuit
3	Mid bending moment	4 arm strain gage circuit
4	Mid torsion	4 arm strain gage circuit
5	Inboard bending moment	4 arm strain gage circuit
6	Inboard torsion	4 arm strain gage circuit
7	0° lower laminate strain #1	strain gage circuit
8	0° lower laminate strain #2	strain gage circuit
9	+45° lower laminate strain #1	strain gage circuit
10	+45° lower laminate strain #2	strain gage circuit
11	Wing tip accelerometer	Endevco model 2264 accelerometer
12	Canard angle of attack	Precision rotary potentiometer
13	Fuselage angle of attack	

TABLE 10 - STRAIN GAGE SENSTIVITIES.

INBOARD CIRCUITS:

$$BM_5 = K_1 (\theta_{BM_5}) - K_2 (\theta_{T_6})$$

$$T_6 = K_3 (\theta_{T_6}) - K_4 (\theta_{BM_5})$$

OUTBOARD CIRCUITS:

$$BM_1 = K_9 (\theta_{BM_1}) + K_{10} (\theta_{T_2})$$

$$T_2 = K_{11} (\theta_{T_2}) + K_{12} (\theta_{BM_1})$$

MID CIRCUITS:

$$BM_3 = K_5 (\theta_{BM_3}) + K_6 (\theta_{T_4})$$

$$T_4 = K_7 (\theta_{T_4}) + K_8 (\theta_{BM_3})$$

LAMINATE STRAINS:

$$s_{7,8}^{0^\circ} = K_{13} (\theta_{7,8})$$

$$s_{9,10}^{+45} = K_{14} (\theta_{9,10})$$

WHERE:

BM_i = BENDING MOMENT, IN. LBS.

T_i = TORSION, IN. LBS.

S_{ij} = LAMINATE STRAIN 0° DIRECTION, μe

S_{ij}^{+45} = LAMINATE STRAIN $+45^\circ$ DIRECTION, μe

θ = CIRCUIT OUTPUT, MILLIVOLTS

K = SENSITIVITY, ENG'G. UNITS/MILLIVOLT/VOLT EXCITATION

BENDING & TORSION CIRCUITS:

IN LBS/MILLIVOLT/VOLT

			IN LBS/MILLIVOLT/VOLT		
K_1	=	5295.0	K_7	=	2527.0
K_2	=	1251.5	K_8	=	406.3
K_3	=	7146.0	K_9	=	1376.8
K_4	=	954.3	K_{10}	=	186.8
K_5	=	2568.3	K_{11}	=	1168.7
K_6	=	350.2	K_{12}	=	337.4

LAMINATE STRAINS:

μe/MILLIVOLT/VOLT

K_{13}	=	5015
K_{14}	=	5014

0612-062 P

TABLE 11 – AERODYNAMICS DERIVATIVES FOR
CONFIGURATIONS AND TEST POINTS RUN.

CONFIGURATION	MACH NUMBER	DYNAMIC PRESSURE PSF	C_{L_o}	C_{M_o}	C_{L_α} PER RAD	C_{M_α} PER RAD	C_{L_δ} PER RAD	C_{M_δ} PER RAD
FUSELAGE ALONE	0.60	37	0.004	0.021	0.2925	0.625	–	–
	0.60	44	0.005	0.018	0.275	0.63	–	–
	0.61	52	0.002	0.017	0.260	0.605	–	–
	0.61	71	0.001	0.016	0.2575	0.625	–	–
	0.90	69	0.002	0.018	0.2625	0.6325	–	–
	0.90	83	0.001	0.017	0.250	0.6225	–	–
	0.91	99	0.00	0.016	0.2255	0.600	–	–
	1.10	68	0.003	0.022	0.36	0.72	–	–
	1.07	87	0.003	0.022	0.30	0.73	–	–
	1.04	100	0.003	0.023	0.29	0.67	–	–
FUSELAGE/WING	0.60	53	0.105	-.044	4.09	-0.62	–	–
	0.61	71	0.110	-.048	4.55	-0.63	–	–
	0.60	99	0.115	-.052	5.16	-0.94	–	–
	0.91	71	0.115	-.060	5.31	-0.96	–	–
	0.90	100	0.115	-.065	6.59	-1.21	–	–
	1.04	85	0.085	-.080	6.39	-2.40	–	–
FUSELAGE/CANARD	0.60	37	0.016	0.028	0.875	0.955	0.435	0.305
	0.91	70	0.015	0.025	0.915	1.065	0.455	0.32
	1.11	70	0.016	0.027	1.03	1.19	0.49	0.32

TABLE 11 CONTINUED – AERODYNAMICS DERIVATIVES FOR
CONFIGURATIONS AND TEST POINTS RUN.

CONFIGURATION	MACH NUMBER	DYNAMIC PRESSURE PSF	C_{L_o}	C_{M_o}	C_{L_α} PER RAD	C_{M_α} PER RAD	C_{L_δ} PER RAD	C_{M_δ} PER RAD
FUSELAGE/WING/CANARD	0.60	37	0.118	-.033	4.50	+0.015	0.25	0.415
	0.60	52	0.118	-.037	4.70	+0.010	0.245	0.42
	0.60	71	0.118	-.041	5.05	+0.002	0.255	0.43
	0.90	56	0.125	-.052	5.60	0.00	0.29	0.475
	0.90	70	0.127	-.055	6.05	-0.075	0.32	0.48
	0.90	84	0.124	-.054	6.45	-0.125	0.335	0.445
	0.90	99	0.124	-.057	7.35	-0.325	0.37	0.44
	1.05	70	0.090	-.076	5.92	-1.50	0.50	0.45
	1.05	84	0.070	-.075	6.47	-1.26	0.52	0.41

TABLE 12 - FORMAT OF REDUCED BALANCE DATA.

Card No.	DATA FIELDS						
	COL 1 - 4	COL 5 - 8	COL 13 - 24	COL 27 - 38	COL 41 - 52	COL 55 - 66	COL 69 - 80
1	TAB b	Tab No.	Mach. No.	Dynamic Pressure	α Turntable	α Fuselage	$i_c\,(\delta)$
2	Load		Lift	Drag	Pitching Moment	Rolling Moment	Yawing Moment
3	COEF		C_L	C_D	C_{MY}	C_{MX}	C_{MZ}
4	DER b		C_{L_α}	C_{D_α}	C_{MY_α}	C_{MX_α}	C_{MZ_α}

TABLE 13 - RIGID AERO DERIVATIVES AT M = 0.9.

CONFIGURATION	C_{L_α} PER RADIAN			C_{M_α} PER RADIAN			C_{L_δ} PER RADIAN			C_{M_δ} PER RADIAN		
	TEST	ANALYSES		TEST	ANALYSES		TEST	ANALYSES		TEST	ANALYSES	
		ORIG.	FINAL		ORIG.	FINAL		ORIG.	FINAL		ORIG.	FINAL
FUSELAGE ALONE	0.30	0.38	0.25	0.66	0.69	0.58	-	-	-	-	-	-
FUSELAGE/CANARD	0.92	1.25	1.00	1.07	1.68	1.38	0.46	0.71	0.42	0.32	0.67	0.37
FUSELAGE/WING/CANARD	4.60	4.54	4.93	0.15	1.00	0.22	0.25	0.18	0.25	0.49	1.00	0.52

TABLE 14 - FLUTTER MODEL INERTIA DATA.

CONFIGURATION	WEIGHT (lbs)	C.G. LOCATION	PITCH INERTIA $(lb-in^2)$
FORWARD	324	213	1.72×10^6
NOMINAL	↓	225	1.195×10^6
AFT	↓	231	1.35×10^6

TABLE 15 - BALLAST WEIGHTS AND LOCATIONS.

C.G. LOCATION	BALLAST WEIGHT (lbs)	BALLAST LOCATION		
		FS 117.2	FS 225	FS 319
FORWARD FS 213	33.2	x	-	-
NOMINAL FS 225	3	-	-	x
	30.2	-	x	-
AFT FS 231	25	-	-	x
	8.2	-	x	-

TABLE 16 - CANARD FLEXIBILITY TEST RESULTS.

PITCH

    HYDRAULICS ON $1.74 - 2.08 \times 10^{-5}$ rad/in-lb

    HYDRAULICS OFF 1.16×10^{-5} rad/in-ib
    & ACTUATOR BOTTOMED

ROLL

    HYDRAULICS OFF   TIP: 3.01×10^{-6} rad/in-lb

STATIC RELEASE -   Point at which loading overcame actuator spring when hydraulics are off.

    First Motion: 528 in-lb
    Pegged: 624 in-lb

TABLE 17 - FLUTTER MODEL LOAD LIMITS.

Component	Ref. Pt. (In)		Lift	Pitching Moment	Rolling Moment
	FS	BL	(Lbs)	(In-Lbs)	(In-Lbs)
Wing	269.9	5.1	768	39,600	39,996
Canard	187.2	4.0	212	500	4,235

TABLE 18 - FLUTTER MODEL SAFETY FACTORS.

ITEM	FACTOR	ITEM	FACTOR
Roll Rod	3.9	Canard Bracket Bolts	27.6
Universal Joints	5.7	-Link 1	5.7
Roll Rod Bolts	16.3	-Link 2	5.7
		-Link 3	15.7
Wing Mount Fitting		-Link 4	5.7
-Bearing Load	3.3		
-Shear On Tang	8.8	Hydraulic Actuator	1.44
Wing Bolts			
-Shear	5.1	Drag Restraint	4+
-Tension	5.1		
Helicoil Assembly	7.8	Snubber Cable	5.8
Bulkhead		Lift Plate	4.2
-Inner Flange	8.6		
-Outer Flang	8.4	Lift Cable Attachment	16.0

TABLE 19 - SUMMARY OF DESIGNED CONTROL LAWS.

CONFIG	M	$\bar{Q}$ (PSF)	S.M.	ω (RAD./SEC.) TARGET	ACTUAL	DAMPING RATIO TARGET	ACTUAL	K_I	K_F	GAINS K_{NZ}	K_Q	K_L
C1-1	0.9	37	-.12	6.82	7.60	0.78	0.89	0.680	0.189	0.583	6.137	1.0
C1-2	0.9	65	-.09	9.58	12.38	0.75	0.81	1.86	0.282	0.653	5.11	1.2
C1-3	0.9	82.8	-.07	11.46	11.77	0.72	0.73	0.8	0.163	0.533	6.88	1.1
C1-4	0.9	110	-.05	11.46	11.60	0.72	0.74	0.4	0.060	0.162	12.34	1.0
C1-5	0.9	130	-.04	11.46	11.38	0.72	0.71	0.2	0.028	0	16.87	1.3
C2-1	0.9	37	-.25	6.82	7.50	0.78	0.87	0.909	0.188	0.535	6.845	1.0
C2-2	0.9	65	-.23	9.58	11.34	0.75	0.88	2.37	0.273	0.638	5.33	1.0
C2-3	0.9	82.8	-.21	11.46	11.50	0.72	0.70	1.1	0.158	0.505	7.29	1.2
C2-4	0.9	110	-.19	11.46	12.76	0.72	0.75	0.60	0.06	0.216	10.00	1.6
C2-5	0.9	130	-.17	11.46	11.74	0.72	0.72	0.33	0.029	0	14.93	1,75
C3-2	0.9	82.8	+.20	11.46	12.30	0.72	0.65	0.4	0.195	0.60	12.00	0.30

TABLE 20 - GAINS FOR CONTROL LAWS TESTED.

DESIGNATION		K_I	K_F	K_{NZ}	K_Q	K_L	K_α
CG 225	C1-1	0.68	0.189	0.583	6.14	1.0	0.481
	C1-2	1.86	0.282	0.653	5.11	1.2	0.169
	C1-3	0.80	0.163	0.533	6.88	1.1	0.399
	C1-4	0.40	0.060	0.162	12.34	1.0	0.785
	C1-4A	0.40	0.060	0.162	12.34	1.5	0.785
CG 231	C2-1	0.91	0.188	0.535	6.85	1.0	0.351
	C2-2	2.37	0.273	0.638	5.33	1.0	0.131
	C2-3	1.10	0.158	0.505	7.29	1.2	0.285
	C2-4	0.60	0.060	0.216	10.00	1.6	0.714
	C2-4A	0.60	0.060	0.216	10.00	2.4	0.714

TABLE 21 - FLUTTER MODEL INSTRUMENTATION LIST.

ITEM	MEASUREMENT	DEVICE
1	OUTBOARD BENDING MOMENT	4-ARM STRAIN GAGE CIRCUIT
2	OUTBOARD TORSION	4-ARM STRAIN GAGE CIRCUIT
3	MID BENDING MOMENT	4-ARM STRAIN GAGE CIRCUIT
4	MID TORSION	4-ARM STRAIN GAGE CIRCUIT
5	INBOARD BENDING MOMENT	4-ARM STRAIN GAGE CIRCUIT
6	INBOARD TORSION	4-ARM STRAIN GAGE CIRCUIT
7	0° LOWER LAMINATE STRAIN #1	STRAIN GAGE CIRCUIT
8	0° LOWER LAMINATE STRAIN #2	STRAIN GAGE CIRCUIT
9	+ 45° LOWER LAMINATE STRAIN #1	STRAIN GAGE CIRCUIT
10	+ 45° LOWER LAMINATE STRAIN #2	STRAIN GAGE CIRCUIT
11	WING TIP ACCELERATION	ENDEVCO MODEL 2264 ACCELEROMETER
12	CANARD INCIDENCE	LVDT
13	FUSELAGE ANGLE OF ATTACK	
14	FUSELAGE ACCELERATION	SCAEVITZ ACCELEROMETER LSBP-2
15	FUSELAGE PITCH RATE	HAMILTON STANDARD RATE GYRO 10-05435-158
16	HYDRAULICS ΔP	PRESSURE TRANSDUCER
17	SPLITTER PLATE FOULING LIGHTS	
18	SNUBBER LOADS (4)	LOAD CELLS
19	LIFT LOAD	LOAD CELL
20	DRAG LOADS (2)	LOAD CELLS

TABLE 22 - APPLIED LOADS FOR PROOF TEST.

	CONDITION	LIFT (lbs.)	PITCH MOM. FS 269.9 (in.-lbs.)	ROLL MOM. BL 5.1 (in.-lbs.)
W I N G	WORST COMBINED AT Q = 130 PSF	738	35,858	33,437
	RIG CONSTRAIN	1,030	35,858	39,655
	PROOF LOAD	1,236	43,030	47,586
	CONDITION	LIFT (lbs.)	PITCH MOM. FS 187.2 (in.-lbs.)	ROLL MOM. BL 4.0 (in.-lbs.)
C A N A R D	WORST COMBINED	217	1,155	2,544
	RIG CONSTRAIN	212	0	4,240
	PROOF LOAD	254	0	5,080

TABLE 23 - CONFIGURATIONS AND TUNNEL CONDITIONS FOR THE FLUTTER TEST.

CONFIGURATION	CONTROL LAW	MACH NUMBER	DYNAMIC PRESSURE RANGE (PSF)
CG213 STATICALLY STABLE	OPEN LOOP	0.6 0.80 0.85	35 to 130 28 to 111 31 to 112
CG225 MODERATELY UNSTABLE	C1-1	0.6 0.80 0.85	85 to 130 50 to 110 54 to 100
	C1-2	0.80 0.85	67 to 73 55 to 81
	C1-3	0.6 0.80 0.85	86 to 130 86 to 111 55 to 99
	C1-4	0.85	56 to 81
CG231 HIGHLY UNSTABLE	C2-1	0.80 0.85	50 to 60 66 to 84
	C2-2	0.80 0.85	60 66 to 84
	C2-3	0.60 0.80 0.85	68 to 110 77 to 109 66 to 100
	C2-4	0.60 0.80 0.85	69 to 116 77 to 100 85 to 100
	C2-4A	0.60 0.80 0.85 0.90 0.94	108 to 130 100 to 114 85 to 111 101 to 111 109
CG231 WITH WING TIP BALLAST	C2-4A	0.85	59 to 110

TABLE 24 - HISTORY OF WIND-OFF WING FREQUENCIES.

| CONDITION | GAGE* | FREQUENCY, HERTZ | | | |
		1ST BENDING	2ND BENDING	1ST TORSION	3RD BENDNG
Clamped (1979 GVS)	W	10.4	36.8	48.2	76.2
On Model (1983 GVS)	W	10.0	34.4	47.2	73.6
1983 Test (Snubbed)					
Pre Run 1	W	10.0	36.0	47.2	76.8
Pre Run 2	W	9.6	36.0	46.8	-
Pre Run 3	W	10.8	35.4	47.0	-
Pre Run 4	W	10.2	35.6	47.0	72.0
Pre Run 6	G	10.2	36.6	-	-
Pre Run 7	W	11.2	36.8	48.0	-
Pre Run 8	W	10.8	36.2	48.0	74.0
Pre Run 8	G	8.8	37.4	42.2	-
Pre Run 10	W	10.8	36.0	47.2	75.2
Pre Run 10	G	8.0	39.6	55.0	75.2
Pre Run 11	W	9.6	36.0	47.6	-
Pre Run 12	W	10.0	-	47.0	70.0
Pre Run 12	G	8.4	31.2	46.0	-
Pre Run 14	W	7.6	-	-	-
Pre Run 14	G	8.0	25.6	45.0	54.0

*W - Wing Bending Moment Circuit, G - Fuselage Pitch Rate Gyro

TABLE 25 - INSTRUMENTATION PARAMETERS.

NO.	ITEM	BRUSH RECORDS	DIGITAL DISPLAY	ON-LINE COMPUTER	SAFETY	CONTROL SYSTEM	INSTABILITY DETECTION
1	Wing Root Bending	X	X	X	X		X
2	Wing Root Torsion	X	X	X	X		X
3	Wing Tip Acceleration	X		X	X		X
4	Fuselage Acceleration	X				X	X
5	Fuselage Pitch Rate	X				X	
6	Canard Servo Command	X				X	
7	Canard Position (LVDT)	X			X	X	X
8	Canard Trim Command	X				X	
9	Snubber Load, Fwd Top	X	X	X	X		
10	Snubber Load, Fwd Bottom	X	X	X	X		
11	Snubber Load, AFT Top	X	X	X	X		
12	Snubber Load, AFT Bottom	X	X	X	X		
13	Lift Cable Load	X		X	X		
14	Drab Cable Load, Fwd	X		X	X		
15	Drag Cable Load, AFT	X		X	X		
16	Fuselage Incidence	X	X				
17	Hydraulic Pressure	X			X	X	
18	Random Noise Signal	X			X		
19	Time Code	X					
20	Time Code	X					
21	Time Code	X					
22	Fouling Circuit	X			X		

TABLE 26 - SUMMARY OF FLUTTER DATA AND CORRELATION.

CONFIGURATION & CONTROL LAW	M = 0.6, PSF				M = 0.85, PSF			
	EVENT*	TEST, Q_T	SAEL, Q_A	CORRELATION $\sqrt{Q_A/Q_T}$	EVENT*	TEST, Q_T	SAEL, Q_A	CORRELATION $\sqrt{Q_A/Q_T}$
CG 213 (NO SAS)	BFF	145	135	0.97	BFF	112	120	1.03
CG 225 C1-1	BFF	150	138	0.96	BFF/SPI	104	125	1.10
C1-2	--	--	--	--	STABLE	81	UP TO 121	✓
C1-3	BFF	143	138	0.98	BFF/SPI	107	124	1.08
C1-4	--	--	--	--	SPI	54-81	60	✓
C1-4A	--	--	--	--	STABLE	81	UP TO 125	✓
CG 231 C2-1	--	--	--	--	SPI	66-84	90	✗
C2-2	--	--	--	--	STABLE	84	UP TO 120	✓
C2-3	BFF/SPI	124	136	1.04	BFF/SPI	104	120	1.07
C2-4	BFF/SPI	120	136	1.06	SPI	102	120	1.08
C2-4A	BFF	140	141	1.00	BFF	114	126	1.05

*BFF = BODY FREEDOM FLUTTER

SPI = SHORT PERIOD INSTABILITY

TABLE 27 - COMPARISON OF ANALYTICAL FREE-FREE MODES.

FUSELAGE/CANARD CG MOTION IN FLEXIBLE MODES:					
	MODE 1	MODE 2	MODE 3	MODE 4	MODE 5
CG 231	-1.50×10^{-2}	9.21×10^{-3}	-3.02×10^{-3}	8.84×10^{-3}	1.85×10^{-3}
h CG 225	-1.49×10^{-2}	9.16×10^{-3}	-3.02×10^{-3}	8.80×10^{-3}	1.85×10^{-3}
CG 213	-1.47×10^{-2}	9.01×10^{-3}	-3.01×10^{-3}	8.70×10^{-3}	1.85×10^{-3}
CG 231	1.27×10^{-5}	5.3×10^{-5}	1.22×10^{-5}	8.0×10^{-5}	8.0×10^{-6}
θ GC 225	-1.28×10^{-5}	6.8×10^{-5}	0.70×10^{-5}	9.5×10^{-5}	11.2×10^{-6}
CG 213	-6.25×10^{-5}	9.8×10^{-5}	$-.33 \times 10^{-5}$	9.5×10^{-5}	17.6×10^{-6}

GENERALIZED MASS:					
CG 231	1.95	1.19	1.21	2.41	1.66
CG 225	1.95	1.19	1.21	2.41	1.66
CG 213	1.95	1.19	1.21	2.41	1.65
CANTILEVER	2.01	1.22	1.21	2.43	1.68

FREQUENCIES (HERTZ):					
CG 231	10.54	37.25	48.29	76.59	90.26
CG 225	10.54	37.28	48.29	76.63	90.27
CG 213	10.55	37.36	48.29	76.73	90.27
CANTILEVER	10.38	36.85	48.24	76.16	90.24

TABLE 28 - CABLE DATA USED IN GRUMCABLE.

Lift Cable Spring Constant Lift Cable Tension	7.0 Lbs/In 250 Lbs
Rear Cable Spring Constant Rear Cable Tension	16.0 Lbs/In 340 Lbs
Torsional Stiffness from Roll Rods	12,000 Ft-Lbs/Rad
Pulley Radius	2.0 In

TABLE 29 – STRUCTURE OF MODIFIED GRUMCABLE EQUATIONS.

$$
\begin{array}{l}
\text{X-Force} \\
\text{Z-Force} \\
\text{Y-Moment} \\
\text{Constraint} \\
\\
\text{Actuator} \\
\text{Auxiliary}
\end{array}
\begin{bmatrix}
* & * & * & * & * & 0 \\
* & * & * & * & * & 0 \\
* & *+a & * & * & * & 0 \\
* & * & 0 & * & 0 & 0 \\
b & c & 0 & 0 & d & e \\
f & 0 & 0 & 0 & 0 & 1
\end{bmatrix}
\cdot
\begin{Bmatrix}
z \\ \theta \\ \Delta T_F \\ x \\ \delta \\ \dot{z}
\end{Bmatrix}
= 0
$$

Terms   * denotes unchanged element; see Reference 16

$a = K_T$

$b = - (K_L \, K_I \, K_{NZ}/g) \, s^2$

$c = K_L \, K_Q \, (K_I \, s + K_F \, s^2)$

$d = -s - \Upsilon s^2$

$e = - (K_L \, K_F \, K_{NZ}/g) \, s^2$

$f = -s$

92

TABLE 30 - EFFECT OF ANALYSIS VARIATIONS ON BFF PREDICTIONS FOR CG231, C2-4A, M = 0.9.

TYPE OF ANALYSIS	$\bar{Q}_A$ (PSF)	f_A (HZ)	$\sqrt{\bar{Q}_A/\bar{Q}_T}$	$f_T - f_A$ (Hz)
o GRUMCABLE, Aero Corrections, no modes	STABLE	STABLE	-	-
o SAEL, No cable system, No aero corrections, control law as designed	155	2.1	1.18	0.7
o SAEL, No cable system, Aero corrections, control law as tested	125	1.0	1.06	1.8
o CABSAEL, No aero corrections, control law as designed	145	2.2	1.14	0.6
o CABSAEL, No aero corrections, control law as tested, Revised cable data	137	1.8	1.11	1.0
o CABSAEL, Aero corrections, Control law as tested, Revised cable data	122	1.1	1.05	1.7
o CABSAEL, Aero corrections, Control law as tested, arbitrary snubber spring added	121	1.9	1.05	0.9

Note: Q_T = 111 psf, f_T = 2.8 Hz
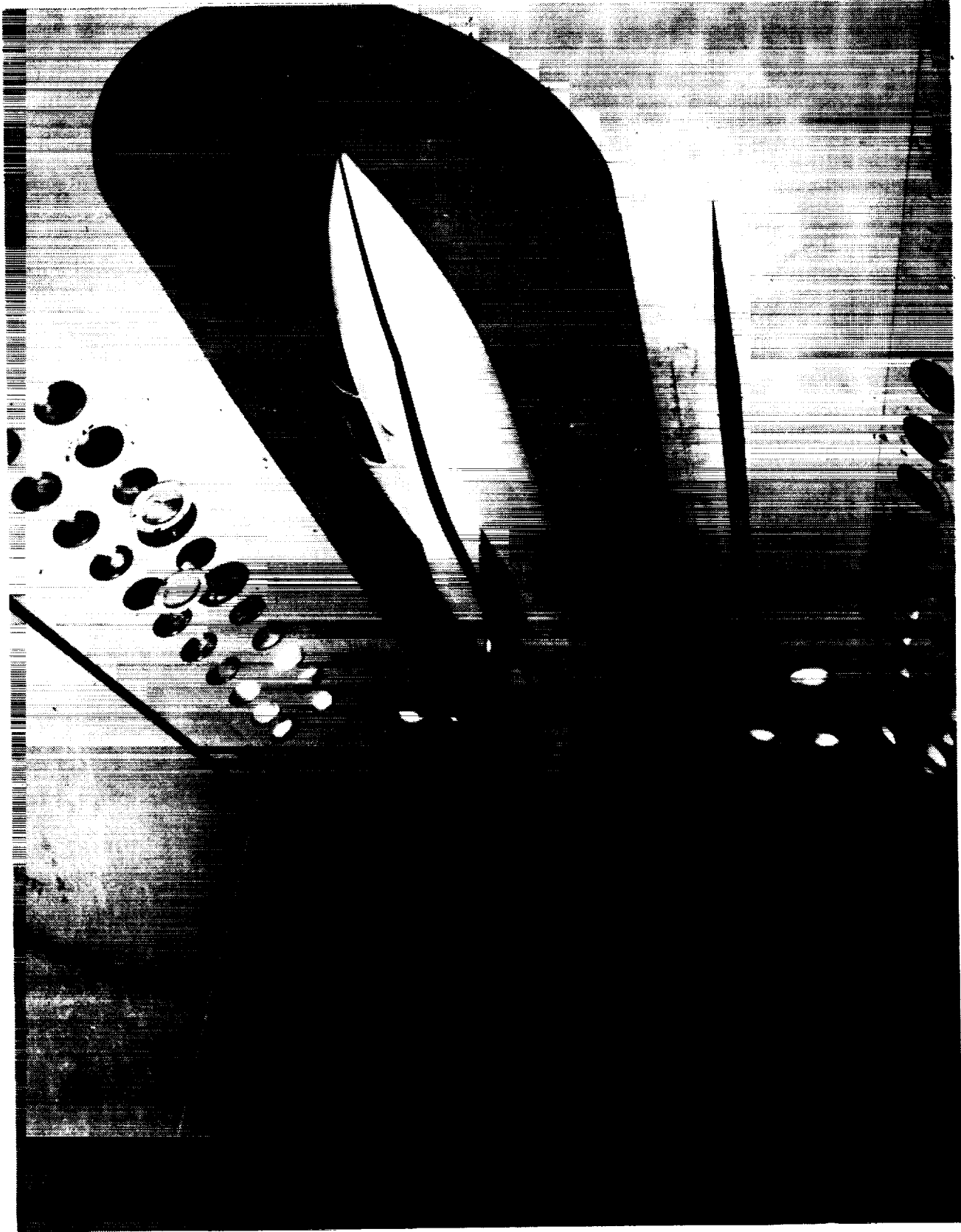
Figure 1. 1/2 Scale FSW Aeroelastic Model Installed in NASA-LaRC TDT.
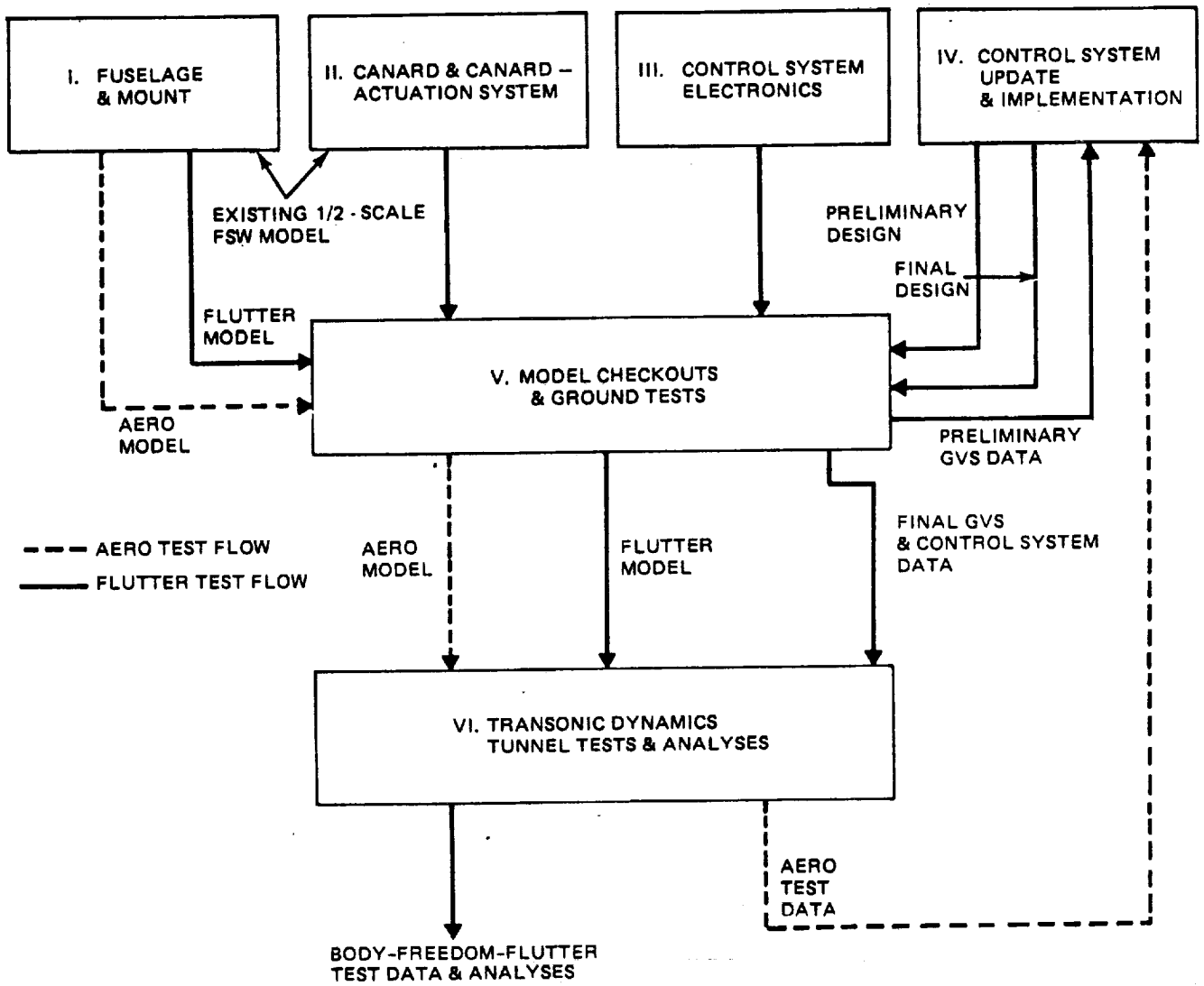
Figure 2. Flow of Work & Data Between Six Major Technical Tasks.

Turntable
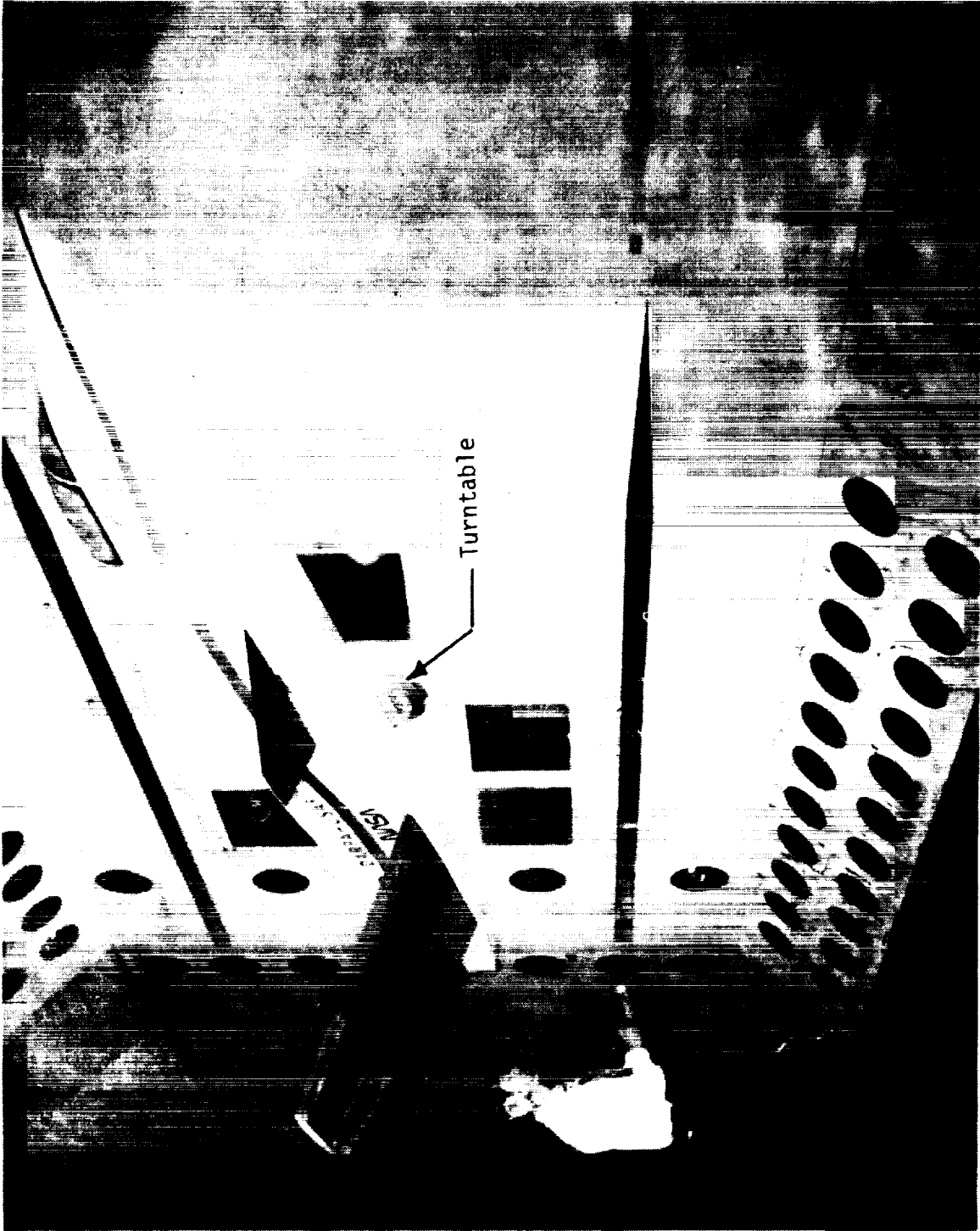
Figure 3. Original Model During Divergence Test In TDT.
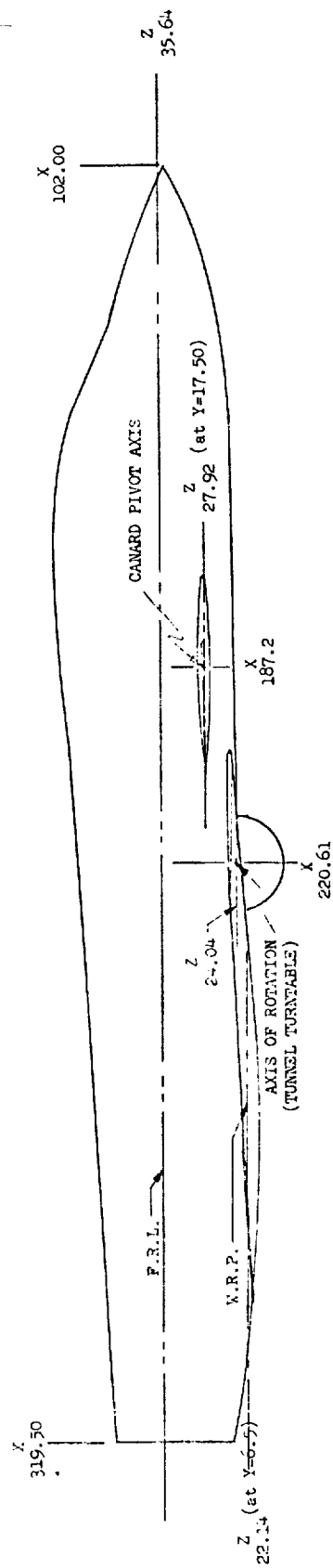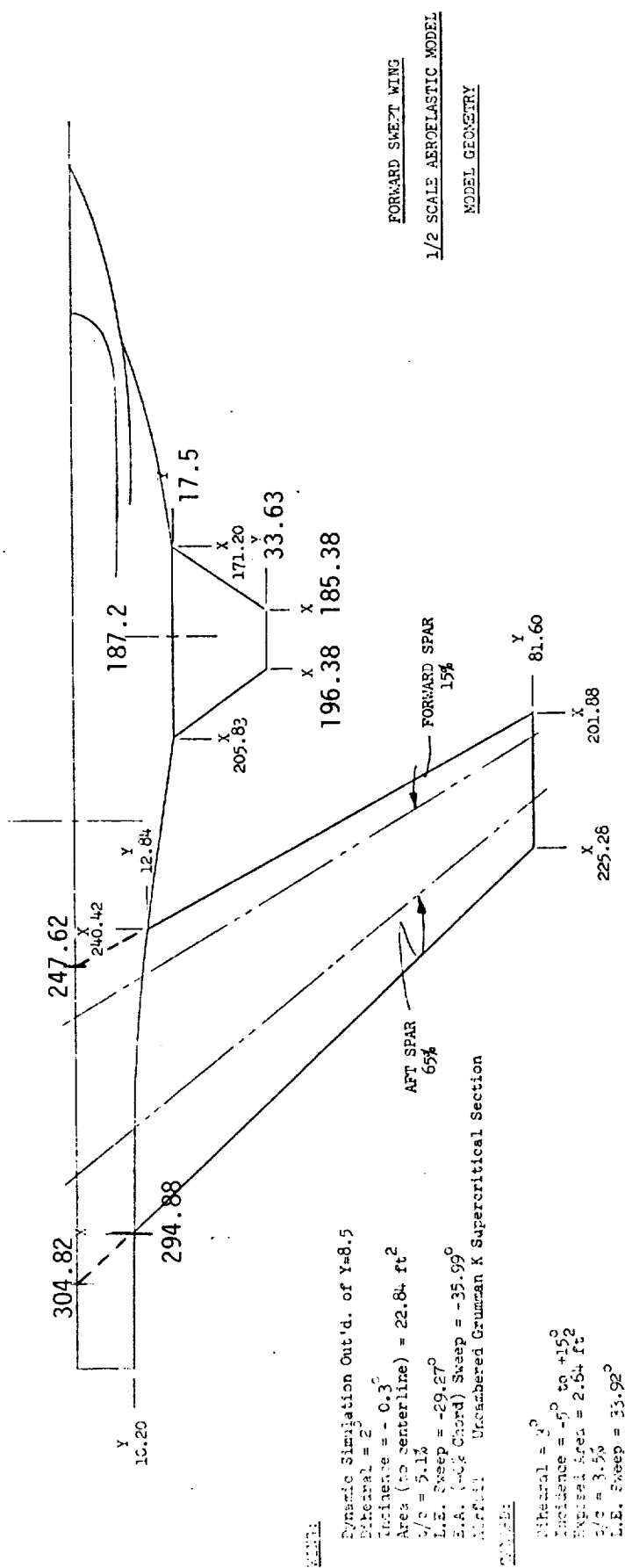
Figure 4. $\frac{1}{2}$-Scale FSW Model – General Arrangement.
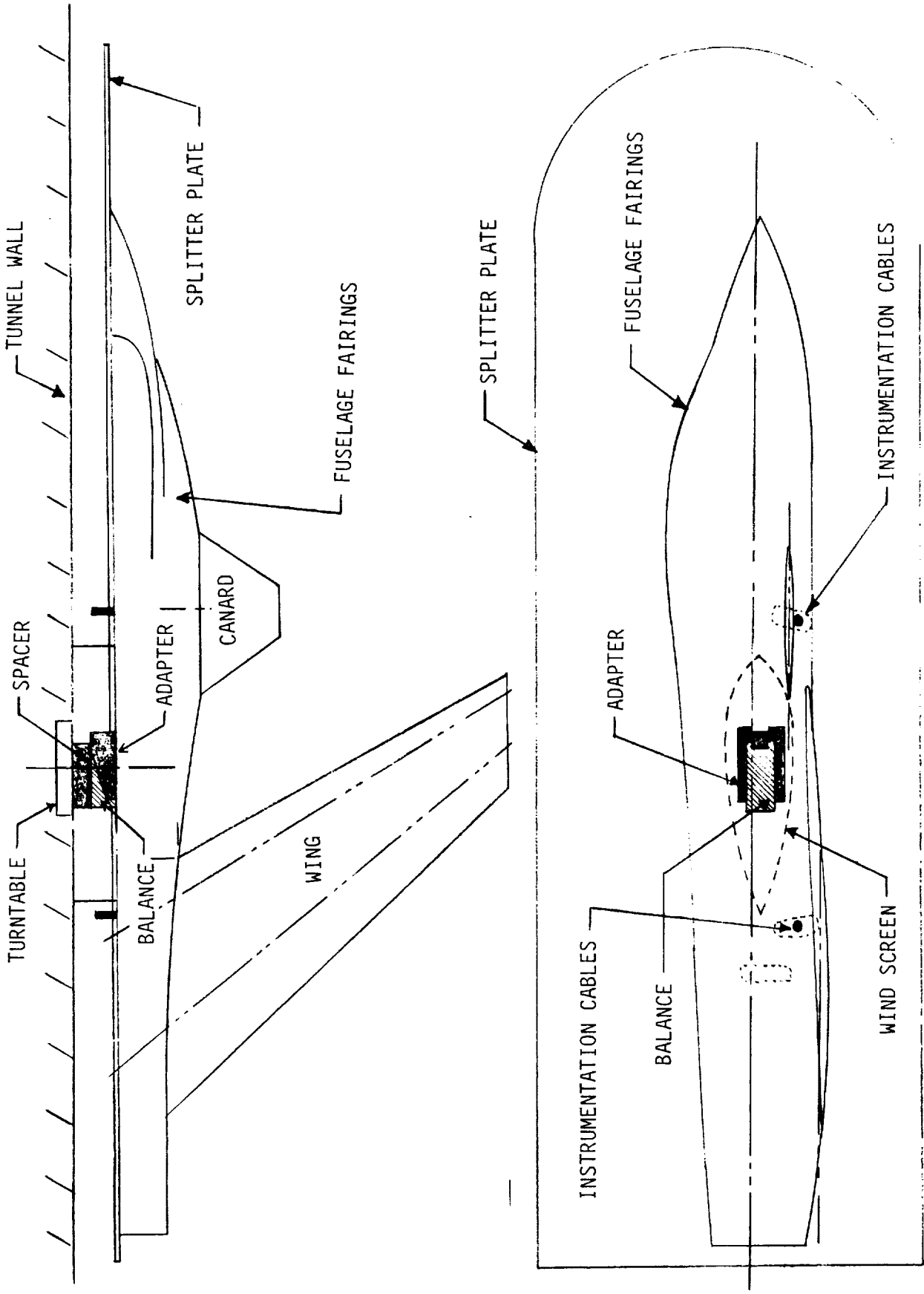
Figure 5. Model Modifications For Aero Test.
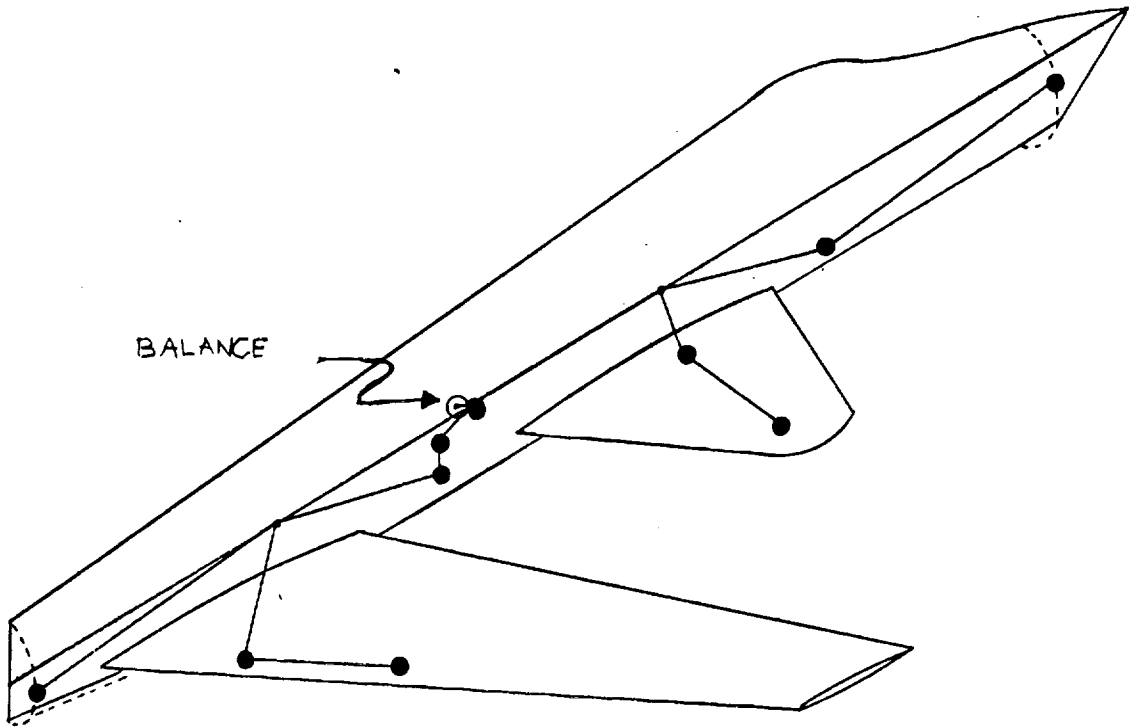
Figure 6. NASTRAN Idealization Of Model.

COORDINATES OF GVS MEASUREMENT POINTS

NODE NO.	X	Y
1	-53.91	8.5
2	-55.65	11.30
3	-59.13	16.90
4	-64.36	25.31
5	-69.59	33.71
6	-74.82	42.12
7	-80.04	50.53
8	-85.27	58.93
9	-90.50	67.34
10	-95.73	75.75
11	-99.36	81.60
12	-40.49	8.5
13	-43.92	13.22
14	-50.91	22.87
15	-56.71	30.86
16	-62.51	38.85
17	-68.31	46.84
18	-74.10	54.84
19	-79.90	62.83
20	-85.70	70.82
21	-91.50	78.81
22	-27.07	9.5
23	-32.53	15.09
24	-43.46	28.27
25	-49.78	35.89
26	-56.09	43.51
27	-62.41	51.12
28	-68.72	53.74
29	-75.04	66.36
30	-81.35	73.98
31	-87.66	81.60
32	-15.00	8.5
33	-19.83	13.75
34	-25.66	20.07
35	-37.33	32.72
36	-44.07	40.03
37	-50.81	47.34
38	-57.55	54.65
39	-64.29	61.96
40	-71.03	69.27
41	-77.77	76.57

Figure 7.   Measurement Grid for Vibration Survey on Cantilevered Wing.

100

WING BENDING MODE

MEASURED f = 10.4 Hz

WING SECOND BENDING MODE

MEASURED f = 36.8 Hz

WING TORSION MODE

MEASURED f= 48.2 Hz
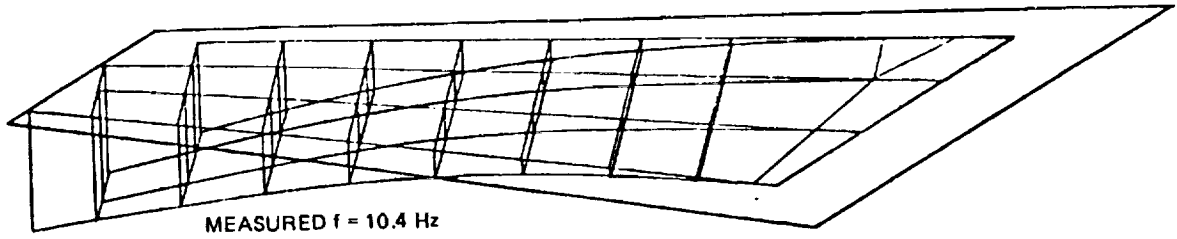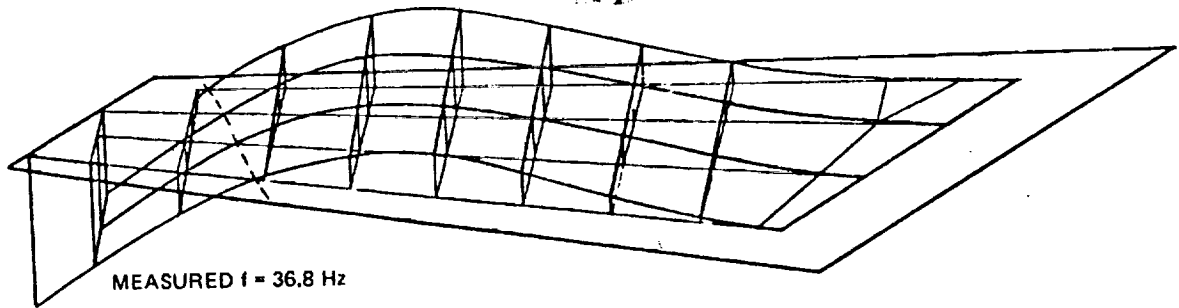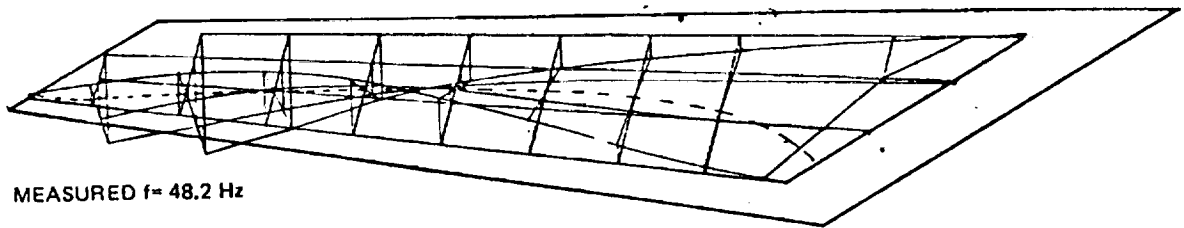
WING THIRD BENDING MODE

MEASURED f = 76.2 Hz
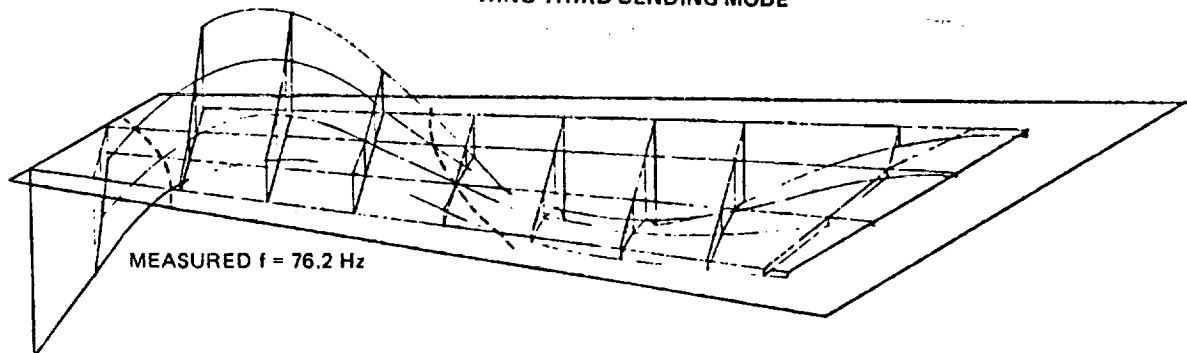
Figure 8.   Measured Mode Shapes On Cantilevered Wing.
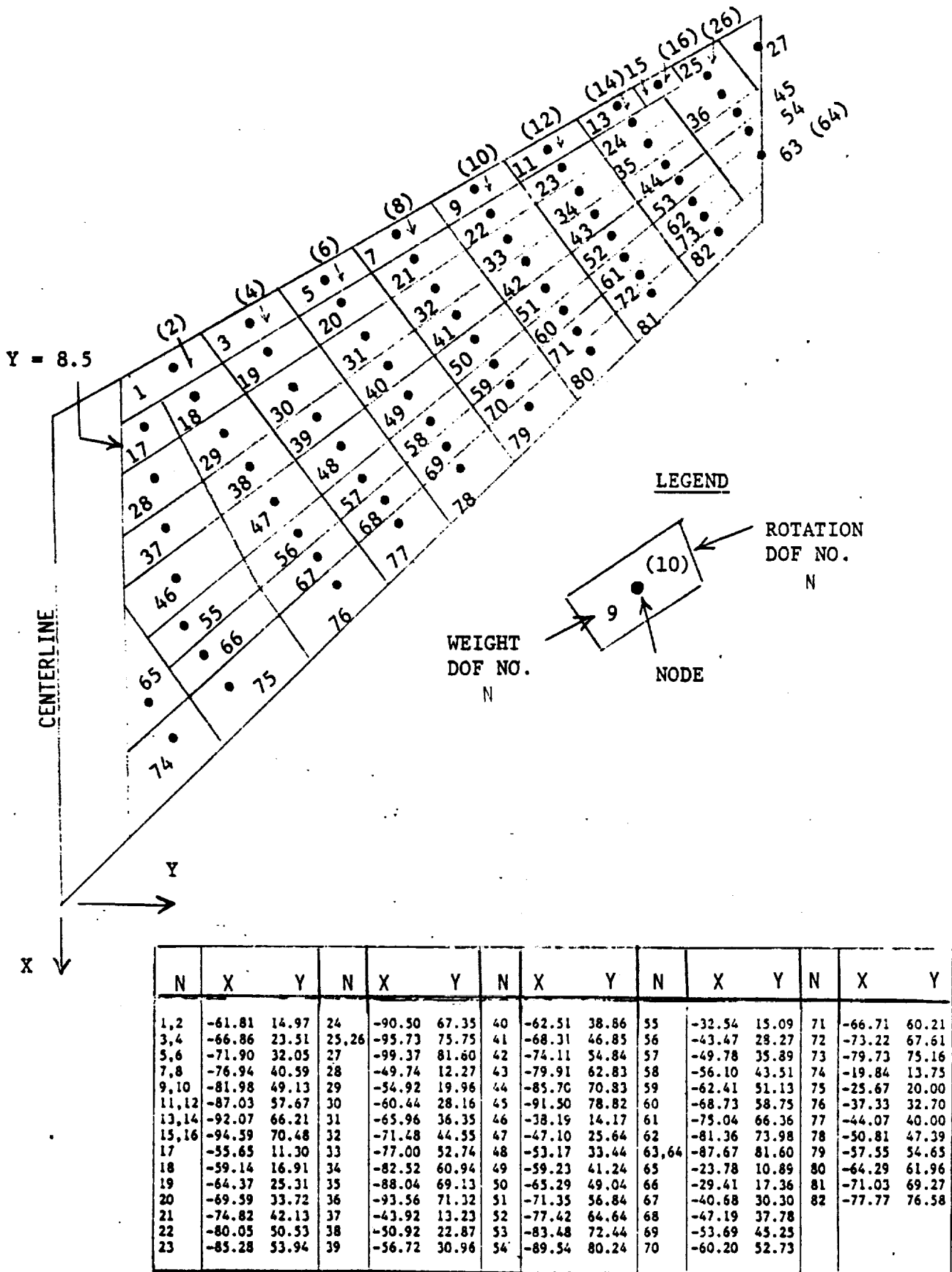
Figure 9. Grid For Model Generalized Mass Calculations.

N	X	Y	N	X	Y	N	X	Y	N	X	Y	N	X	Y
1,2	-61.81	14.97	24	-90.50	67.35	40	-62.51	38.86	55	-32.54	15.09	71	-66.71	60.21
3,4	-66.86	23.51	25,26	-95.73	75.75	41	-68.31	46.85	56	-43.47	28.27	72	-73.22	67.61
5,6	-71.90	32.05	27	-99.37	81.60	42	-74.11	54.84	57	-49.78	35.89	73	-79.73	75.16
7,8	-76.94	40.59	28	-49.74	12.27	43	-79.91	62.83	58	-56.10	43.51	74	-19.84	13.75
9,10	-81.98	49.13	29	-54.92	19.96	44	-85.70	70.83	59	-62.41	51.13	75	-25.67	20.00
11,12	-87.03	57.67	30	-60.44	28.16	45	-91.50	78.82	60	-68.73	58.75	76	-37.33	32.70
13,14	-92.07	66.21	31	-65.96	36.35	46	-38.19	14.17	61	-75.04	66.36	77	-44.07	40.00
15,16	-94.59	70.48	32	-71.48	44.55	47	-47.10	25.64	62	-81.36	73.98	78	-50.81	47.39
17	-55.65	11.30	33	-77.00	52.74	48	-53.17	33.44	63,64	-87.67	81.60	79	-57.55	54.65
18	-59.14	16.91	34	-82.52	60.94	49	-59.23	41.24	65	-23.78	10.89	80	-64.29	61.96
19	-64.37	25.31	35	-88.04	69.13	50	-65.29	49.04	66	-29.41	17.36	81	-71.03	69.27
20	-69.59	33.72	36	-93.56	71.32	51	-71.35	56.84	67	-40.68	30.30	82	-77.77	76.58
21	-74.82	42.13	37	-43.92	13.23	52	-77.42	64.64	68	-47.19	37.78			
22	-80.05	50.53	38	-50.92	22.87	53	-83.48	72.44	69	-53.69	45.25			
23	-85.28	53.94	39	-56.72	30.96	54	-89.54	80.24	70	-60.20	52.73			

102

Figure 10. Forward Swept Wing 1/2-Swept Model Integral Instrumentation.

103
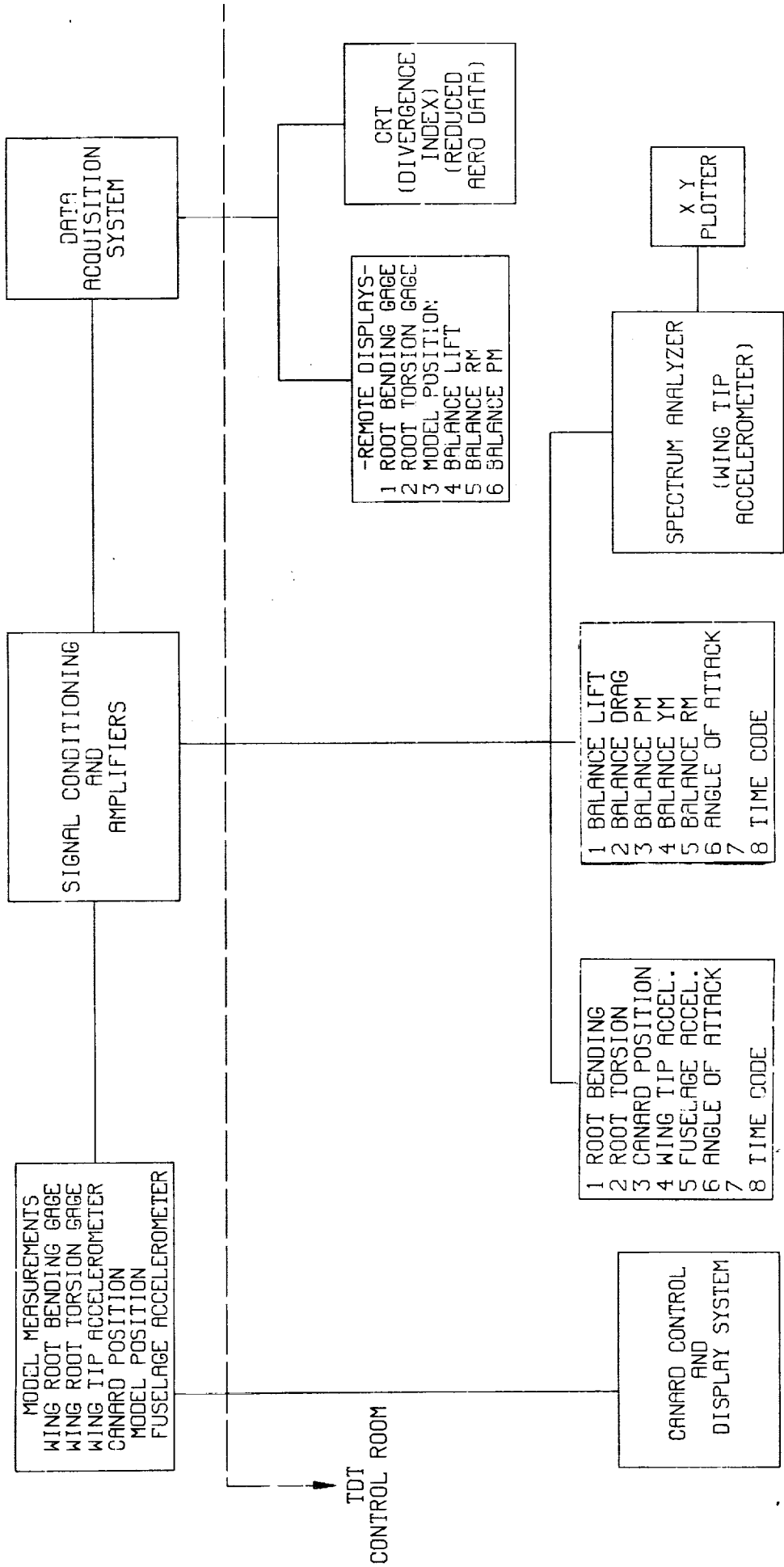
Figure 11. Block Diagram Of Instrumentation For The Aero Test.
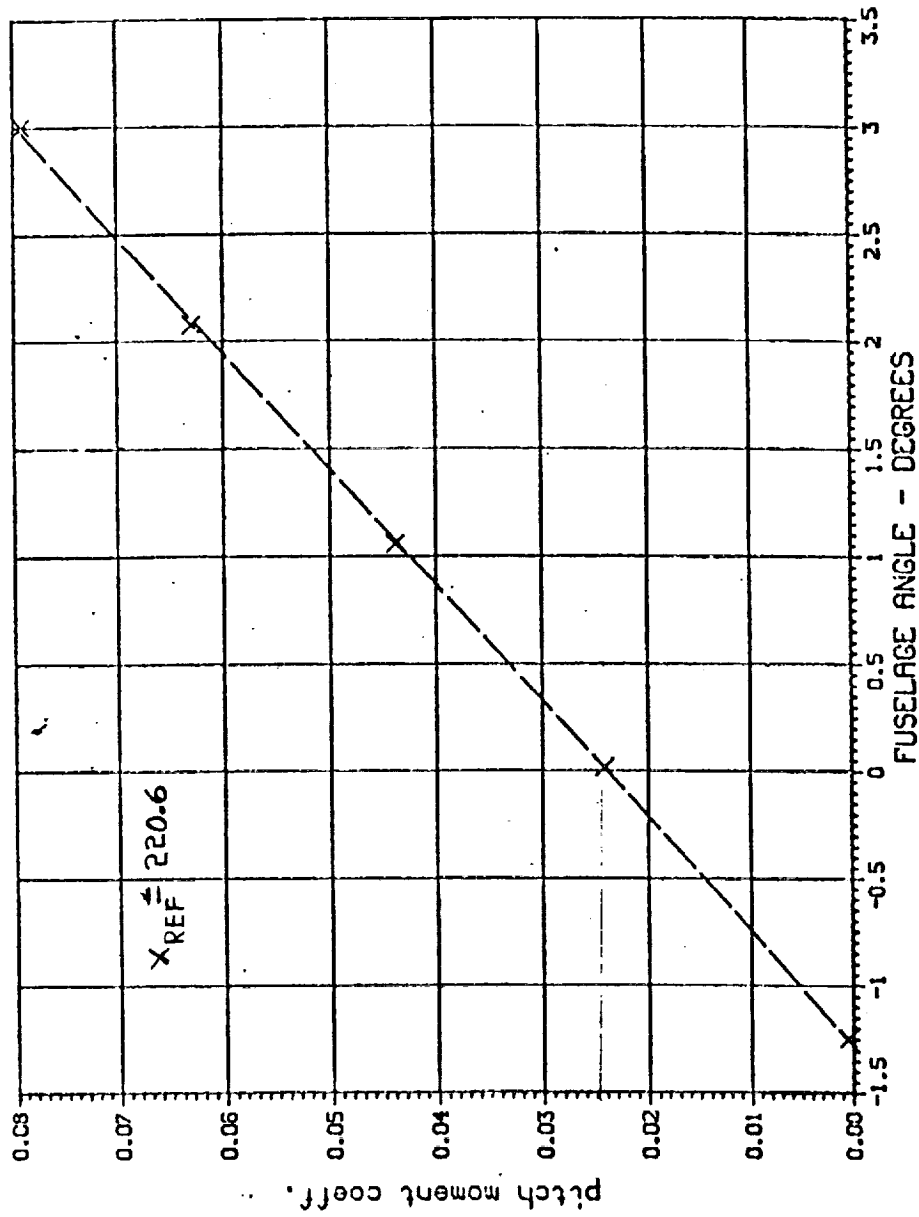
Figure 12. Representative Measured Aero Coefficients, Curve Fit to Determine Alpha Derivatives.

105
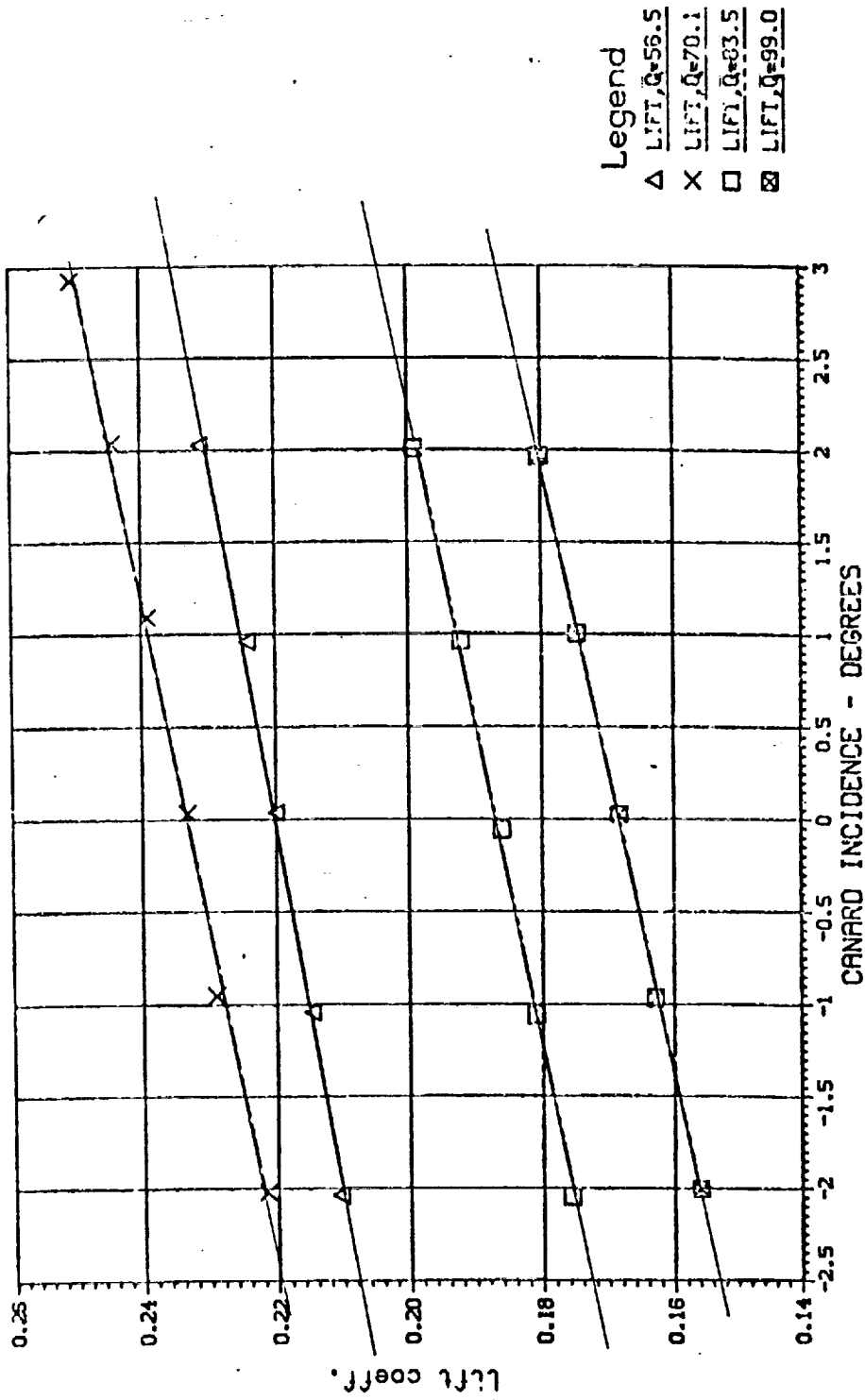
Figure 13. Representative Measured Aero Coefficients, Curve Fit to Determine I_C Derivatives.
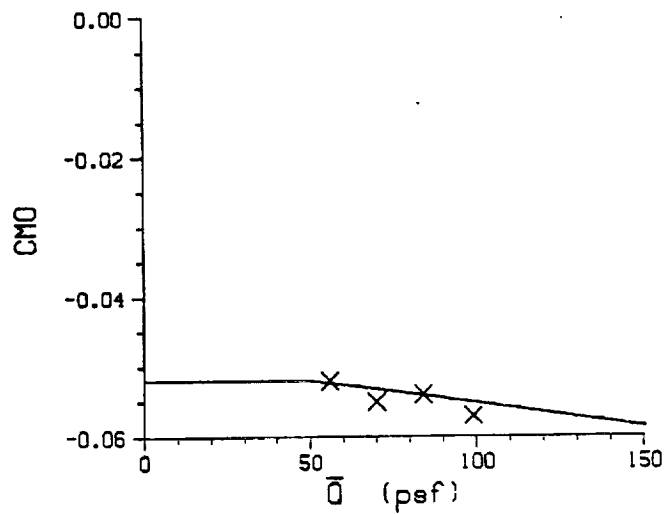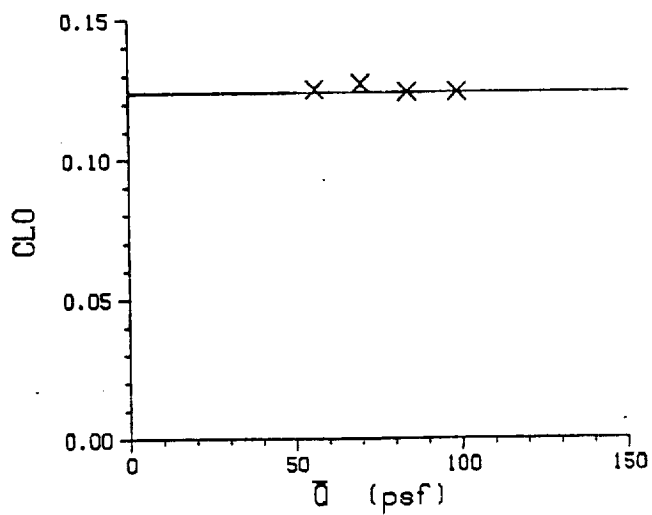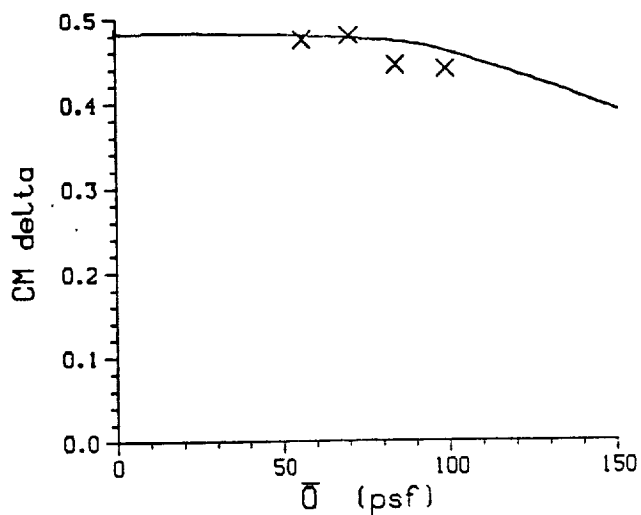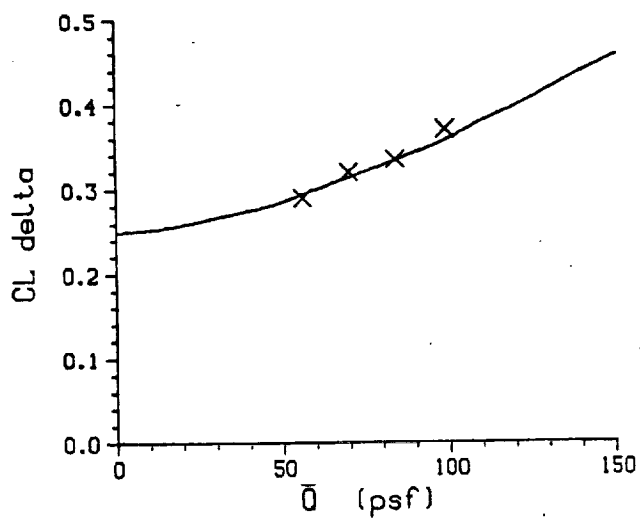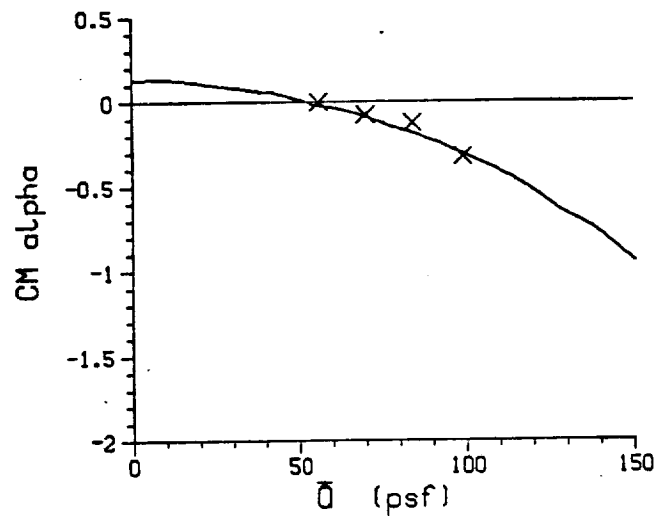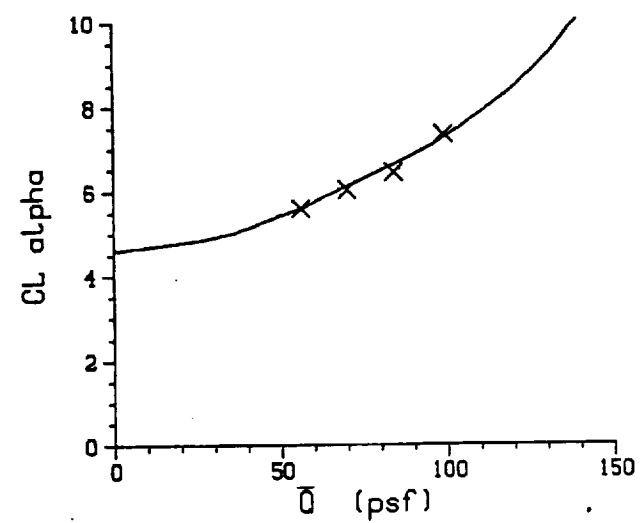
Figure 14.   Measured Aero Data as Functions of Dynamic Pressure, M = 0.9.
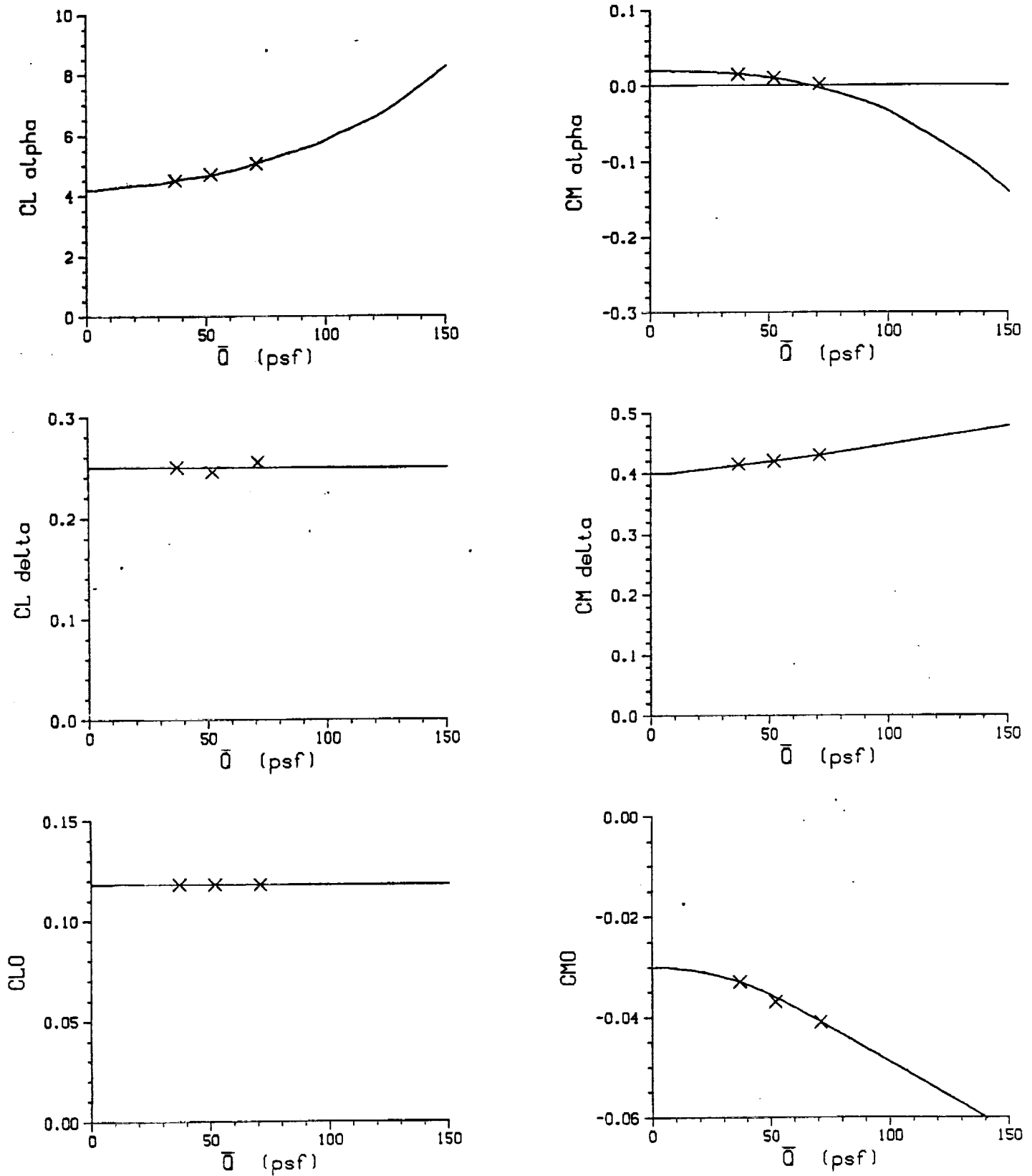
Figure 15. Measured Aero Data as Functions of Dynamic Pressure, M = 0.6.
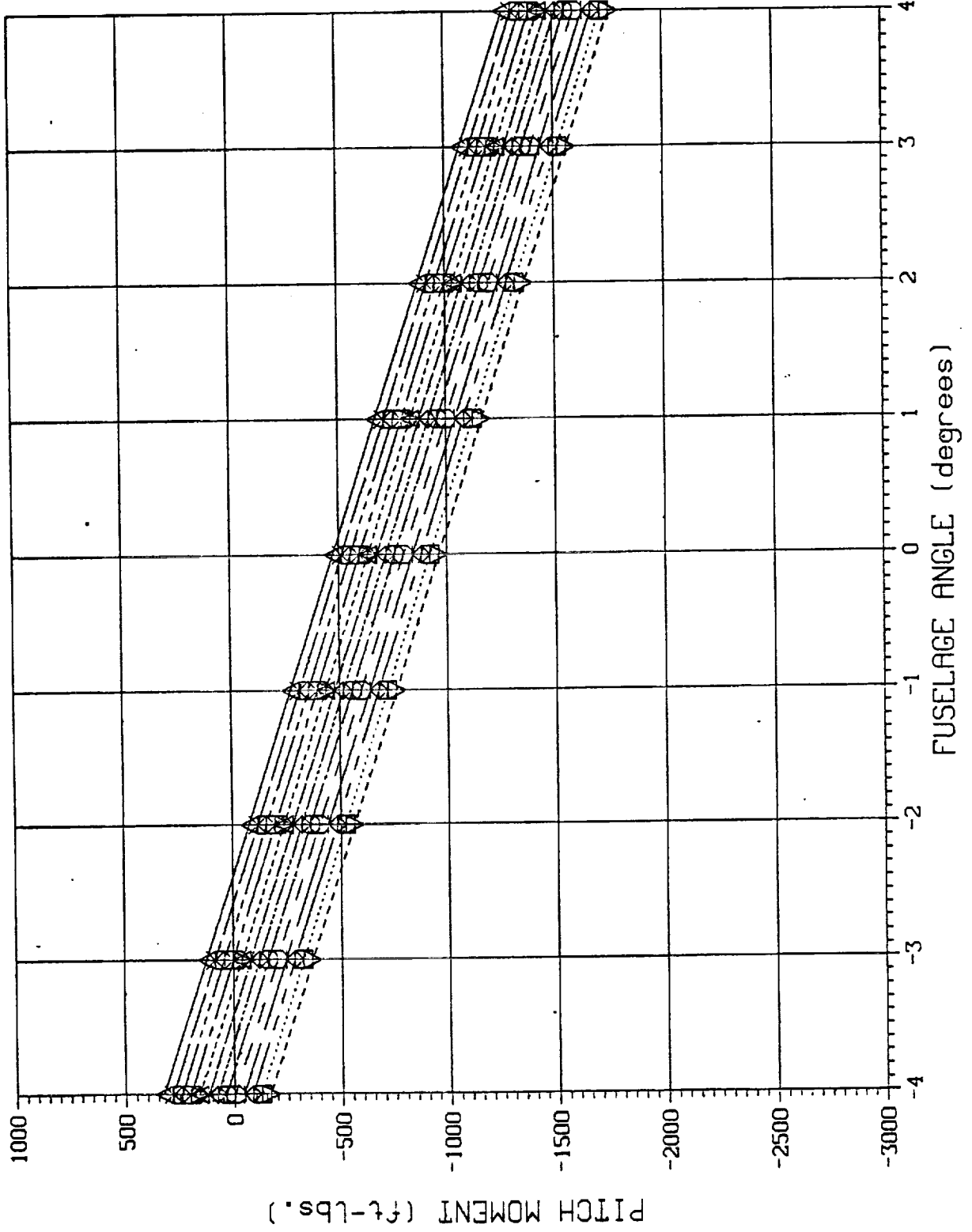
Figure 16. Component Load Trends: Wing Pitching Moment.
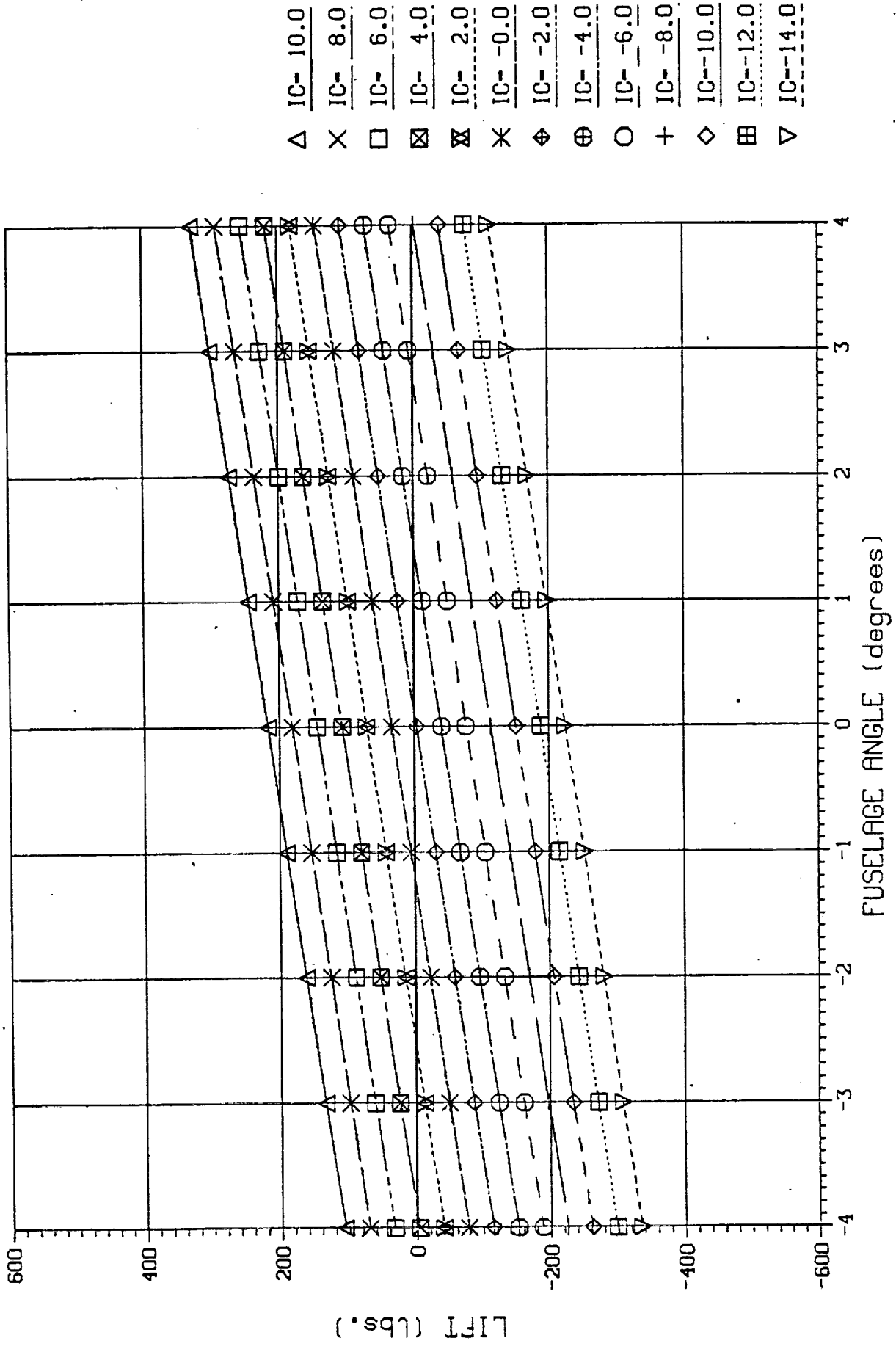
Figure 17. Component Load Trends: Canard Lift.
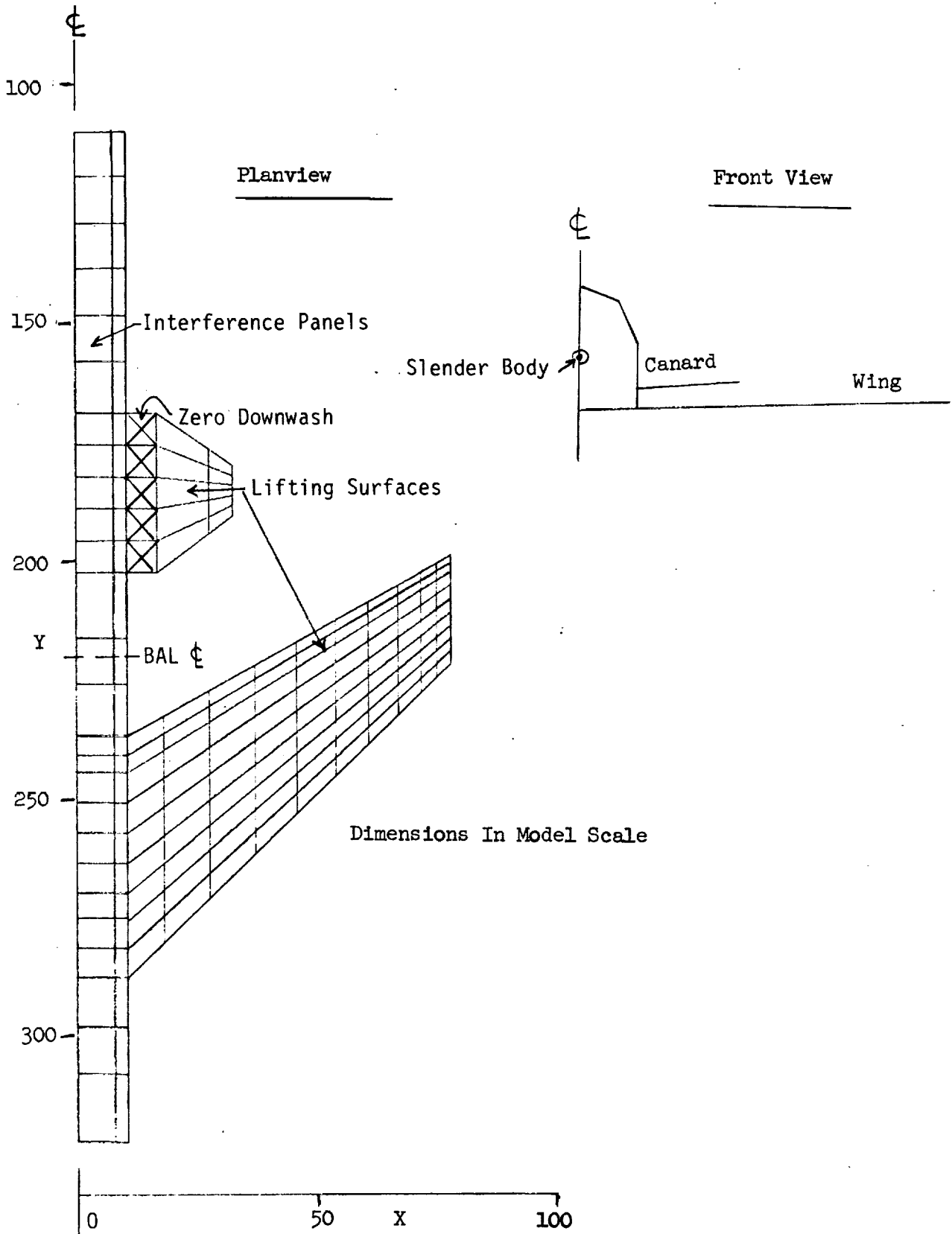
Figure 18. Subsonic Aerodynamic Idealization.
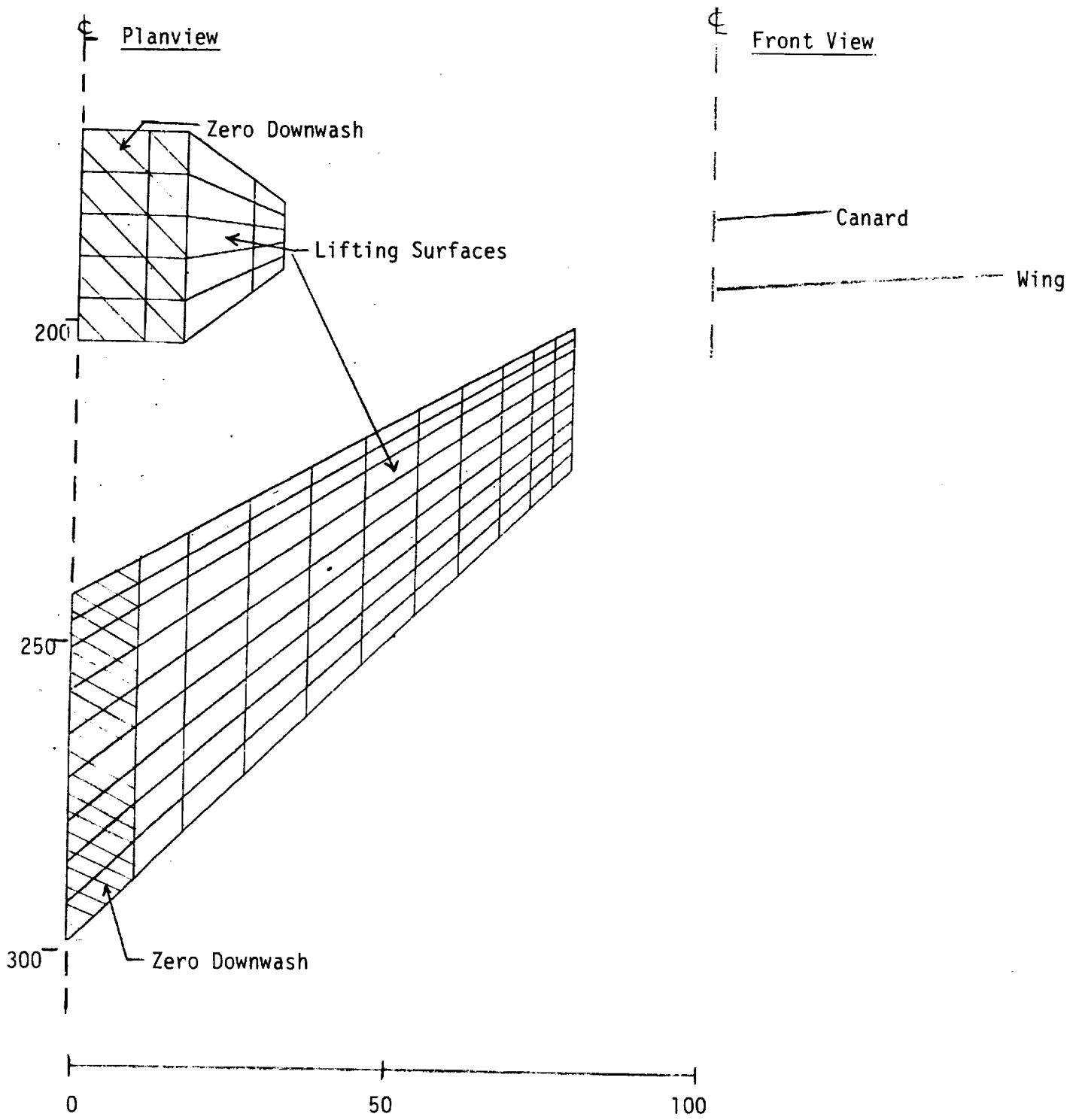
Figure 19. Supersonic Aerodynamic Idealization.
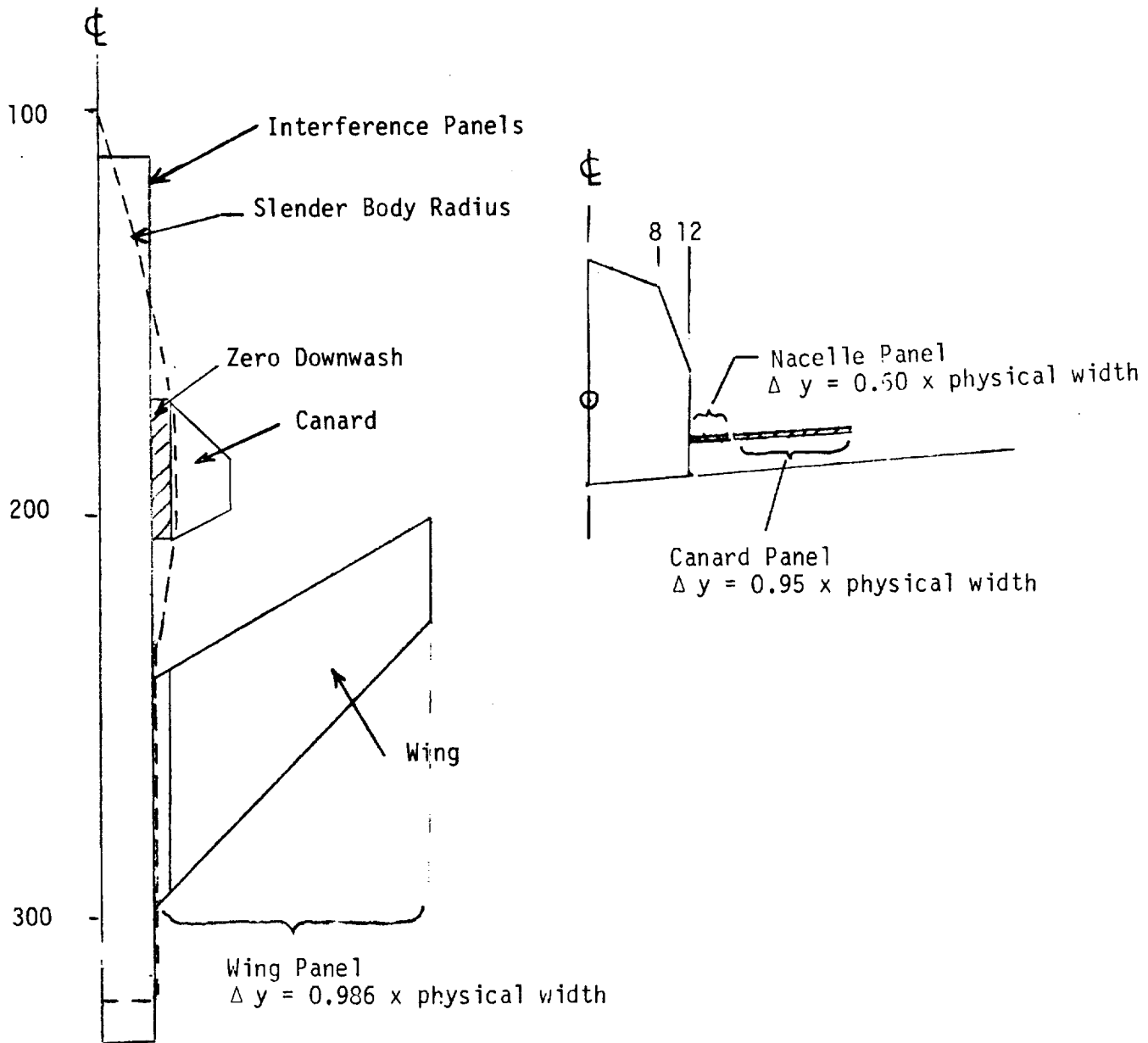
Figure 20. Details of Revised Subsonic Aero Modelling.
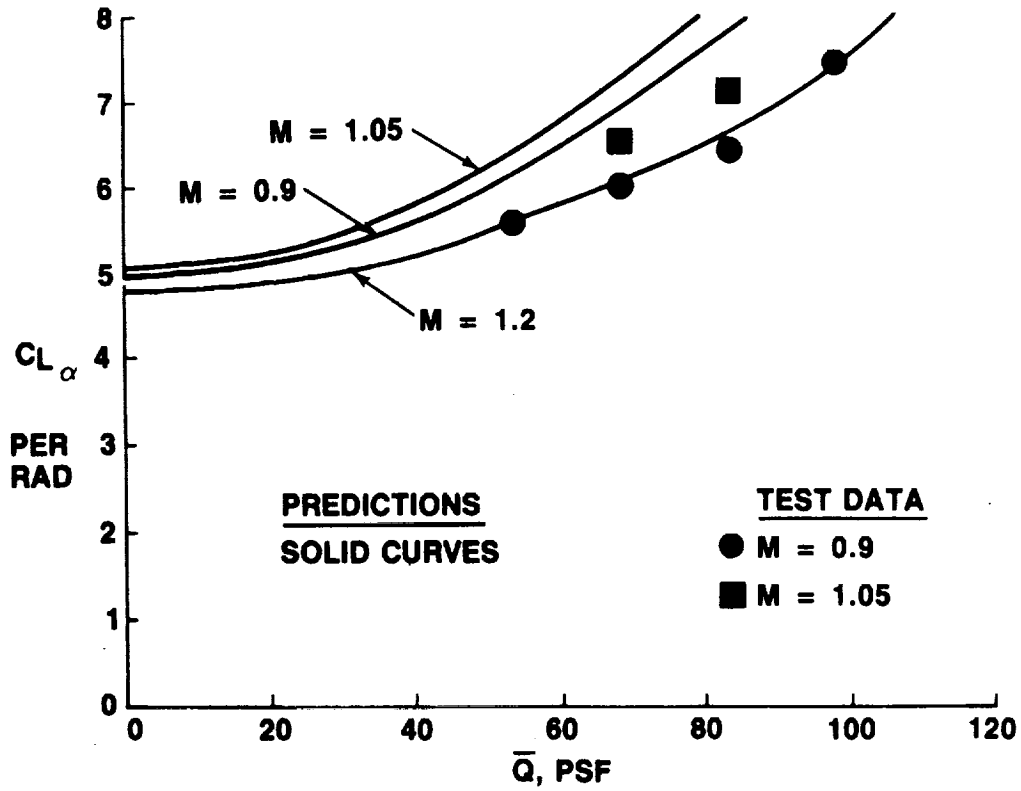
Figure 21. Correlation between Test and Analysis - Flexible Lift Curve Slope.
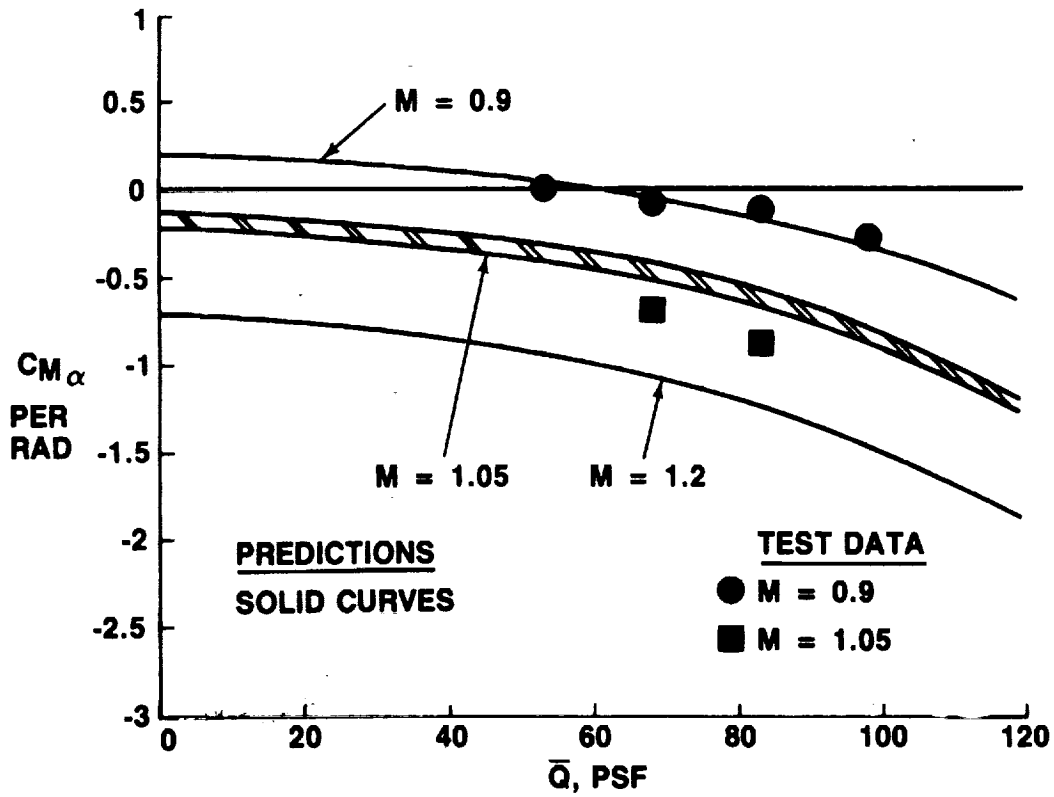
Figure 22. Correlation between Test and Analysis Flexible Moment Curve Slope.

114
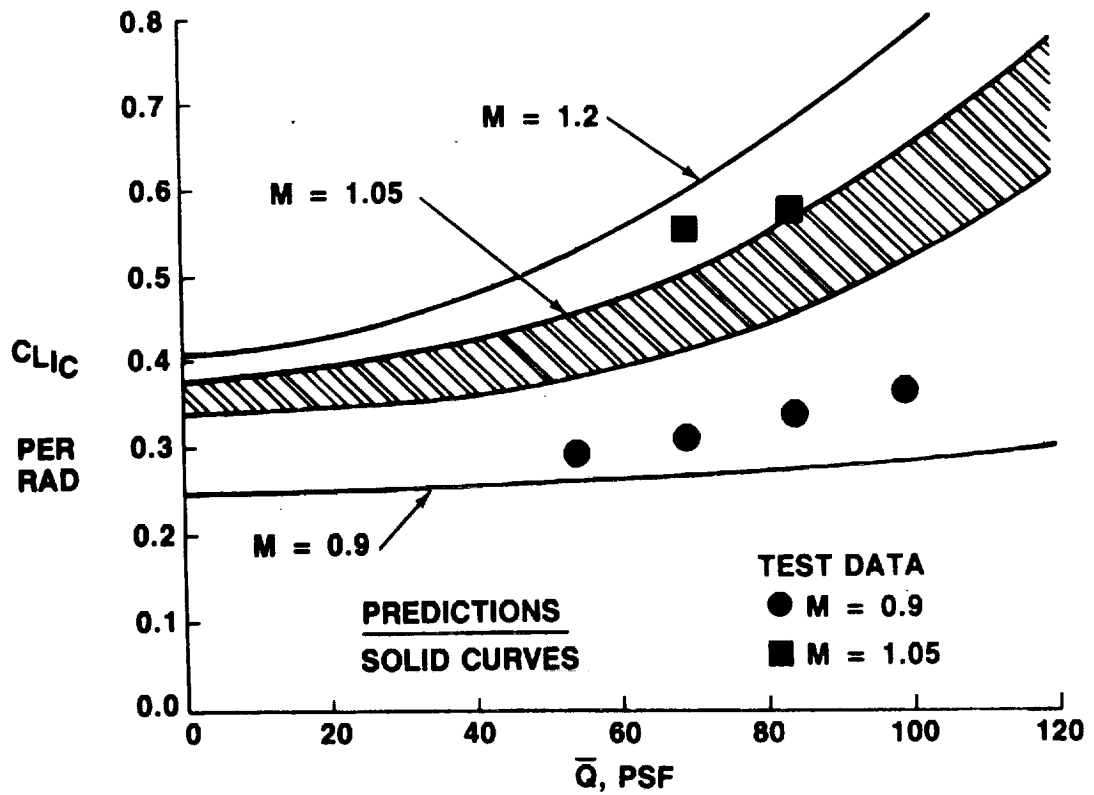
Figure 23. Correlation between Test and Analysis - Flexible Lift due to Canard Incidence.
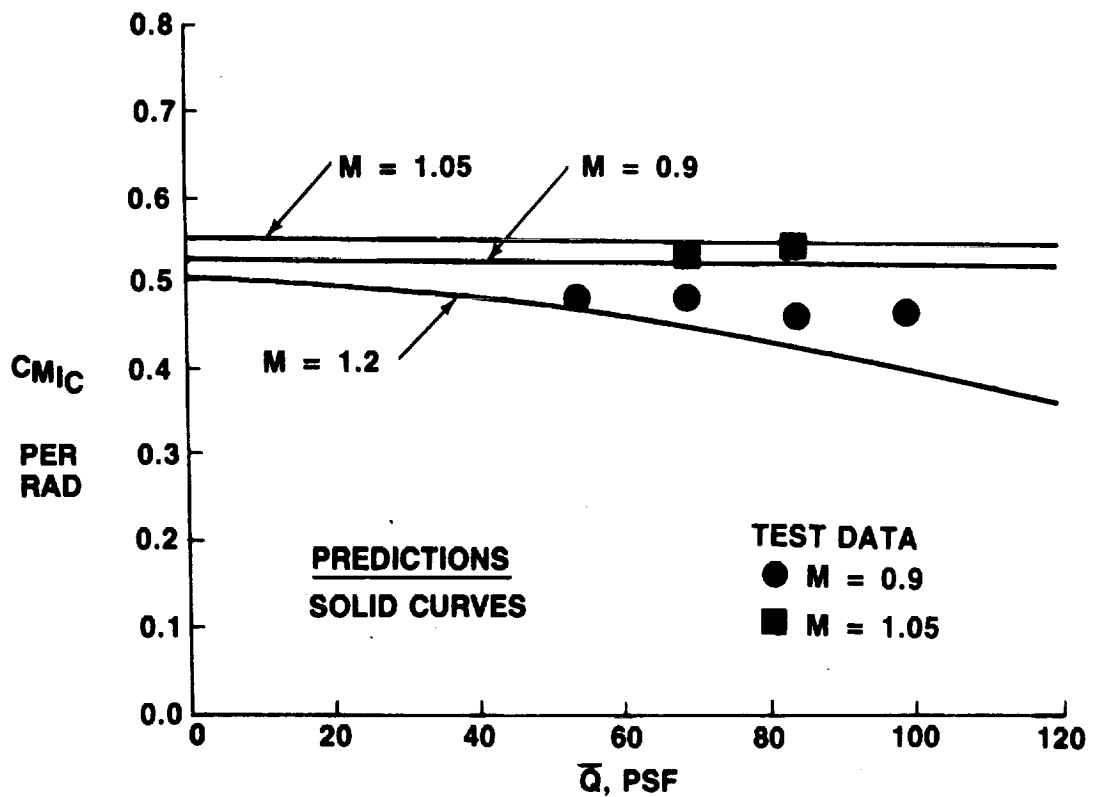
Figure 24. Correlation between Test and Analysis - Flexible Moment due to Canard Incidence.

115
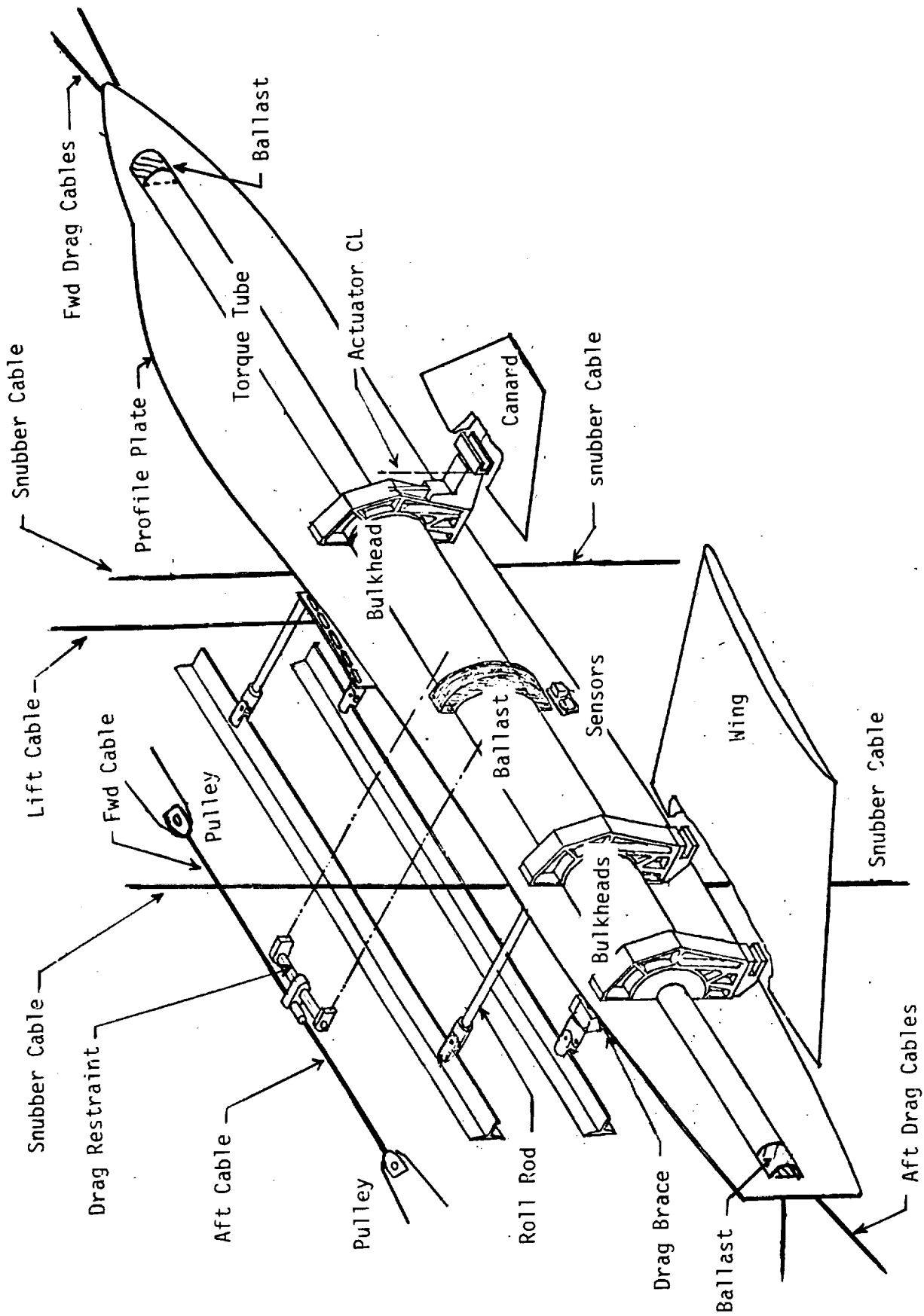
(a) Sketch of Structural Components of Flutter Model.

Figure 25. Model Components.

Back Face Of Profile Plate

Drag Cable Attachment

Aft Top Roll Rod

Drag Brace

Universal

Aft Bottom Roll Rod

Forward Top Roll Rod And Control System Cables

Forward Bottom Roll Rod And Hydraulic Lines

Actuator

Forward Bulkhead

Actuator Mounting Bracket

Linkage
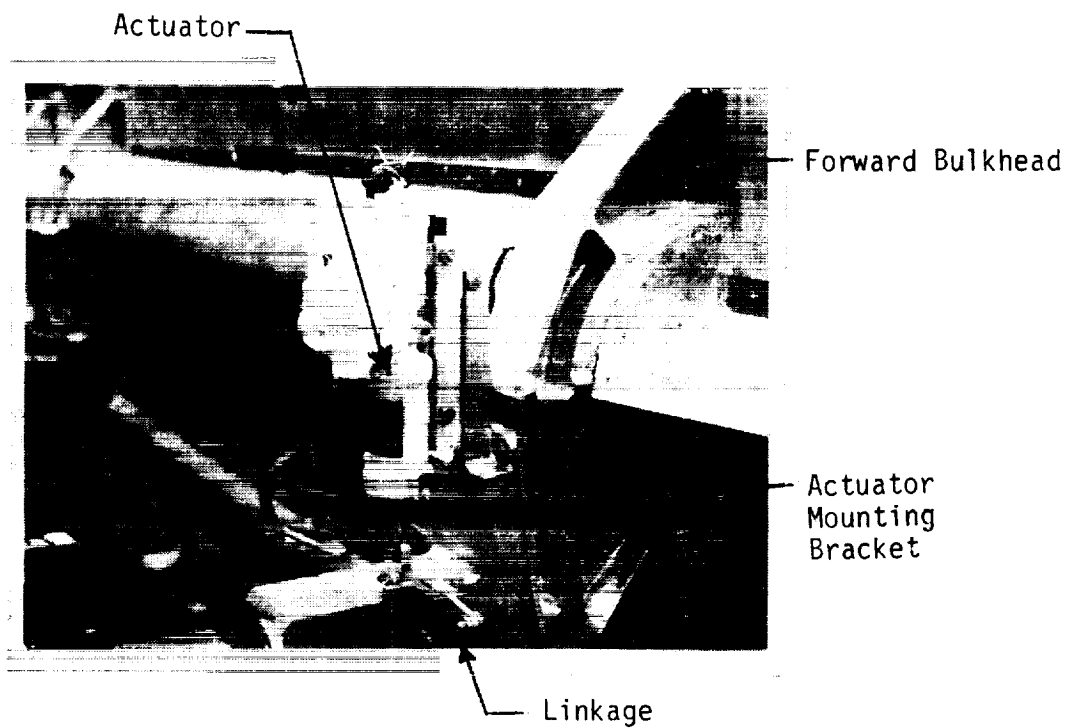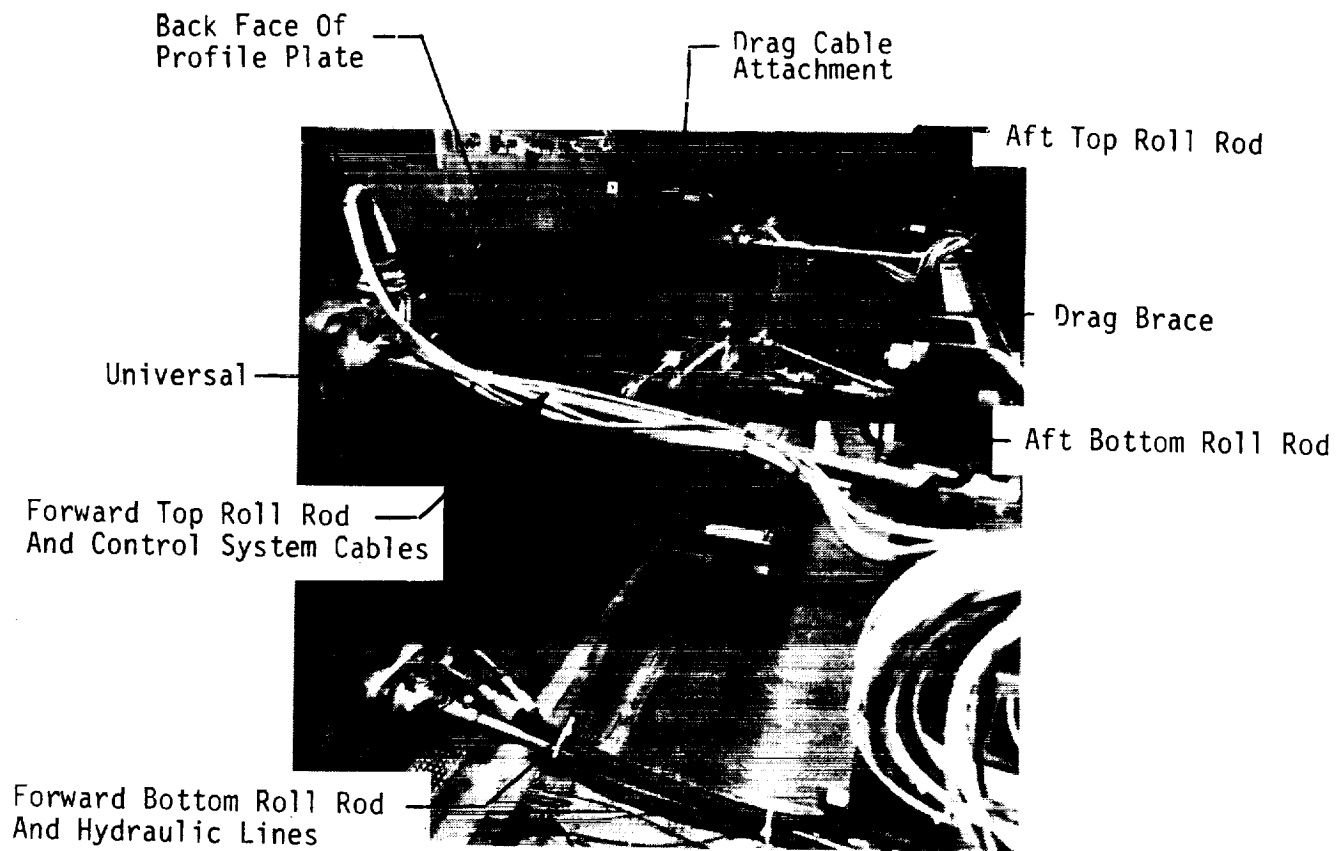
(b) Photographs of Model Components.

Figure 25 Continued. Model Components.
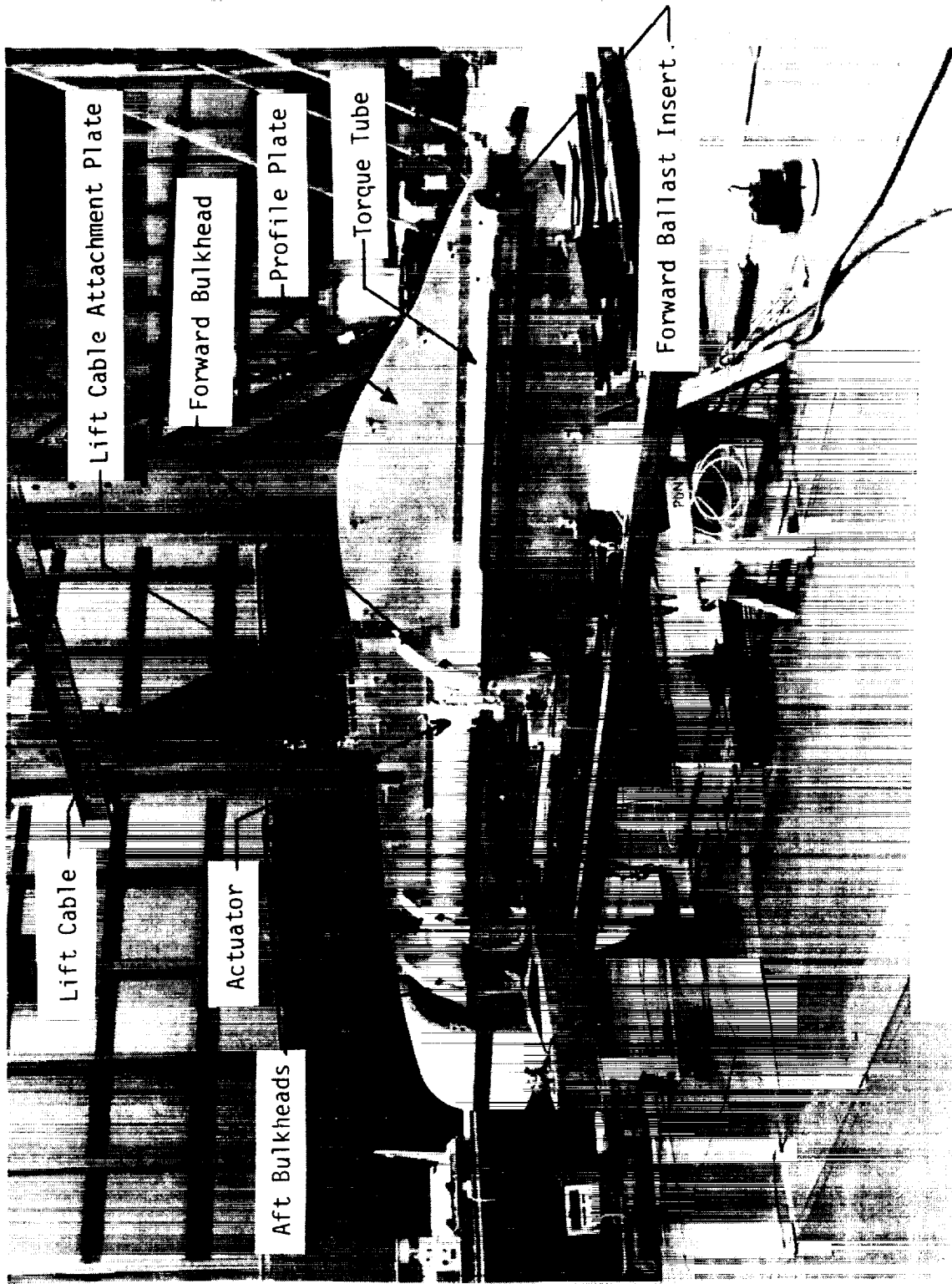
(c) Photograph of Partially Assembled Model.

Figure 25 Concluded. Model Components.
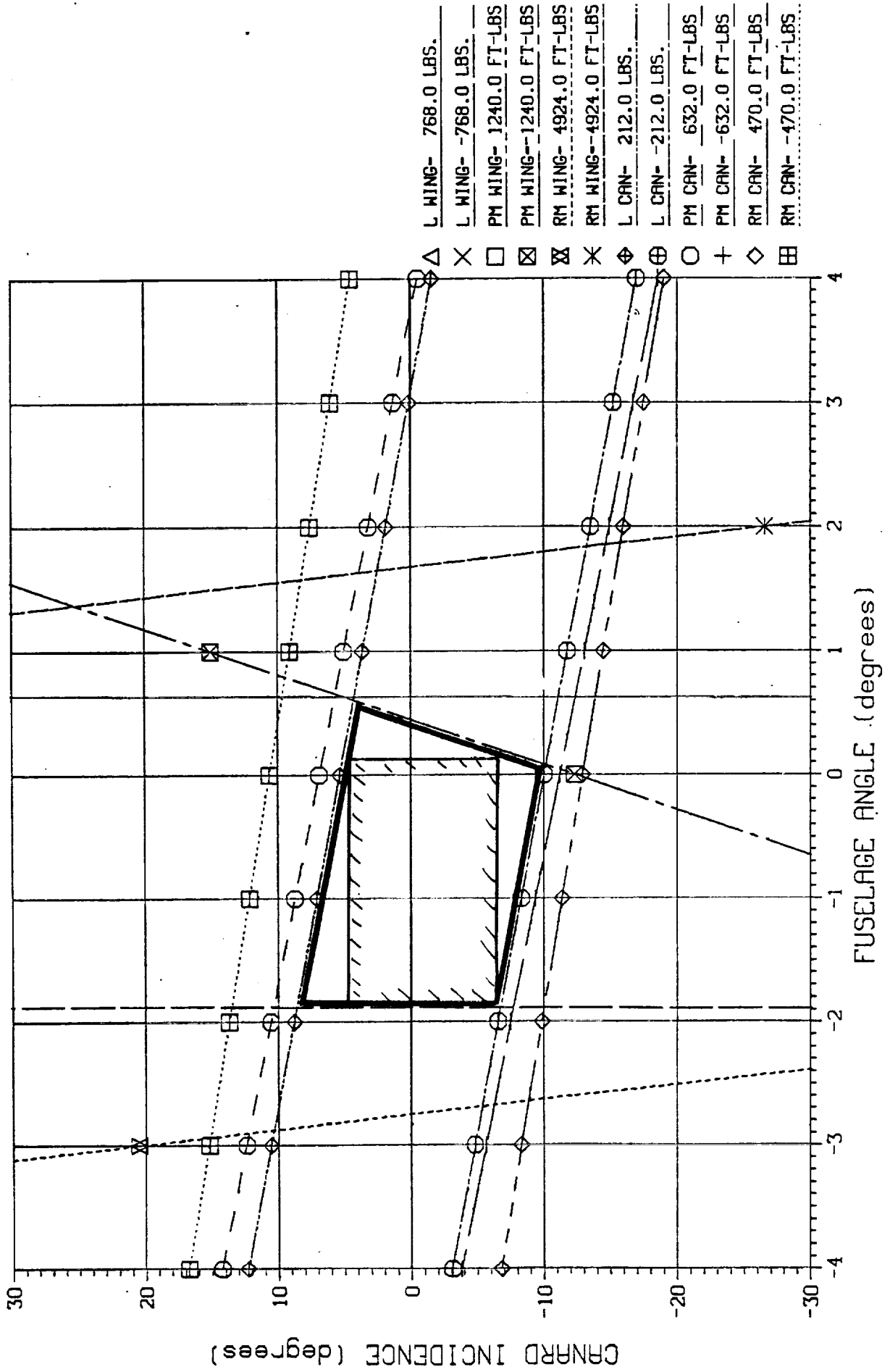
Figure 26. Component Load Limit Constraints.

119

50% FSM MODEL
PRE-TEST ALPHA LIMITS (STOPS)
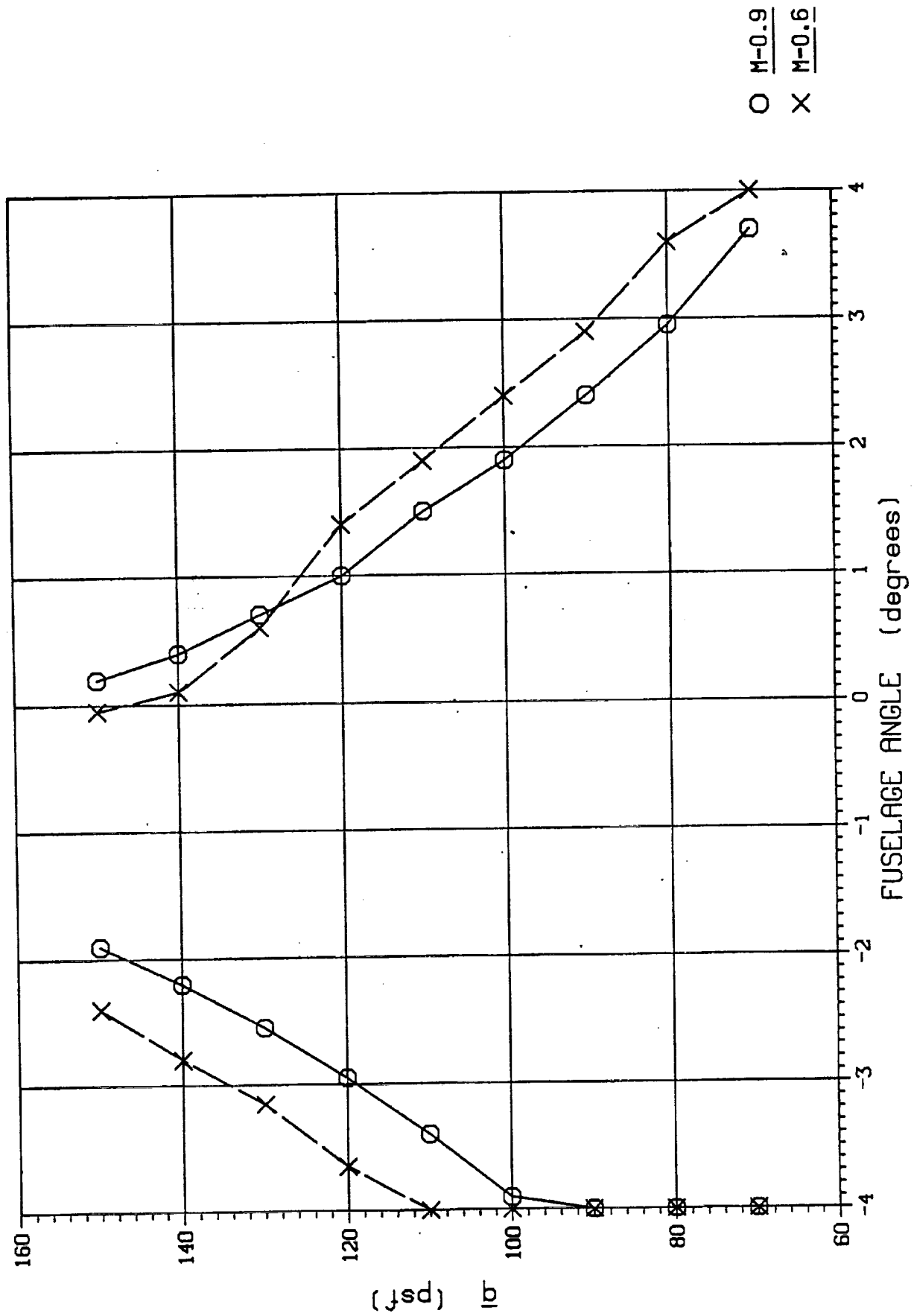
Figure 27. Pre-Test Estimated Angle of Attack Limits.

120
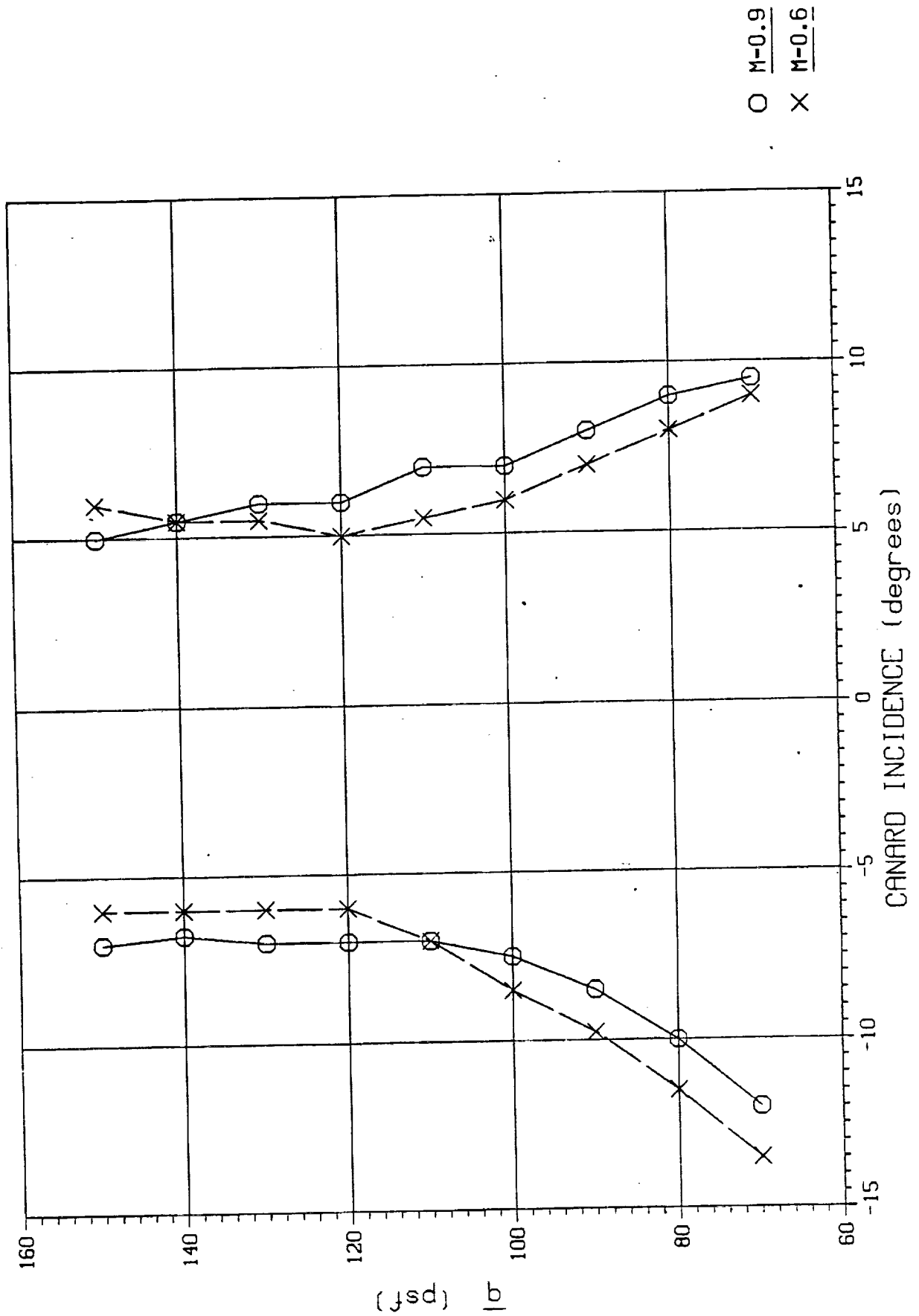
Figure 28. Estimated Canard Incidence Limits.

121
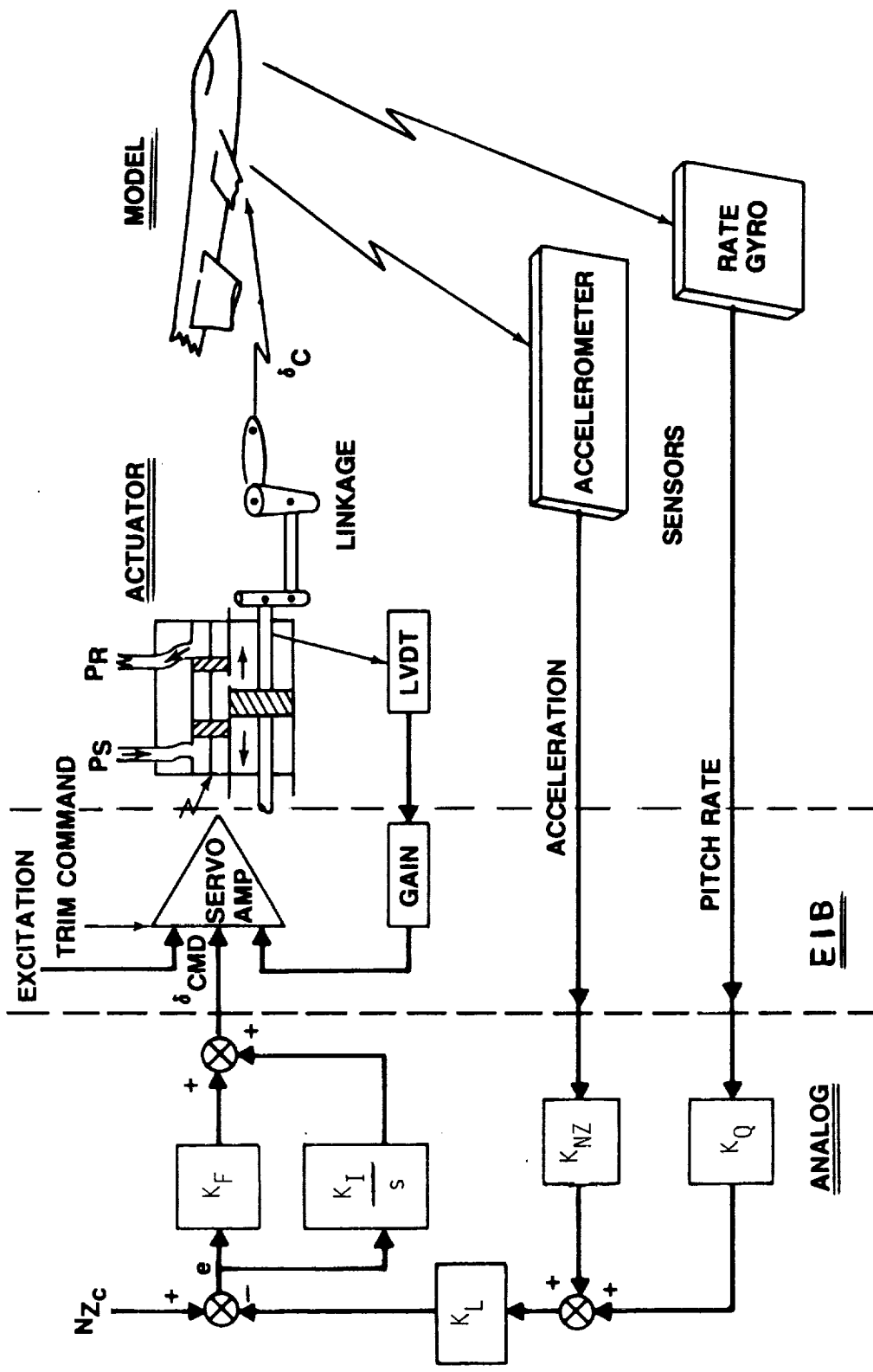
Figure 29. Control System Schematic.
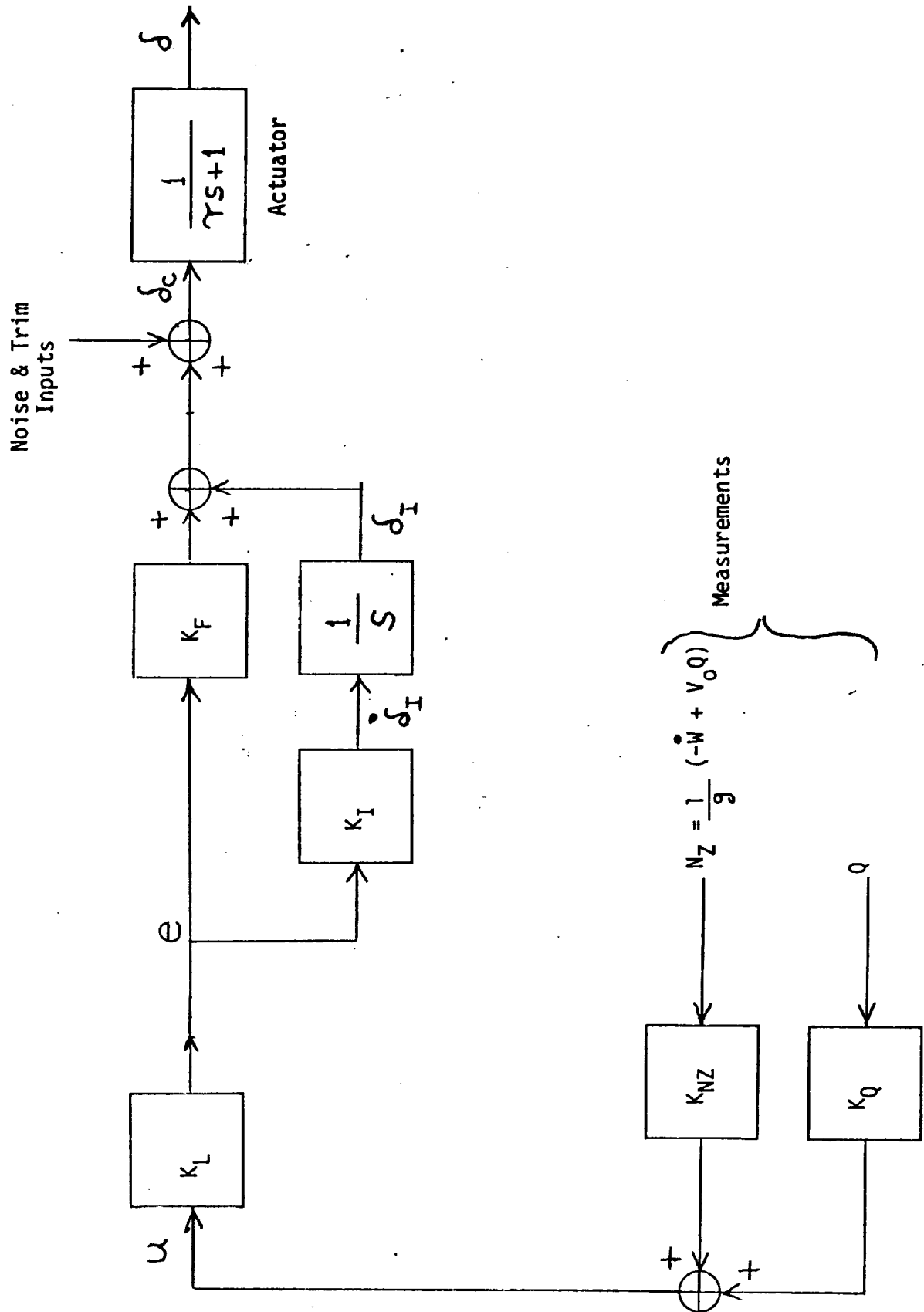
Figure 30. Block Diagram of SAS Control Loop.

Actuator

$\frac{1}{\gamma s + 1}$

δ

δ_c

Noise & Trim Inputs

K_F

$\frac{1}{s}$

δ_I

$\dot{\delta}_I$

K_I

e

K_L

u

$N_Z = \frac{1}{g}(-\dot{W} + V_0 Q)$

Measurements

Q

K_{NZ}

K_Q

123
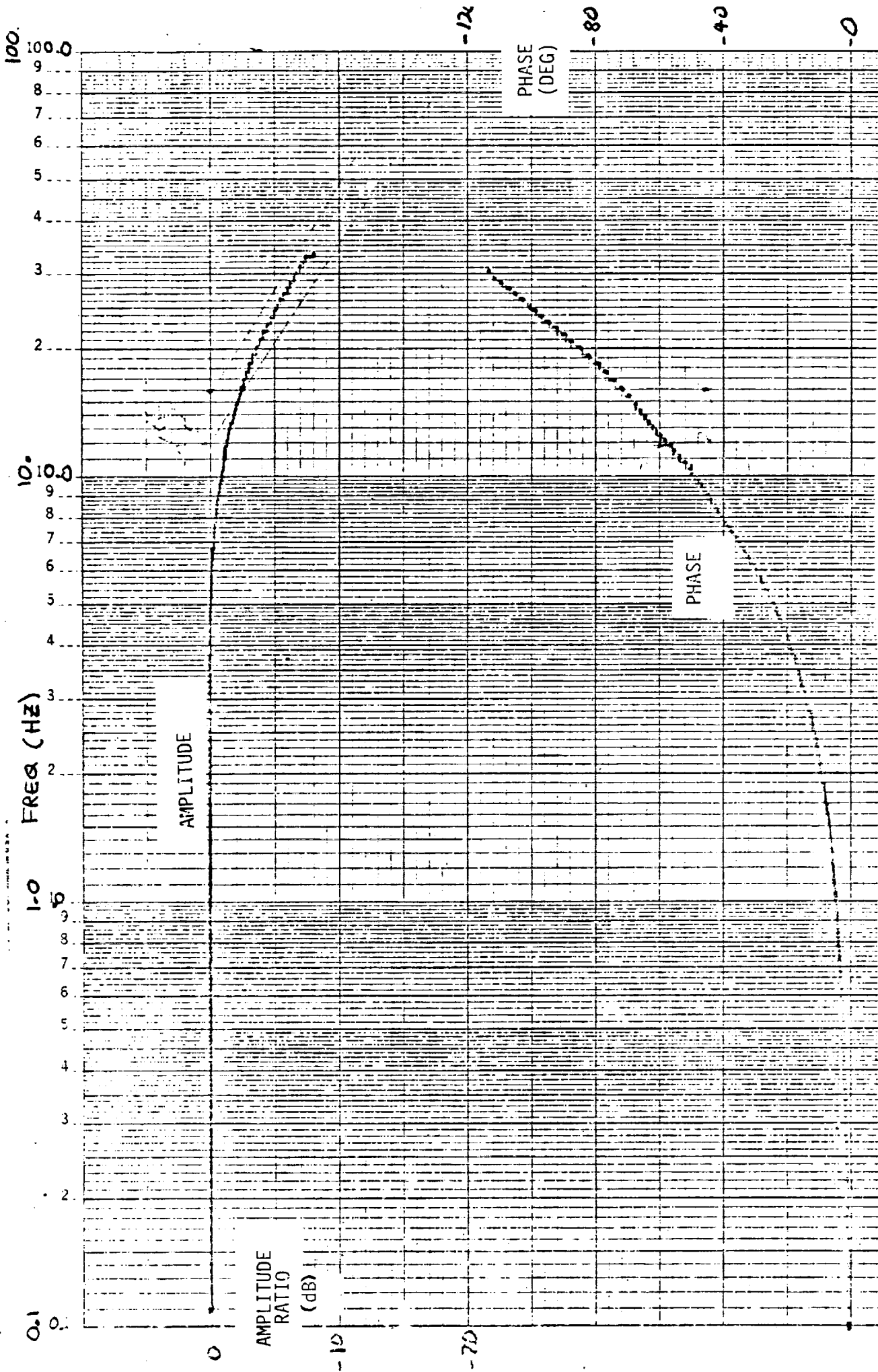
Figure 31. Bench Test Actuator Frequency Response.

124
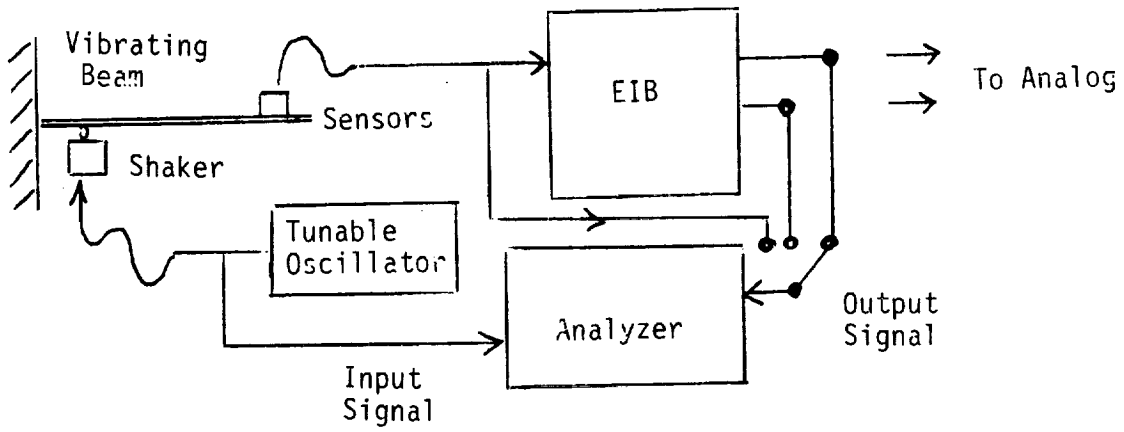
(A) SETUP FOR SENSOR/EIB CHECKOUT
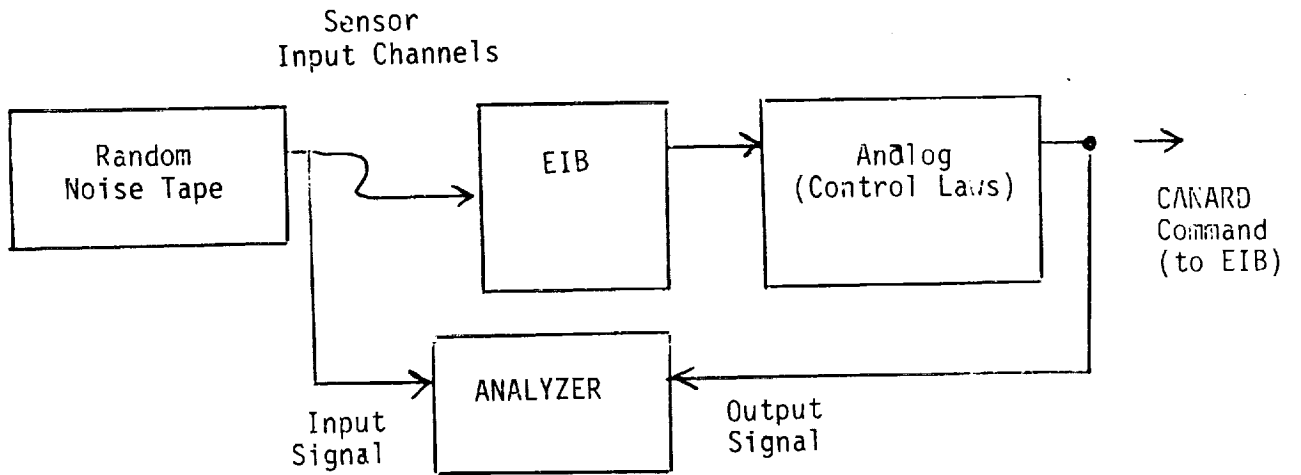
(B) SETUP FOR EIB/ANALOG CHECKOUT

Figure 32. Setup for Component Checkouts.
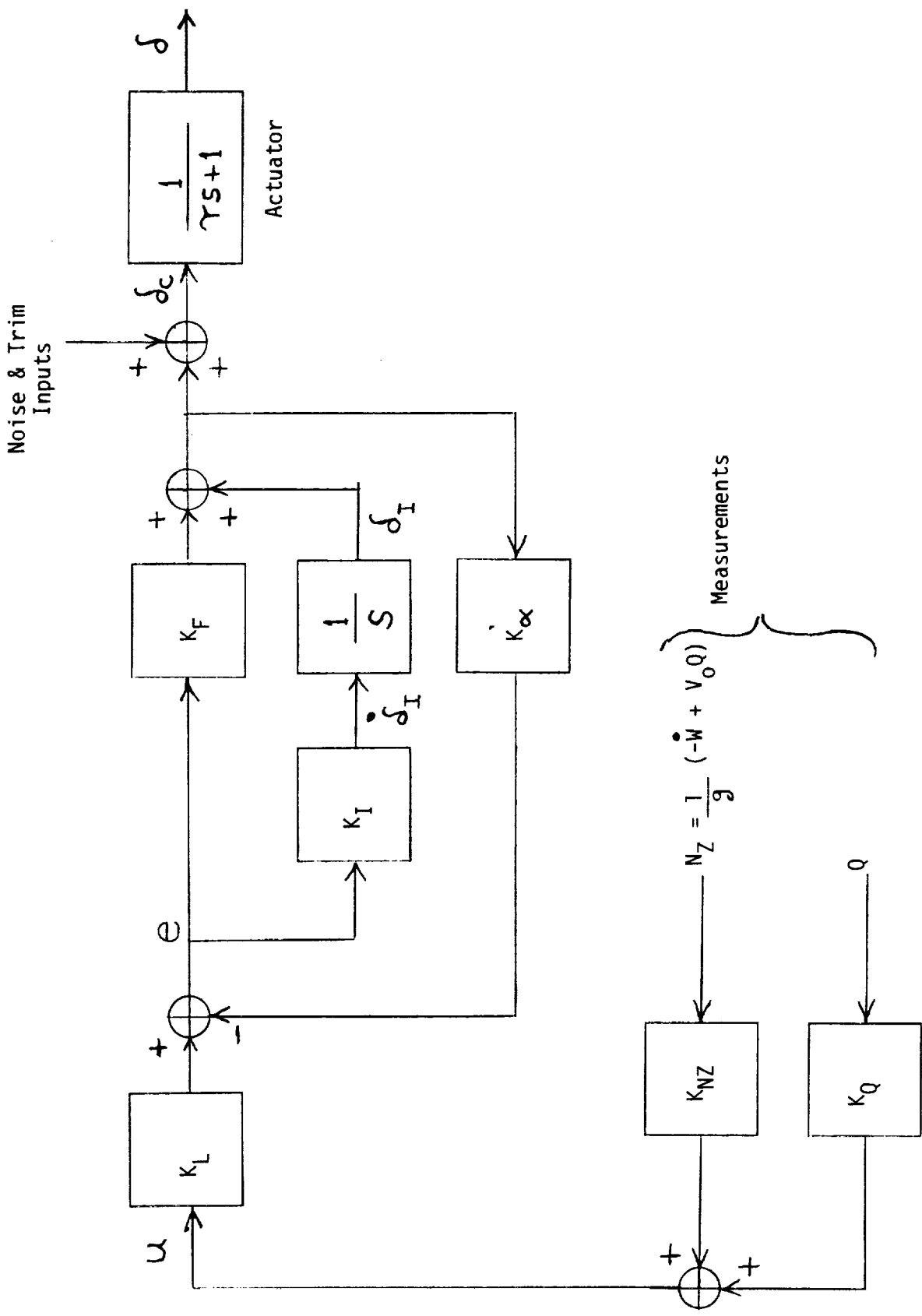
Figure 33. Block Diagram of SAS Control Loop Used in GVT and Wind-Tunnel Test.
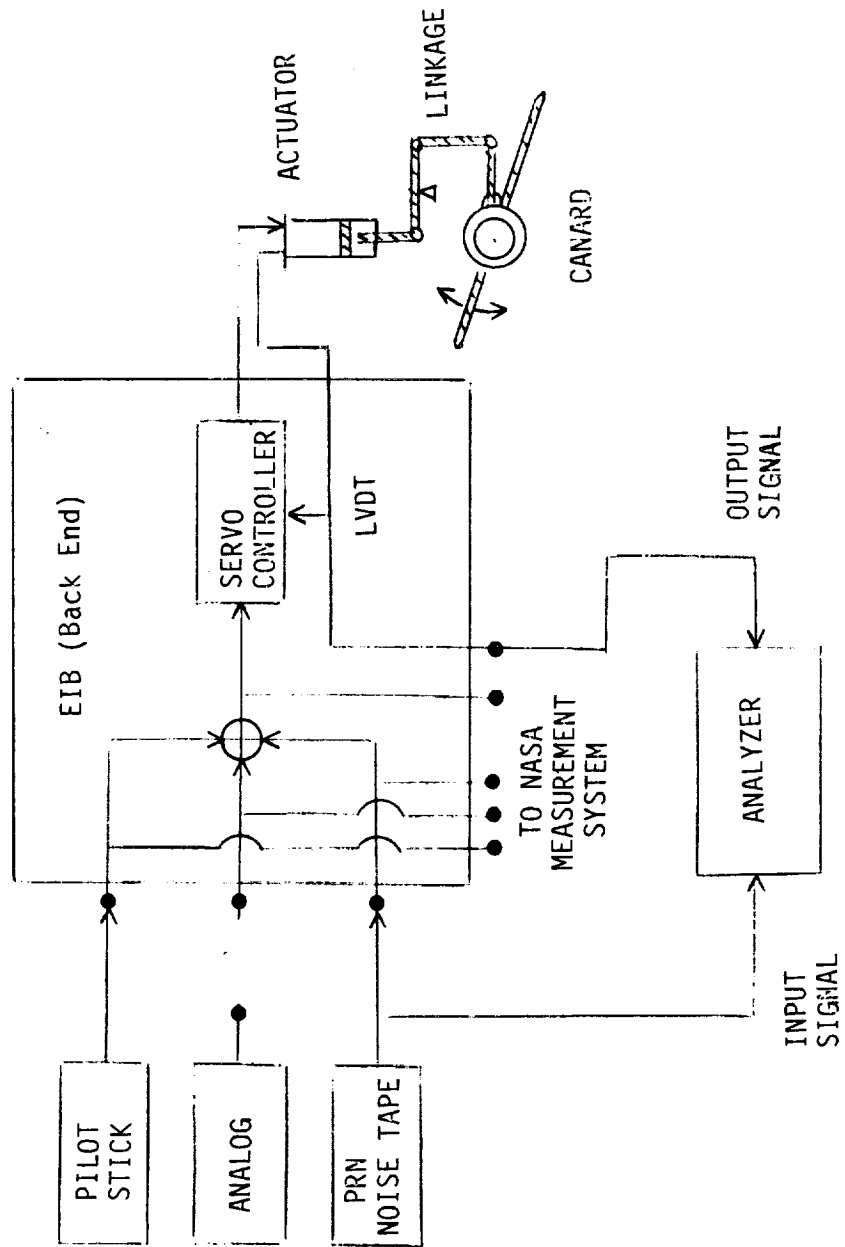
Figure 34. Setup for Actuator/Servo/EI3 Checkout.
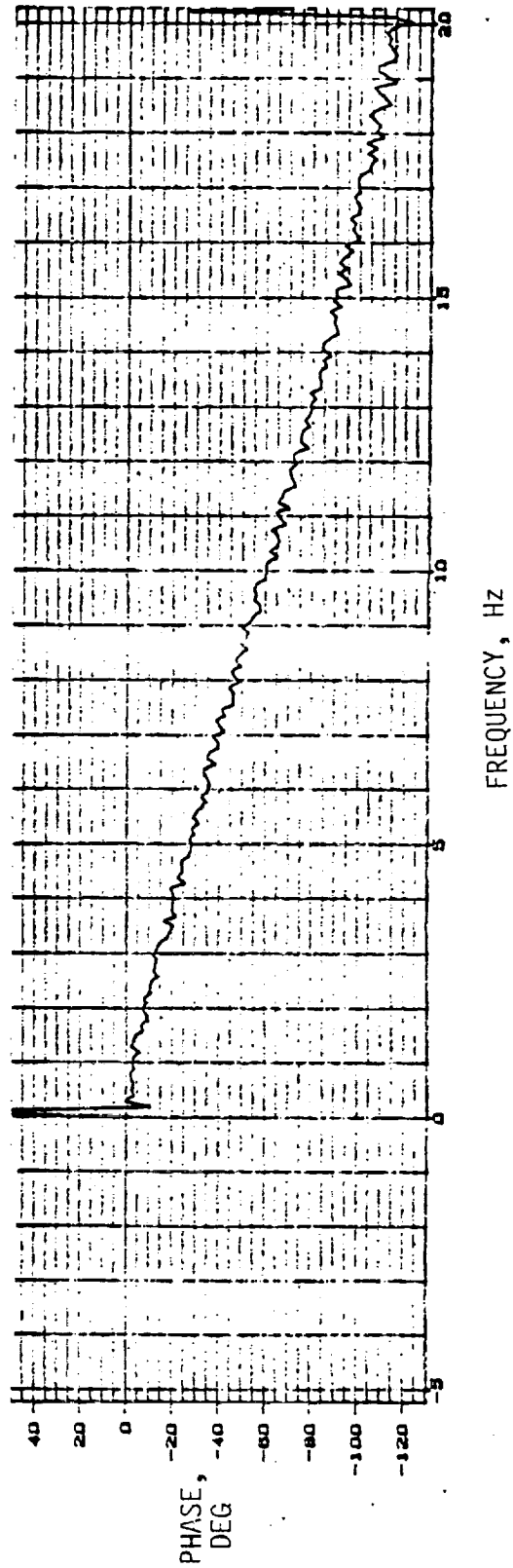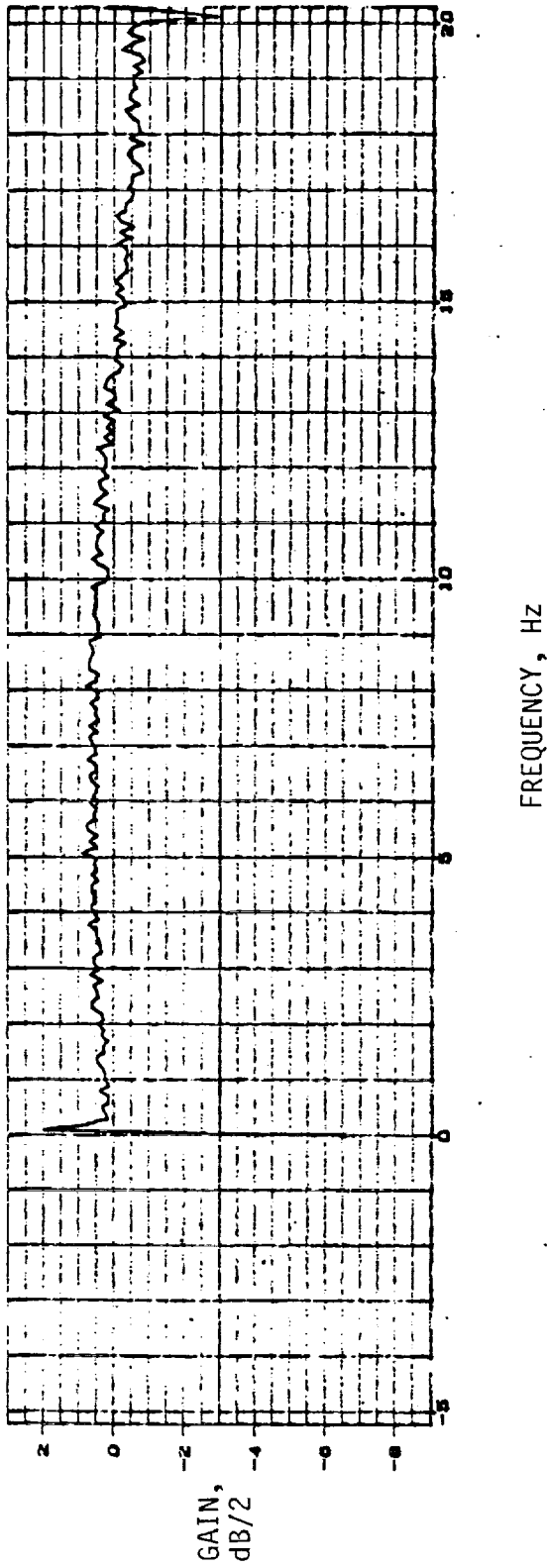
Figure 35. Frequency Response Function for Actuator/Servo/EIB.
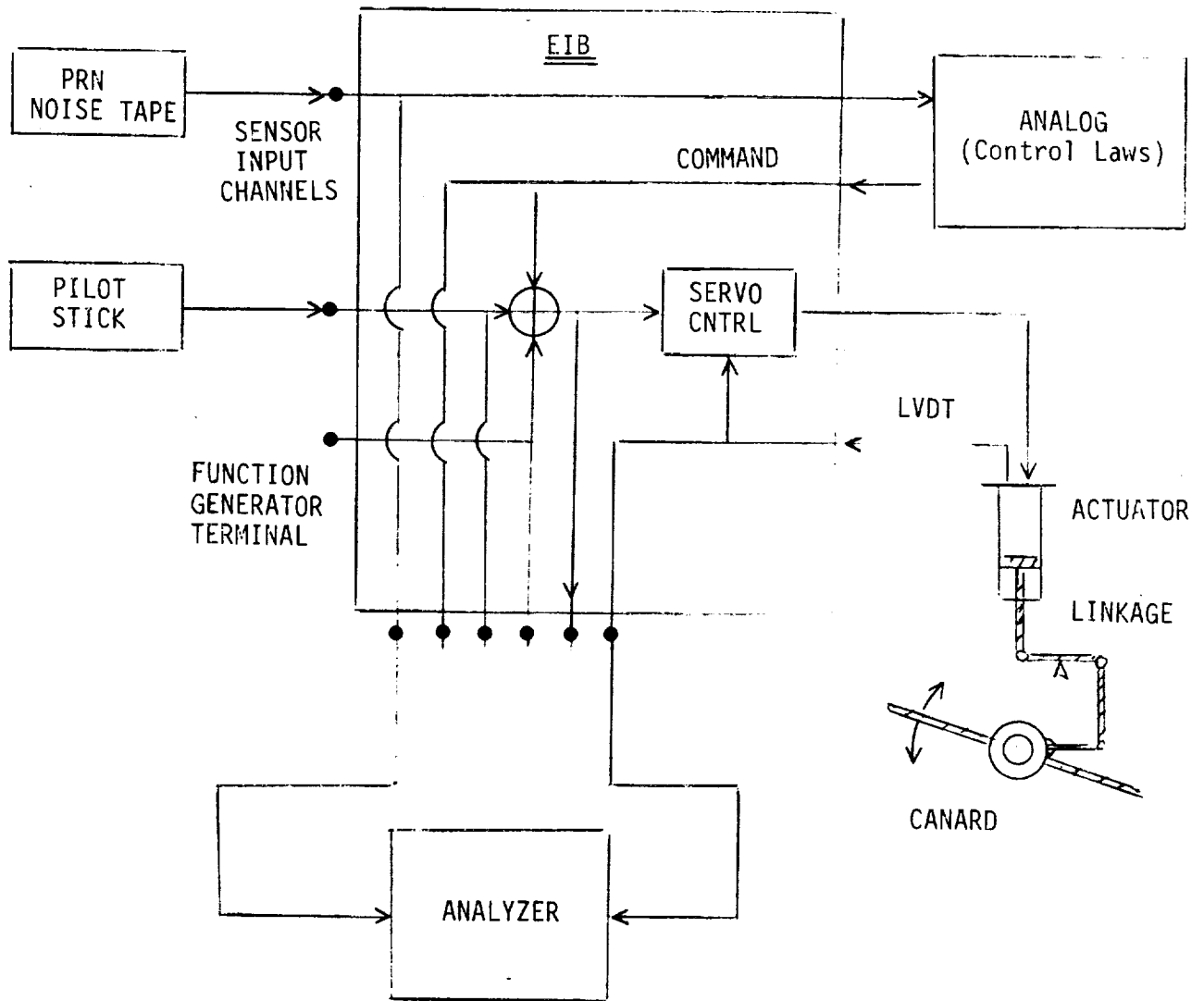
Figure 36.   Setup for End-to-End Checkout.
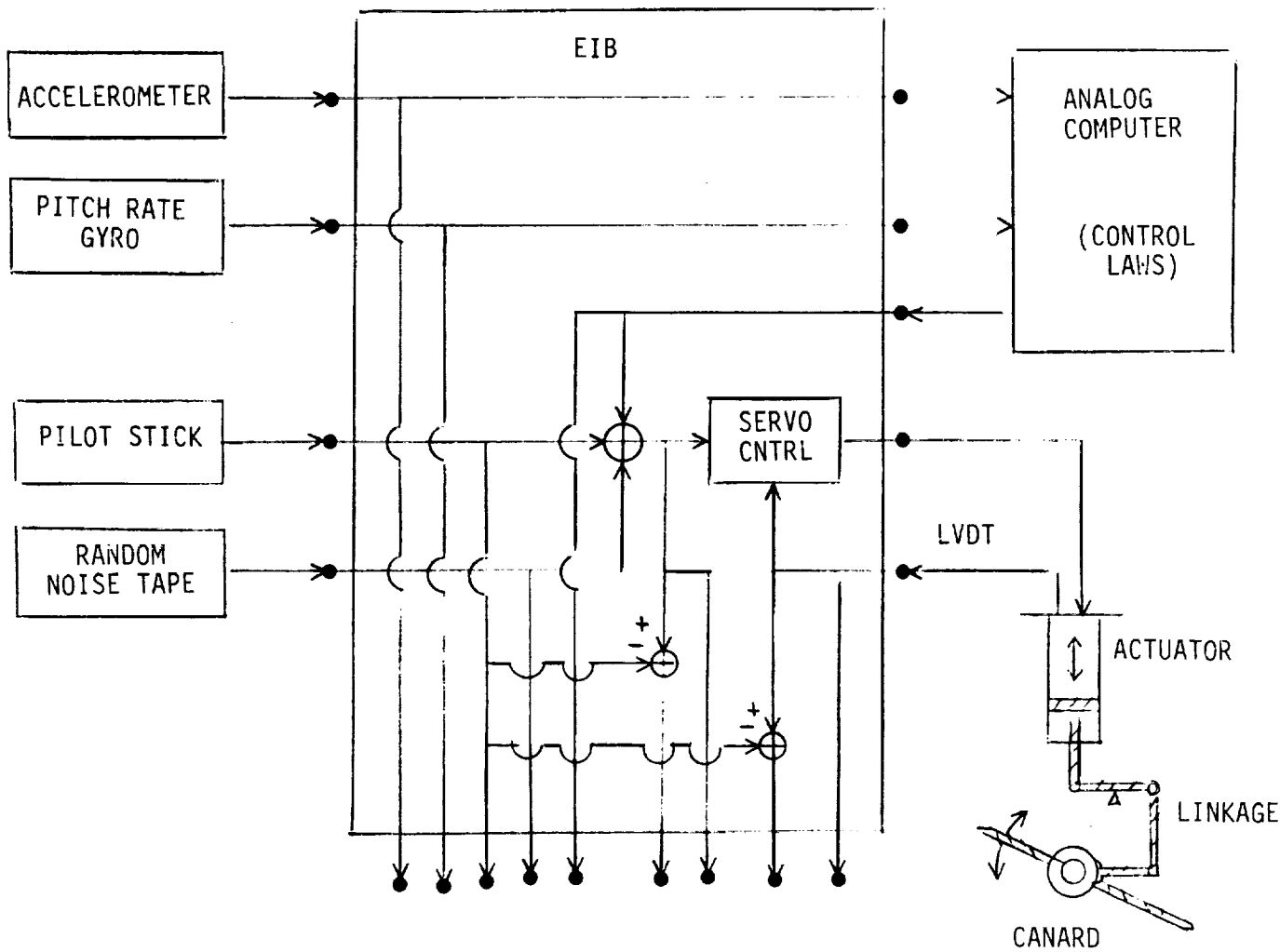
Figure 37. Setup for Open and Closed Loop Ground and Tunnel Tests.
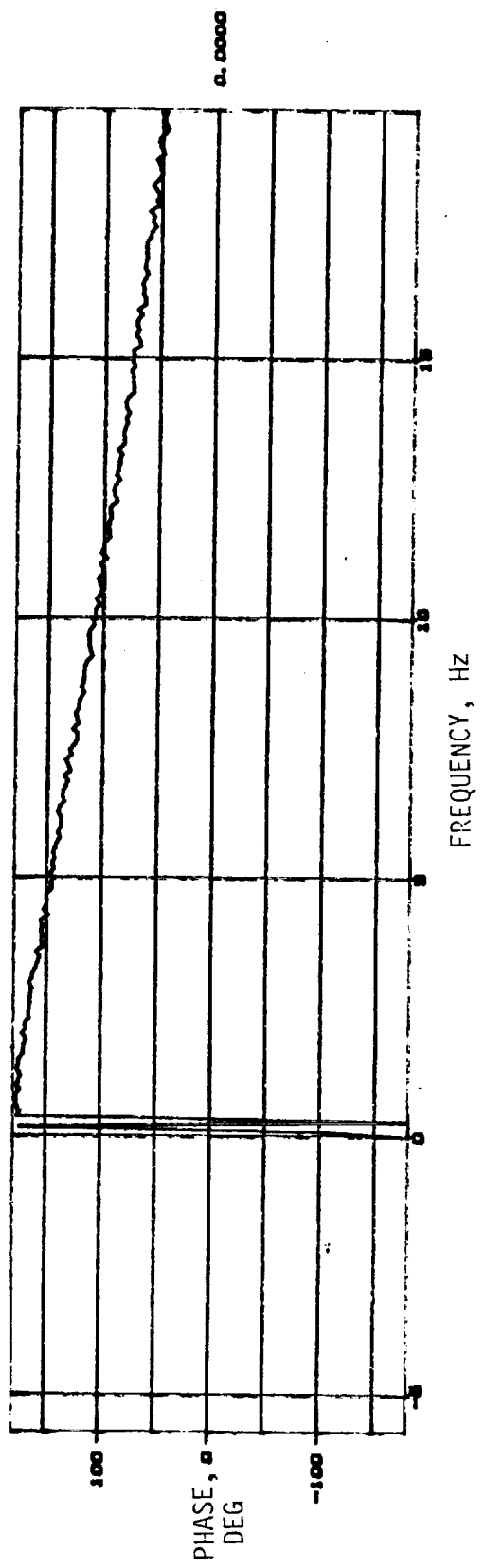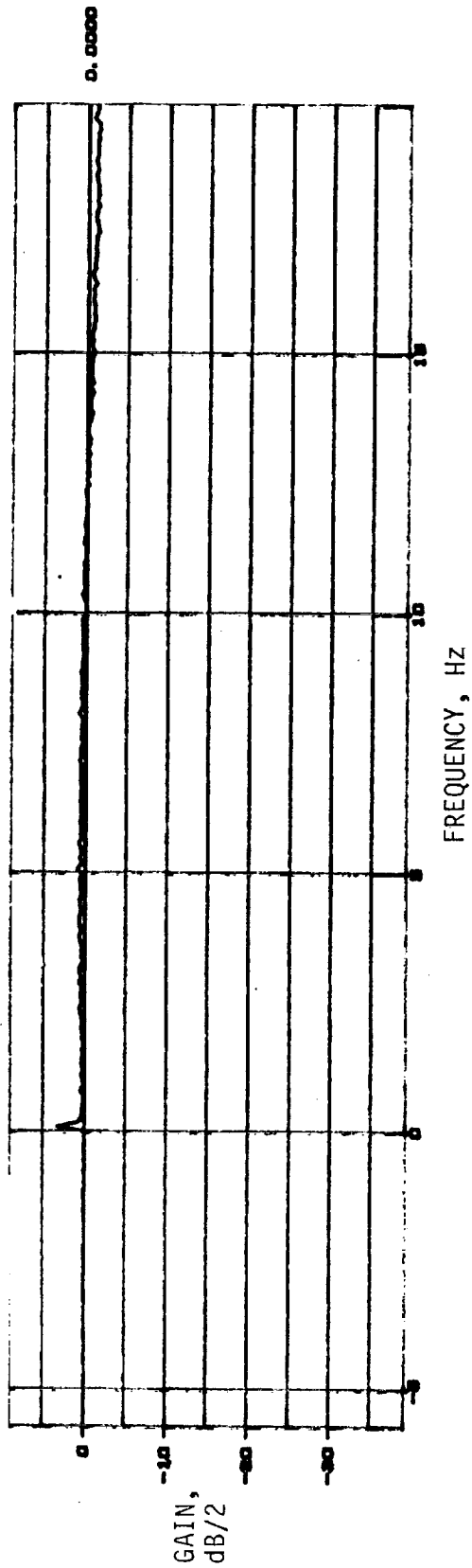
Figure 38. Open Loop FRF for LVDT to Random Noise.

131

FREQUENCY, Hz

FREQUENCY, Hz
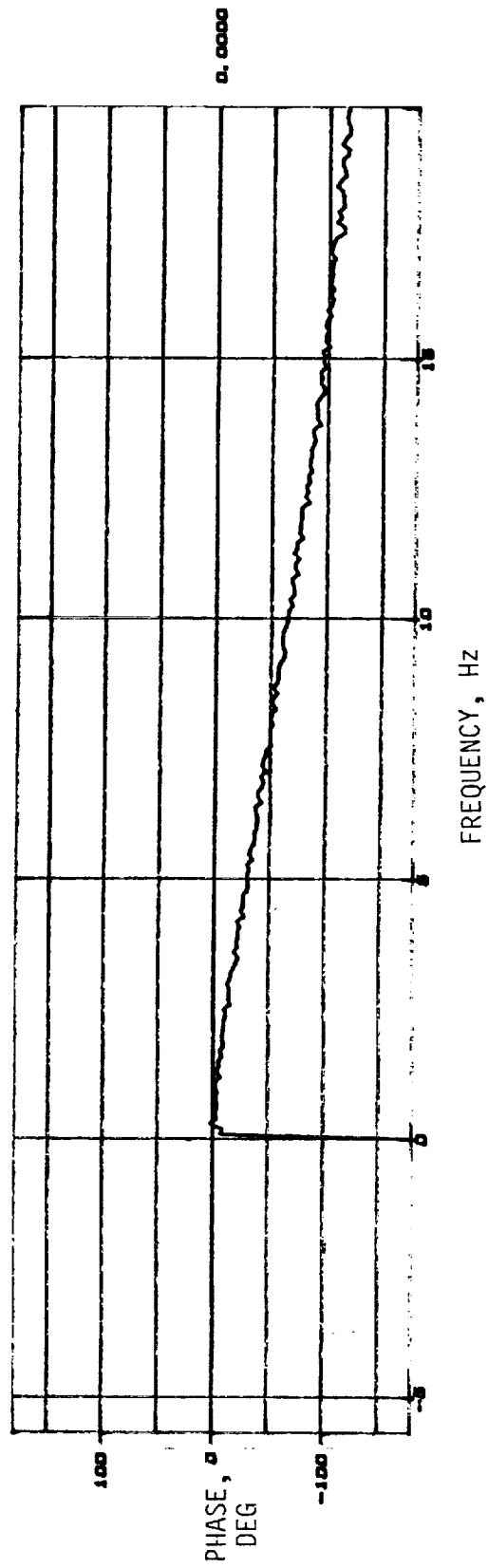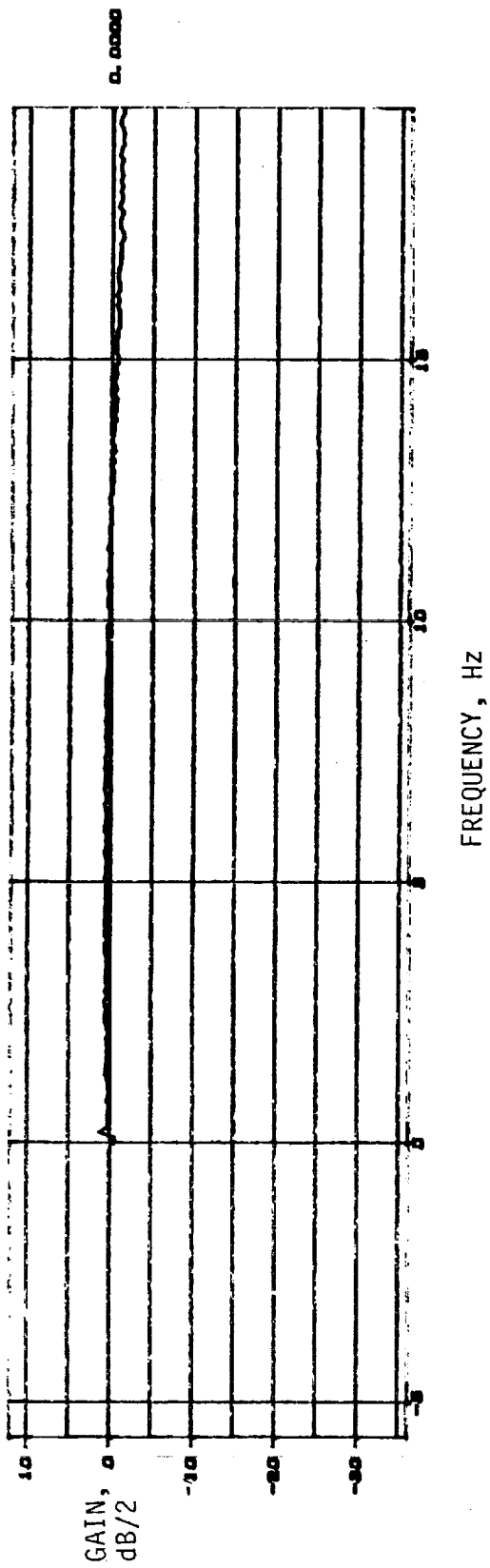
Figure 39. Closed Loop FRF for LVDT to Servo Command.

FREQUENCY, Hz

GAIN,
dB/2

FREQUENCY, Hz

PHASE,
DEG
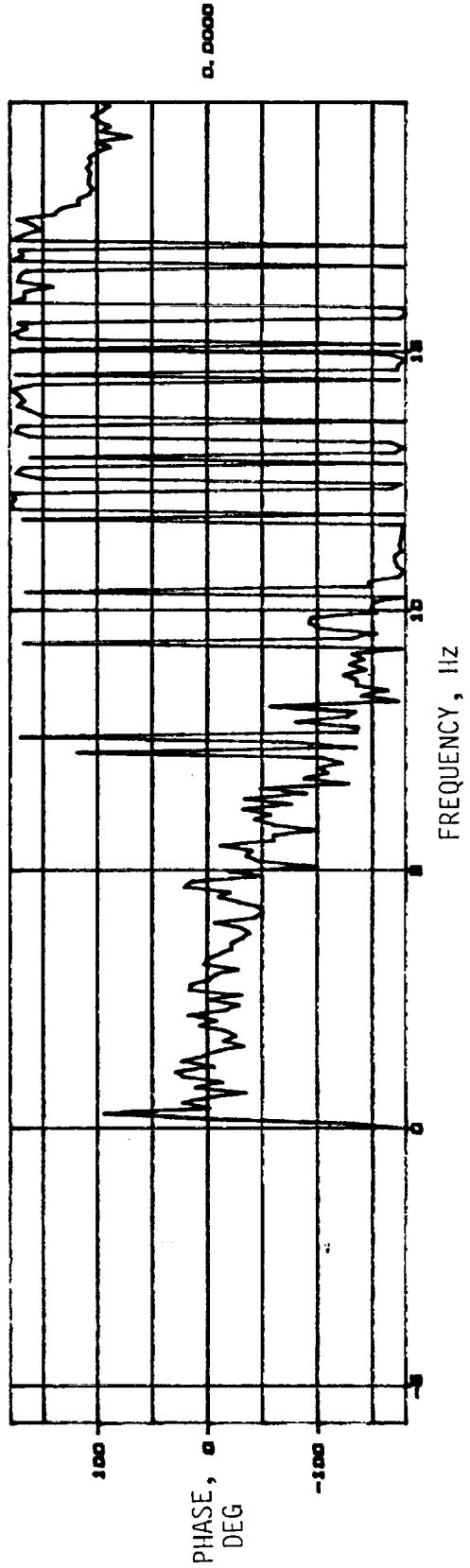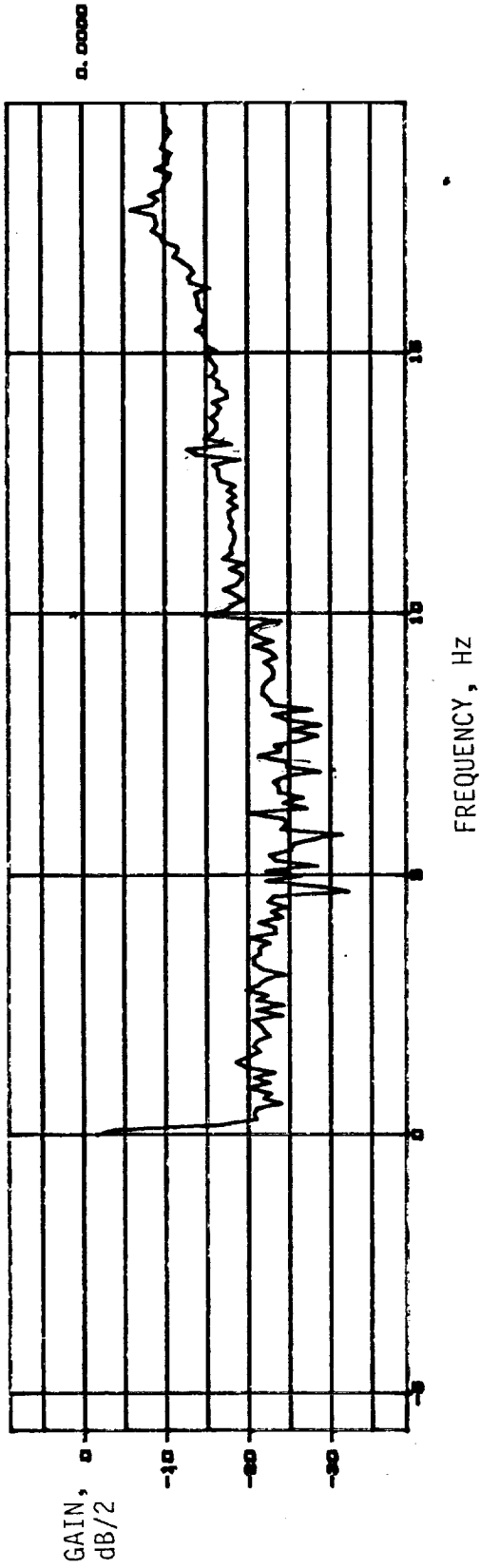
Figure 40.   Open Loop FRF for Gyro to Servo Command.
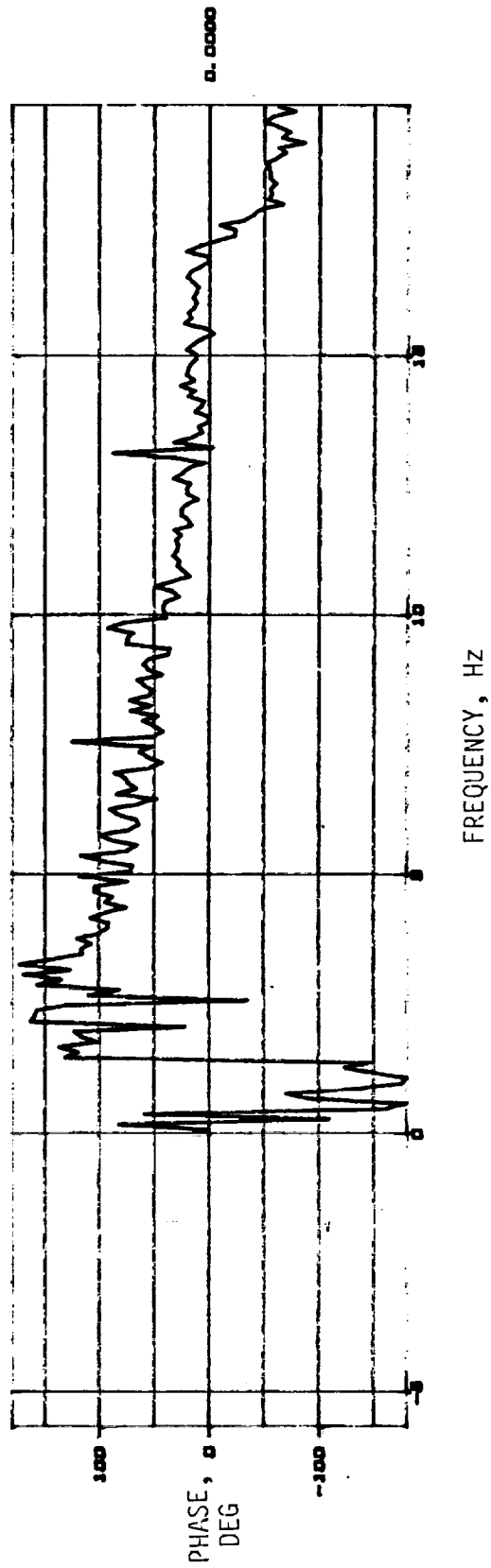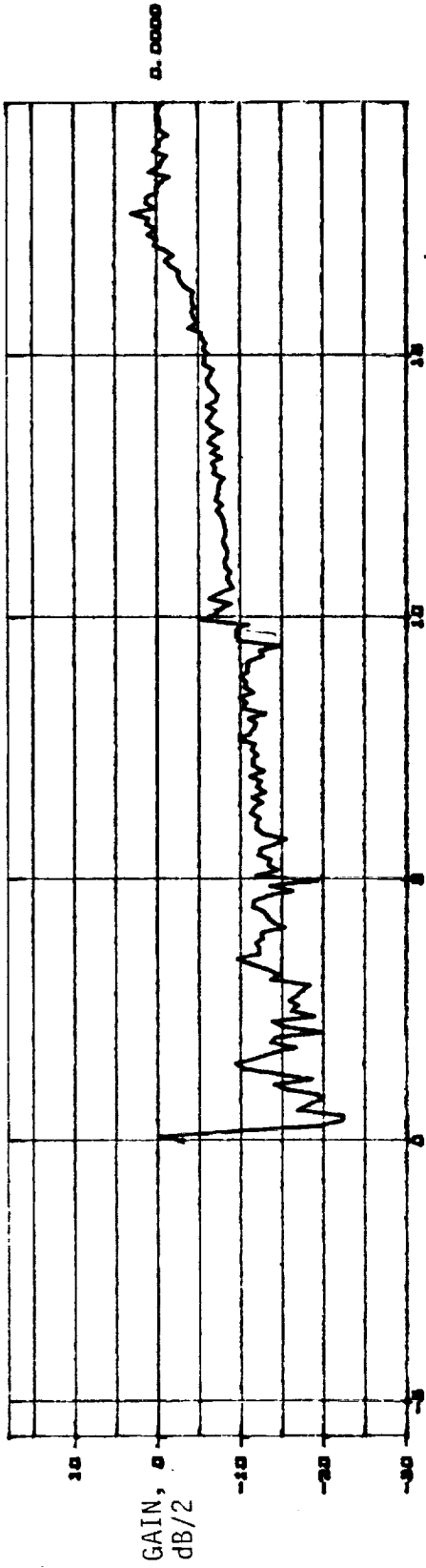
Figure 41. Closed Loop FRF for Gyro to Servo Command.
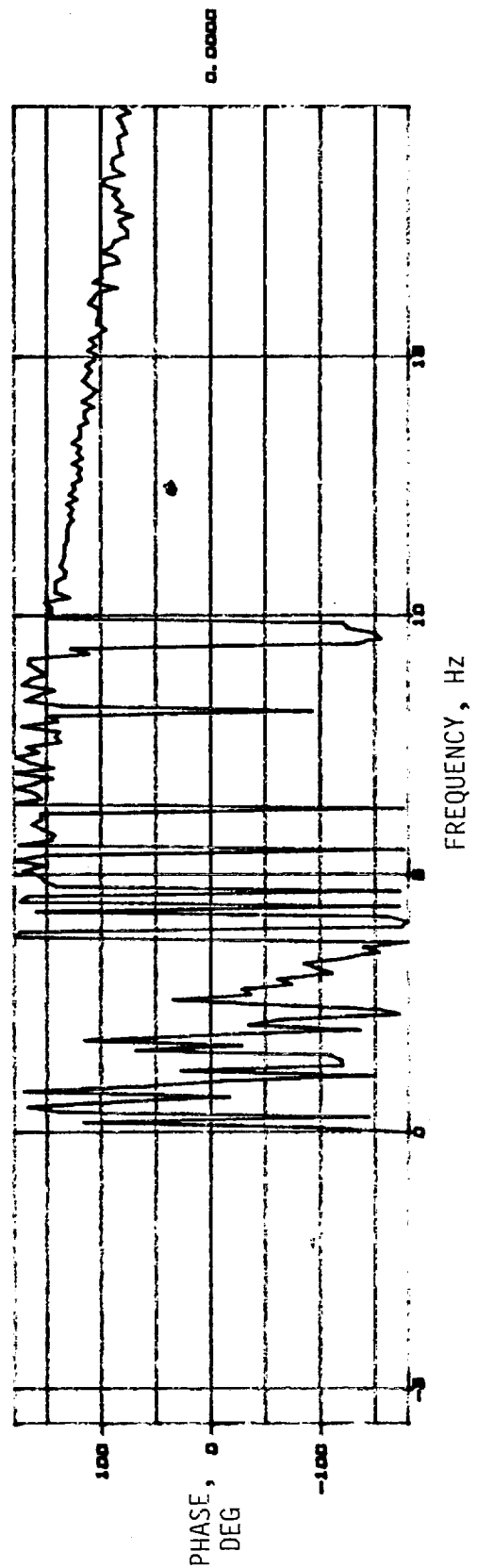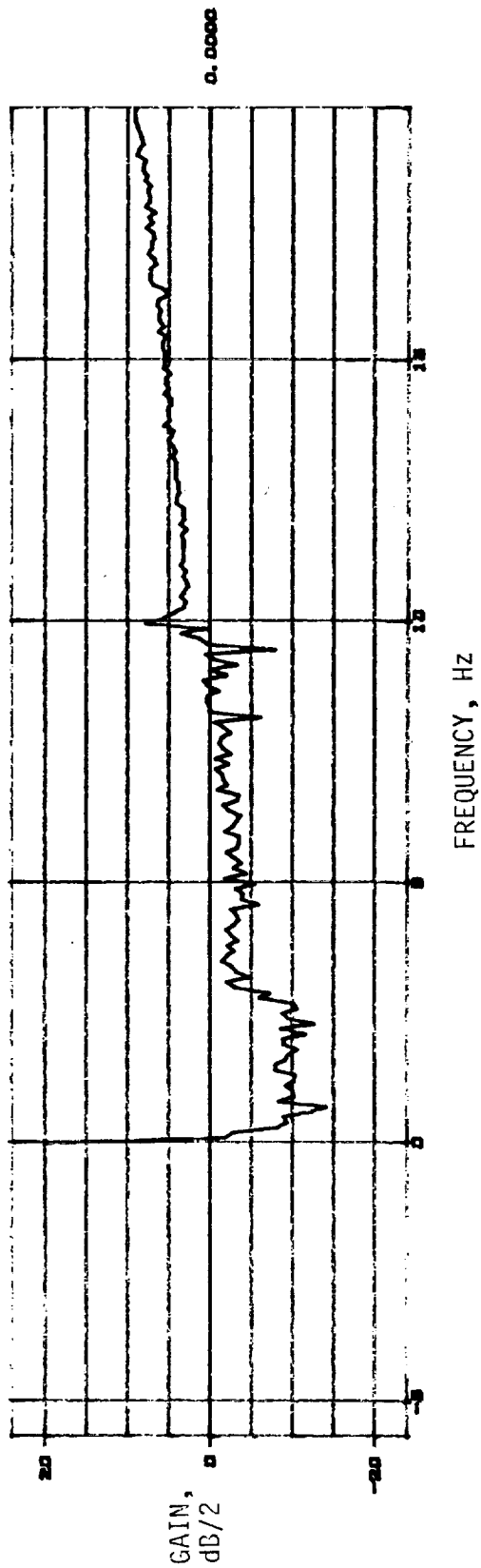
Figure 42. Closed Loop FRF for Accelerometer to Servo Command.

135
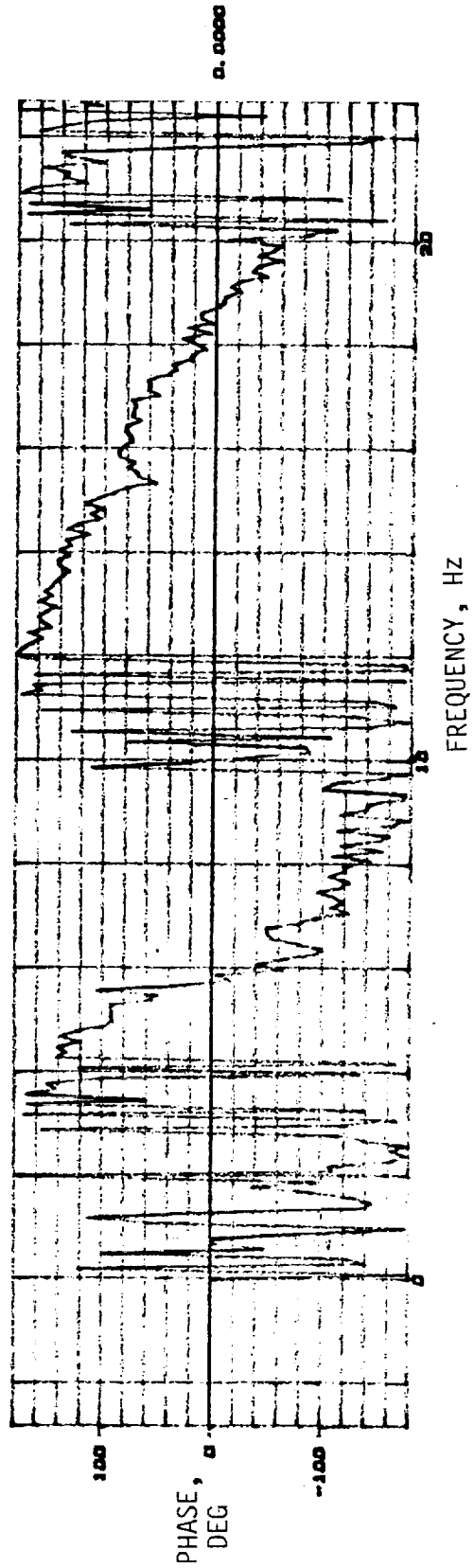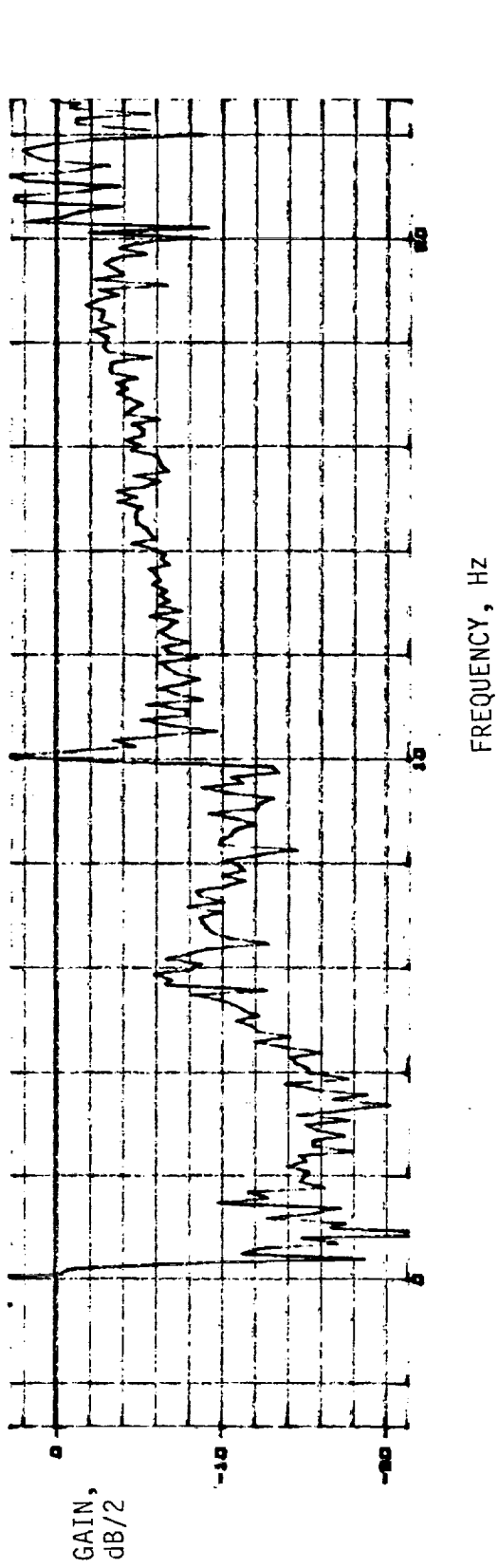
Figure 43.   Open Loop Total System FRF (Nominal Gains),
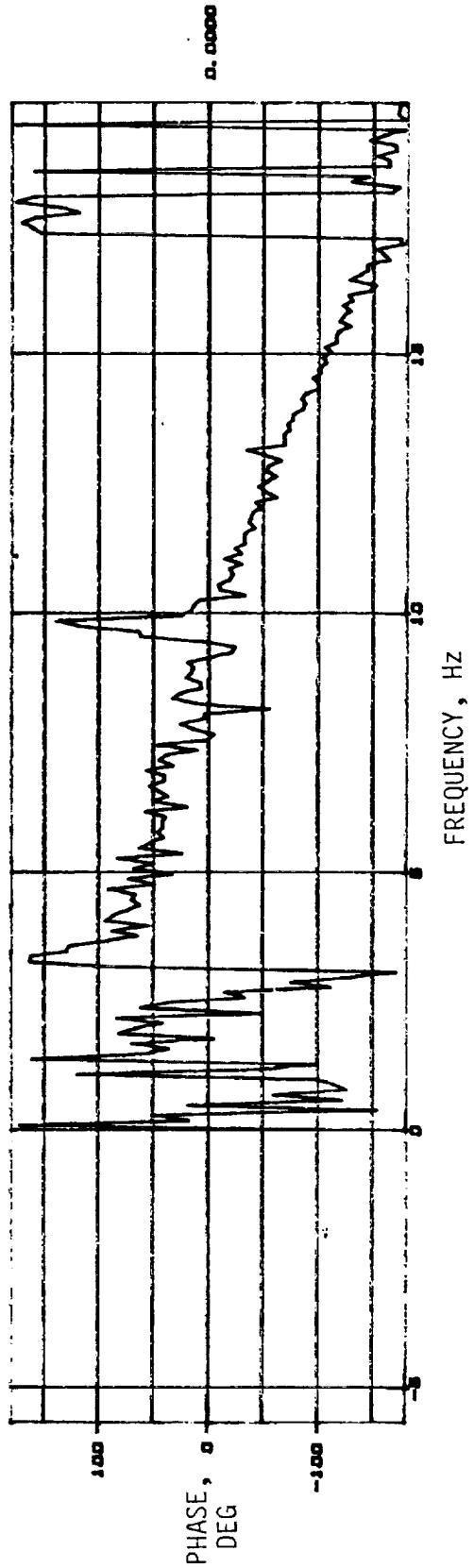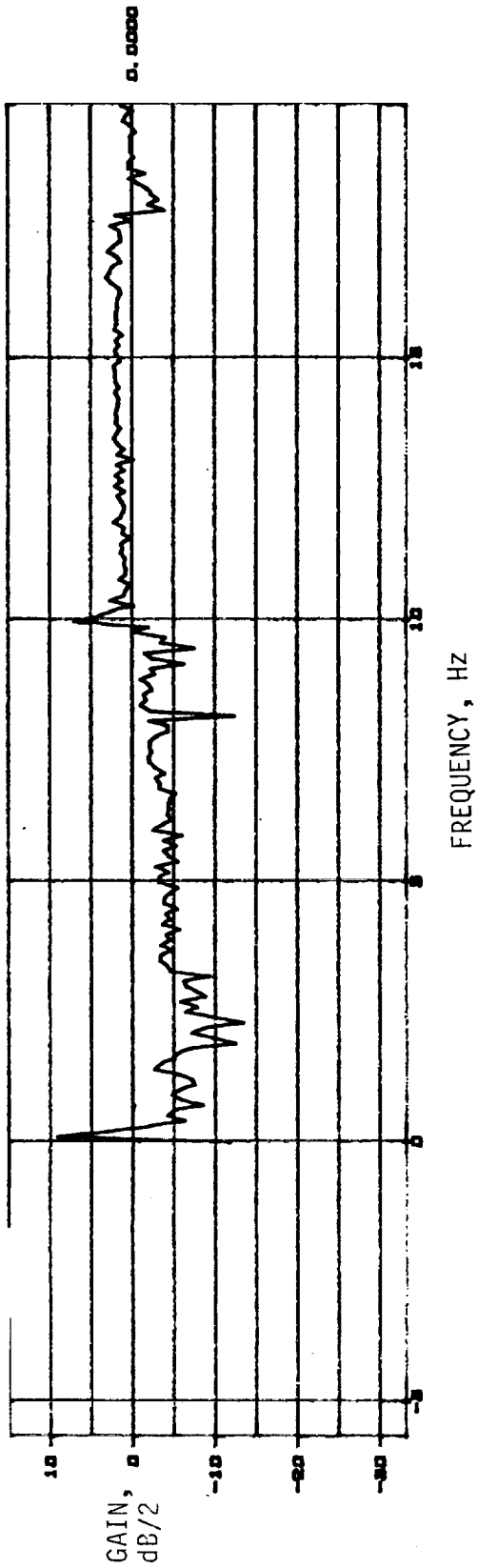
Figure 44. Closed Loop Total System FRF.

137

GAIN, dB/2

FREQUENCY, Hz

PHASE, DEG
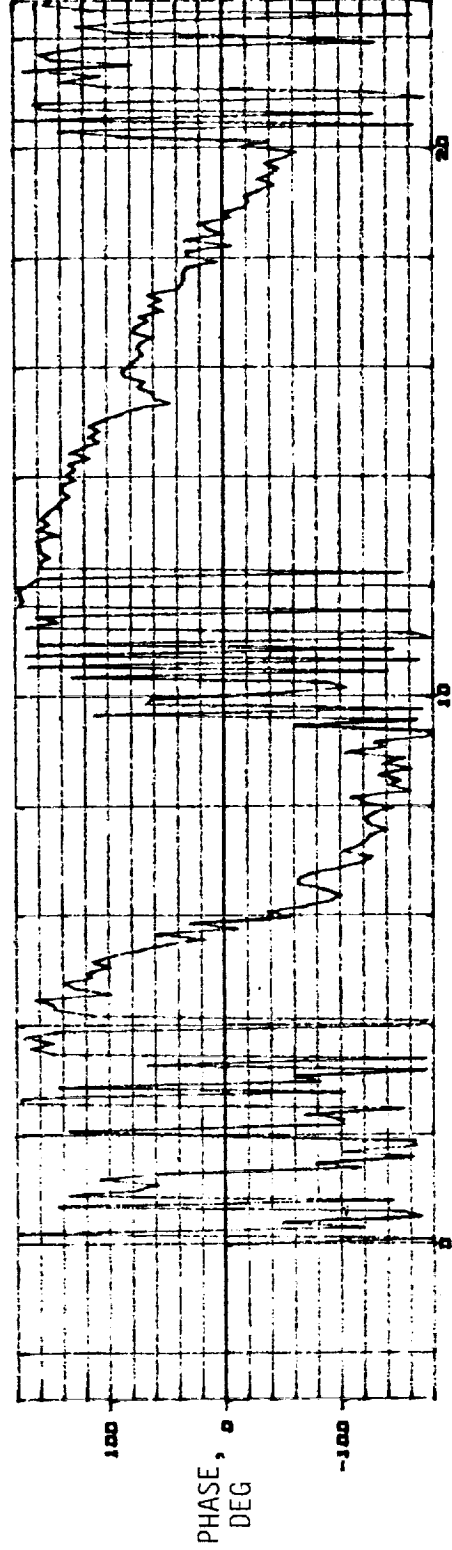
FREQUENCY, Hz

Figure 45. Open Loop Total System FRF (Twice Nominal Gains).
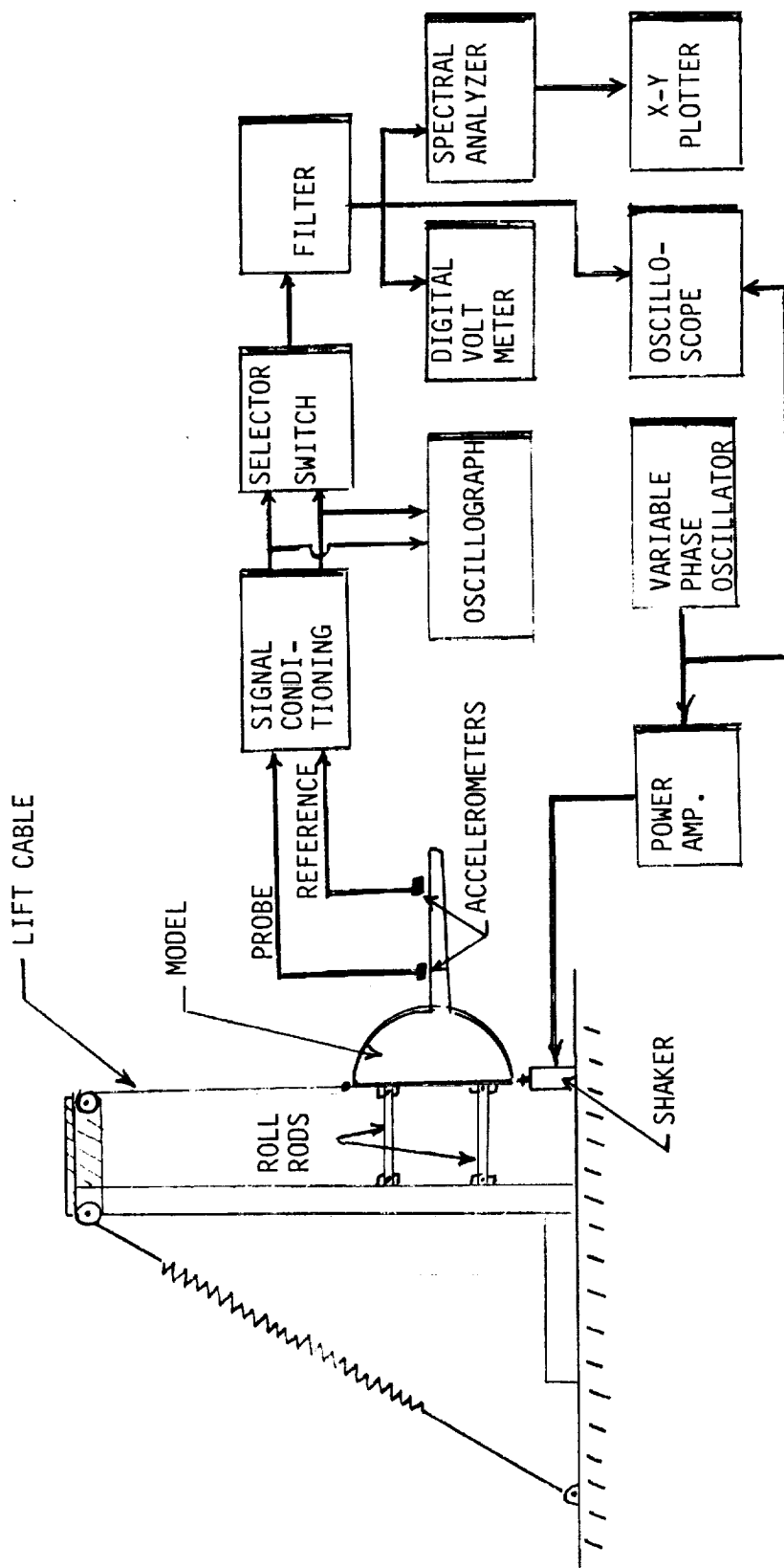
Figure 46. Setup for GVT.

139
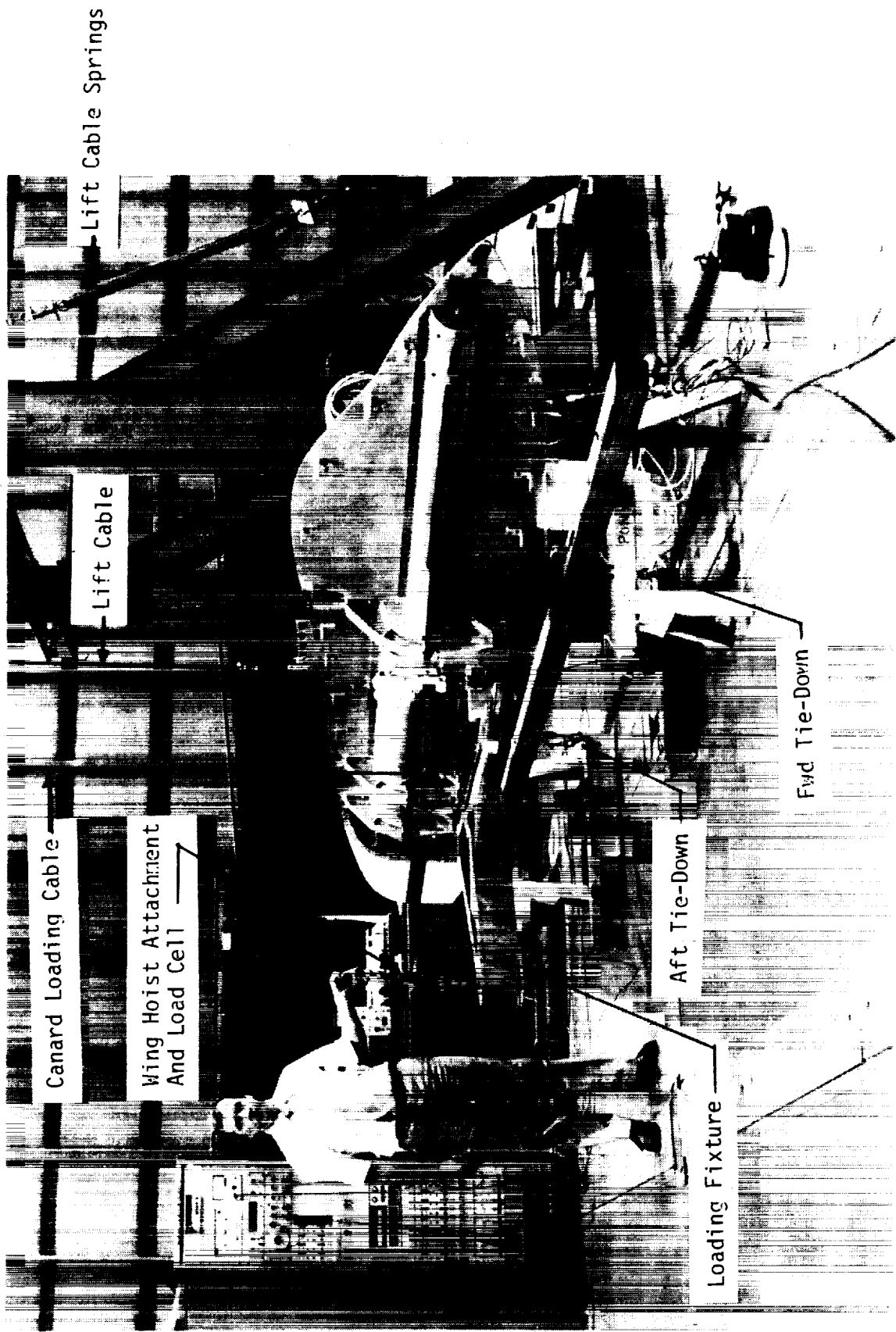
Figure 47. Setup For Proof Load Test.
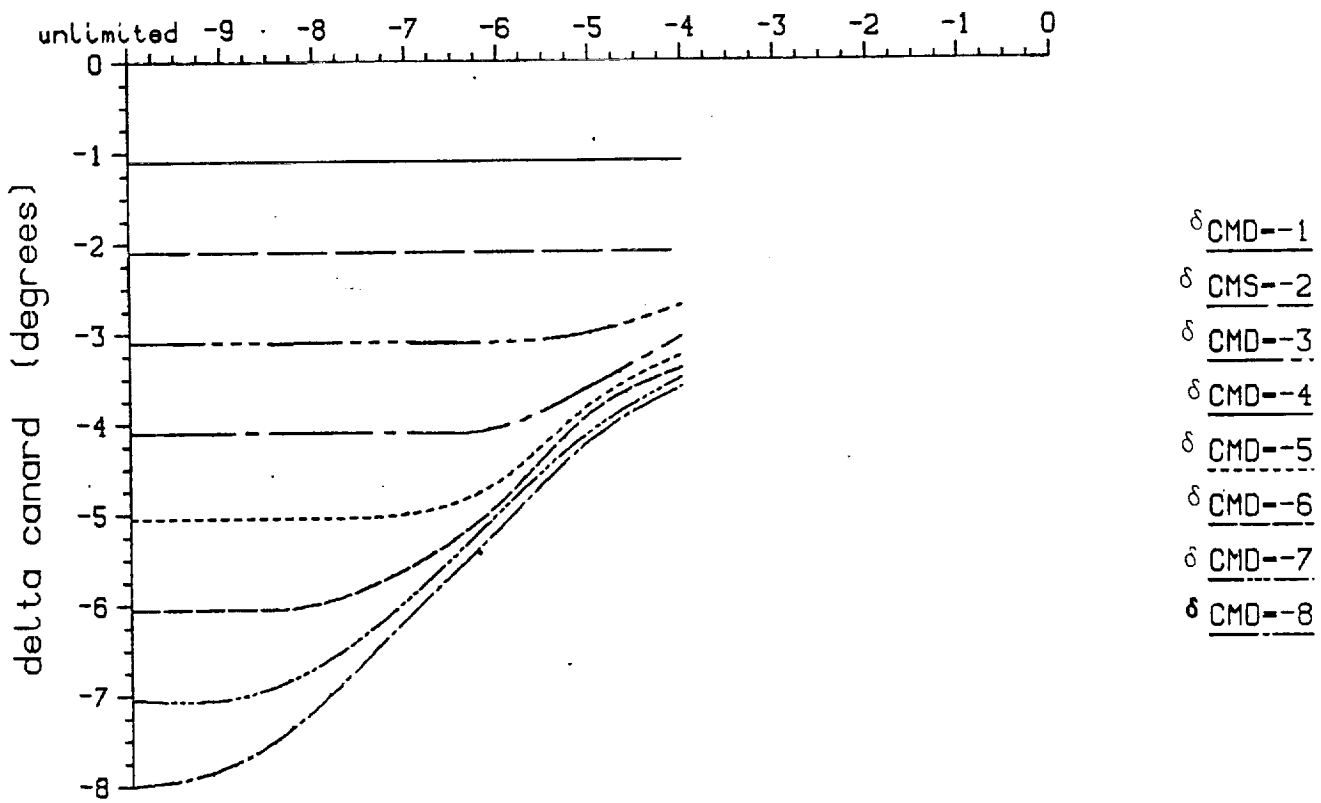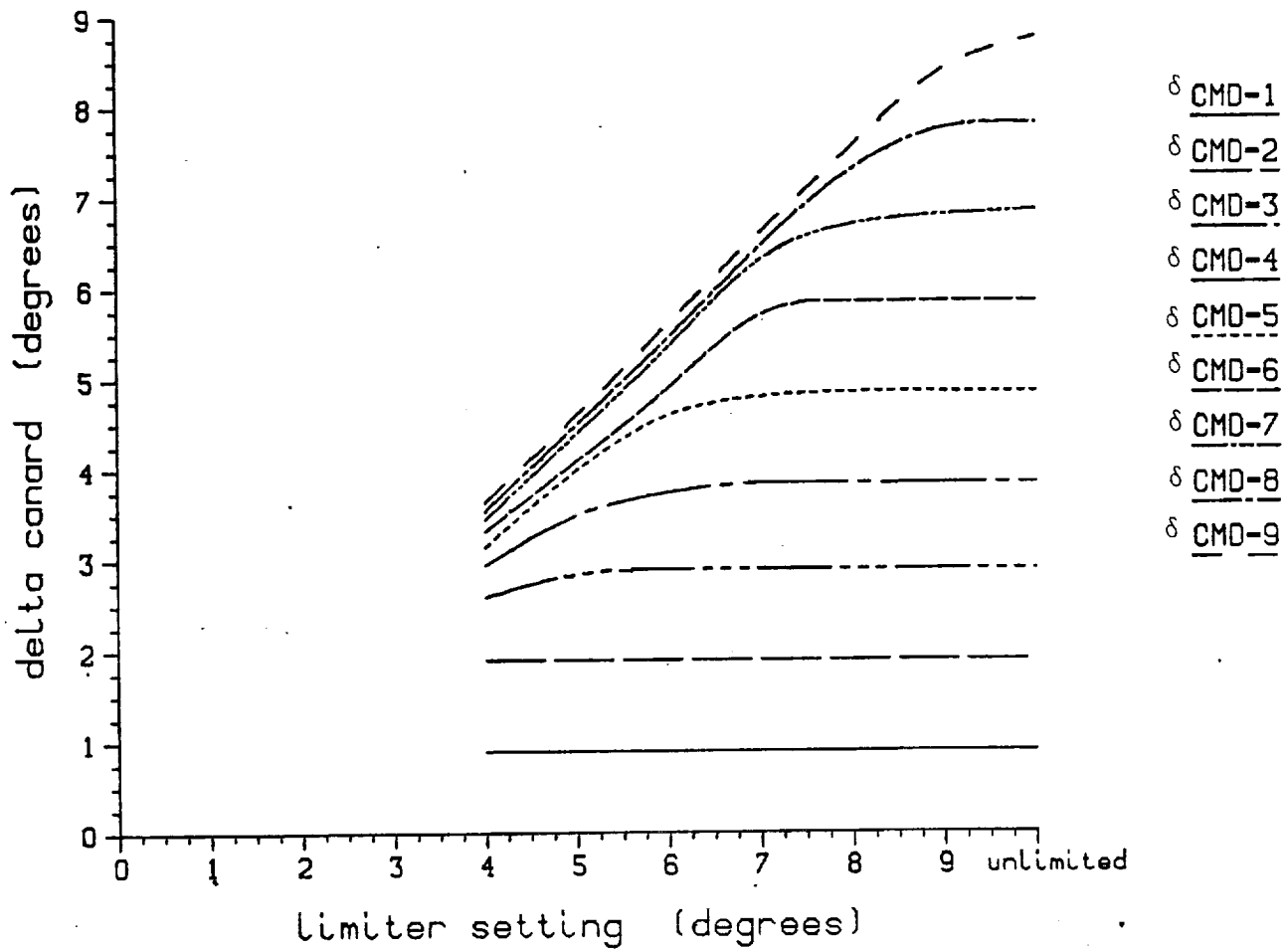
Figure 48.   Canard Incidence Limiter Calibration.

141
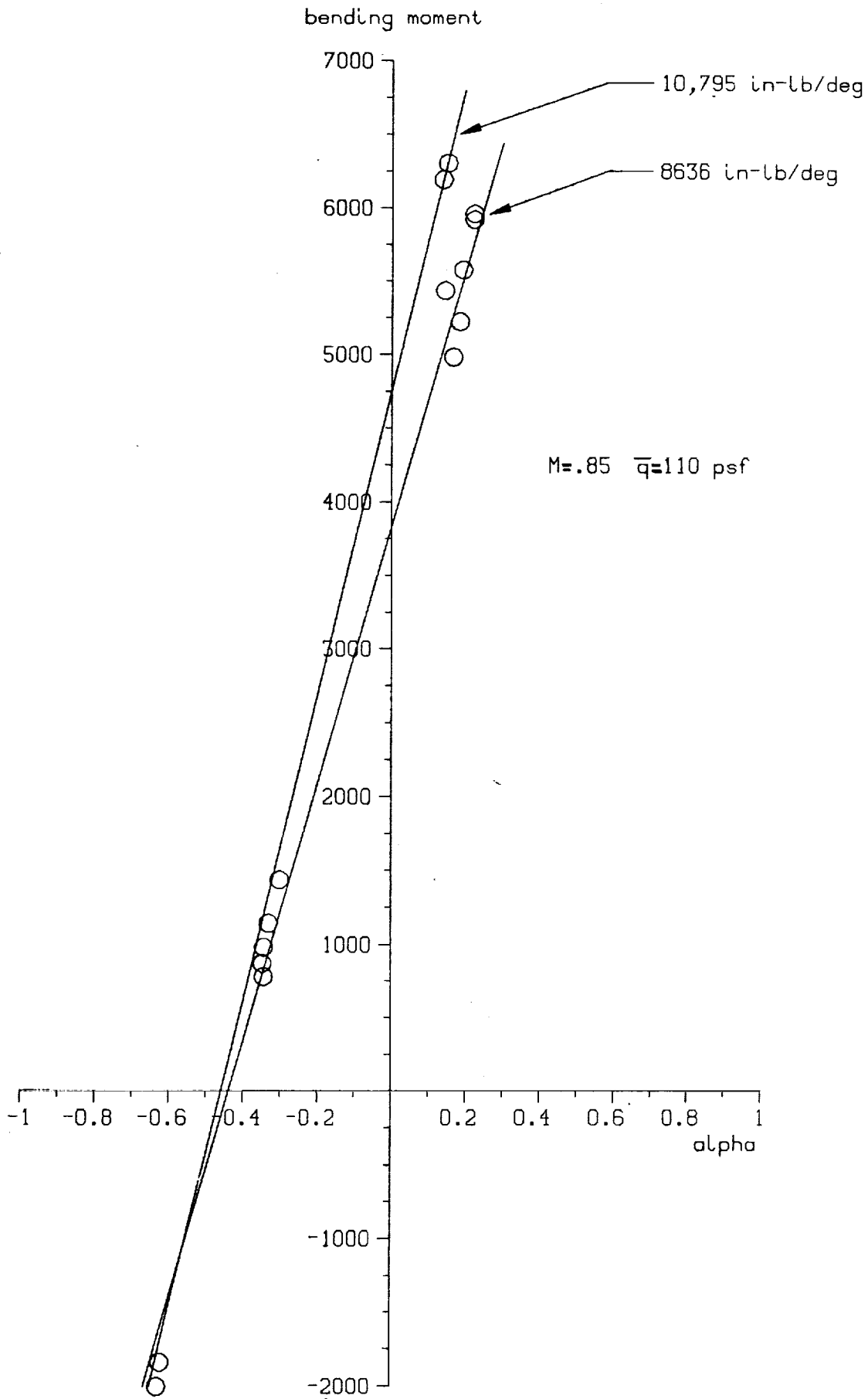
Figure 49. Typical Wing Bending Moment.
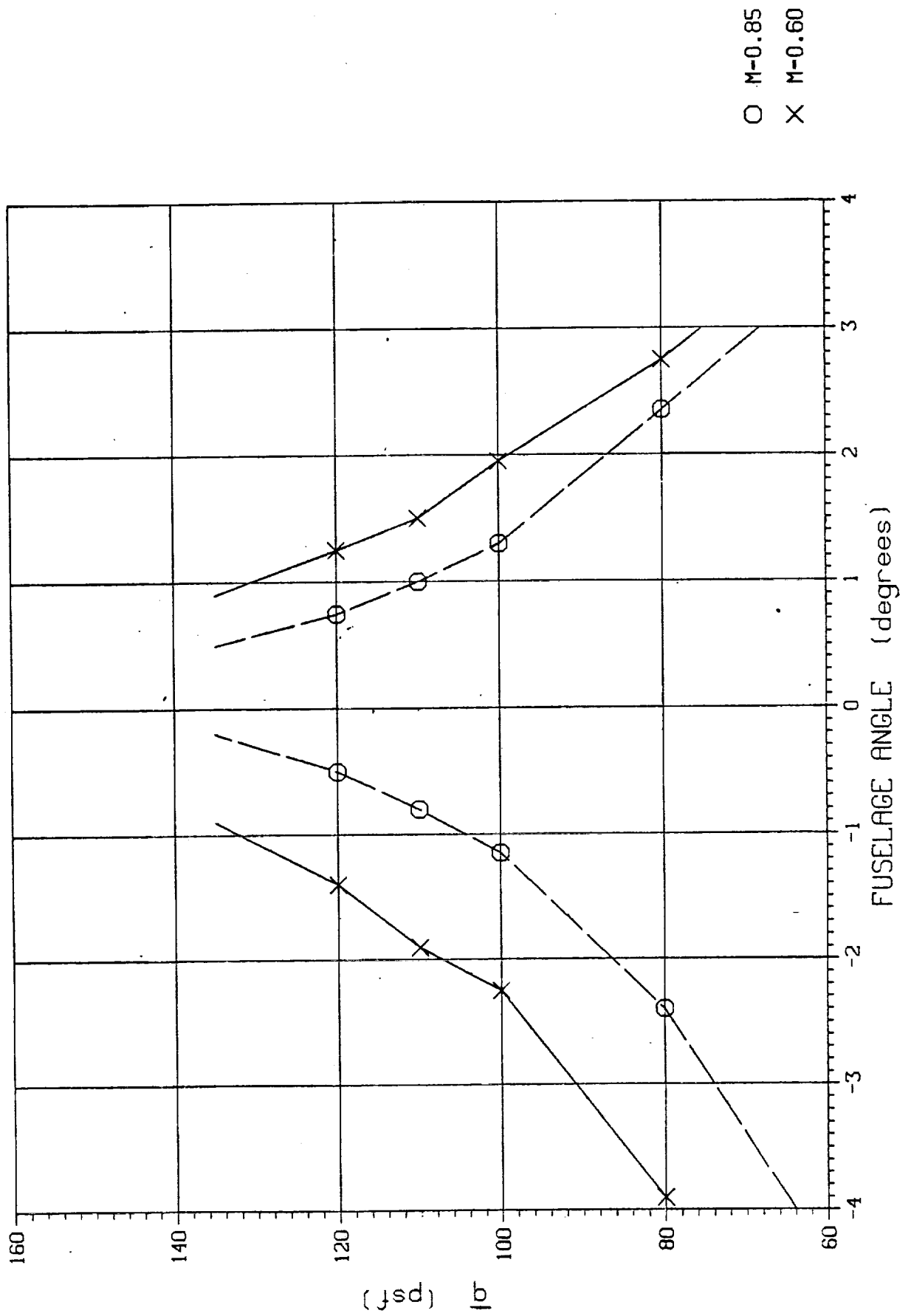
Figure 50. Revised Angle of Attack Limits.
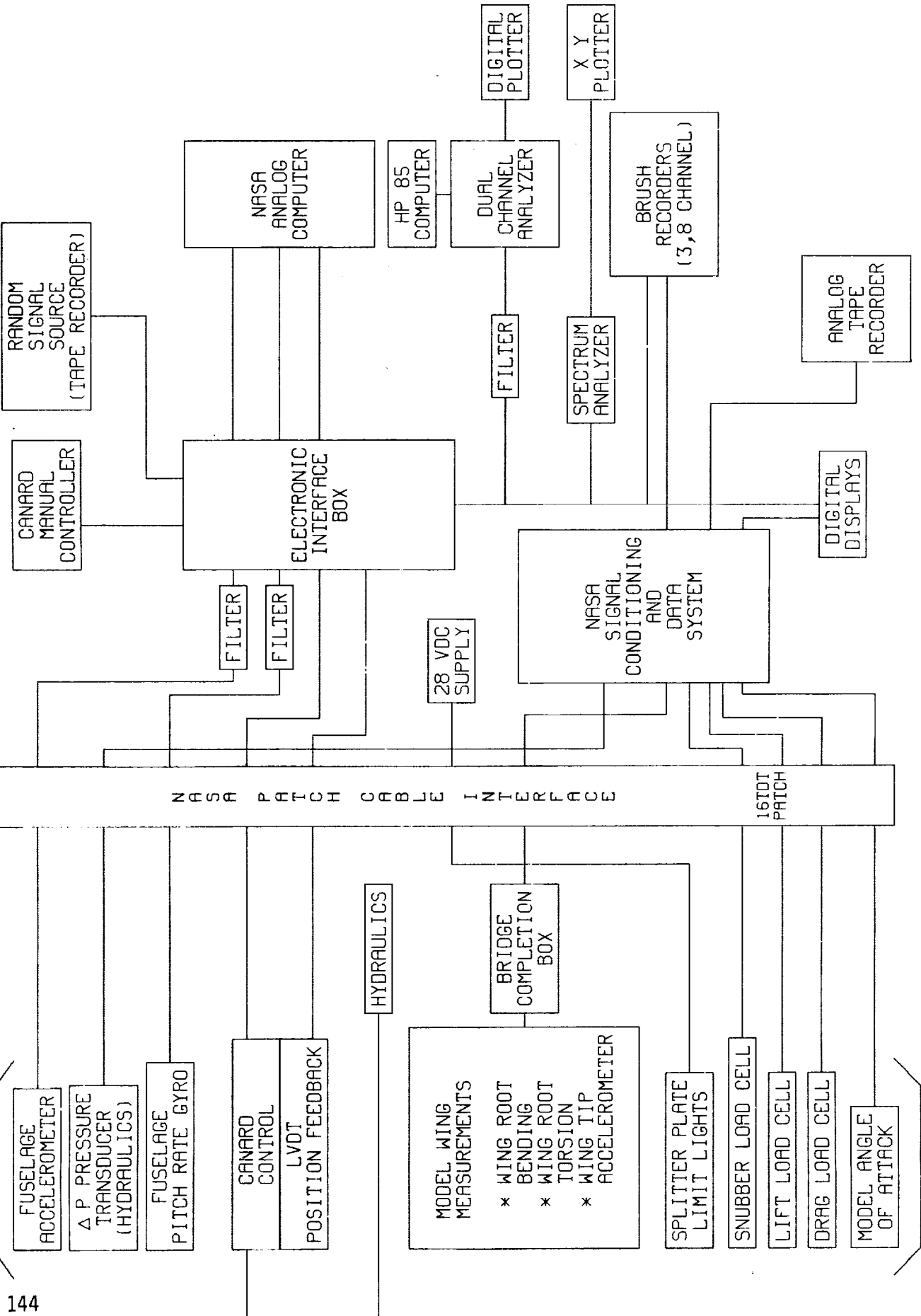
Figure 51. Instrumentation Block Diagram For Flutter Test.

144
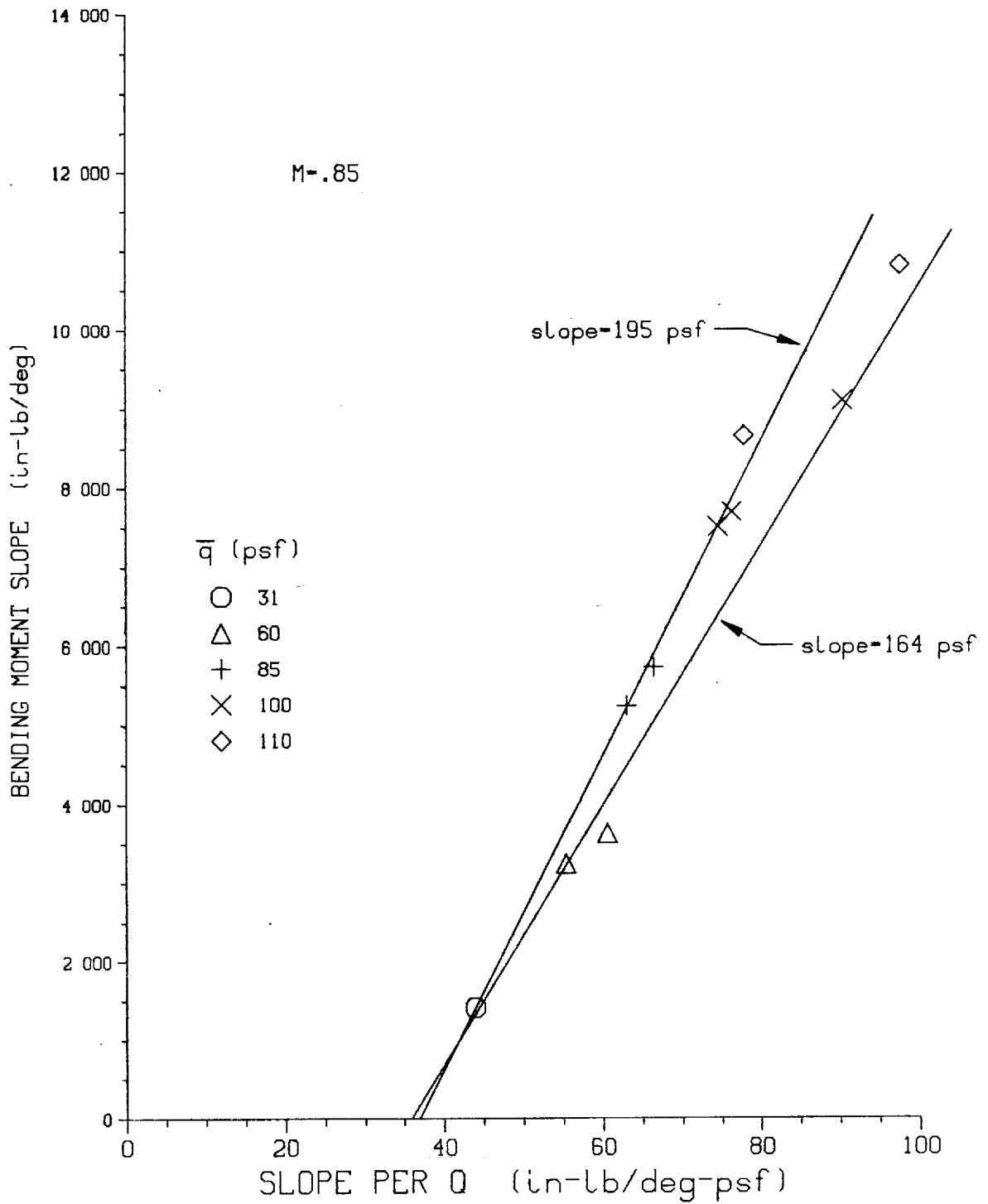
Figure 52. Southwell Method Applied to M=.85 Data.
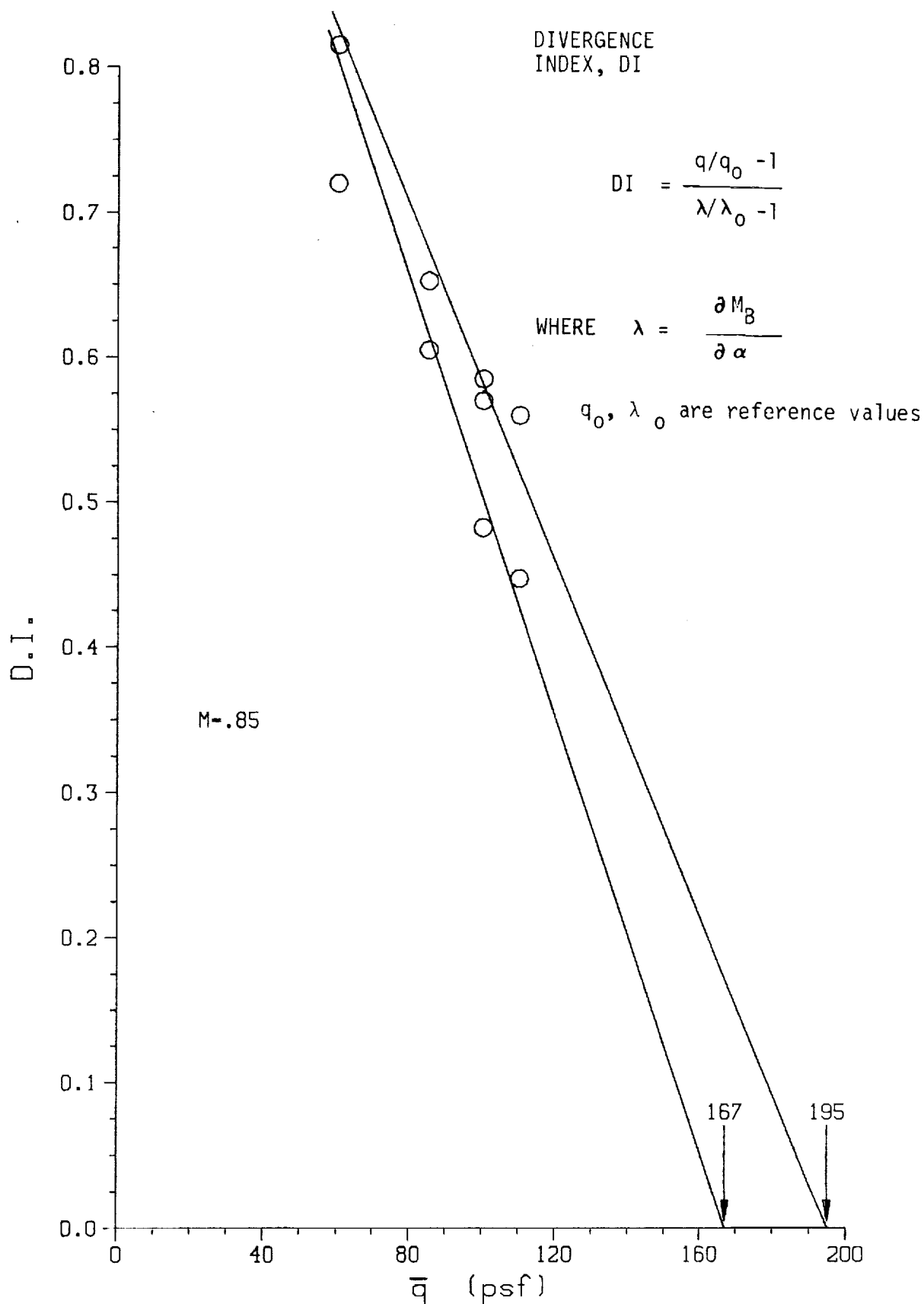
Figure 53. Divergence Index Method Applied to M=.85 Data.
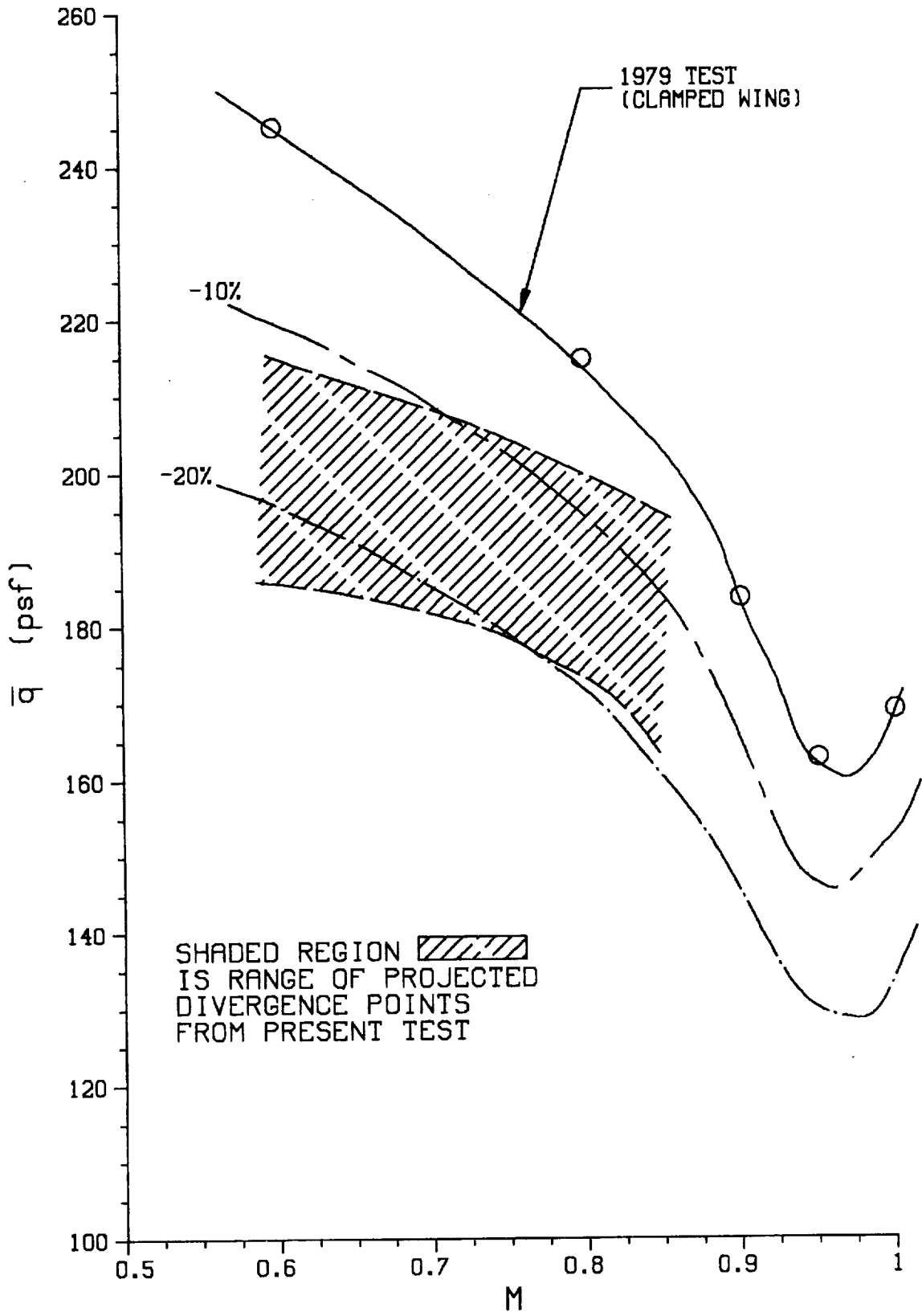
Figure 54. Divergence Boundaries.
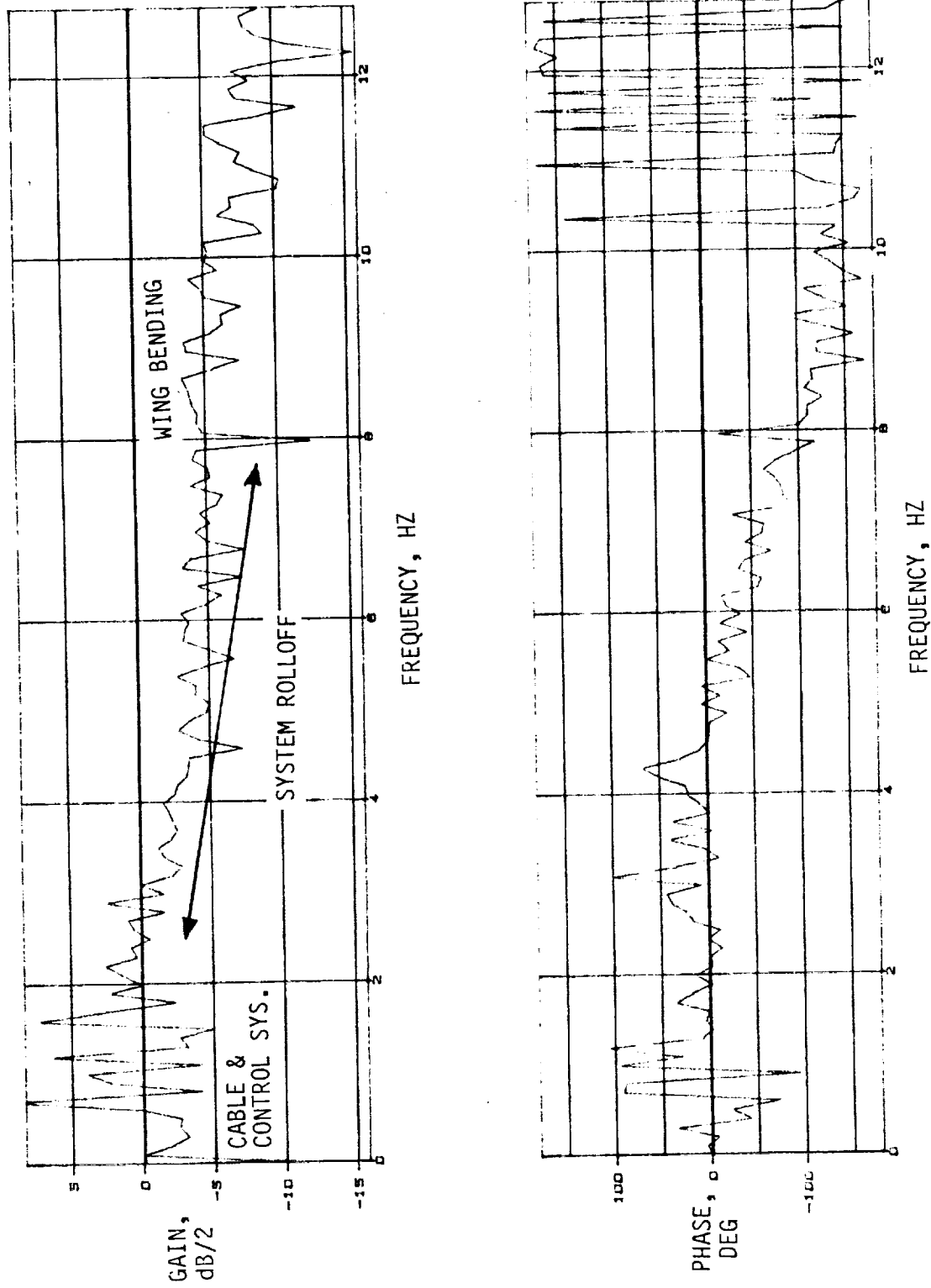
Figure 55. Measured Bode Plots for CG231, C2-4, M = 0.80, $\bar{Q}$ = 77 psf.
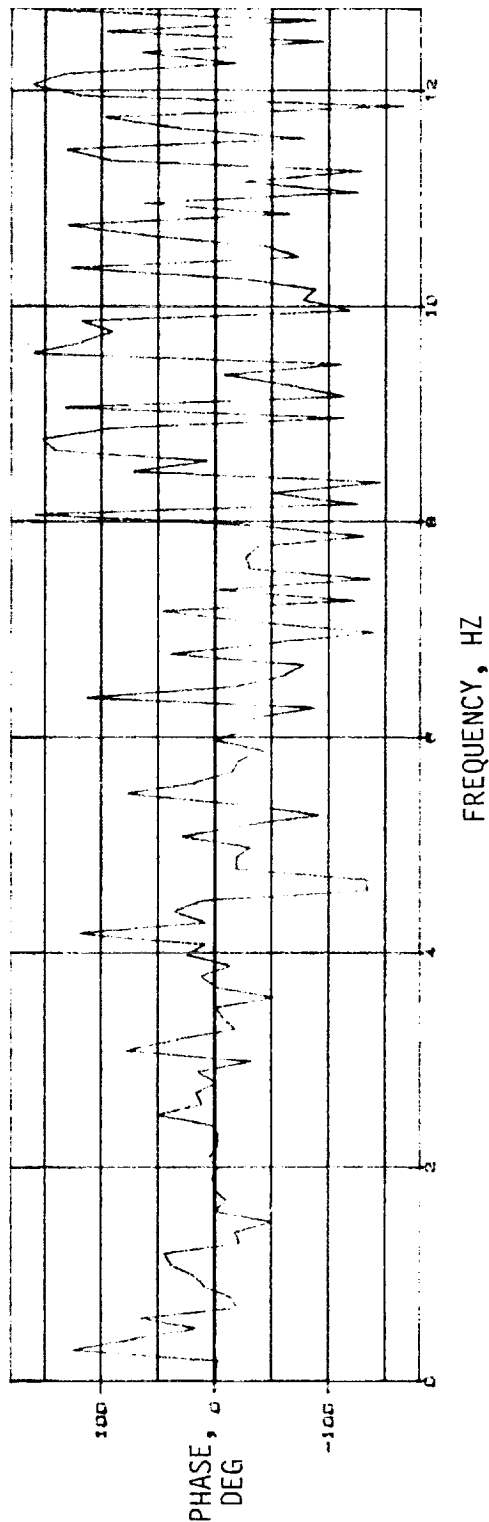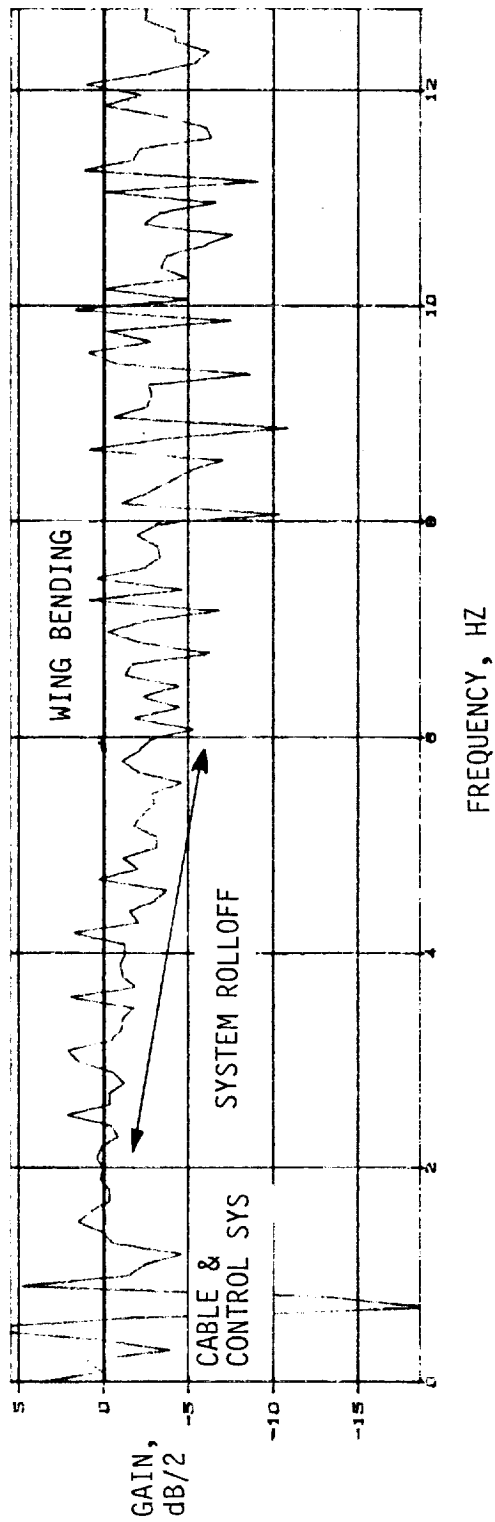
Figure 56. Measured Bode Plots For CG231, C2-4, M = 0.80, $\bar{q}$ = 90 psf.

149
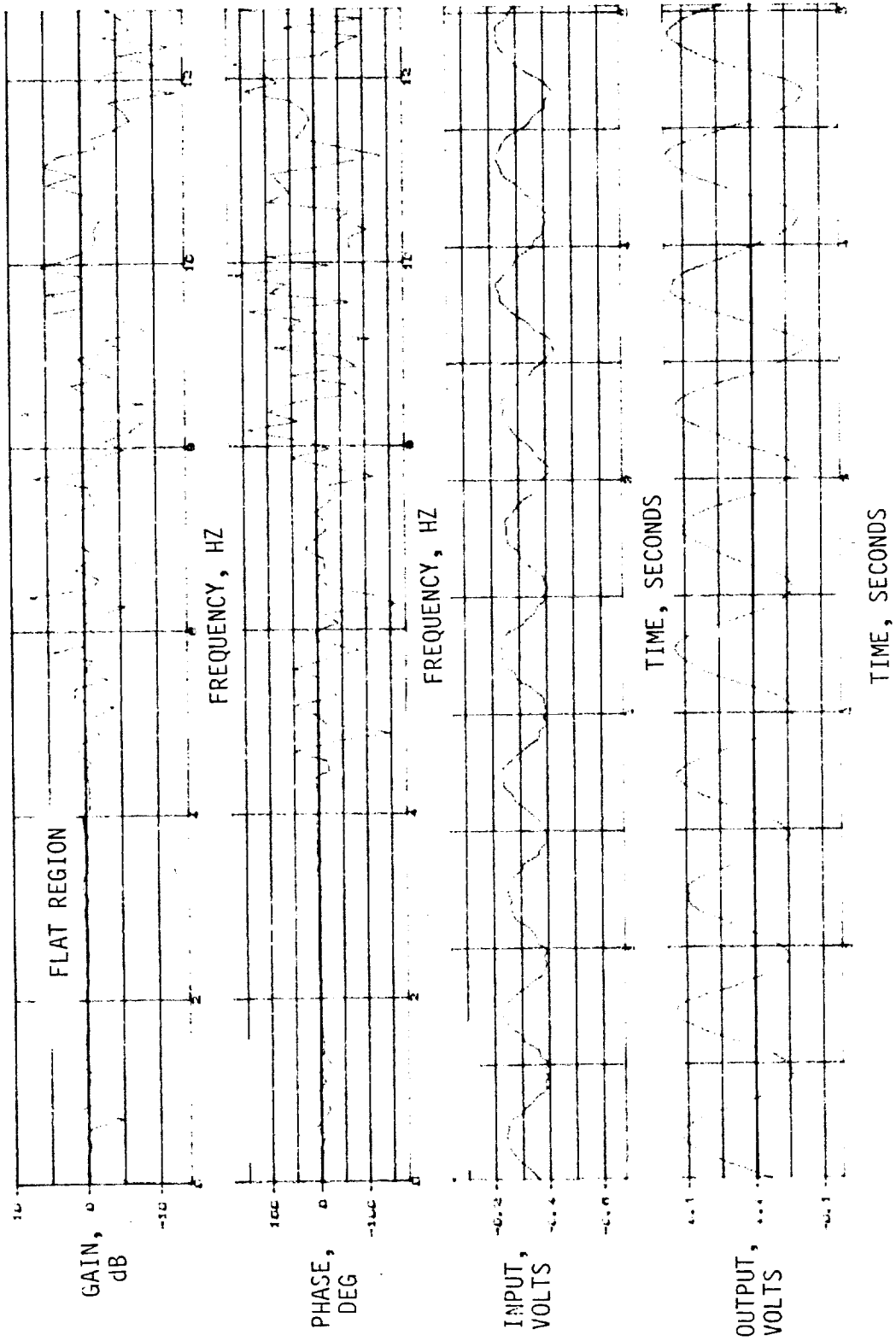
Figure 57. Measured Bode Plots and Time Histories for CG231, C2-4, M = 0.80, $\overline{q}$ = 100 psf.
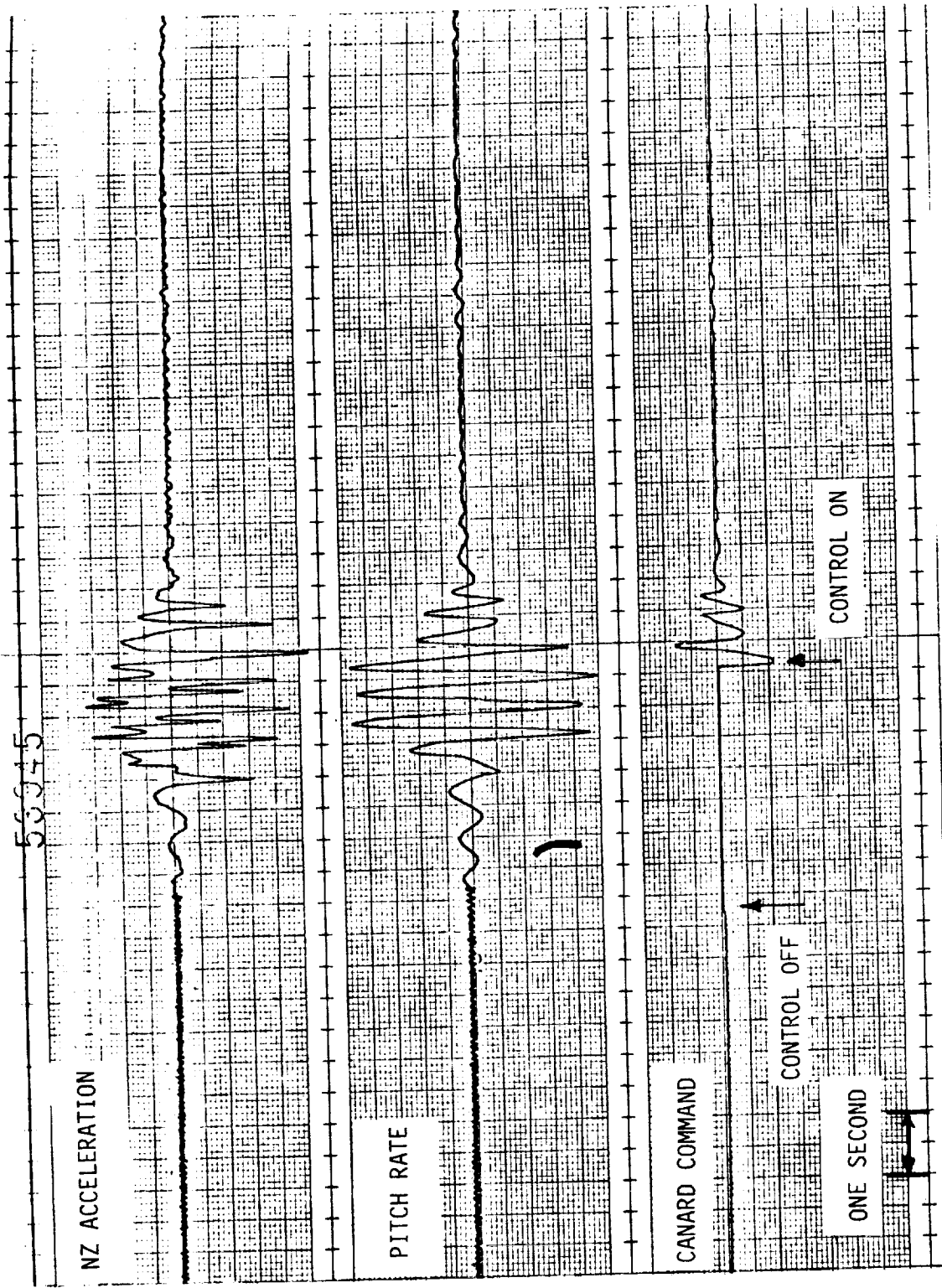
Figure 58. Verification Of SAS Function.

NZ ACCELERATION

PITCH RATE

CANARD COMMAND

CONTROL OFF

CONTROL ON

ONE SECOND

151
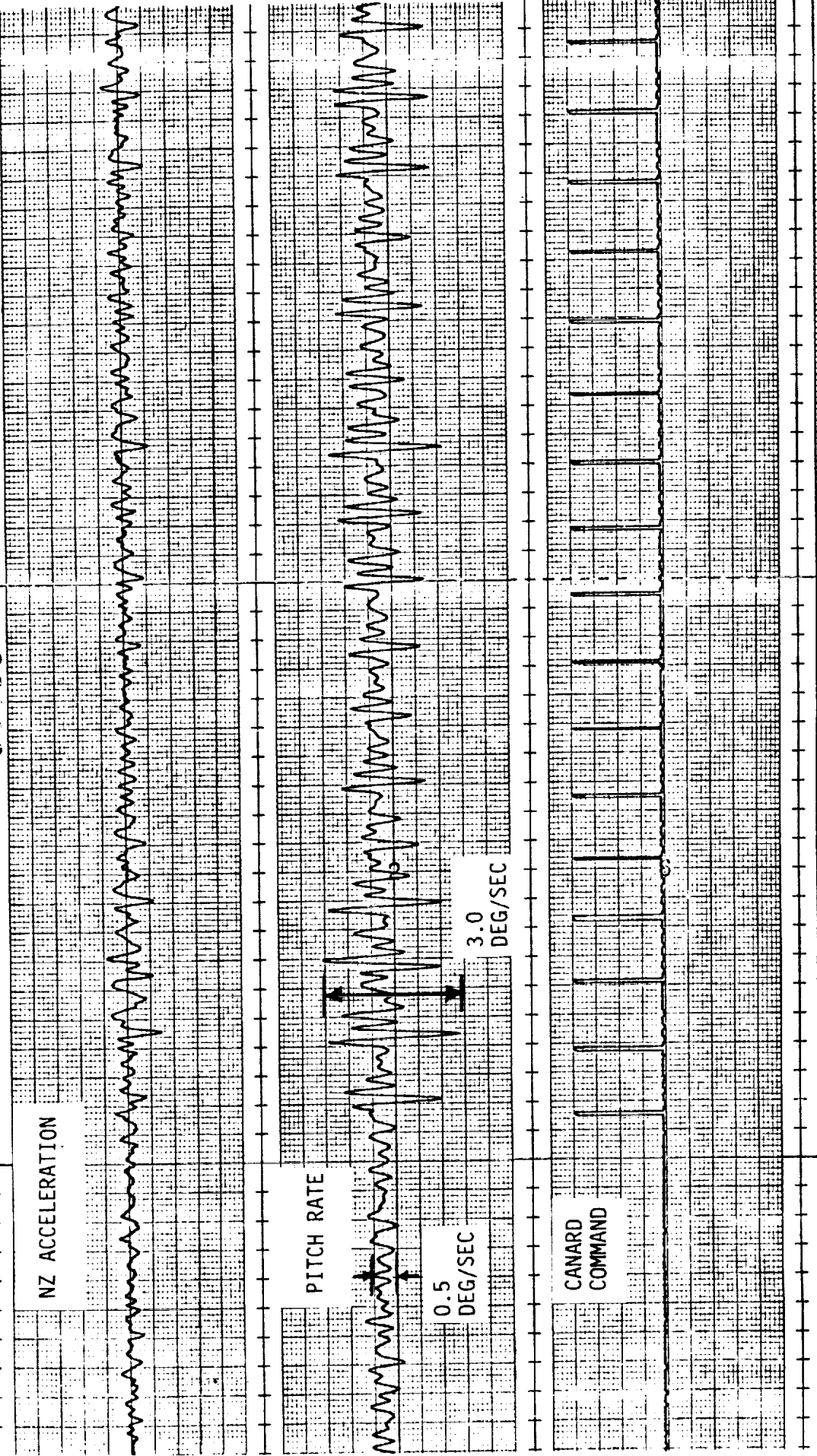
Figure 59. Response Of Model To Command Pulses.

PITCH RATE

WING BENDING MOMENT

WING TORSION

NZ ACCELERATION
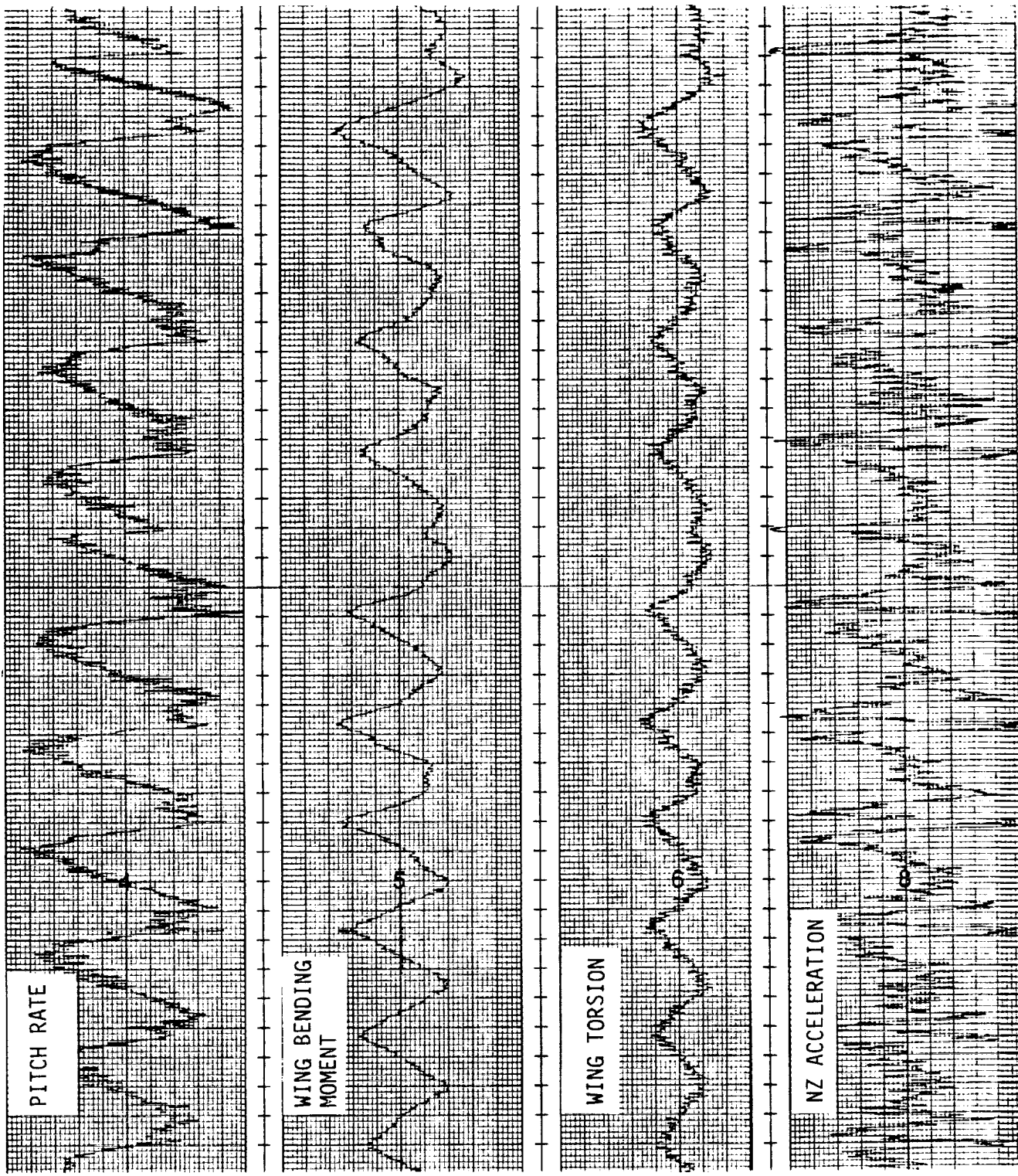
Figure 60.   Time Histories Of Tab Point 200, Neutrally Stable.

153
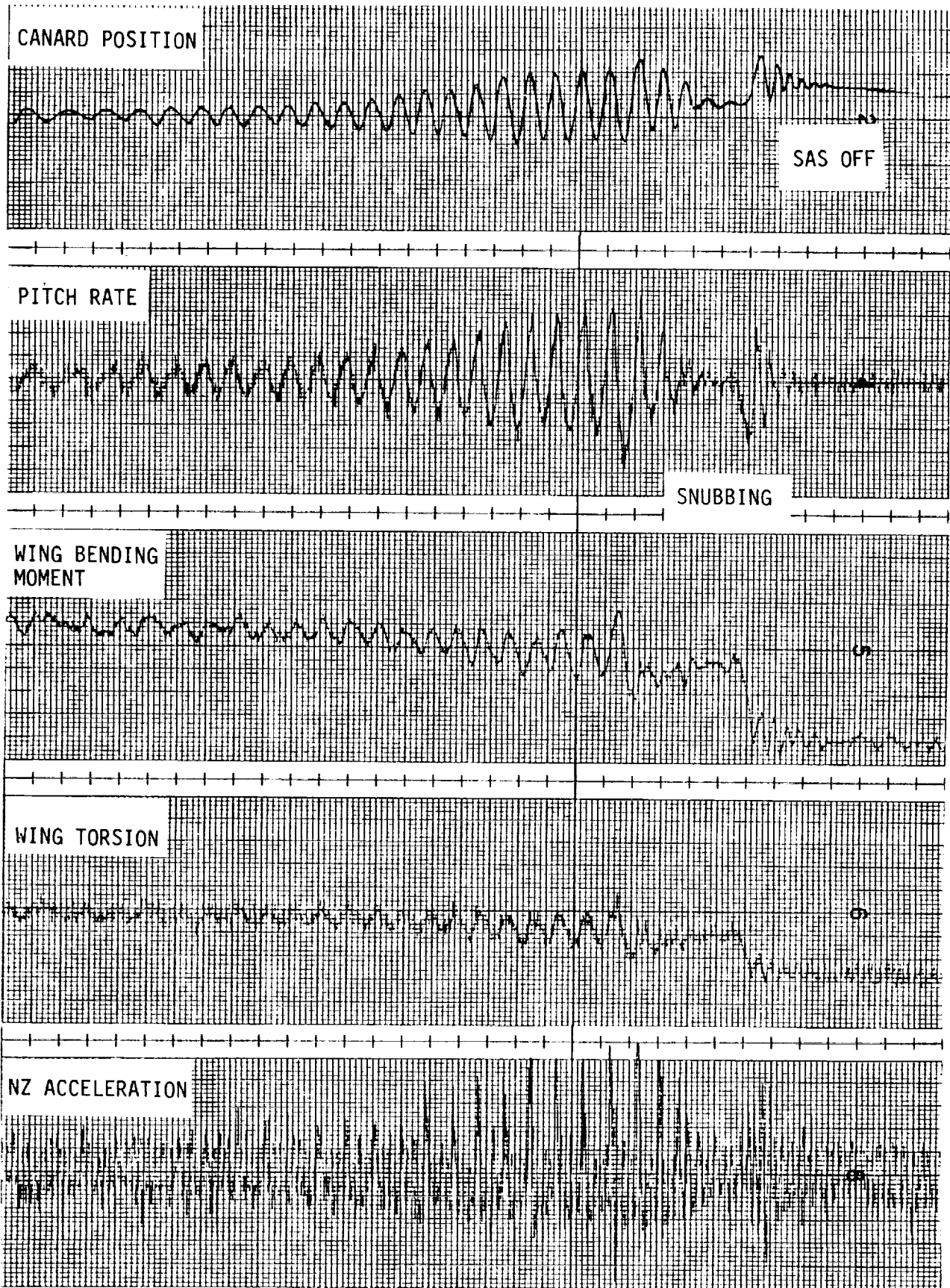
Figure 61. Time Histories Of Tab Point 1001, Unstable.

PITCH RATE

WING BENDING
MOMENT

WING TORSION

NZ ACCELERATION
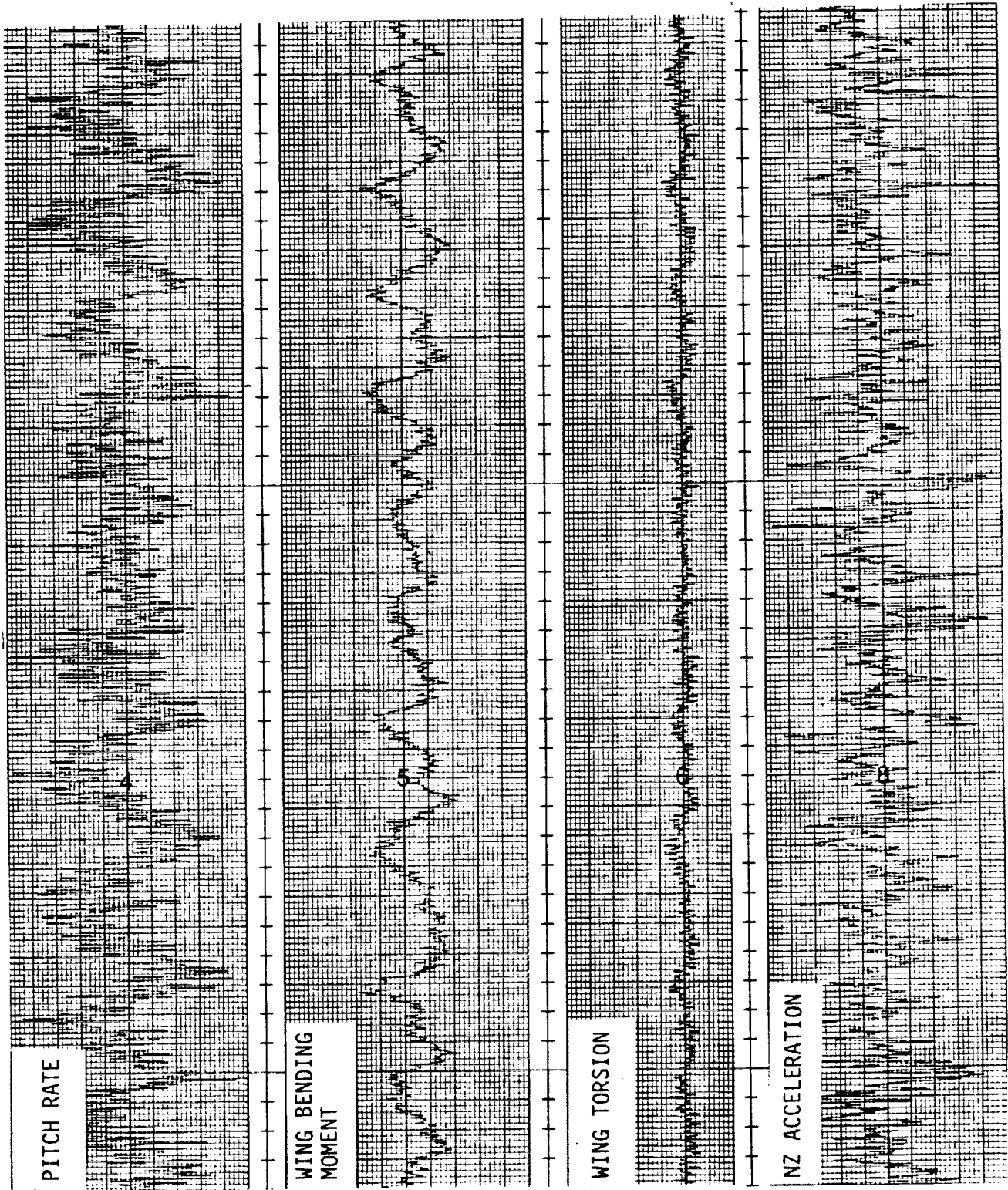
Figure 62.   Time Histories Of Tab Point 365, Lightly Damped.

155
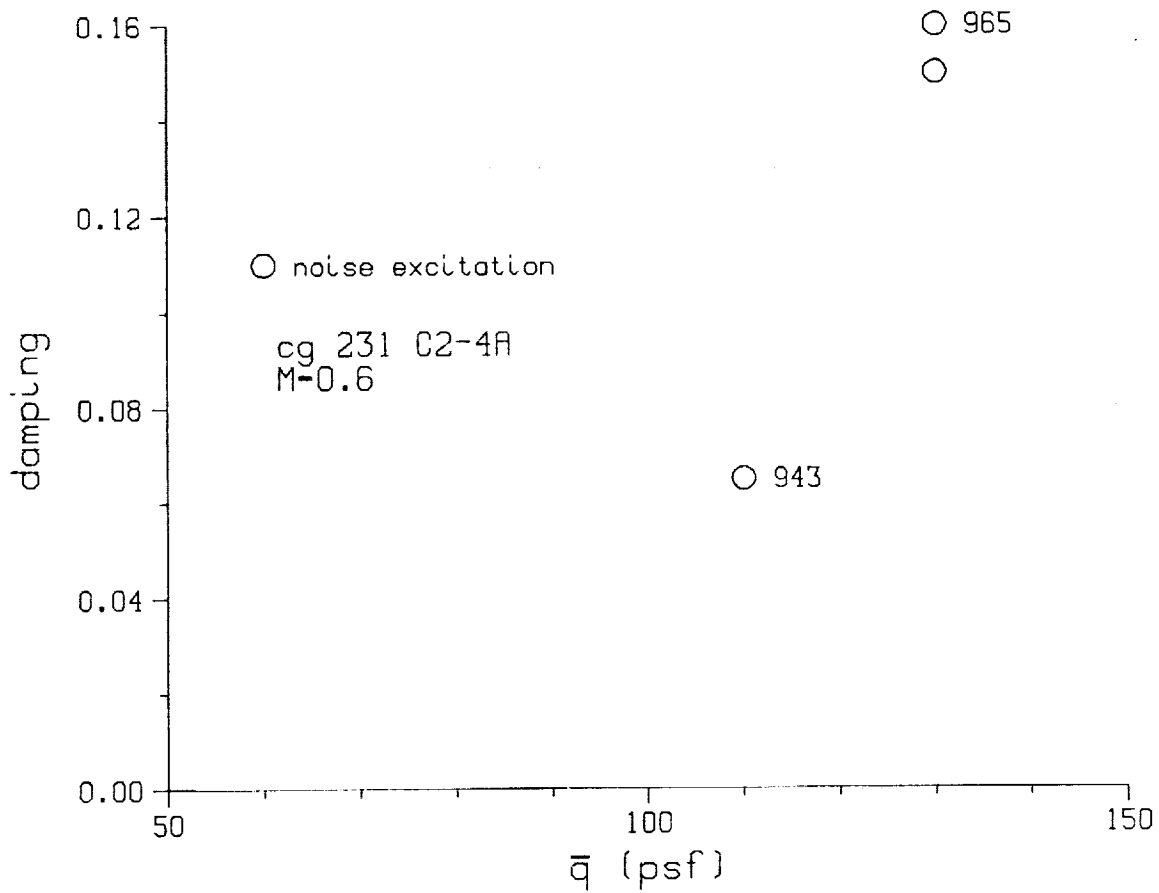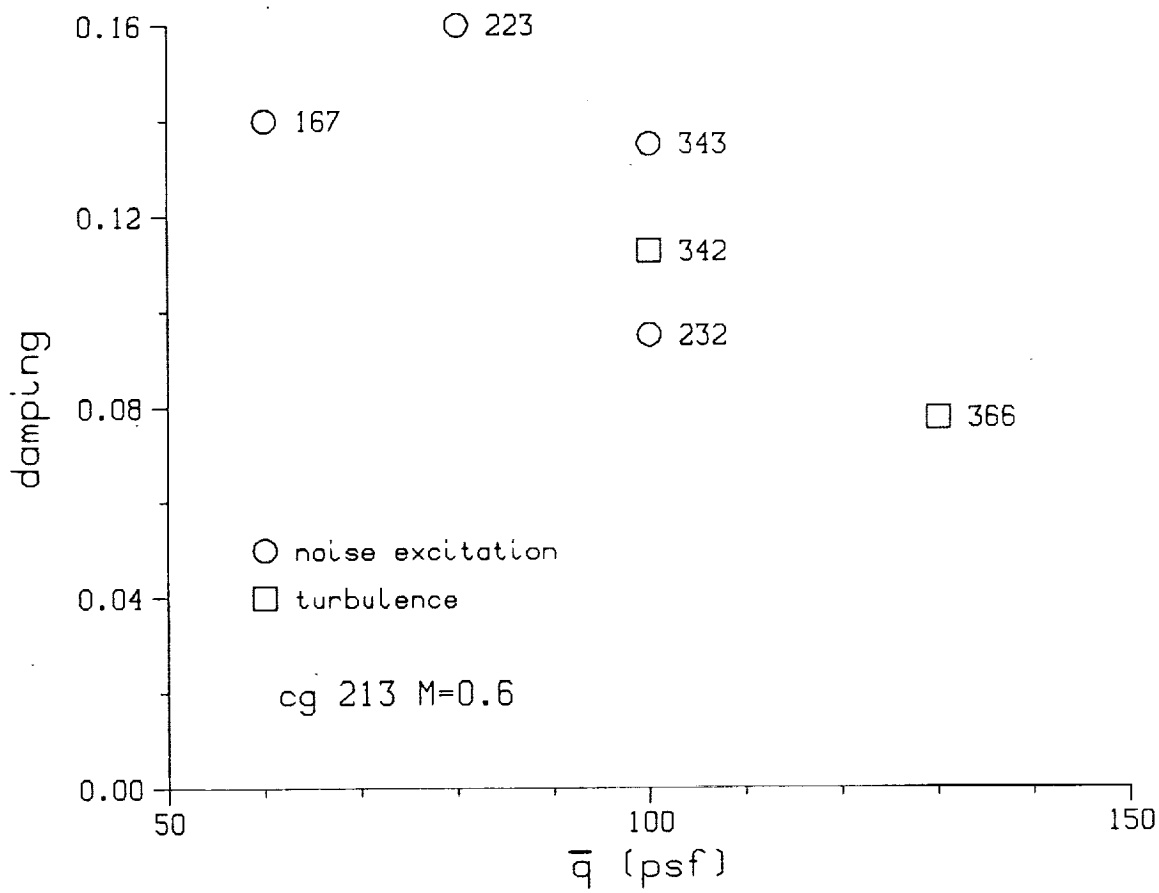
Figure 63. Examples Of Damping Trends From Randomdec Data.
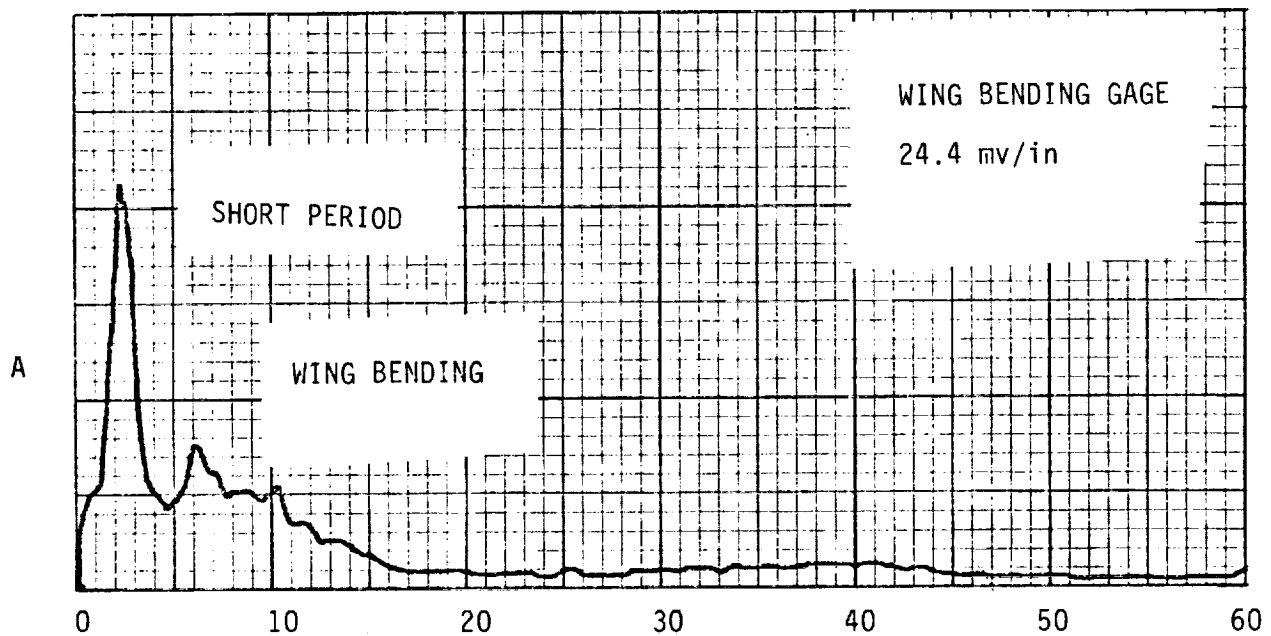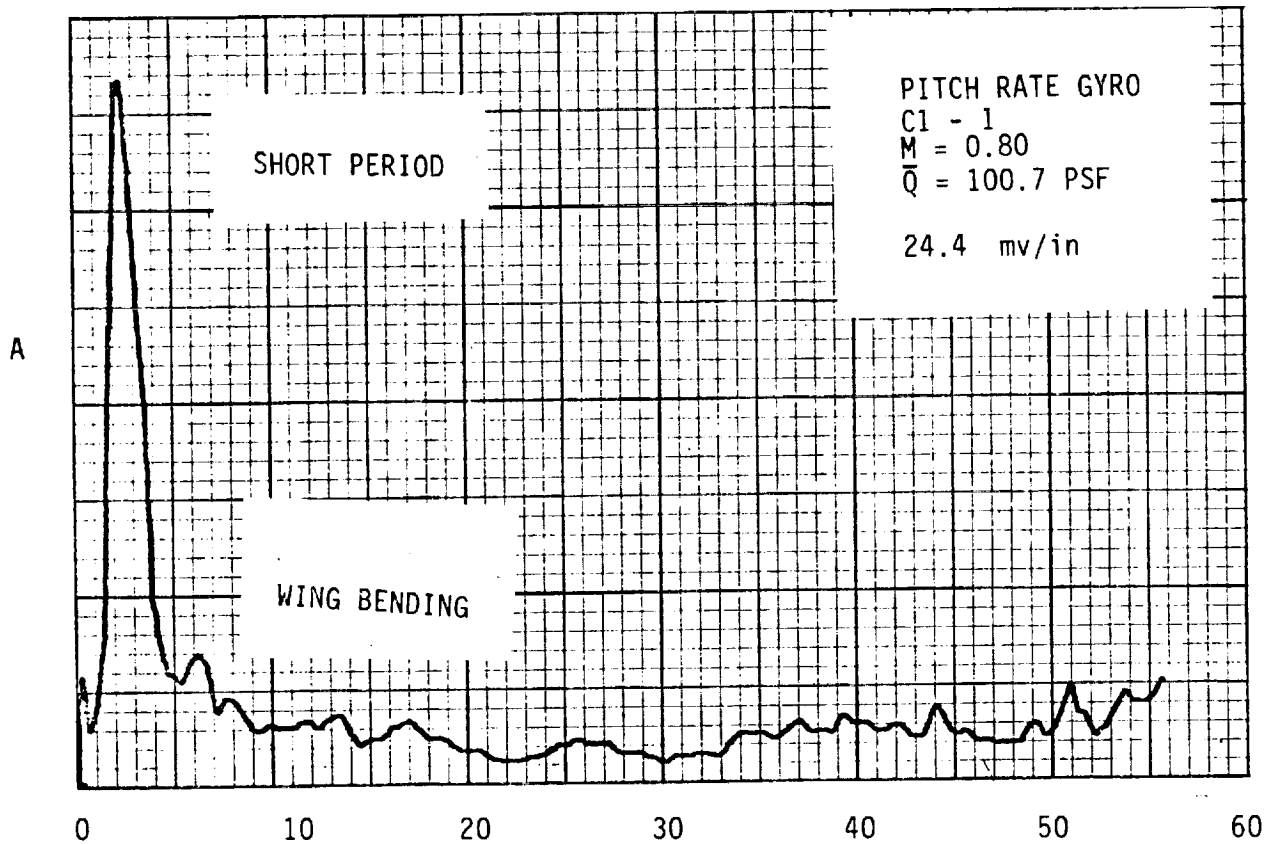
Figure 64. Representative Peak-Hold Spectrum.
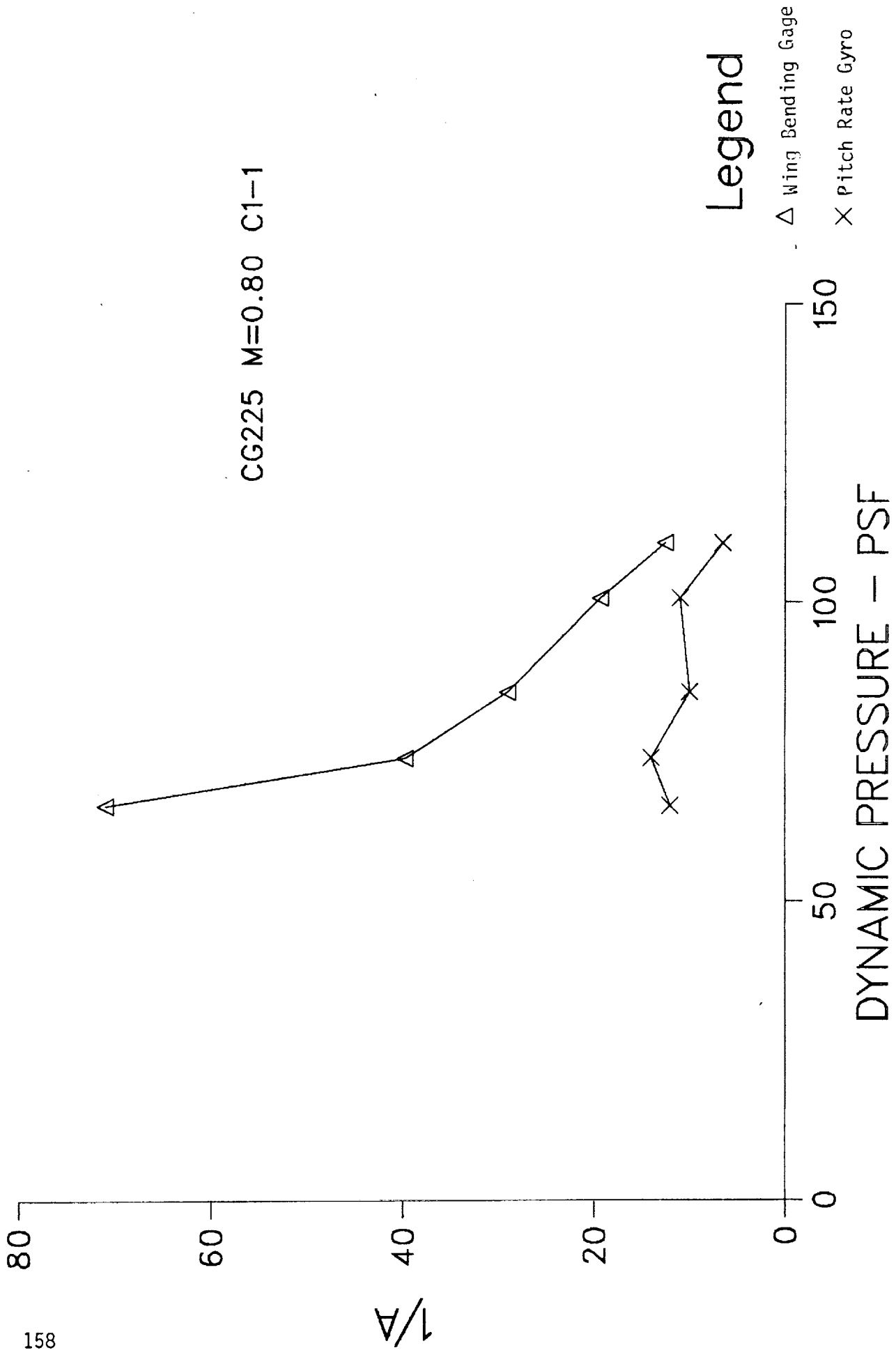
Figure 65.   Representative 1/A Trend.
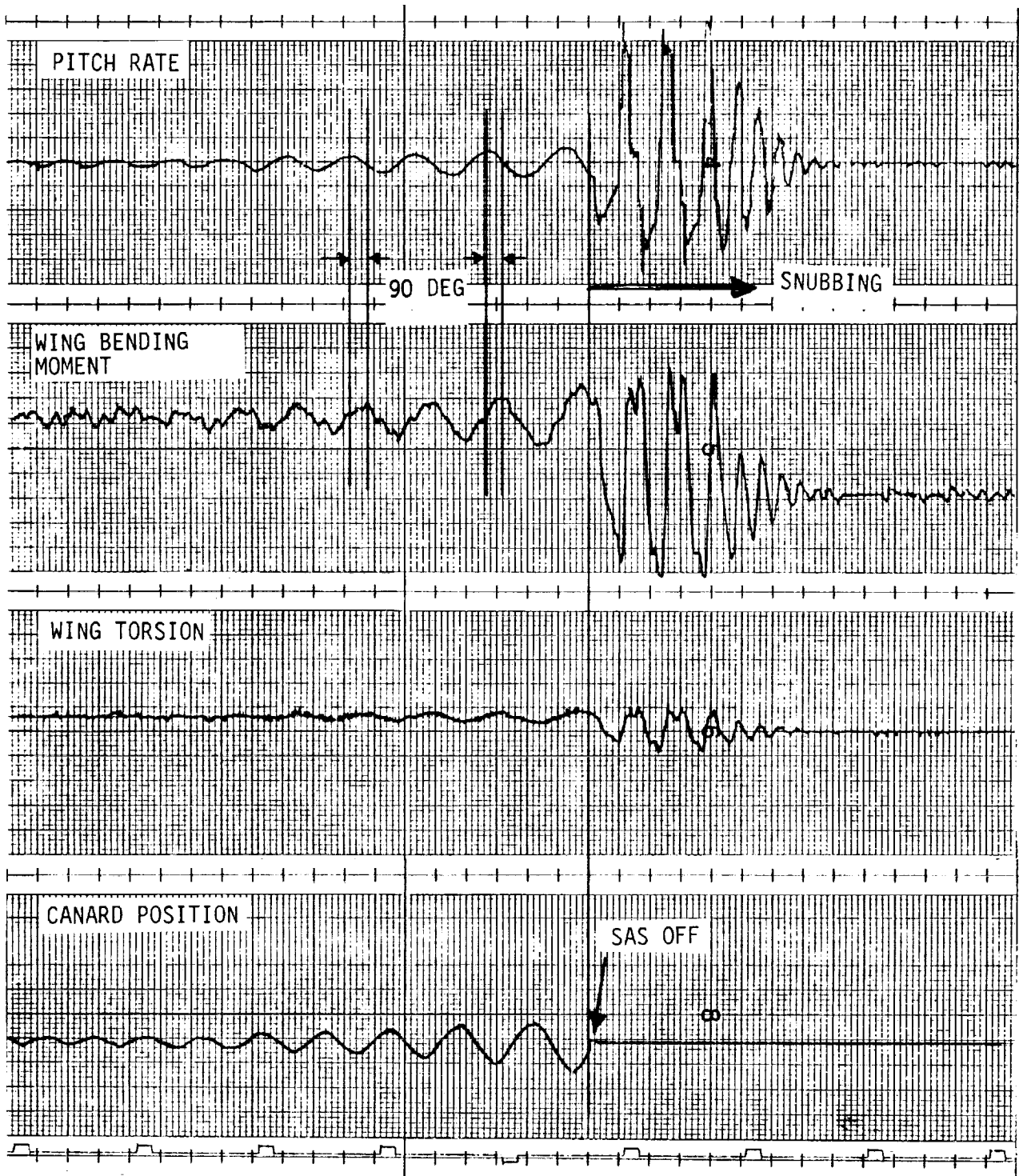
Figure 66. Time History Of Tab Point 489, SPI.
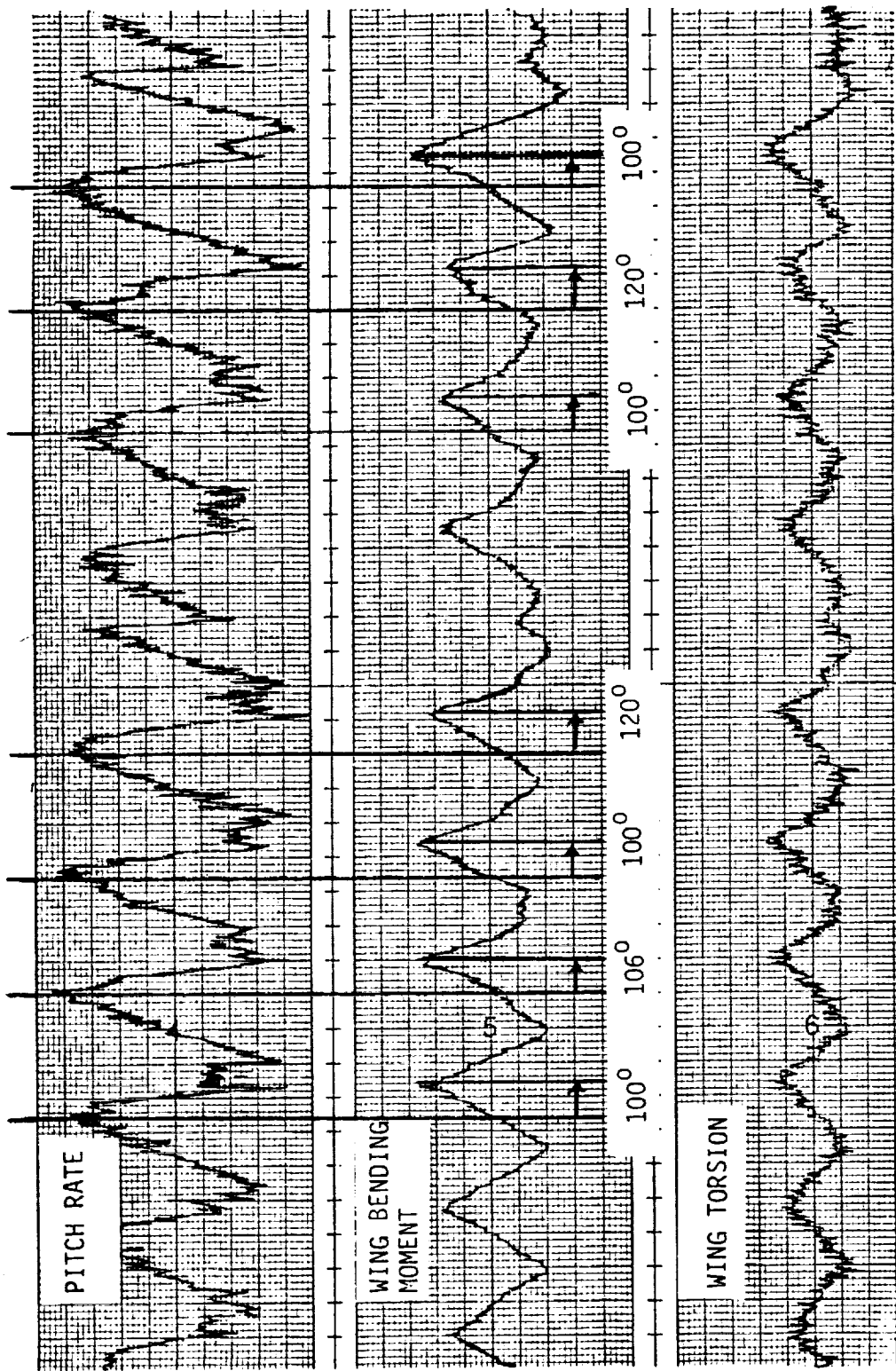
Figure 67. Time Histories Of Tab Point 200, BFF.

160
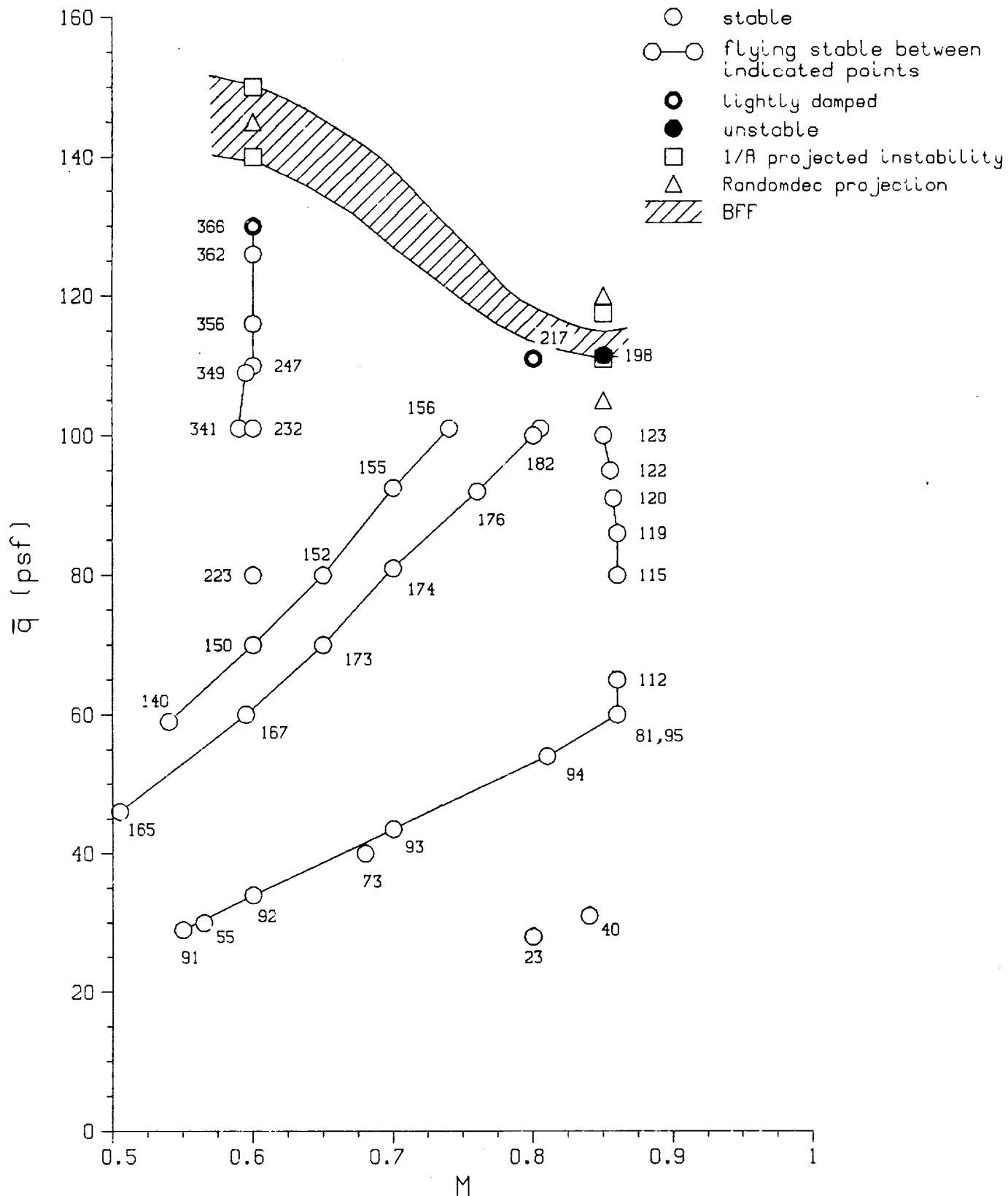
Figure 68. Test Flutter Boundary For CG213, Open Loop.
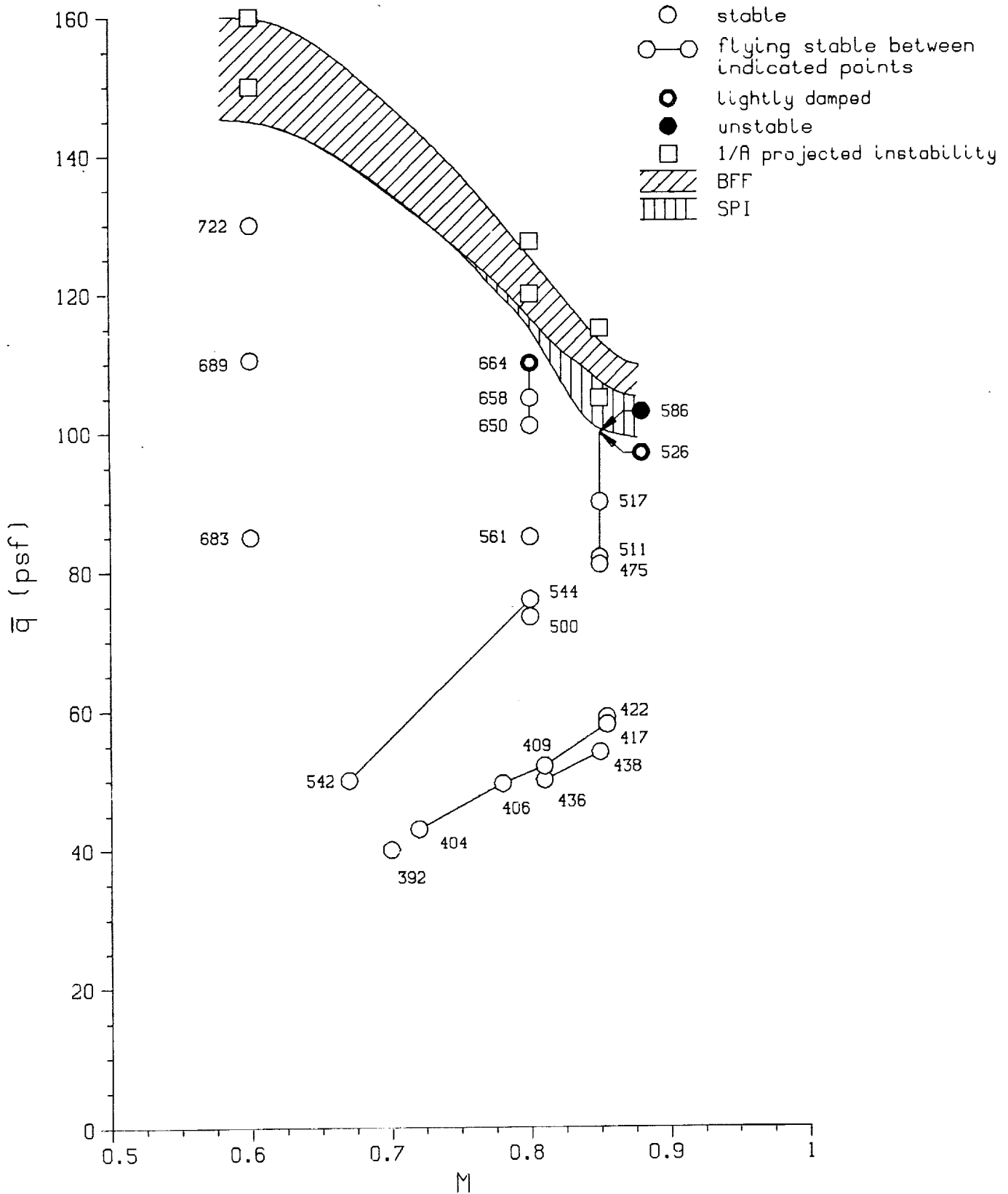
Figure 69. Test Flutter Boundary For CG225, C1-1.

1/2 Scale FSW Test Data
cg 225 C1-3
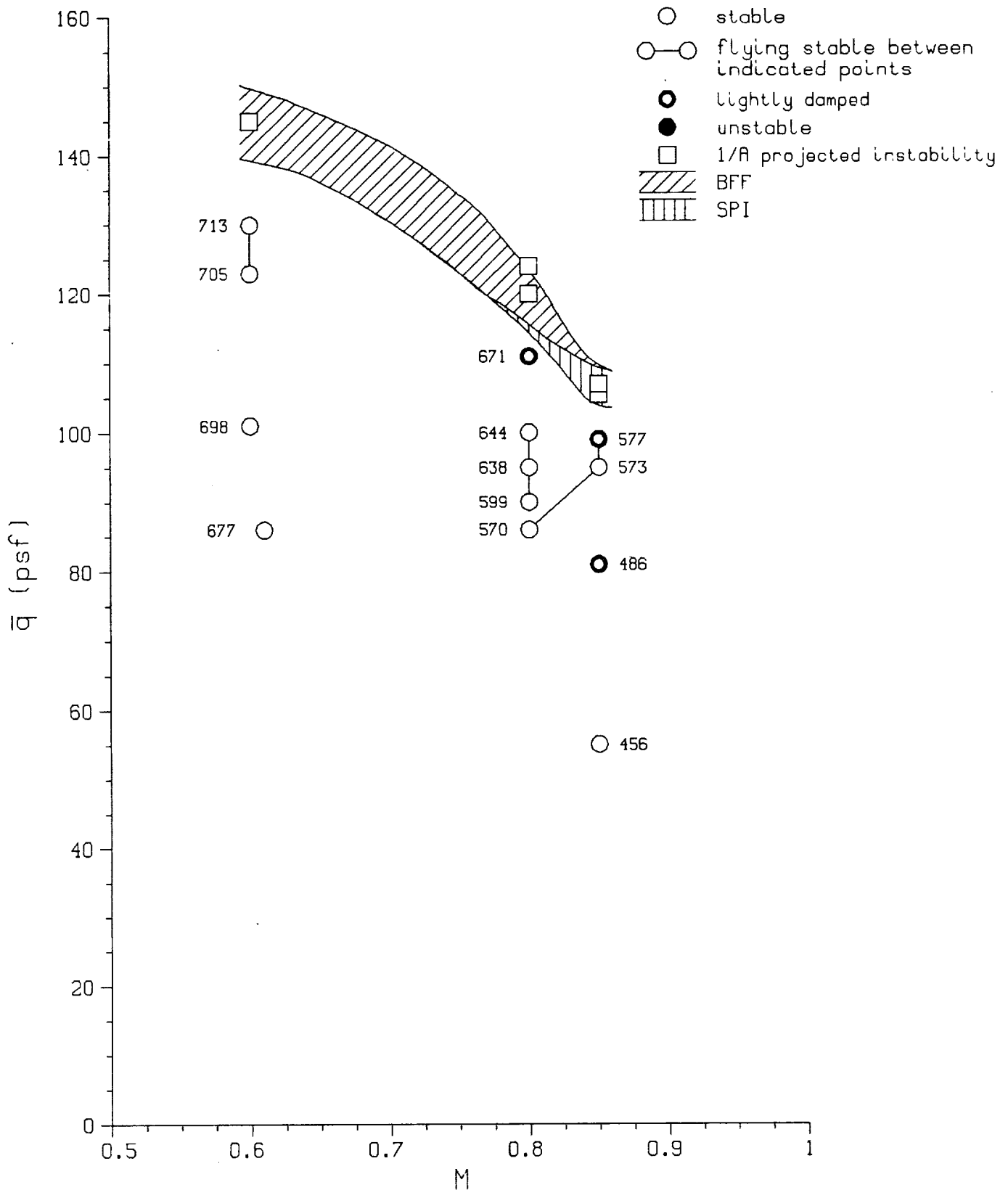
Figure 70. Test Flutter Boundary For CG225, C1-3.

1/2 Scale FSW Test Data
cg 225 C1-2,C1-4
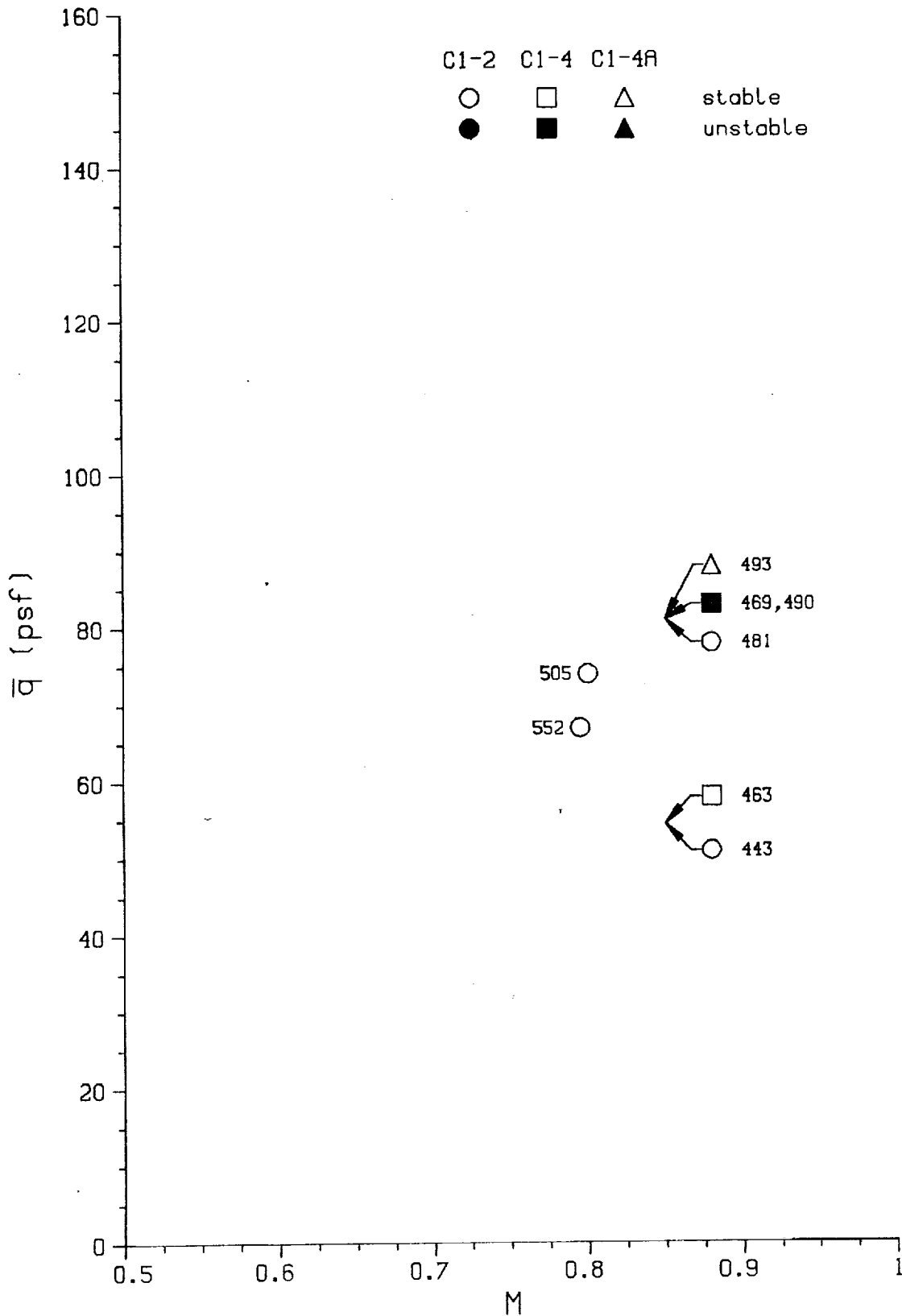
Figure 71.   Test Flutter Data For CG225, C1-2 And C1-4.
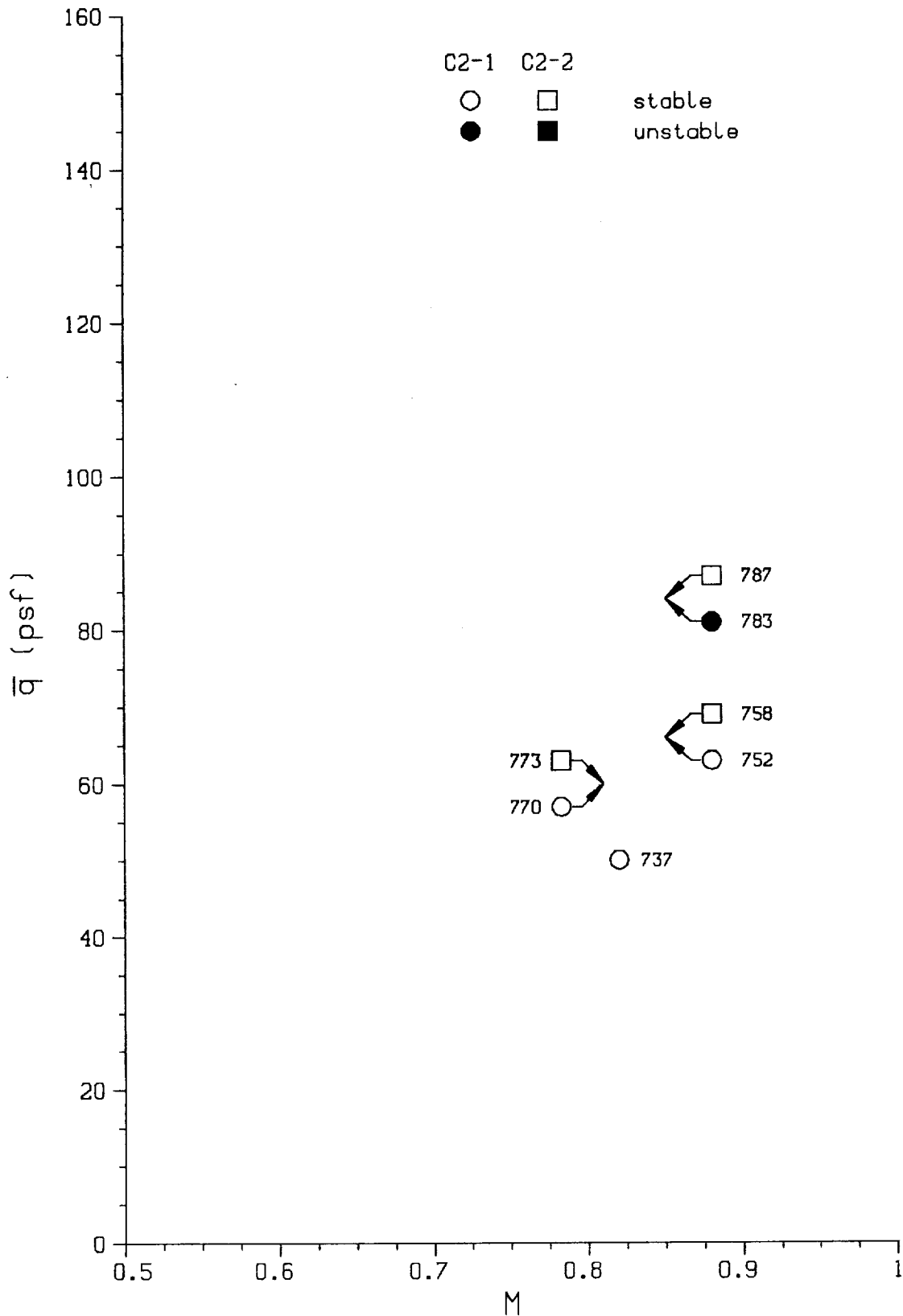
Figure 72. Test Flutter Data For CG231, C2-1 And C2-2.
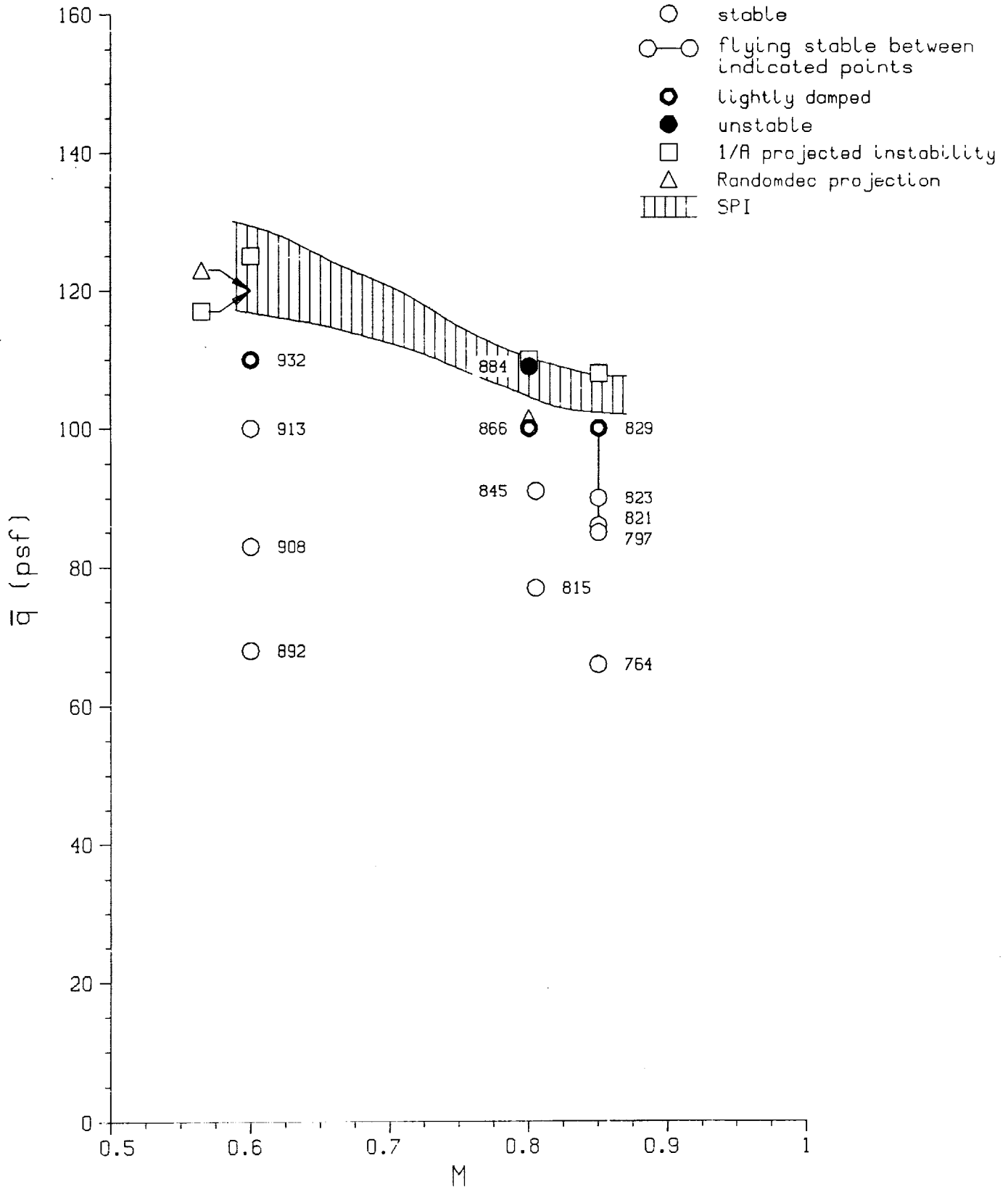
Figure 73. Test Flutter Boundary For CG231, C2-3.

1/2 Scale FSW Test Data
cg231 C2-4
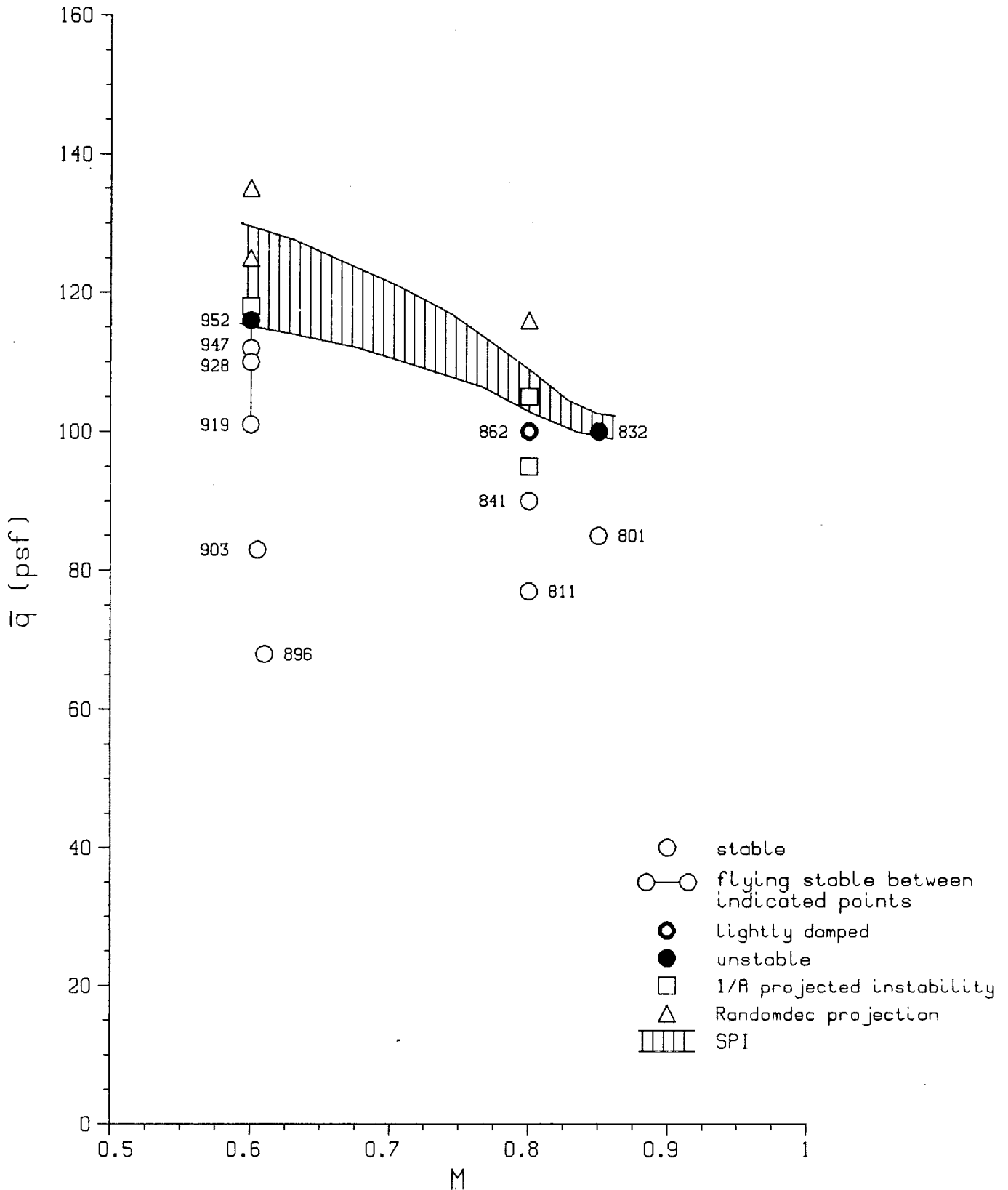
Figure 74. Test Flutter Boundary For CG231, C2-4.
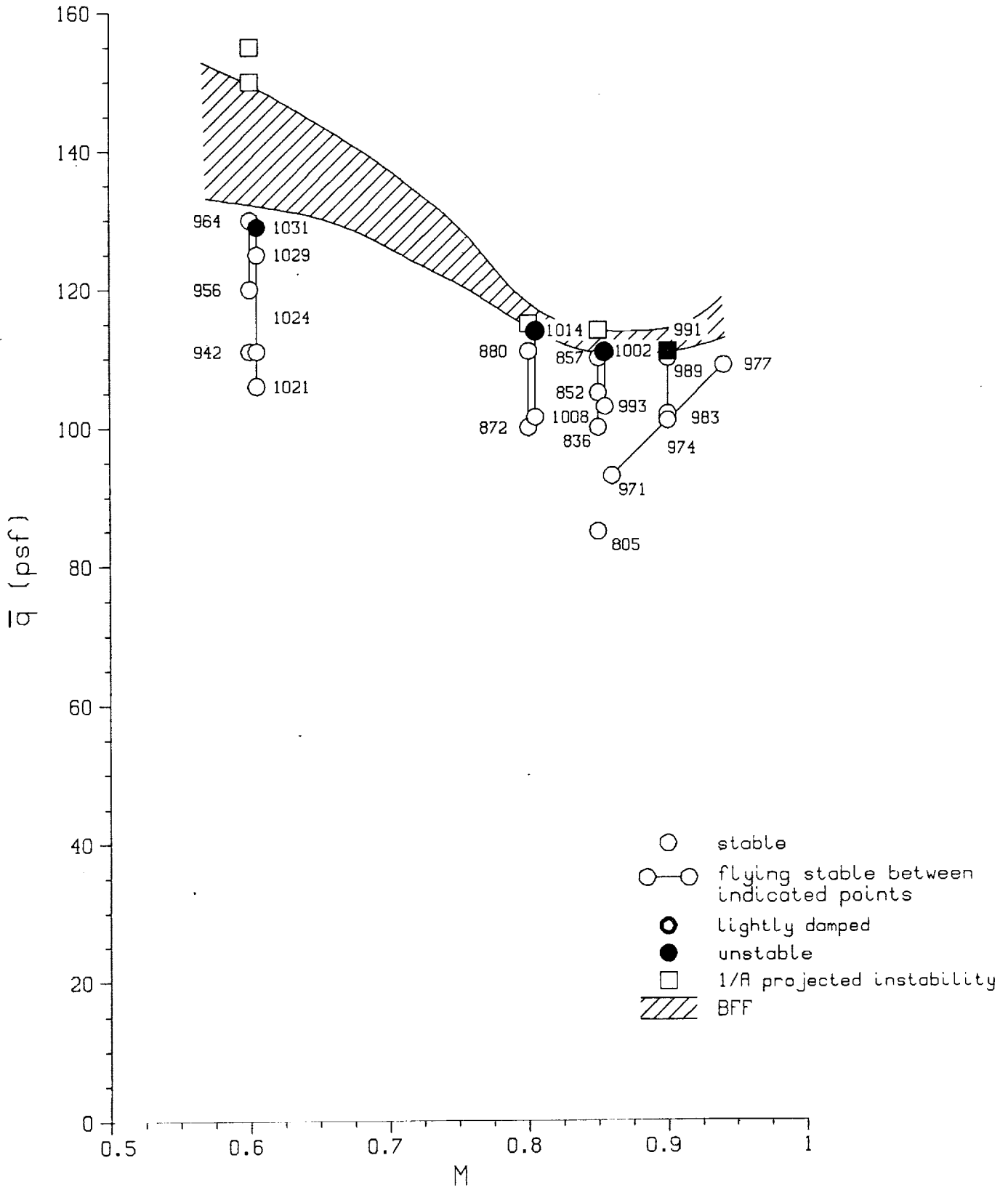
Figure 75. Test Flutter Boundary For CG231, C2-4A.

1/2 Scale FSW Test Data
cg 231 C2-4A
added tip ballast
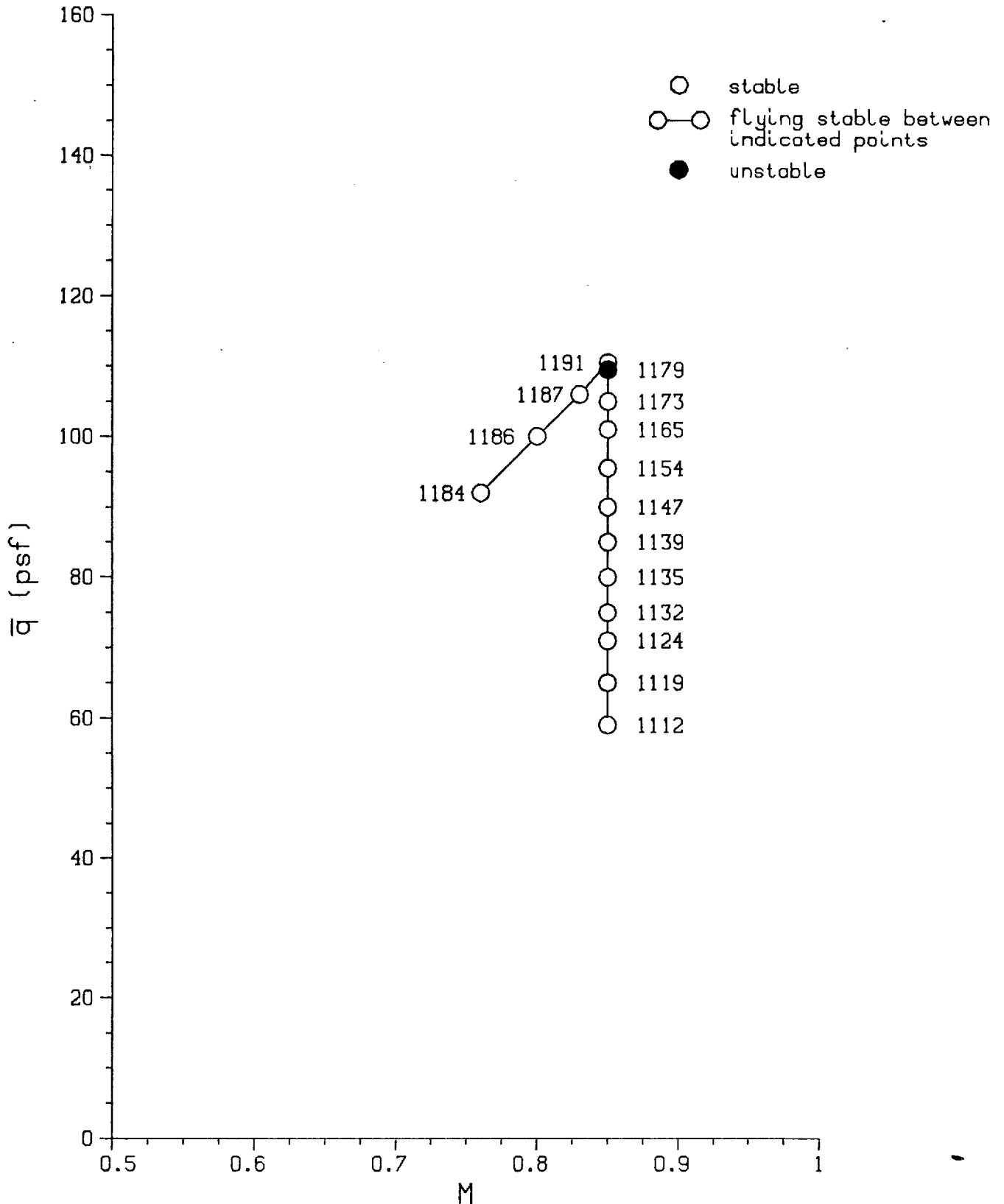
Figure 76. Test Flutter Data For CG231 With Tip Ballast.
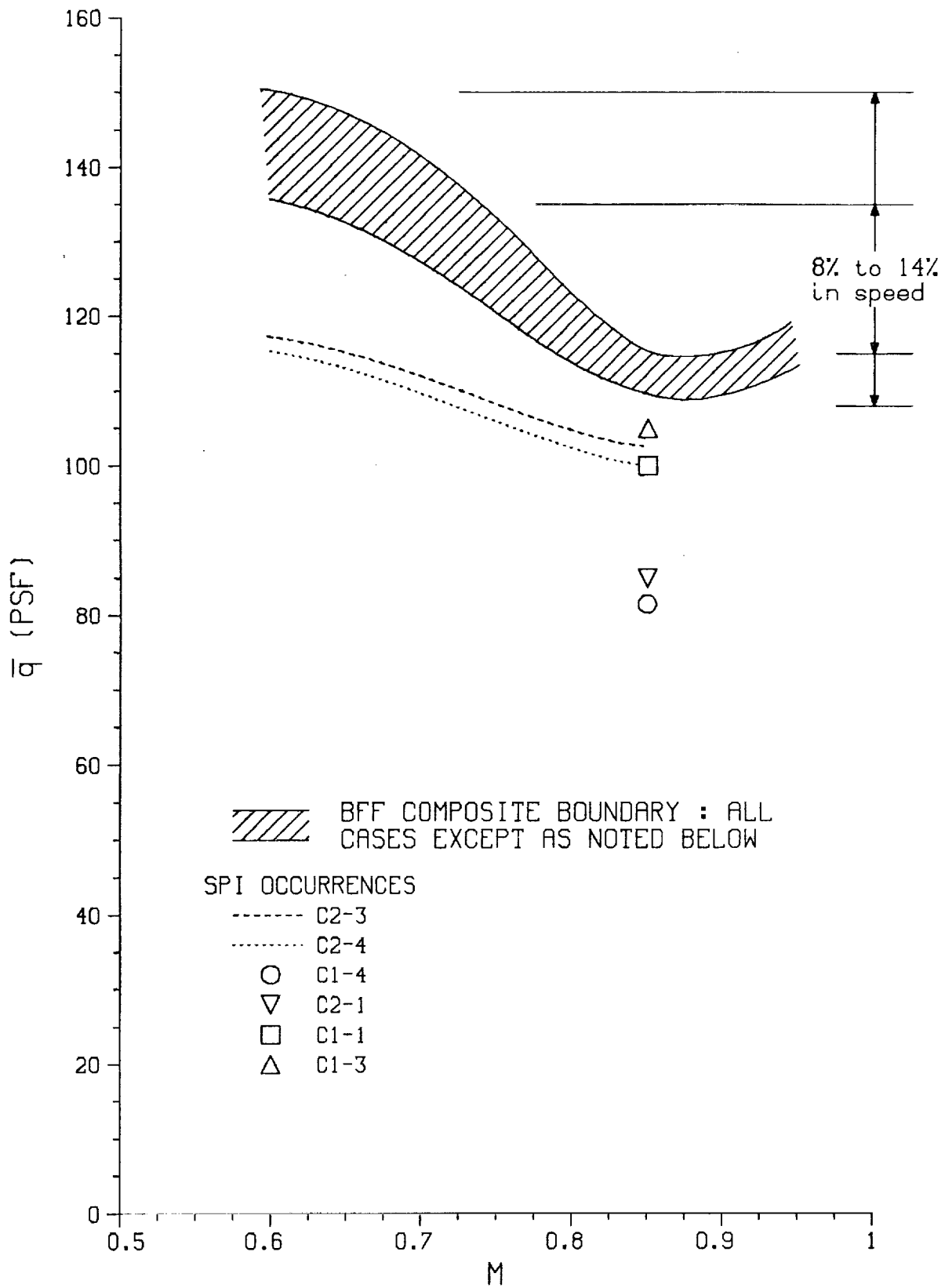
Figure 77. Composite Of Test Flutter Boundaries.
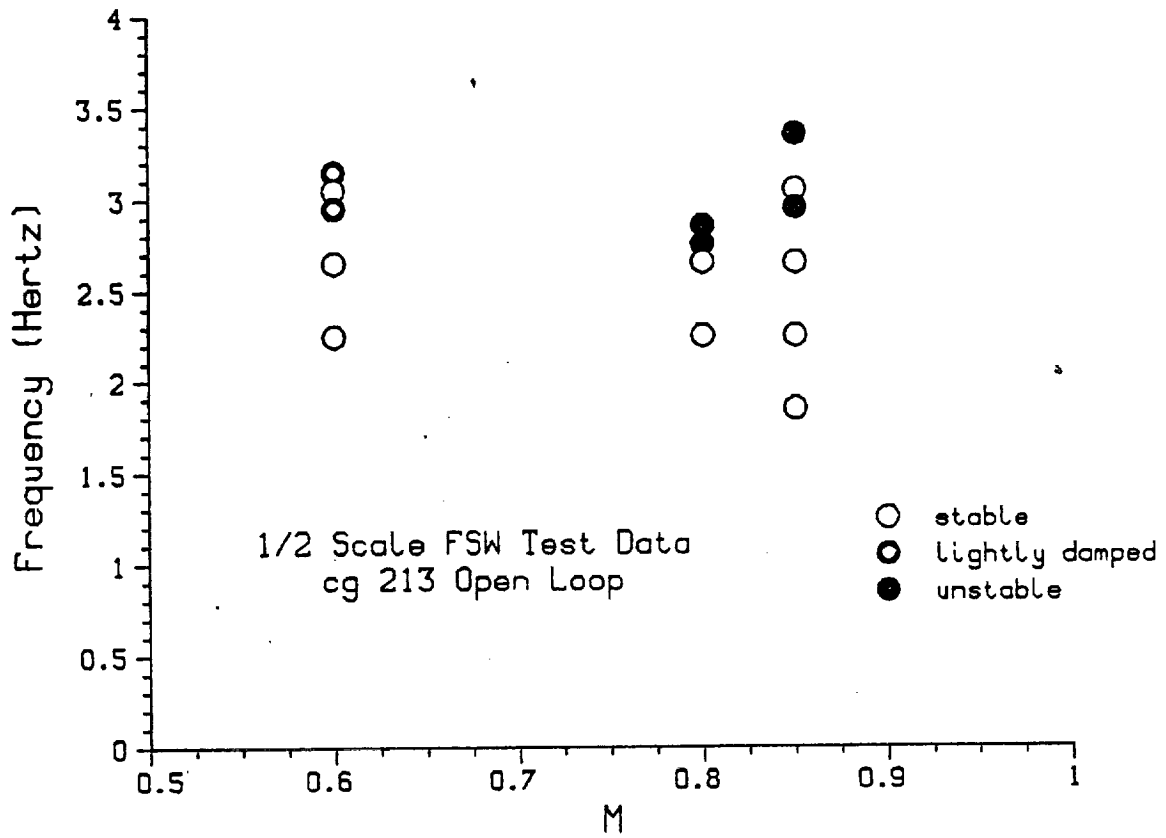
Figure 78. Measured Frequencies for CG213, Open Loop.
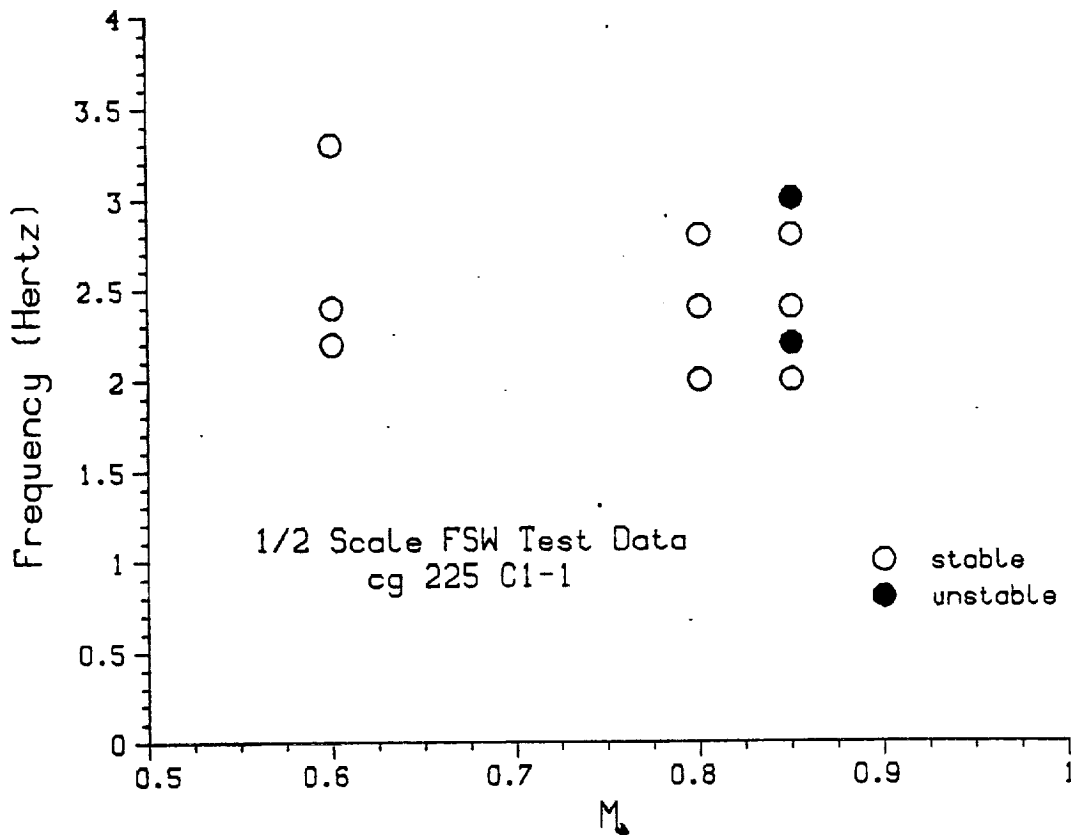
Figure 79. Measured Frequencies for CG225, C1-1.
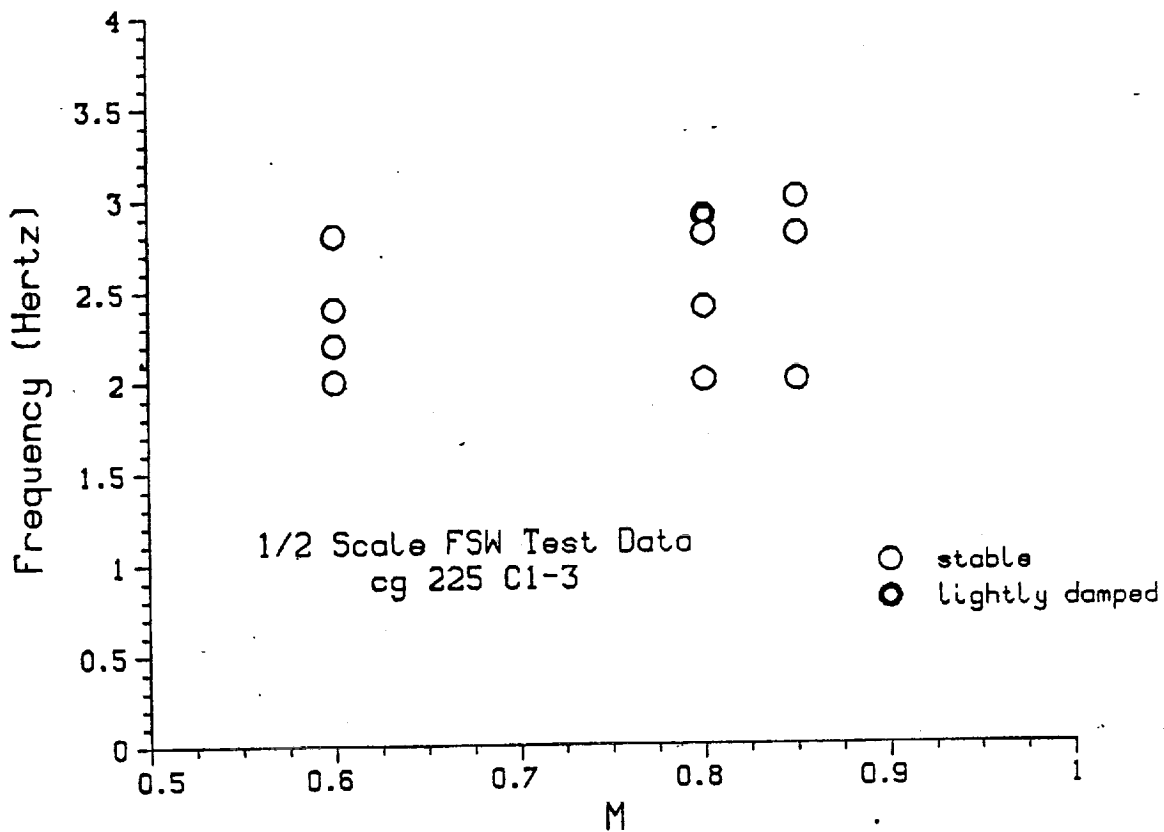
Figure 80. Measured Frequencies for CG225, C1-3.
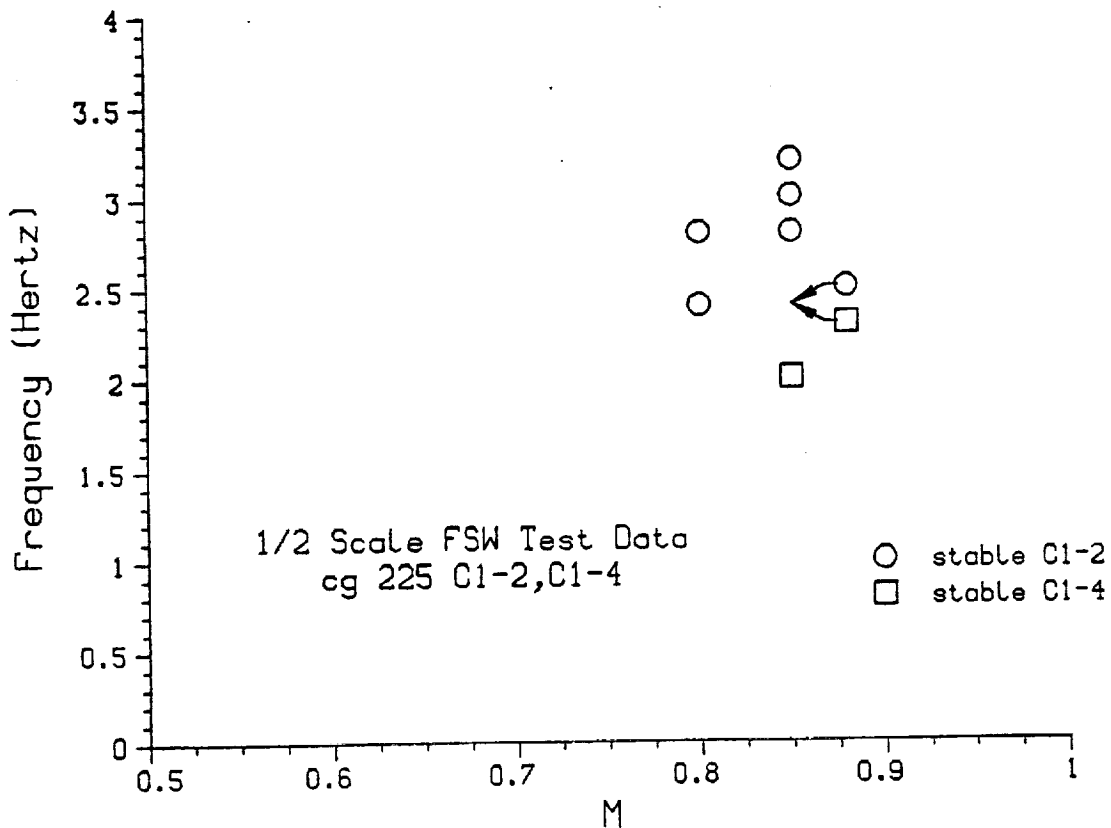
Figure 81. Measured Frequencies for CG225, C1-2 and C1-4.
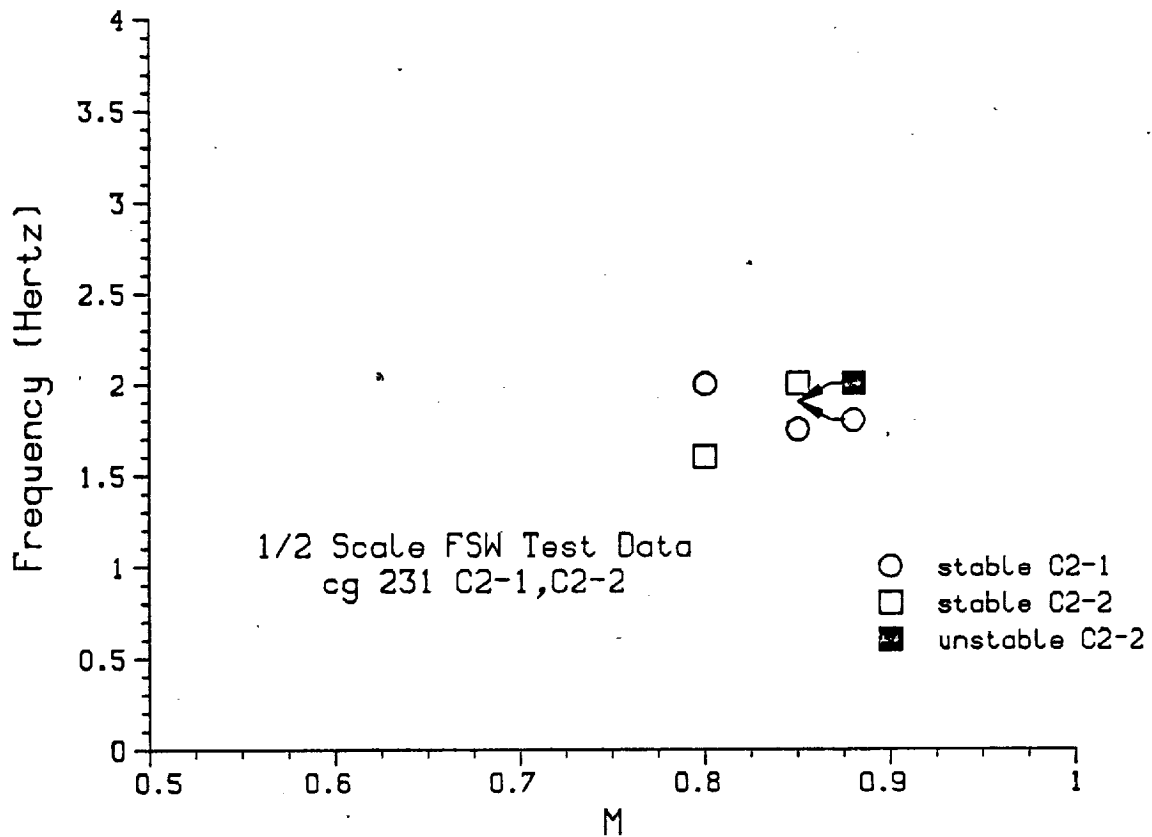
Figure 82. Measured Frequencies for CG231, C2-1 and C2-2.
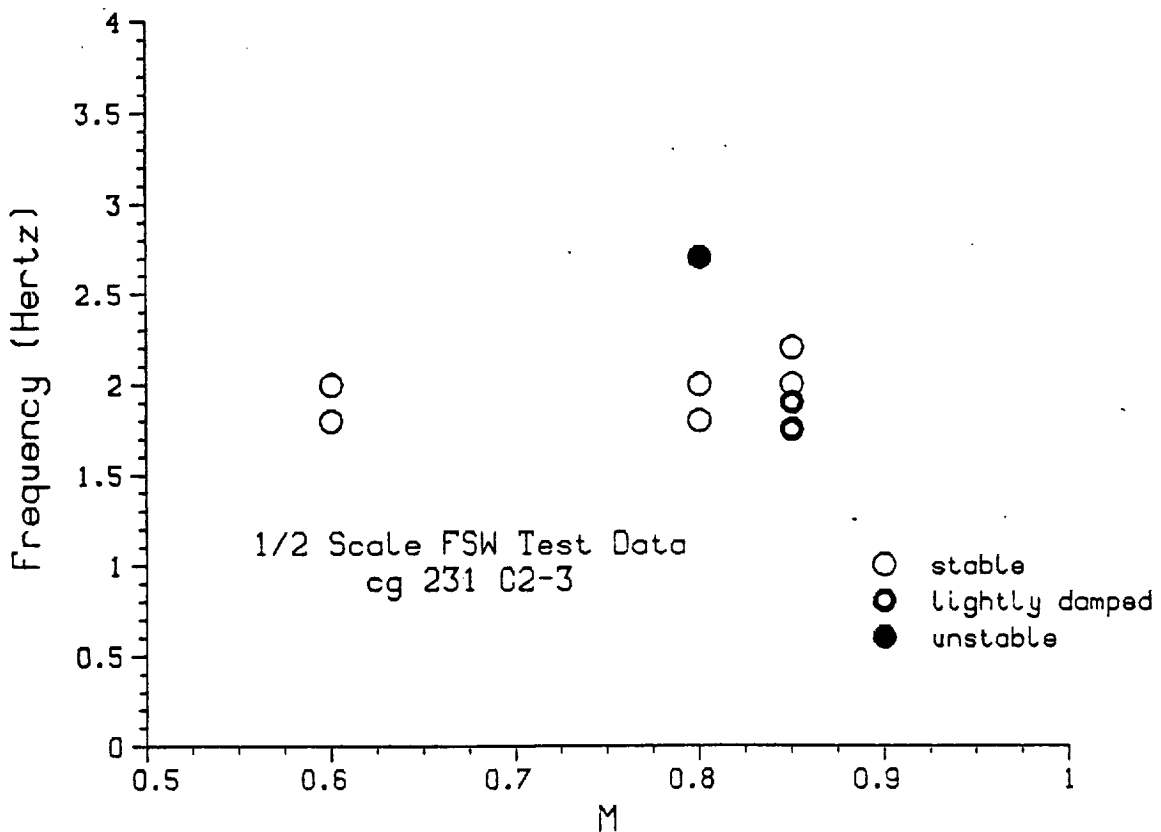
Figure 83. Measured Frequencies for CG231, C2-3.
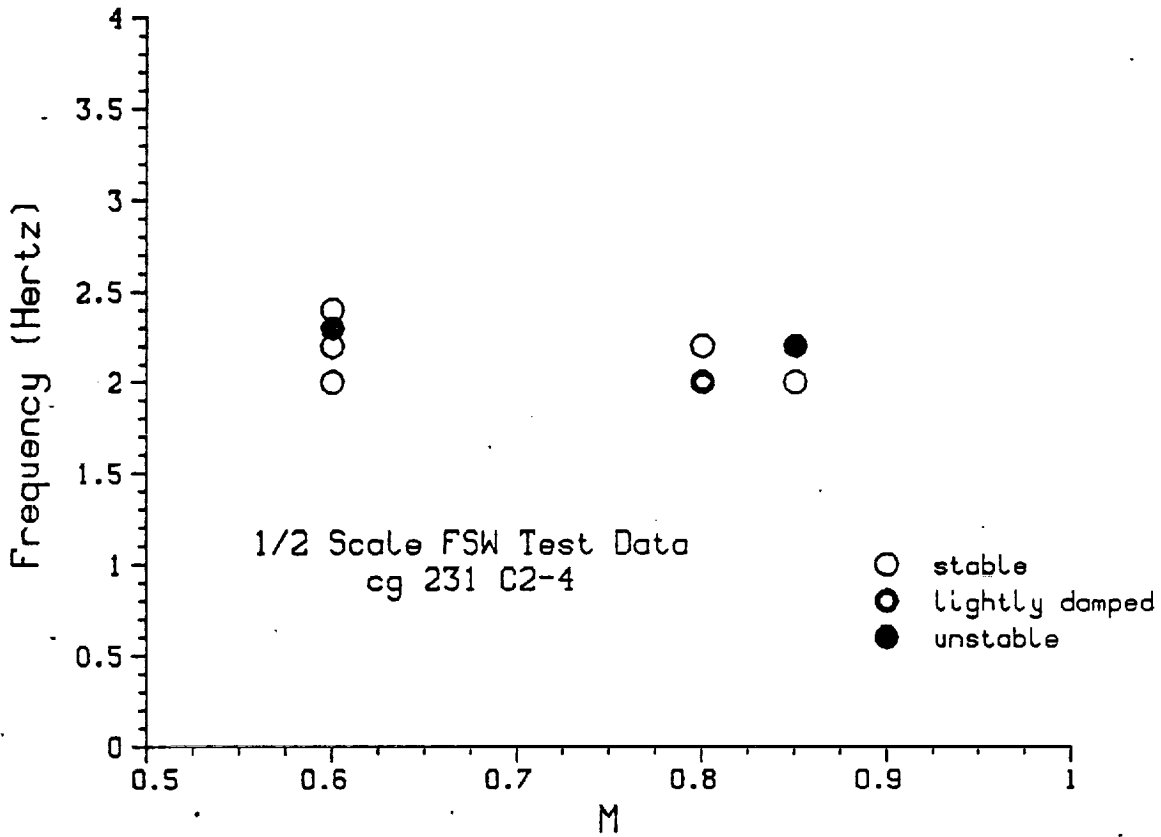
Figure 84. Measured Frequencies for CG231, C2-4.
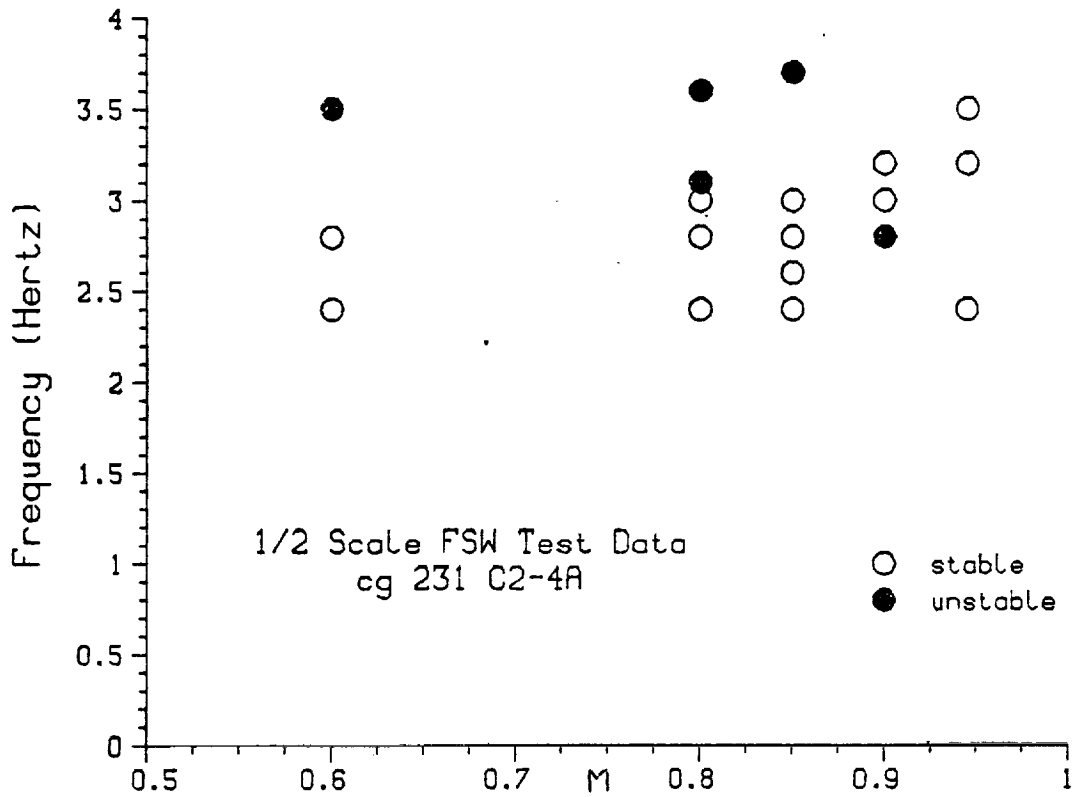
Figure 85. Measured Frequencies for CG231, C2-4A.

1/2 Scale FSW Test Data
cg 231 C2-4A
added tip ballast
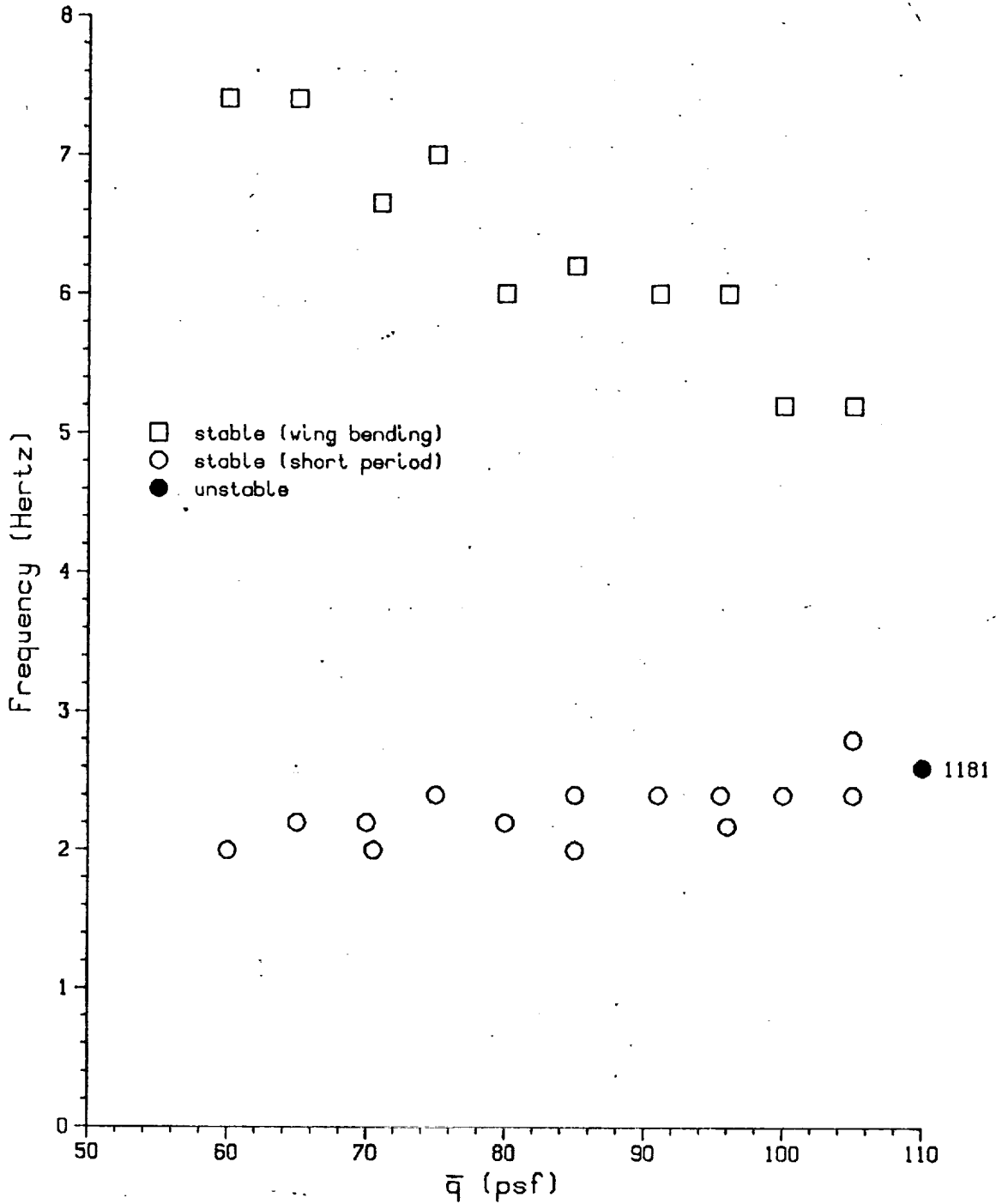
Figure 86. Measured Frequencies vs. $\bar{Q}$ for Ballast Case.
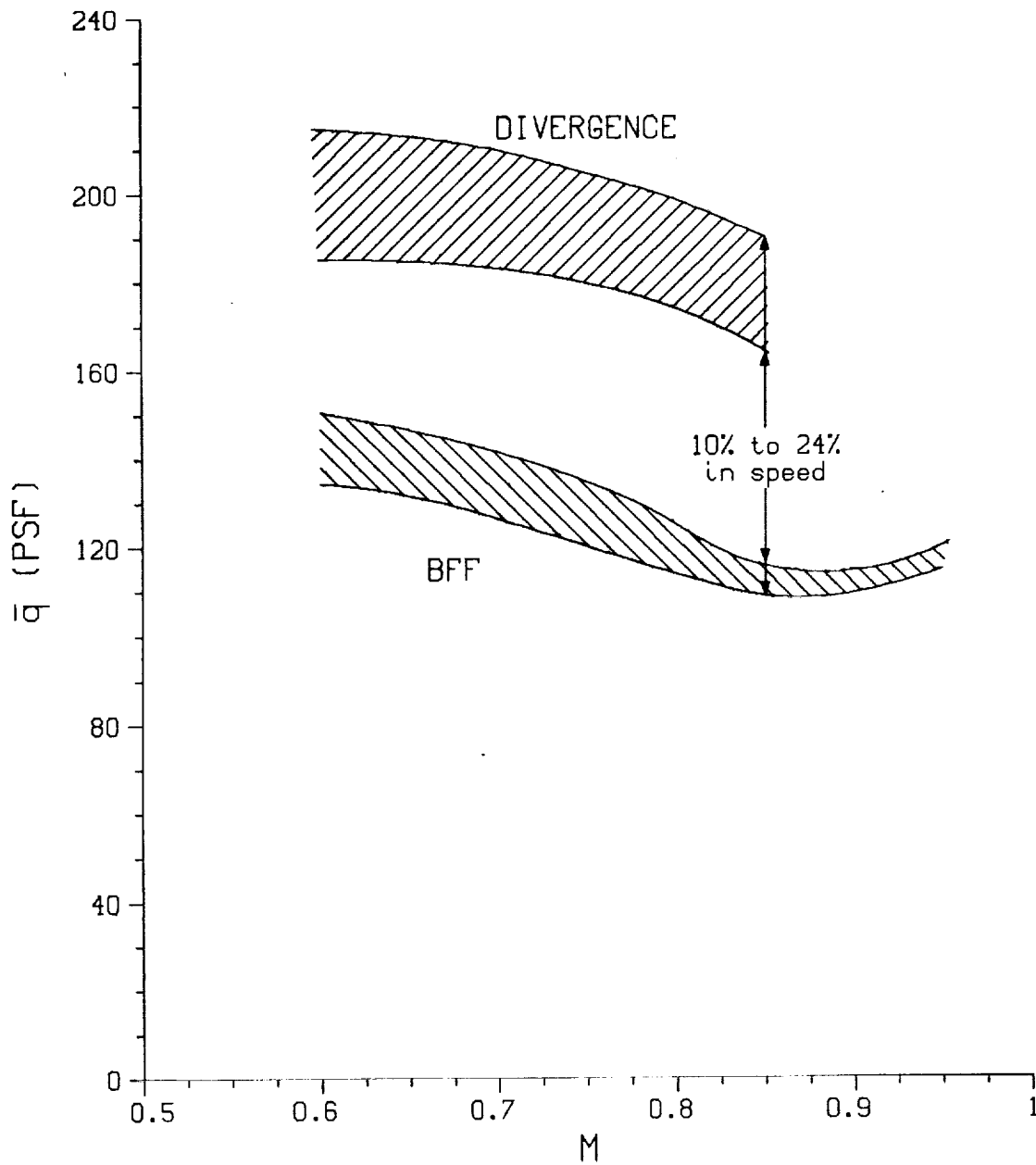
Figure 87. Summary of Test Results.
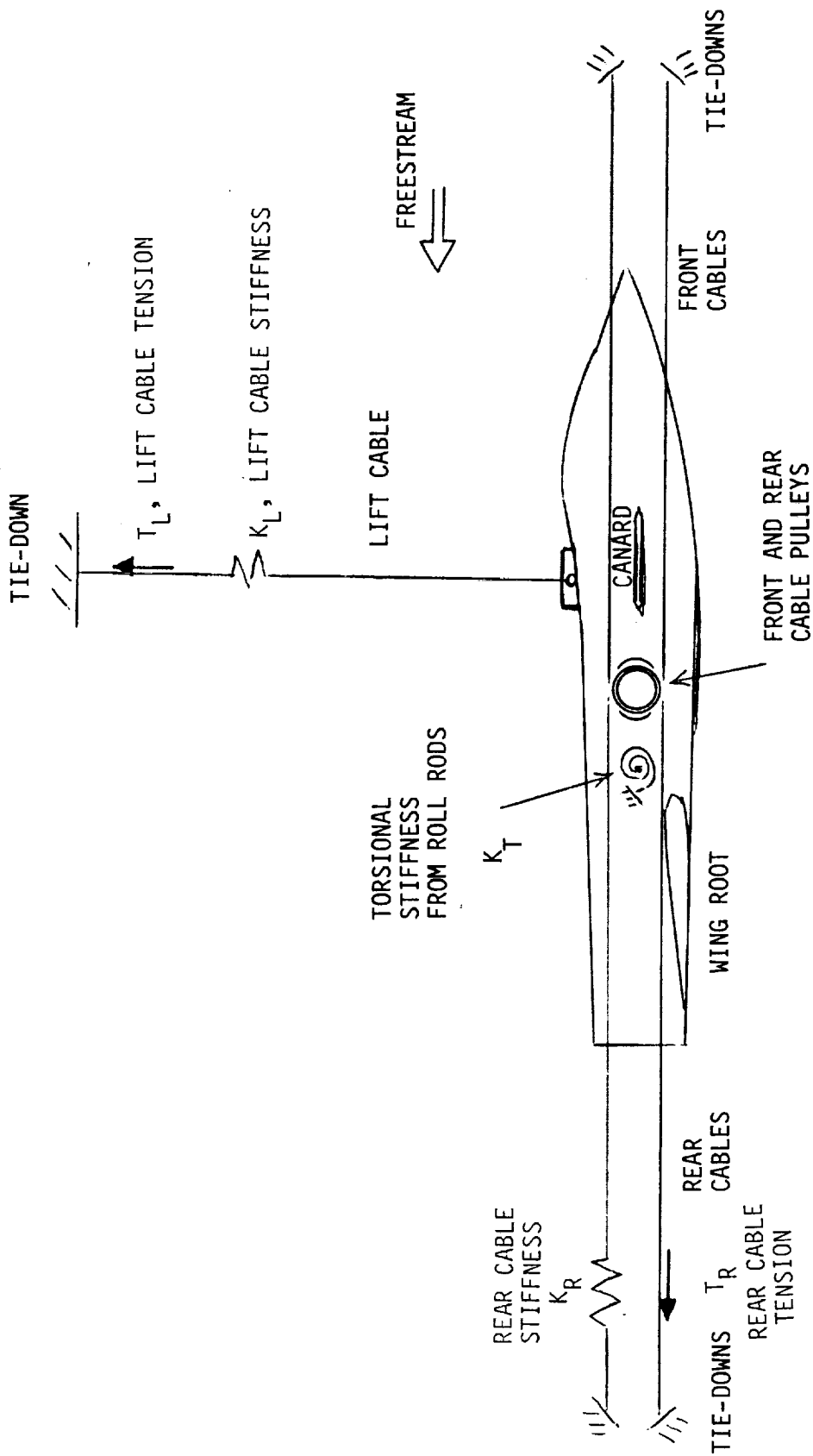
Figure 88. Idealization of Cable Support System used in GRUMCABLE.
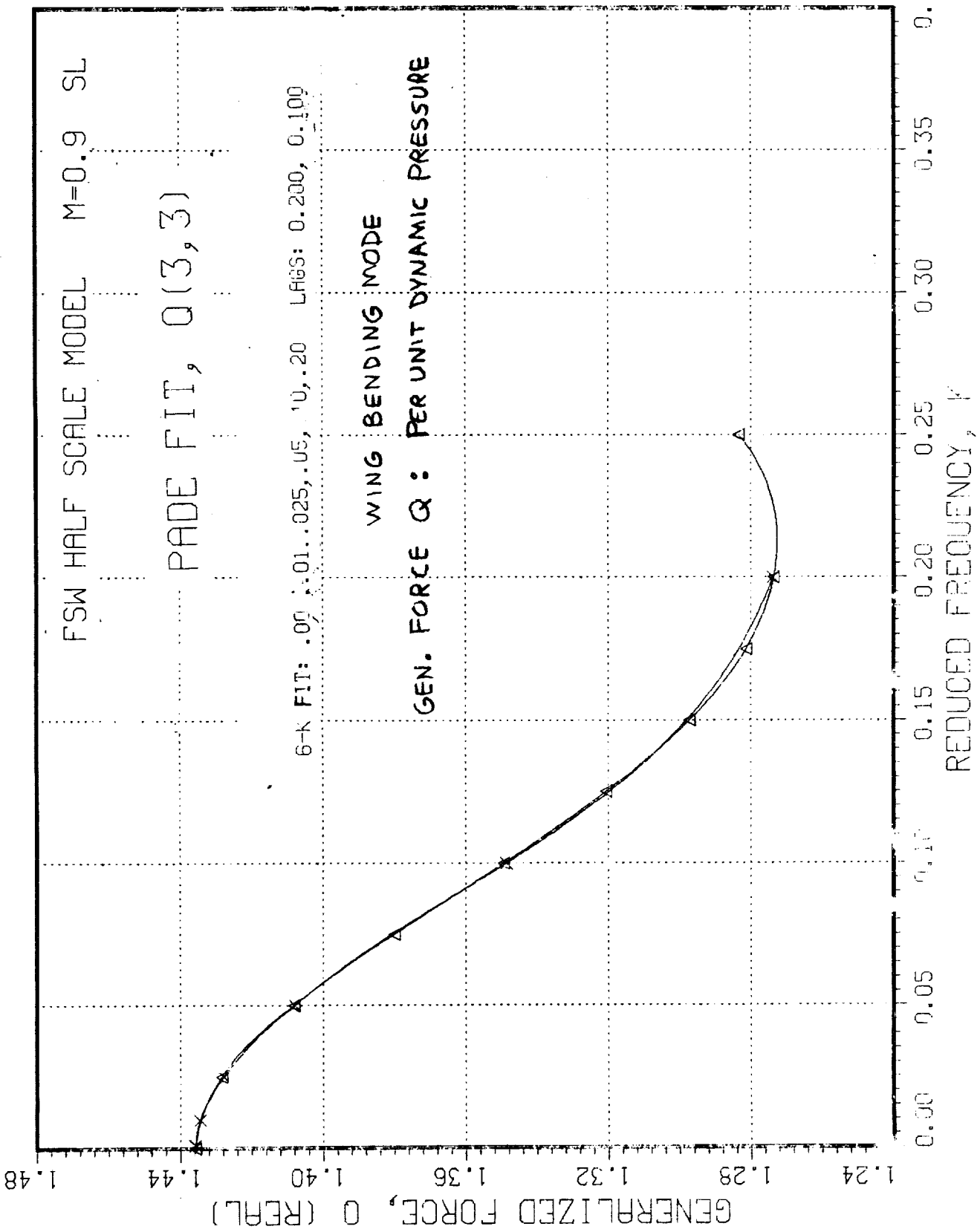
Figure 89. Representative Functional Fit to Unsteady Aerodynamic Generalized Forces, Real Part.
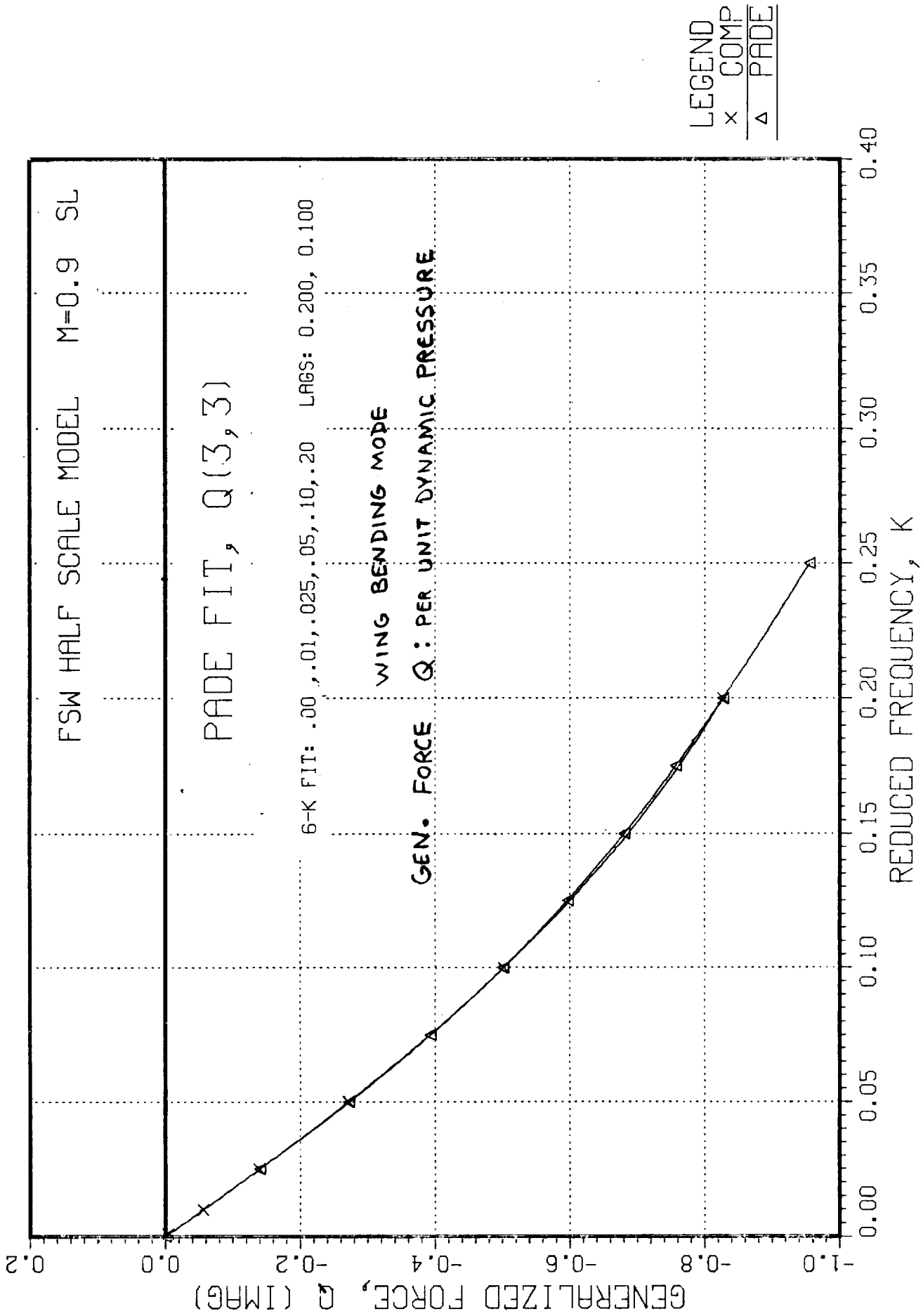
Figure 90. Representative Functional Fit to Unsteady Aerodynamic Generalized Forces, Imaginary Part.
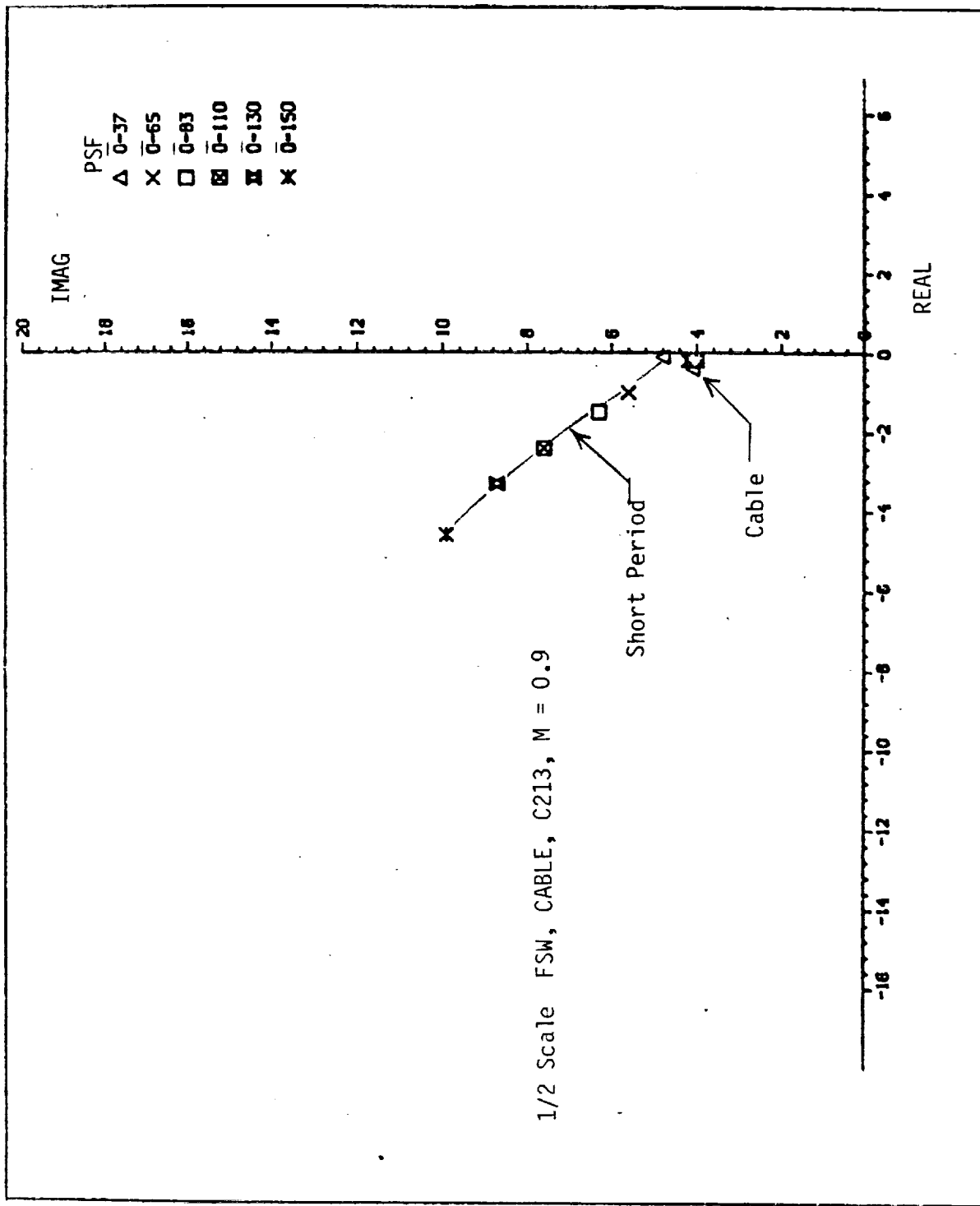
Figure 91. GRUMCABLE Analysis for CG213, Open Loop, M = 0.9.
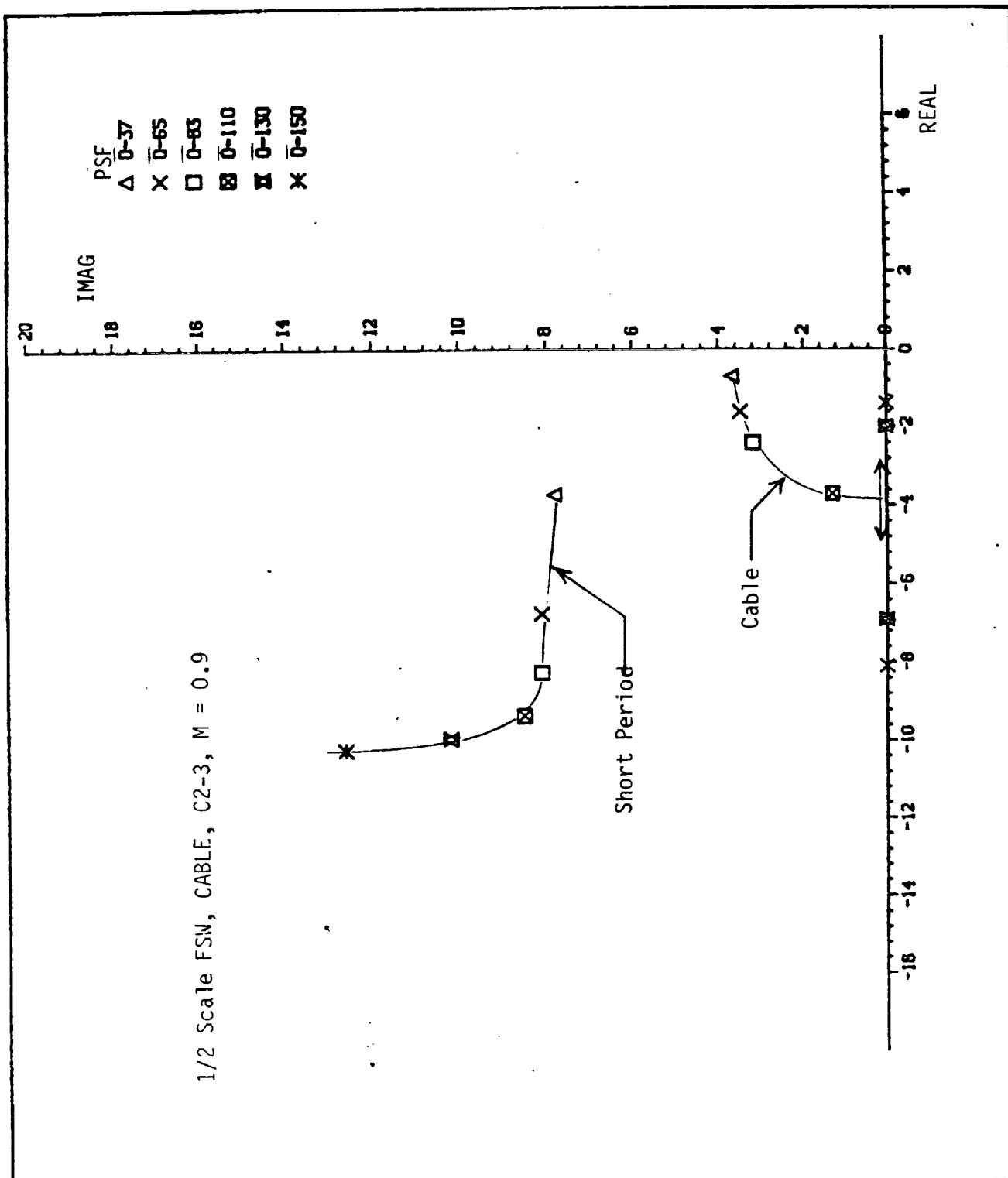
Figure 92. CRUMCABLE Analysis for CG231, C2-3, M = 0.9.
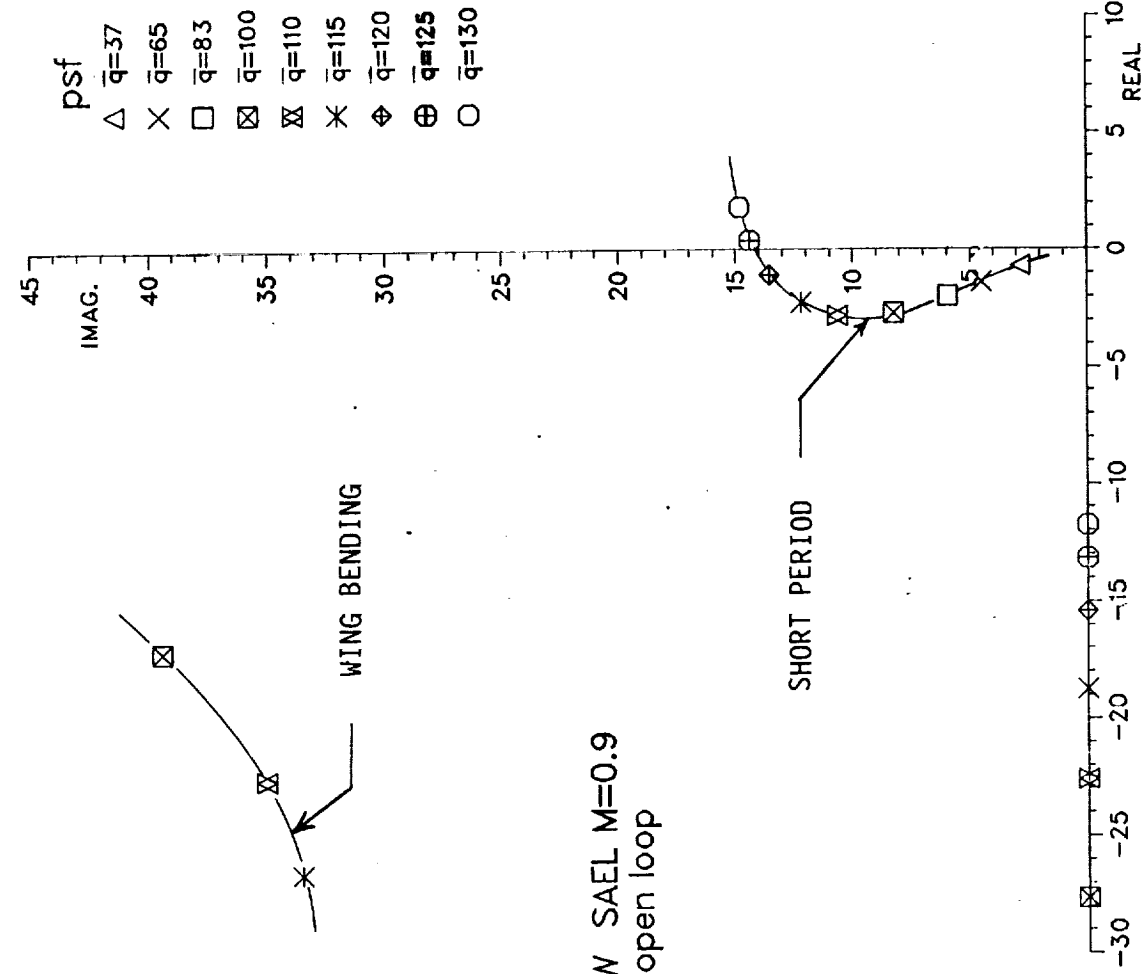
Figure 93. Preliminary SAEL Analysis for CG213, Open Loop, M = 0.9.
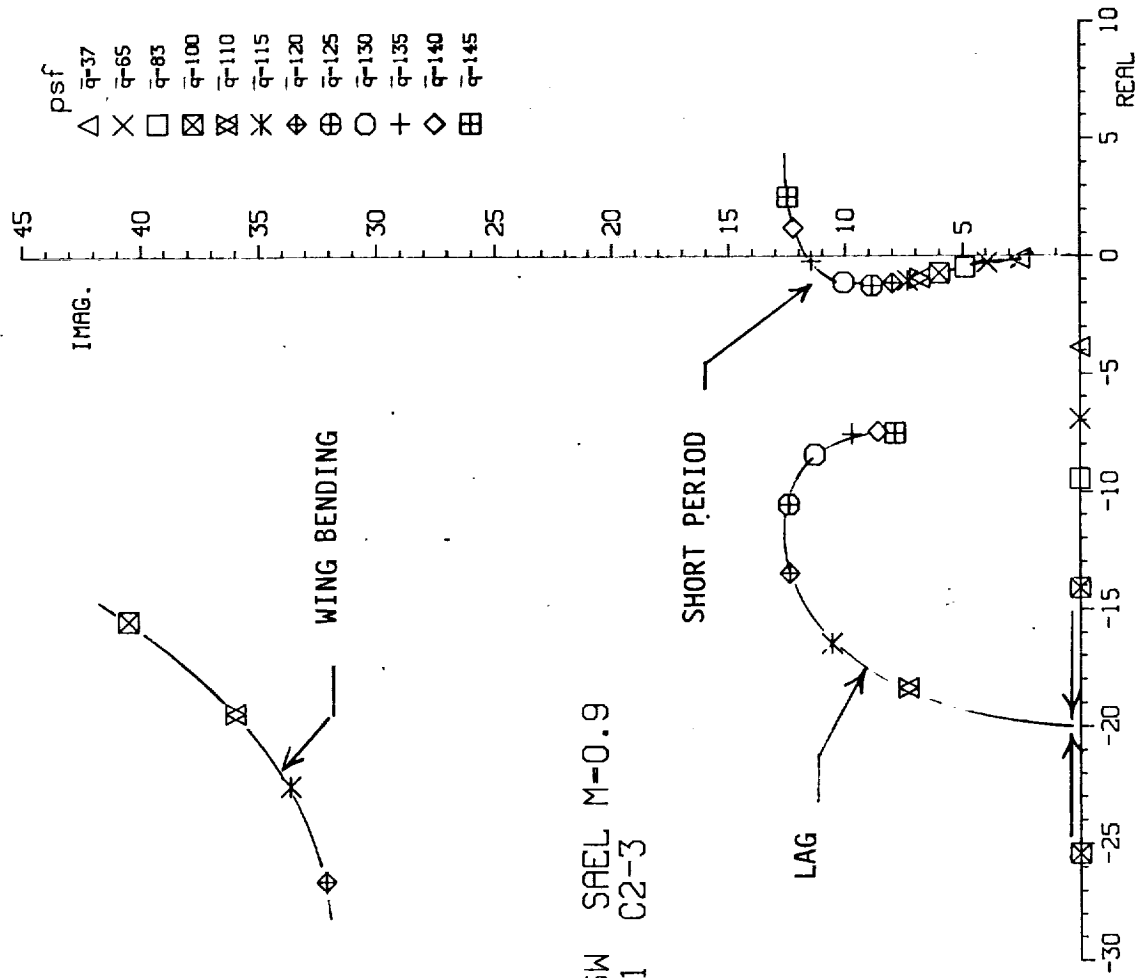
Figure 94. Preliminary SAEL Analysis for CG231, C2-3, M = 0.9.

183
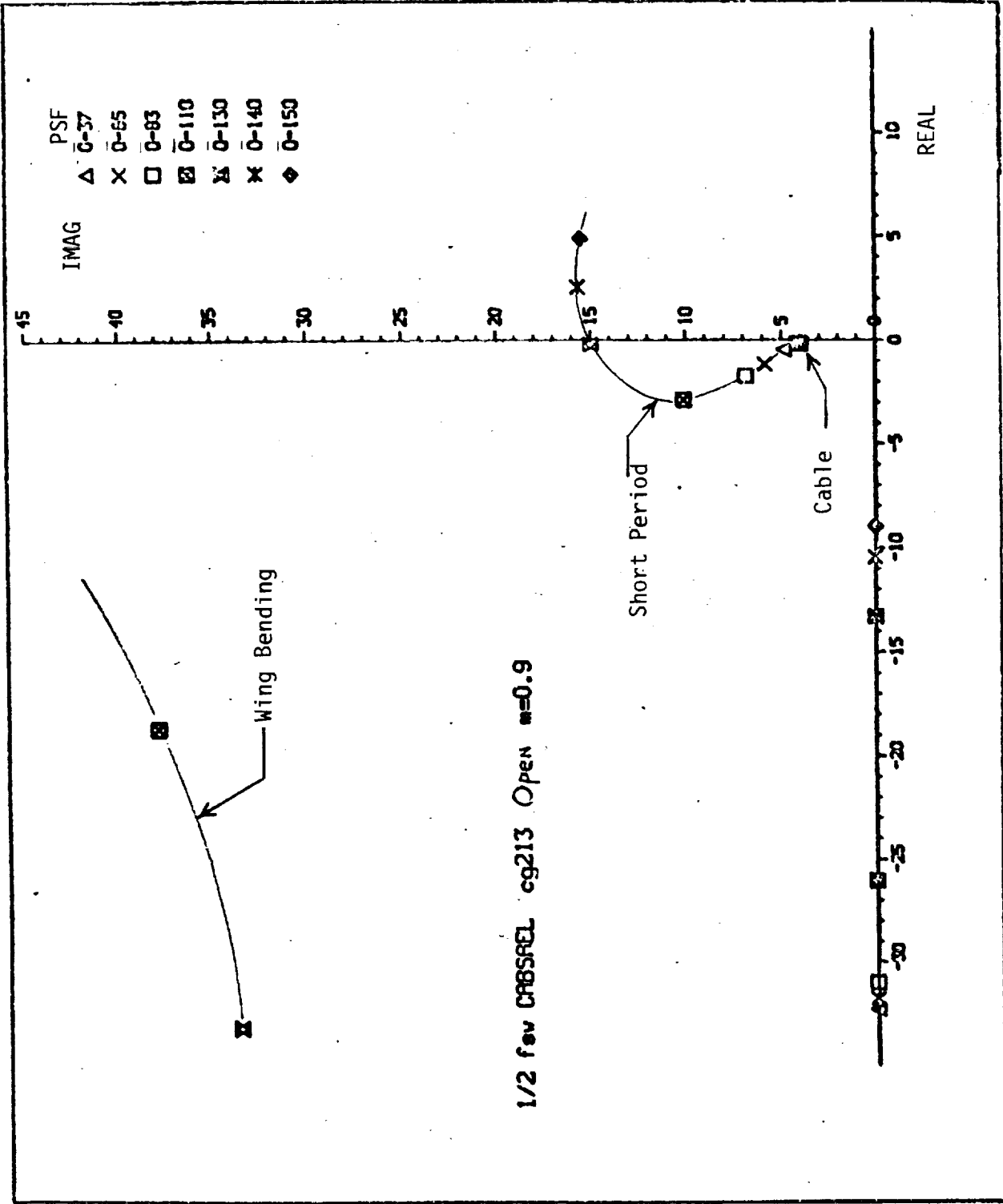
Figure 95. Preliminary CABSAEL Analysis for CG213, Open Loop, M = 0.9.
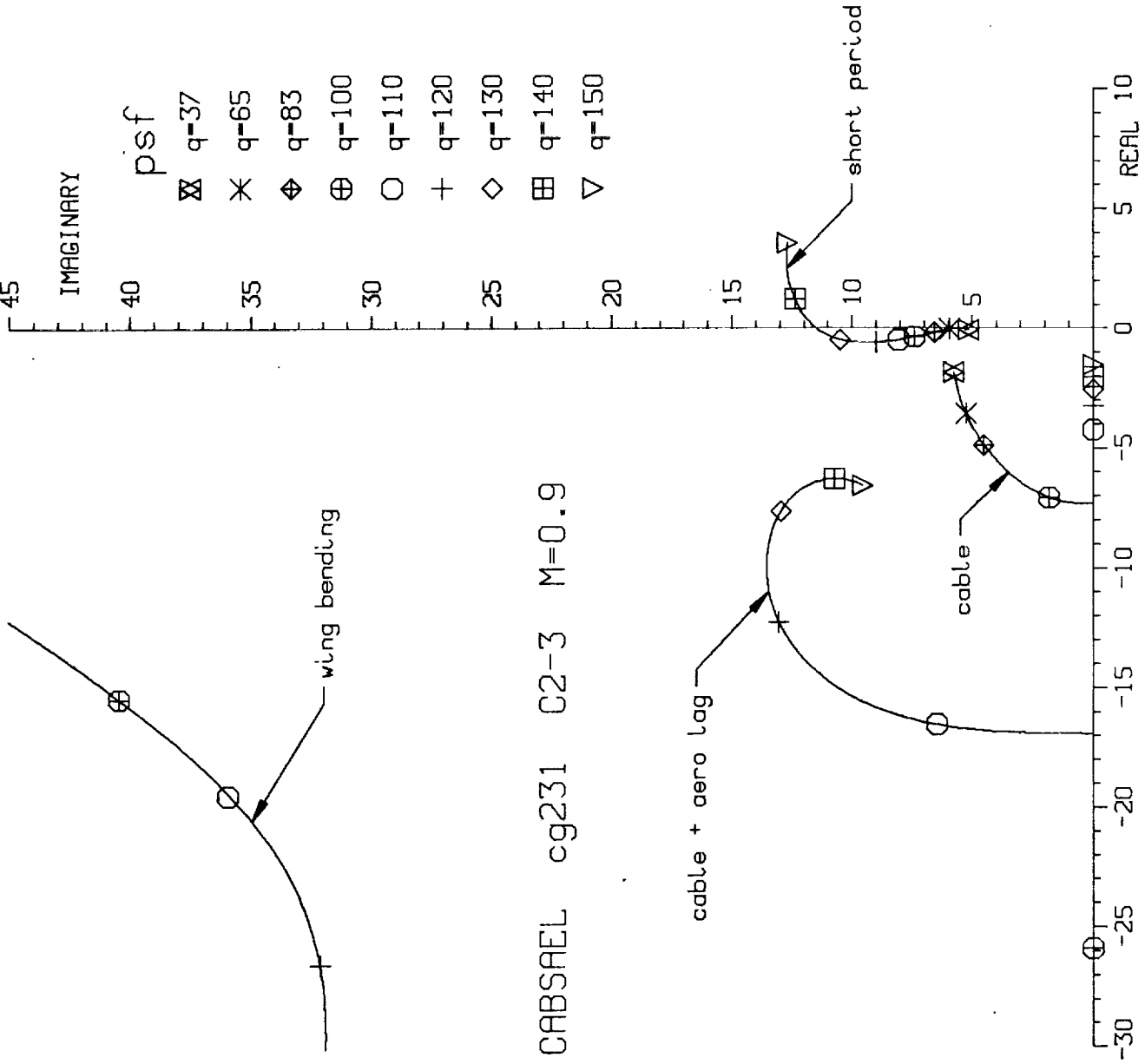
Figure 96. Preliminary CABSAEL Analysis for CG231, C2-3, M = 0.9.

1/2 scale FSW CABSAEL cg231 C2-3 M=0.9

CABLE/SAEL/CABSAEL Comparison
cg 213 open Loop M=0.9
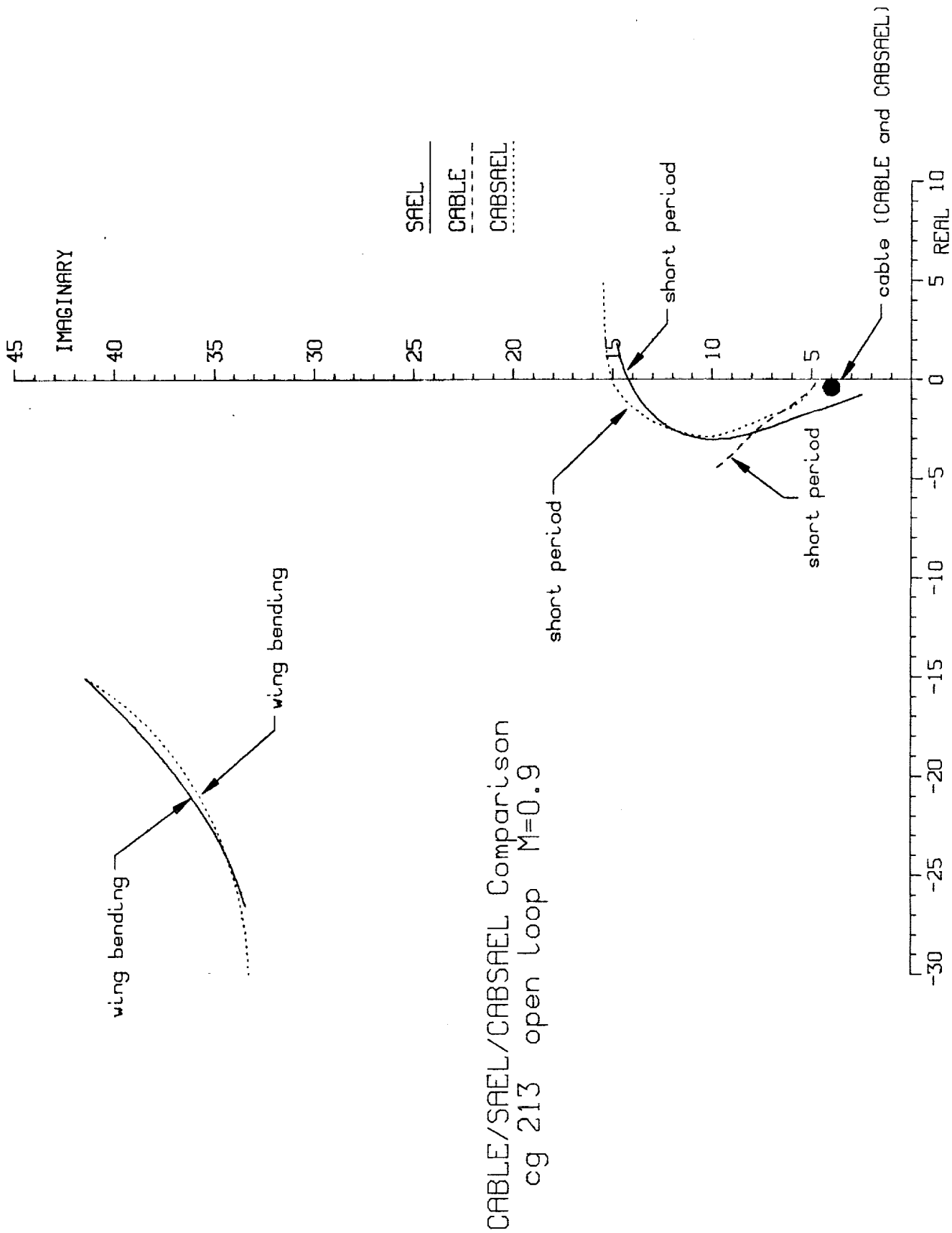
Figure 97. Comparison of GRUMCABLE, SAEL, and CABSAEL Analysis for CG213, Open Loop, M = 0.9.
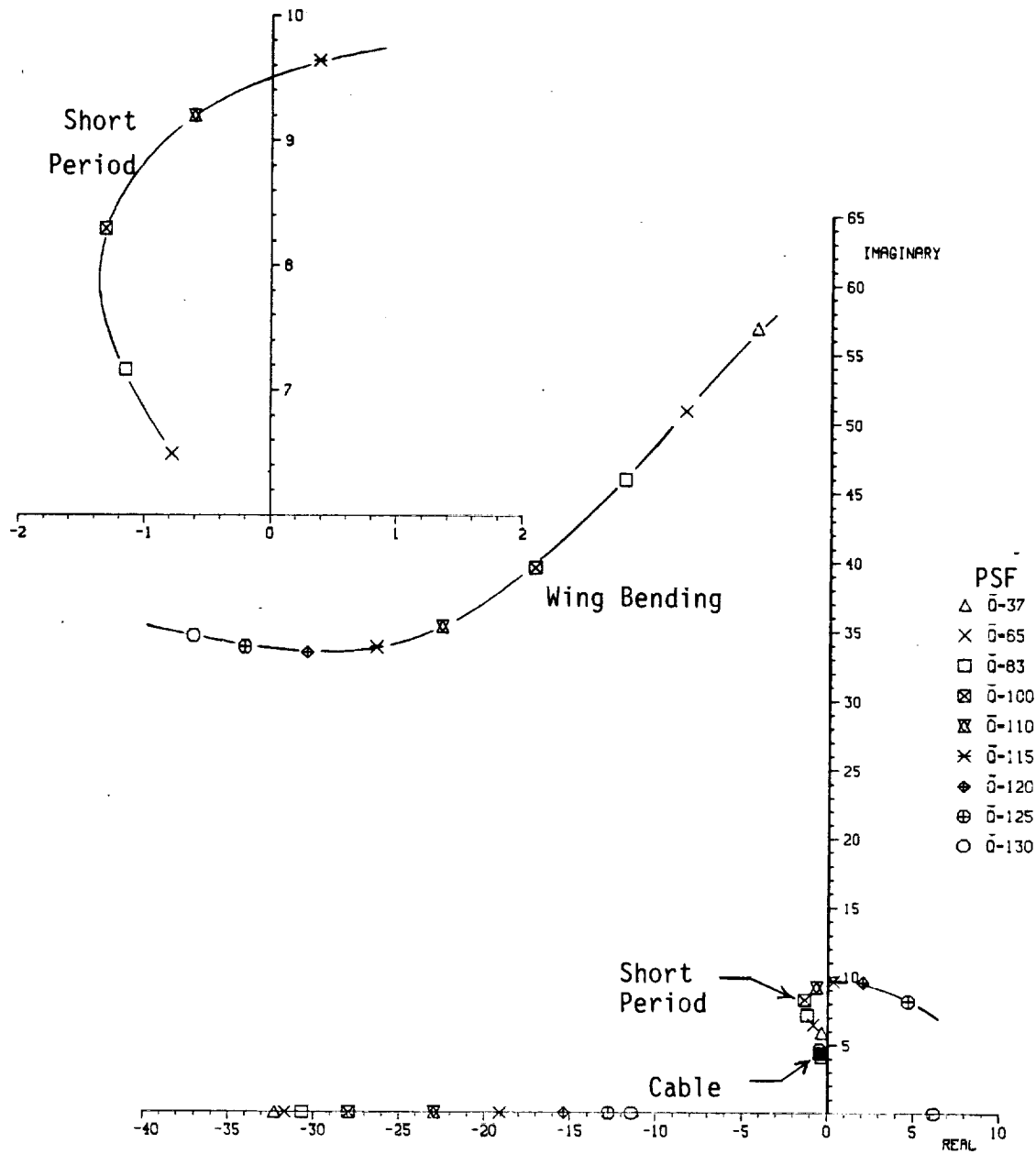
Figure 98. Final CABSAEL Analysis for CG213, Open Loop, M = 0.9.
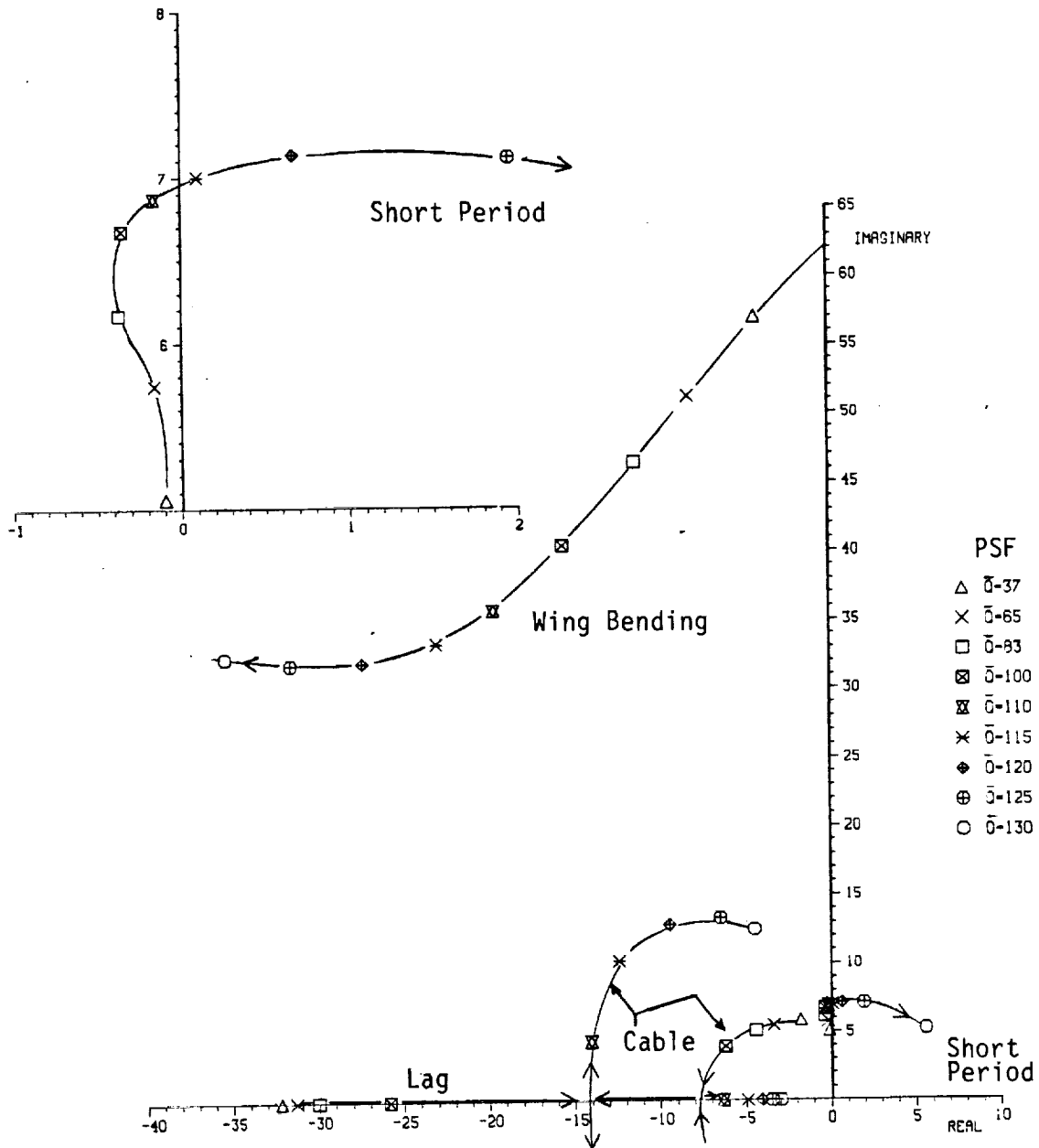
Figure 99. Final CABSAEL Analysis for CG231, C2-3, M = 0.9.

1/2 scale FSW CABSAEL C1-4 M=0.9
control law as tested
Q̄-matched aero corrections
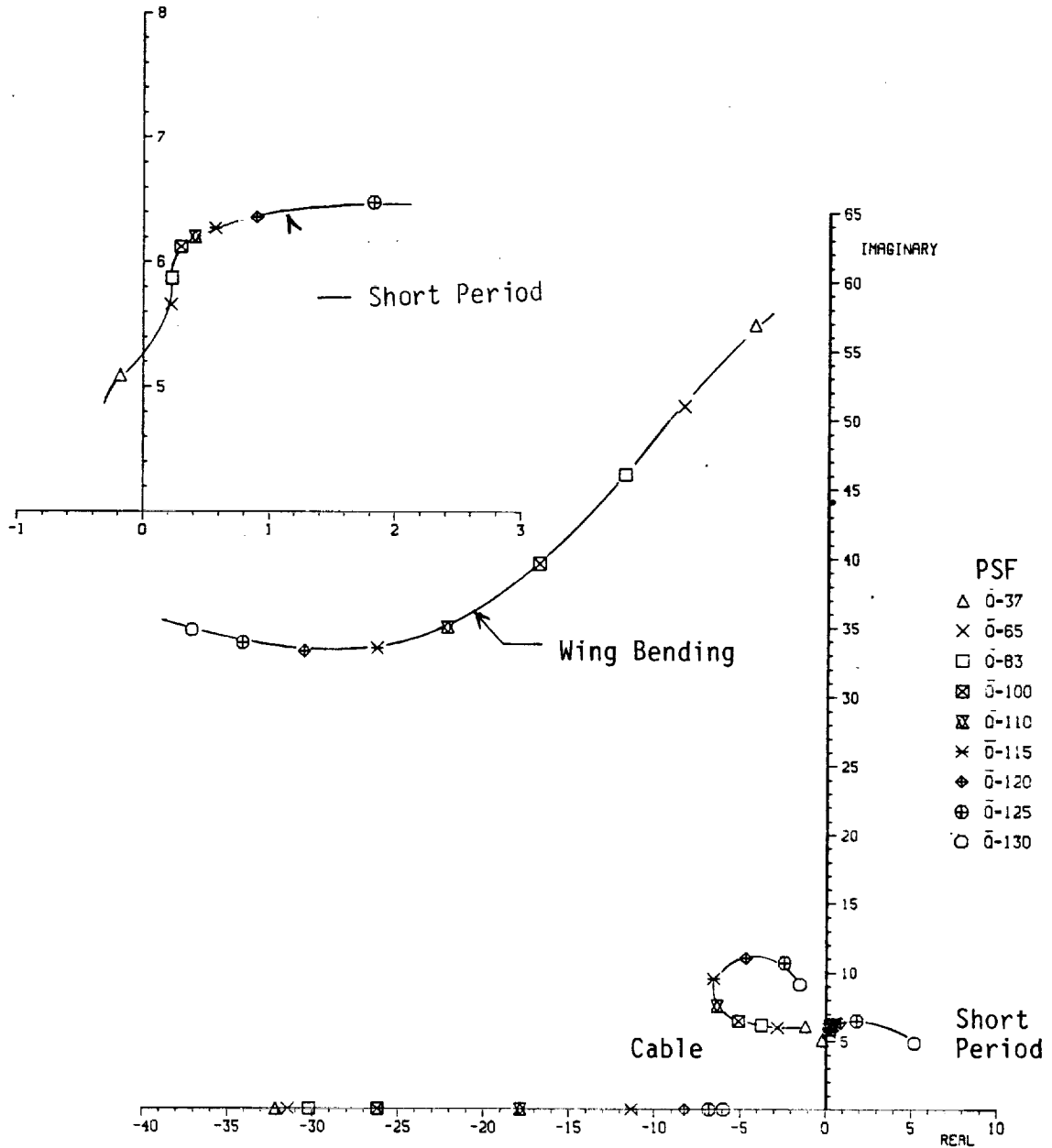
Figure 100. Final CABSAEL Analysis for CG225, C1-4, M = 0.9.

Final CABSAEL Analysis
cg 213 Open Loop

(a) CG213
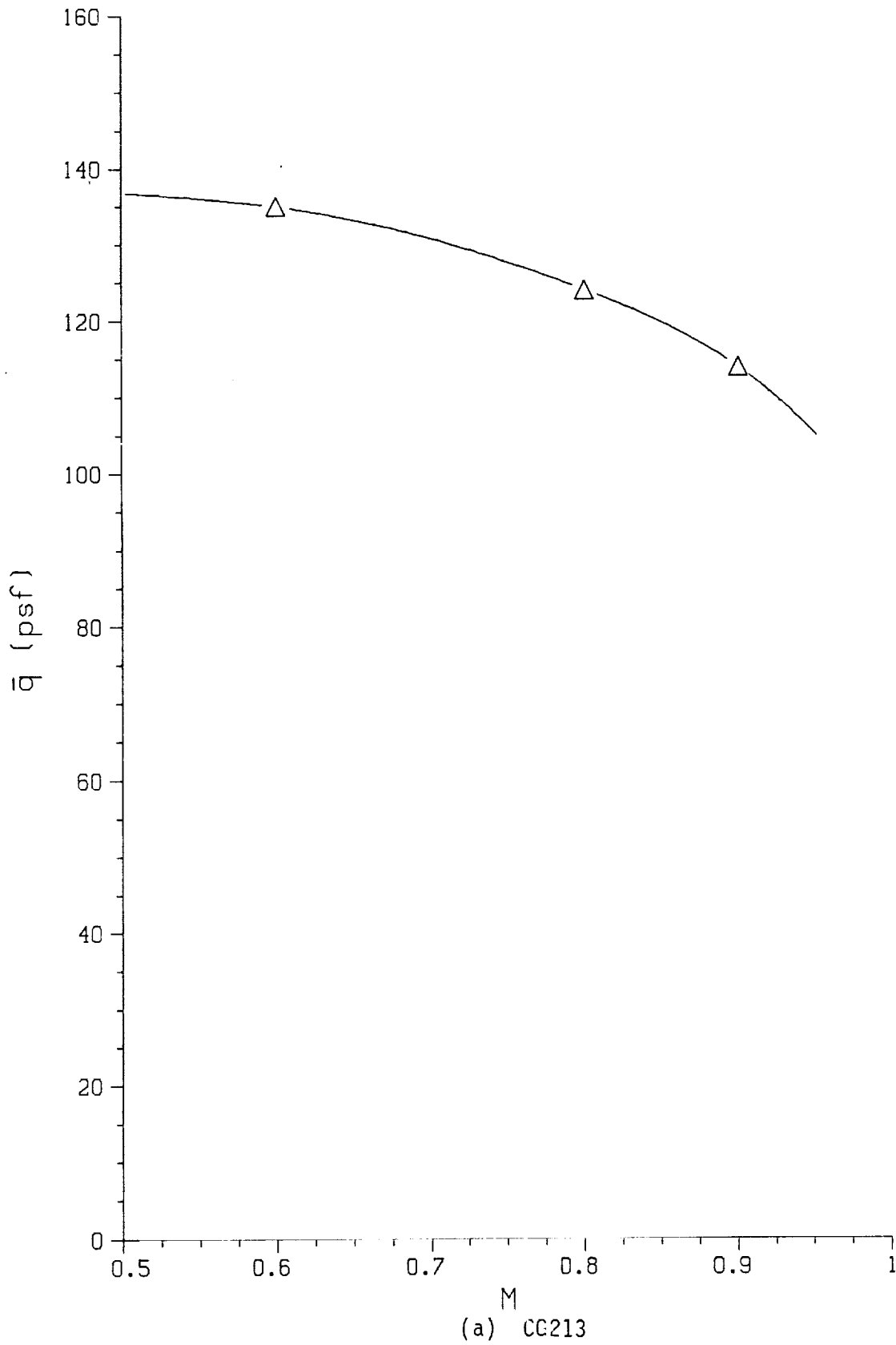
Figure 101. Analytical Flutter Boundaries.

Final CABSAEL Analysis
cg 225

Legend:
- △ C1-1
- + C1-2
- × C1-3
- ◇ C1-4
- ▽ C1-4A
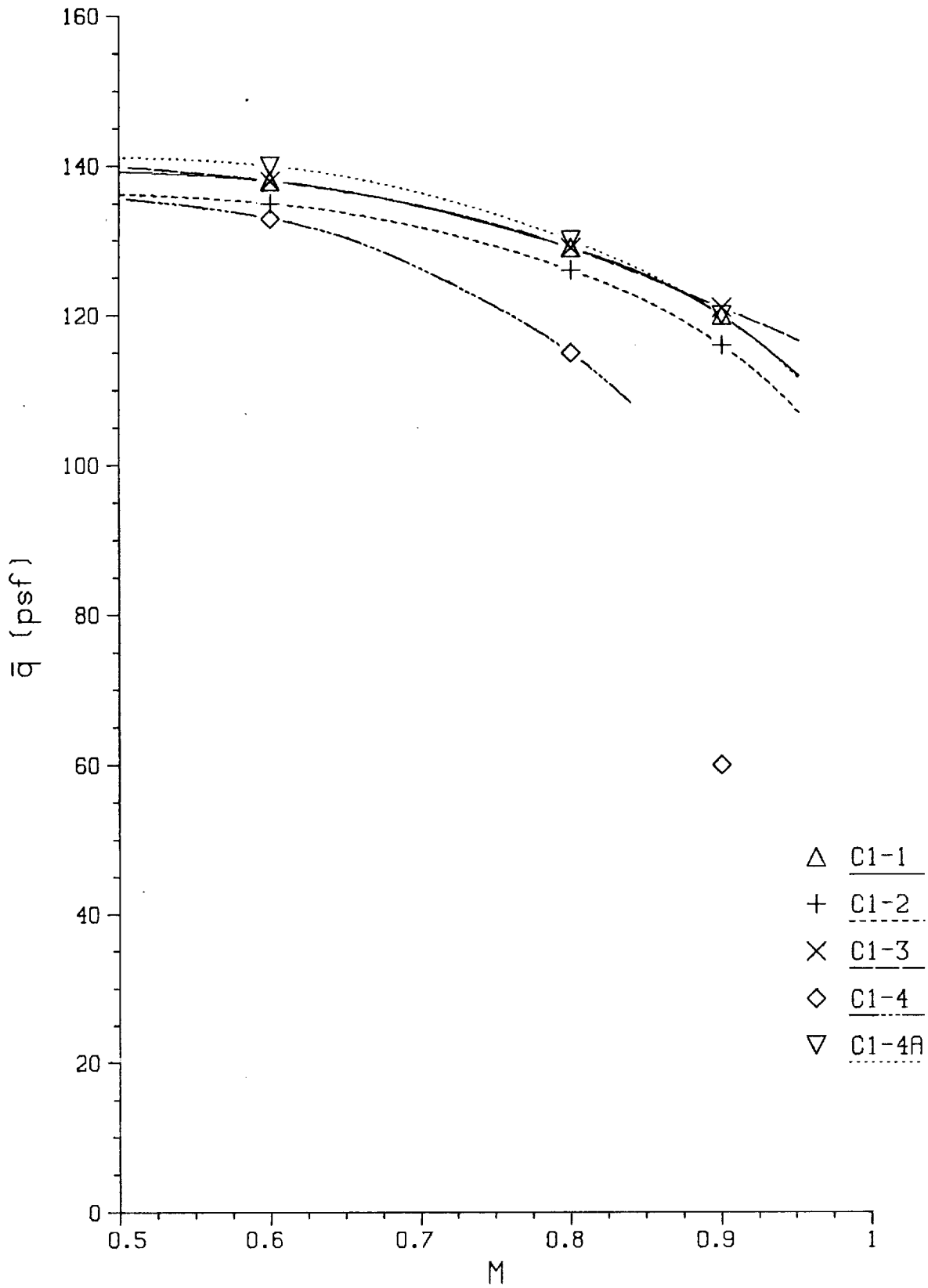
(b) CG225

Figure 101 Continued. Analytical Flutter Boundaries.

Final CABSAEL Analysis
cg 231
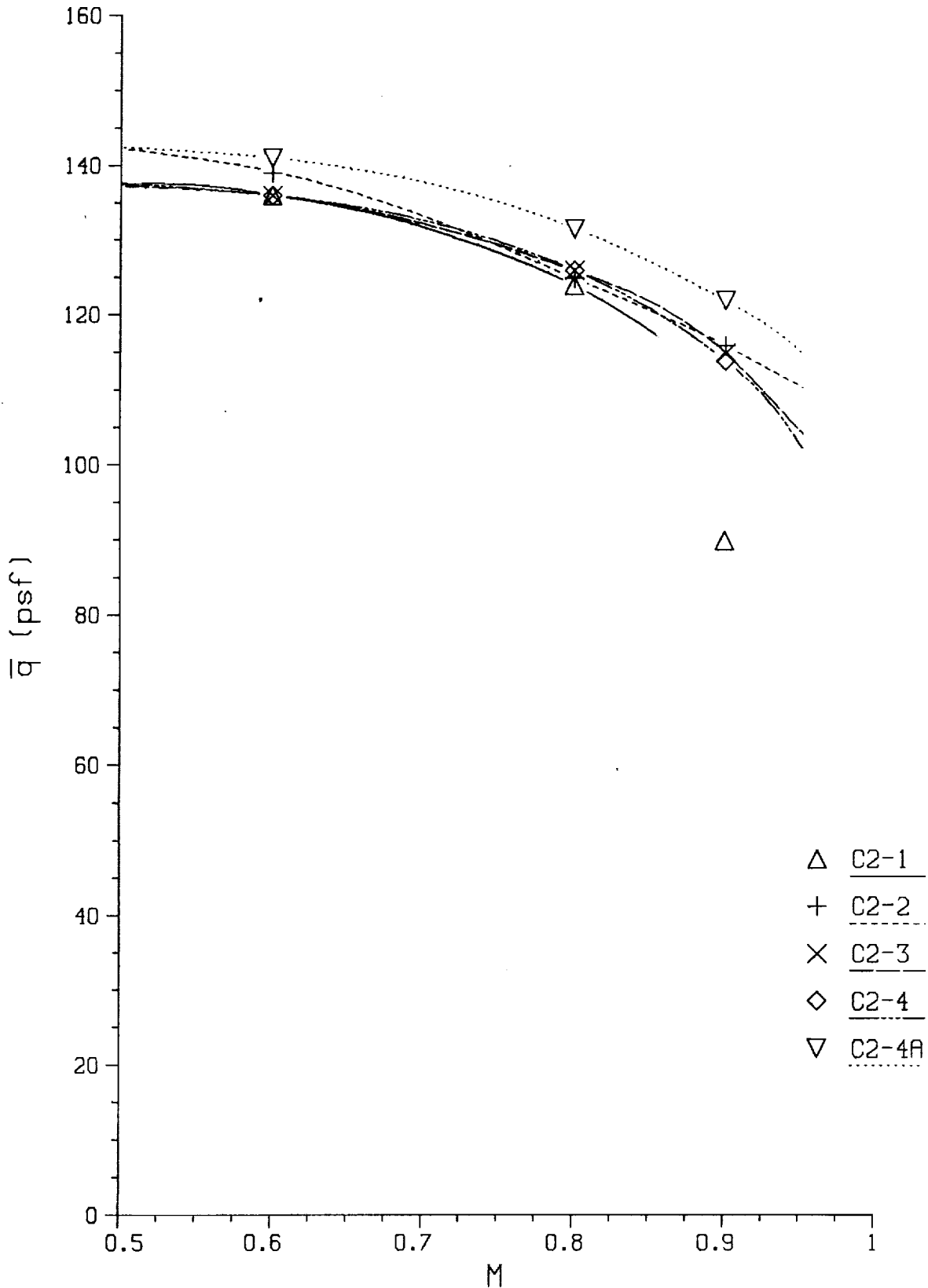
(c) CG231

Figure 101 Concluded. Analytical Flutter Boundaries.

Figure 102. Test/Analysis Correlation, CG213, Open Loop.

Test/Analysis Flutter Boundary Correlation
cg 225 C1-1
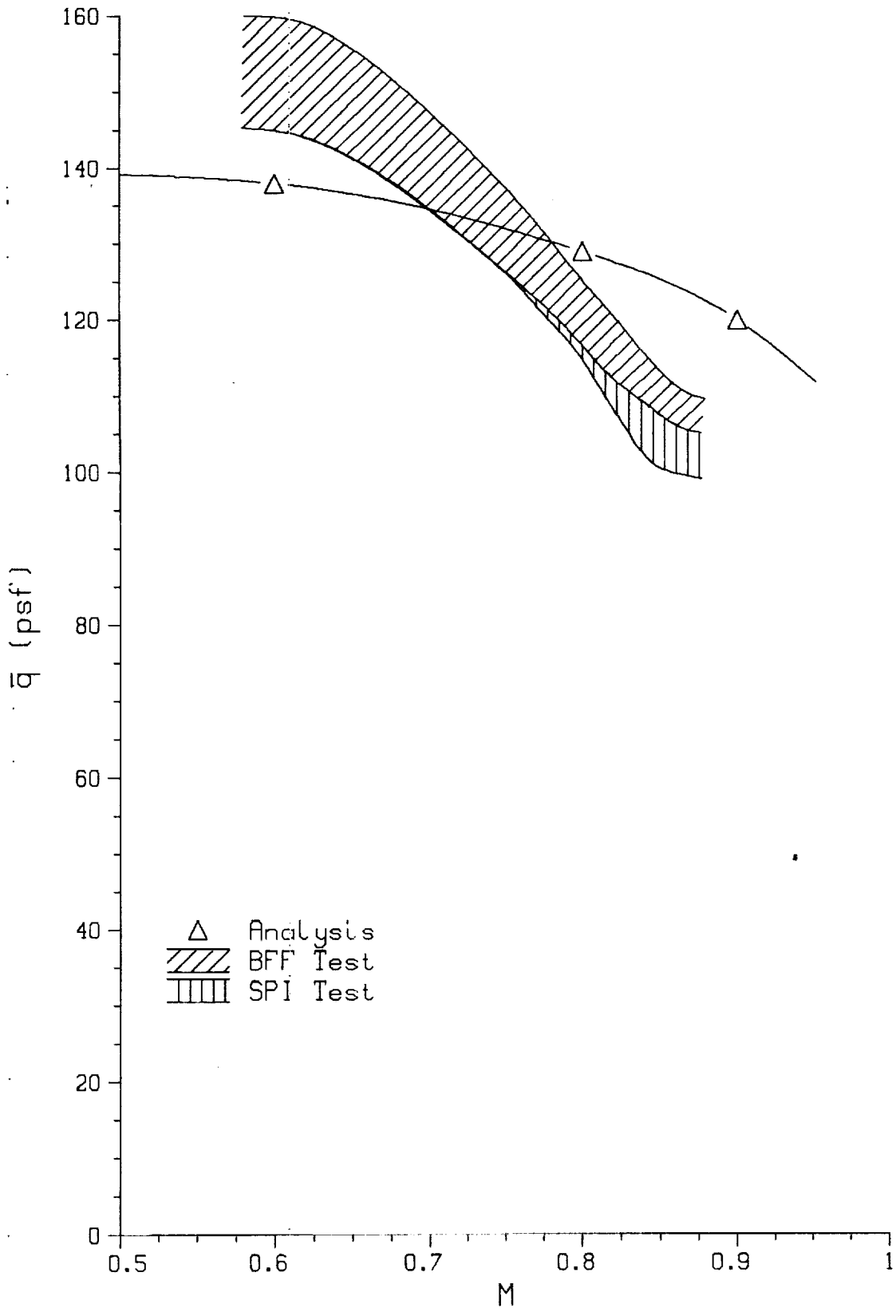
Figure 103.   Test/Analysis Correlation, CG225,C1-1.

Test/Analysis Flutter Boundary Correlation
cg 225 C1-3
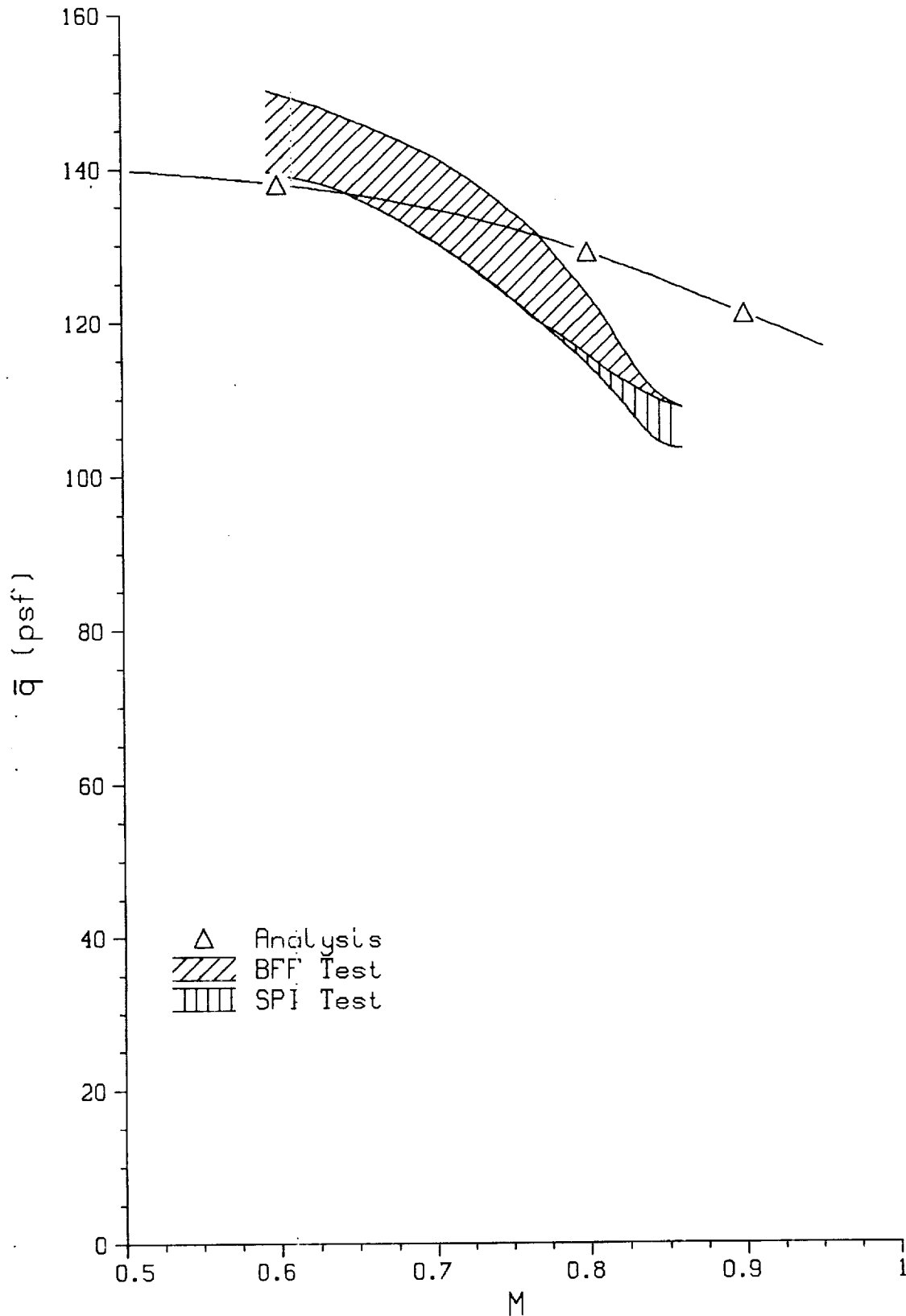
Figure 104. Test/Analysis Correlation, CG225, C1-3.

Figure 105. Test/Analysis Correlation, CG231, C2-3.
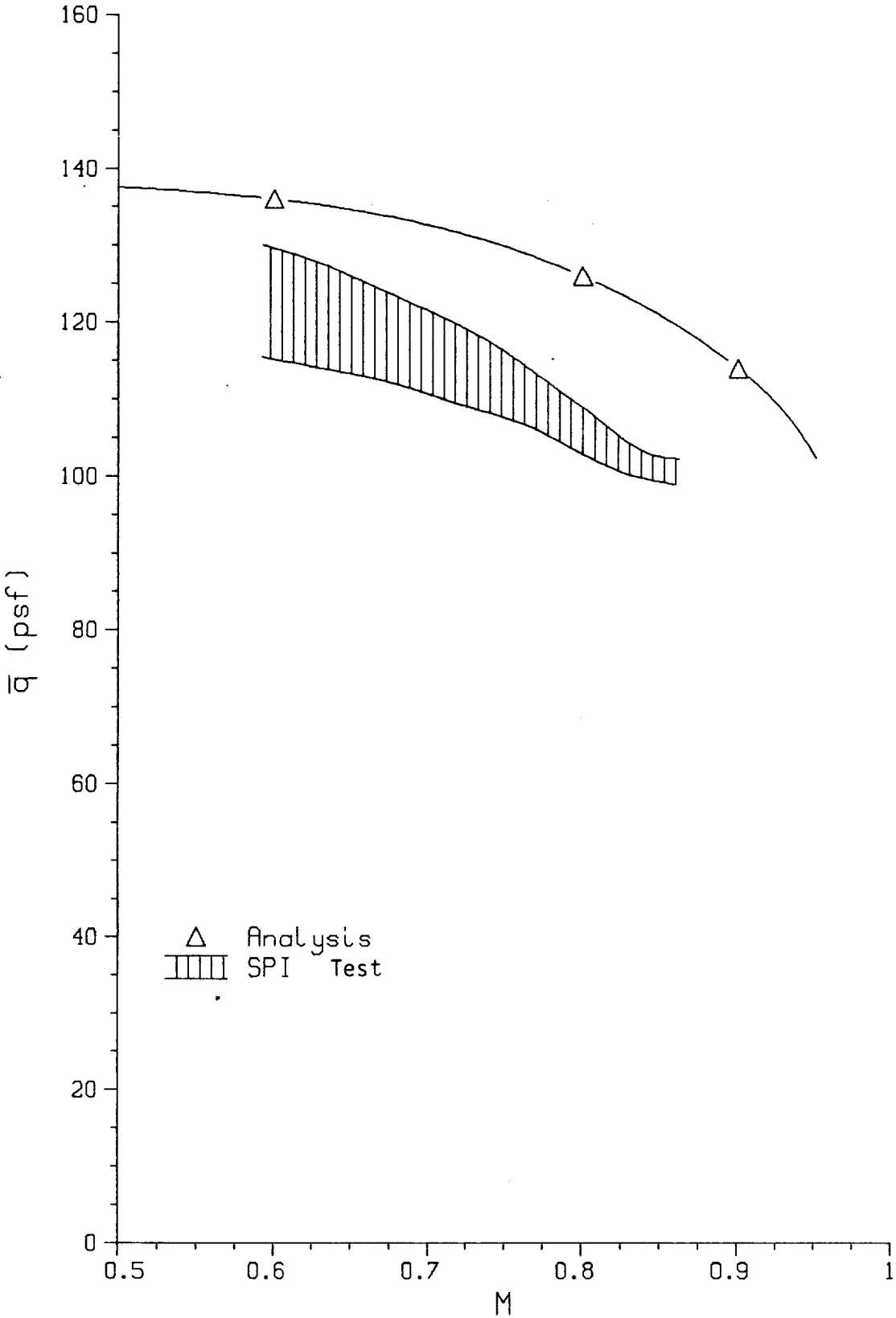
Figure 106. Test/Analysis Correlation, CG231, C2-4.

Test/Analysis Flutter Boundary Correlation
cg 231 C2-4A
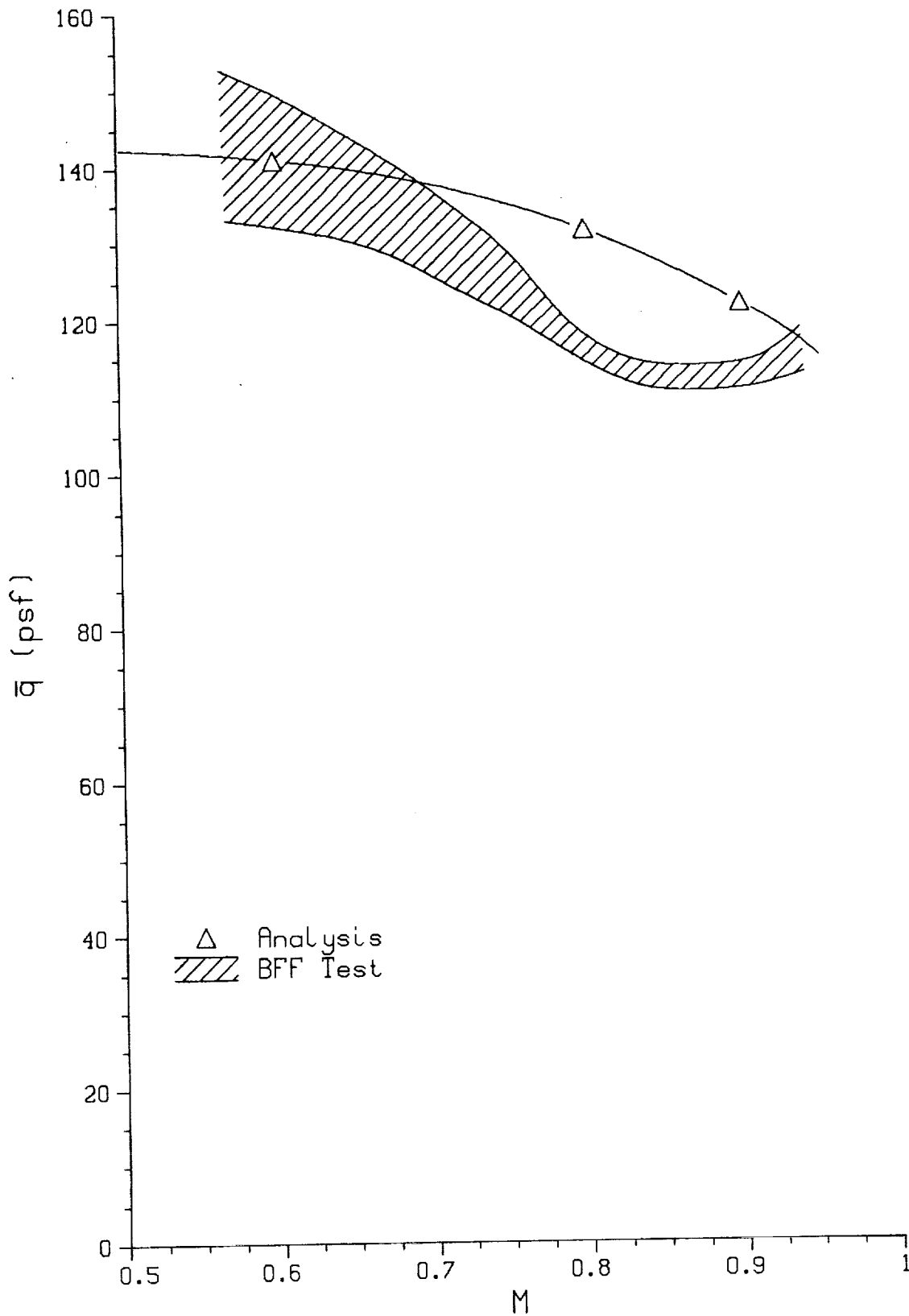
Figure 107. Test/Analysis Correlation, CG231, C2-4A.

Test/Analysis Flutter Boundary Correlation
cg 225 C1-2
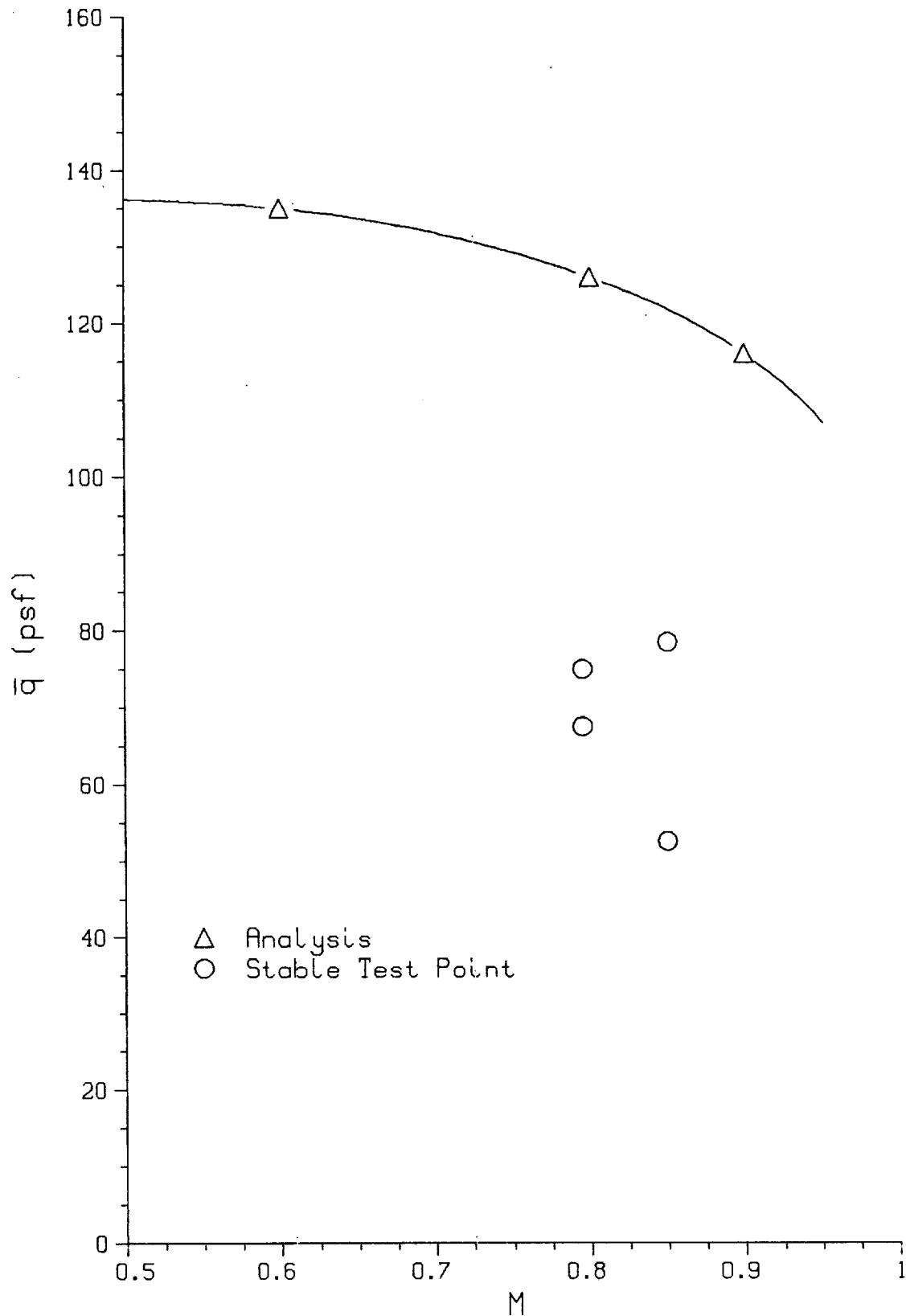
Figure 108. Test/Analysis Correlation, CG225, C1-2.
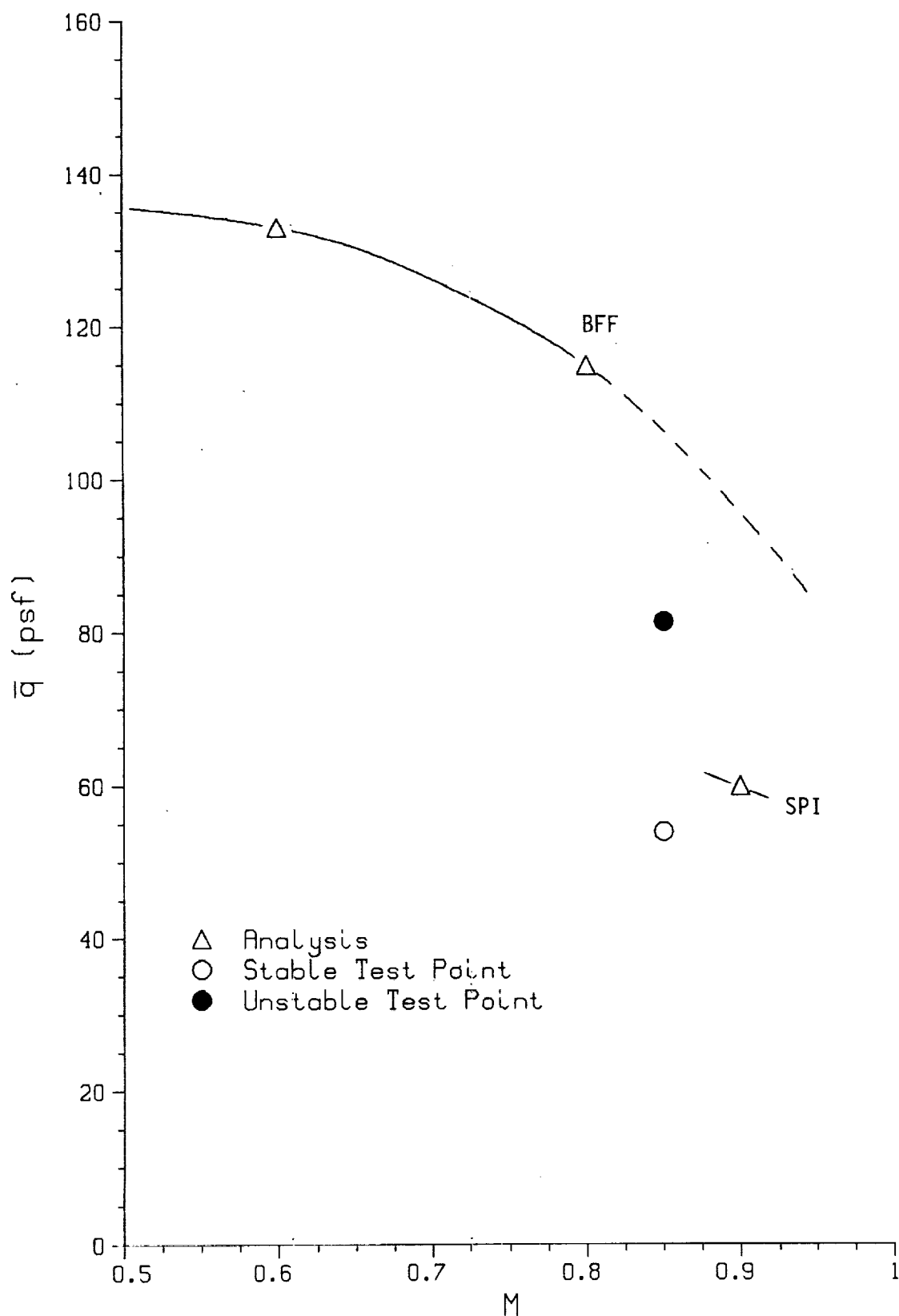
Figure 109. Test/Analysis Correlation, CG225,C1-4.

Test/Analysis Flutter Boundary Correlation cg 225 C1-4A
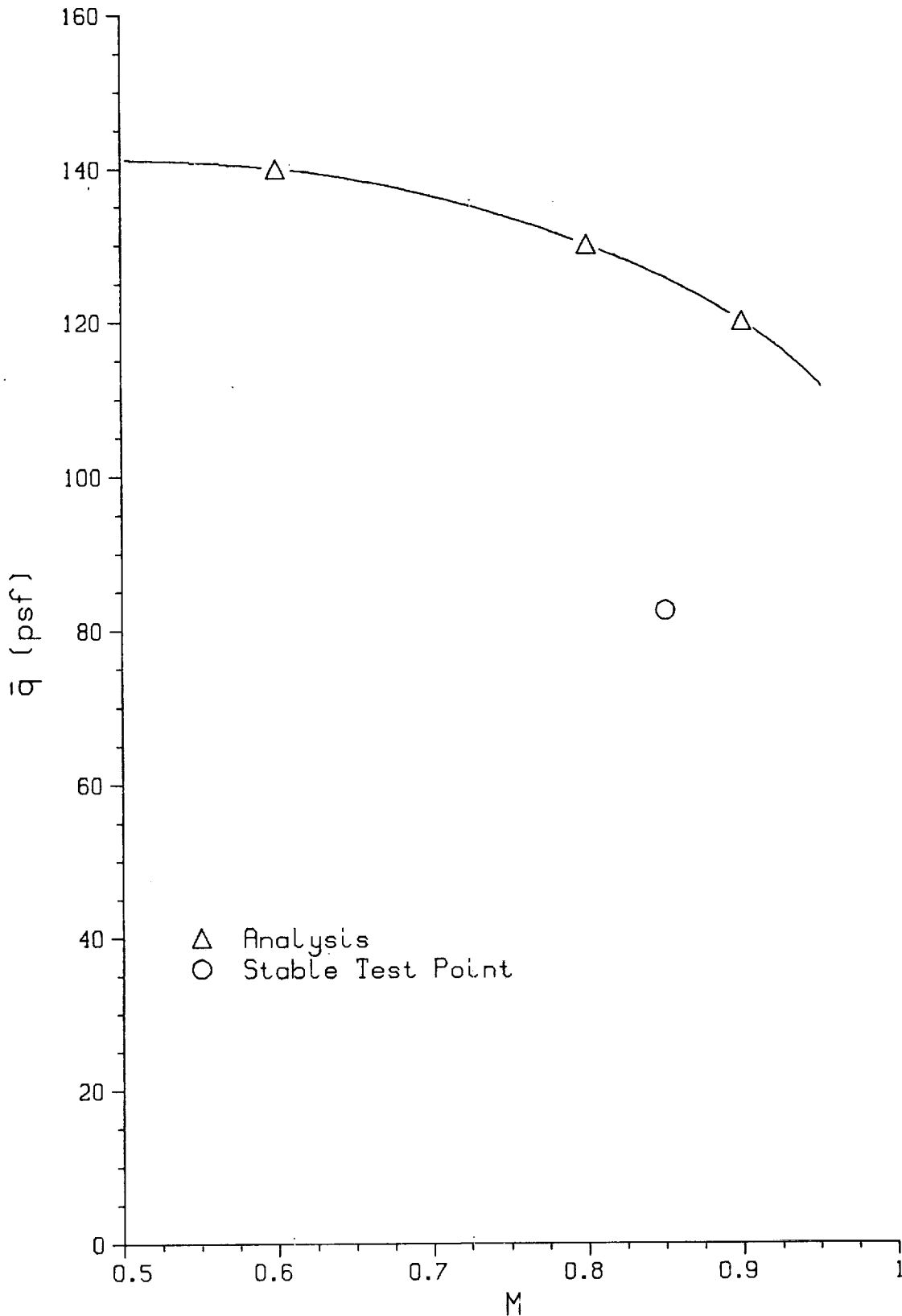
Figure 110. Test/Analysis Correlation, CG225,C1-4A.

Figure 111. Test/Analysis Correlation, CG231, C2-1.

Test/Analysis Flutter Boundary Correlation
cg231 C2-2
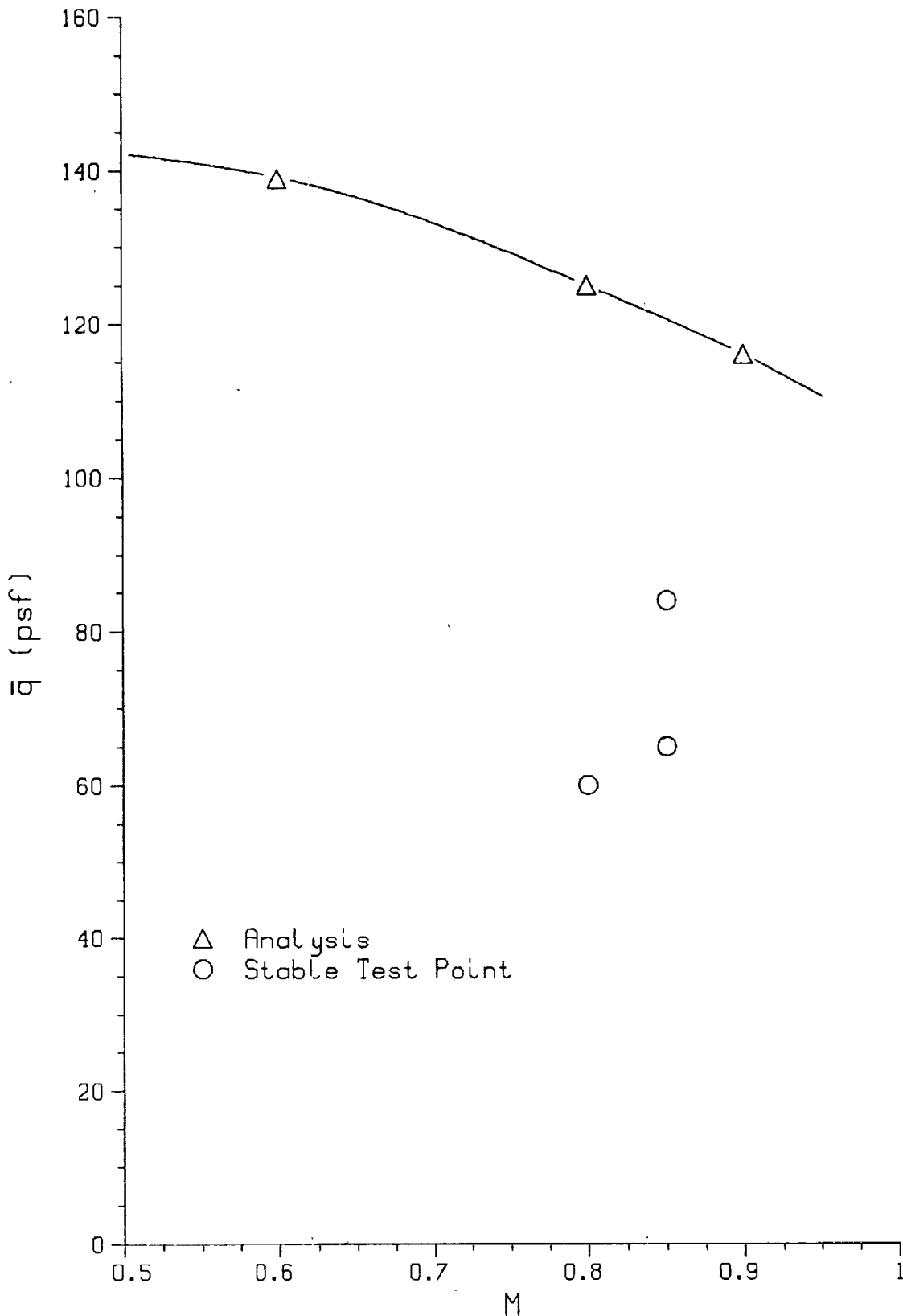
Figure 112. Test/Analysis Correlation, CG 231, C2-2.
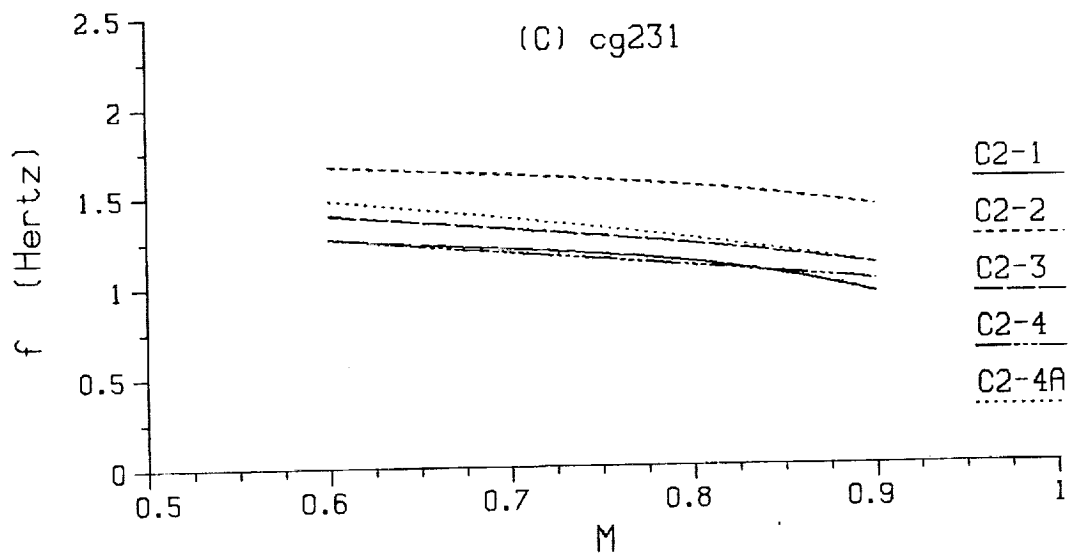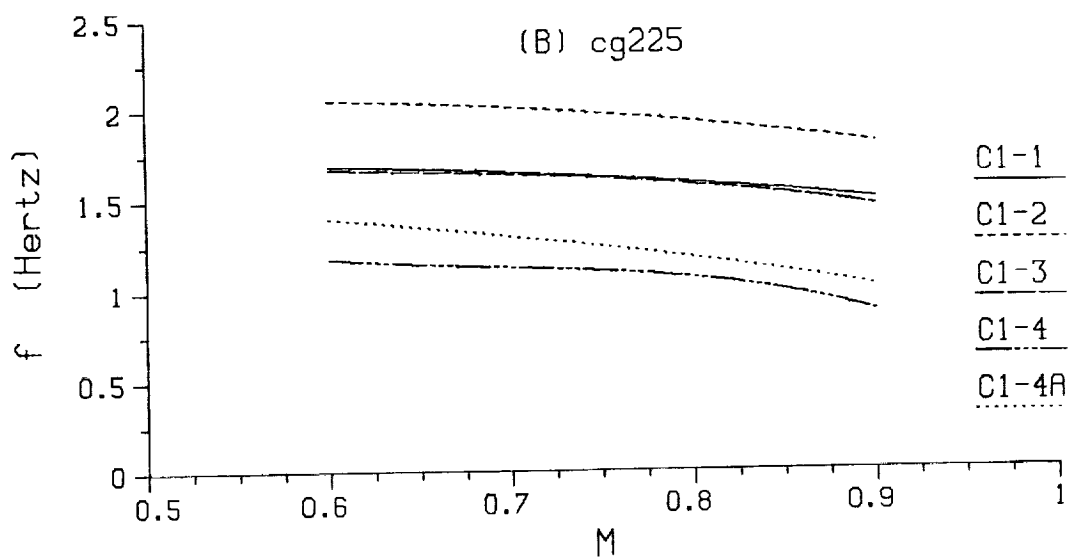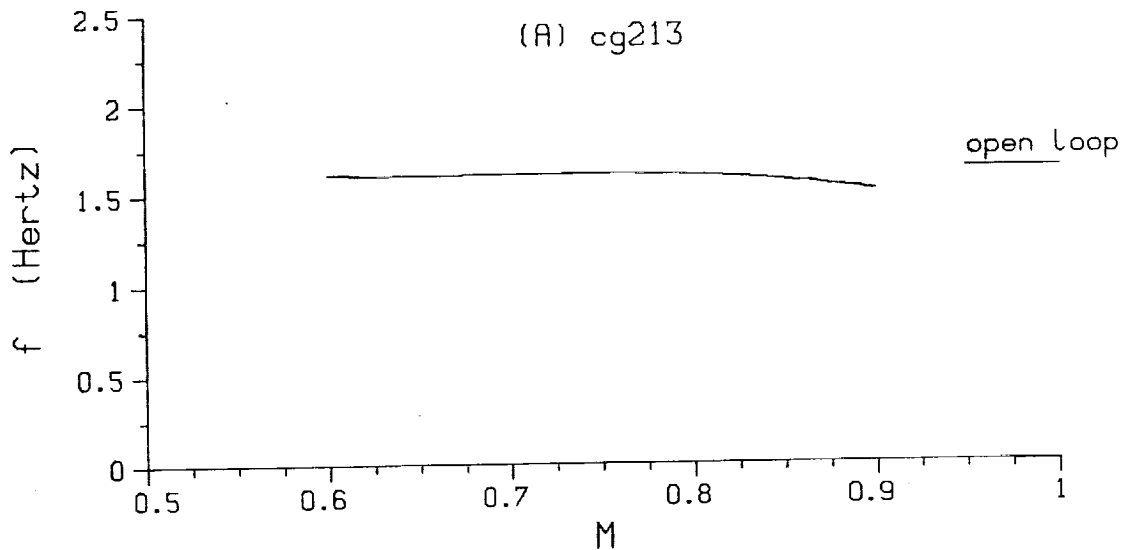
Figure 113. Analytical Instability Frequencies.

1/2 scale FSW   CABSAEL   C2-4A   M=0.9
a14 variation
15 times nominal
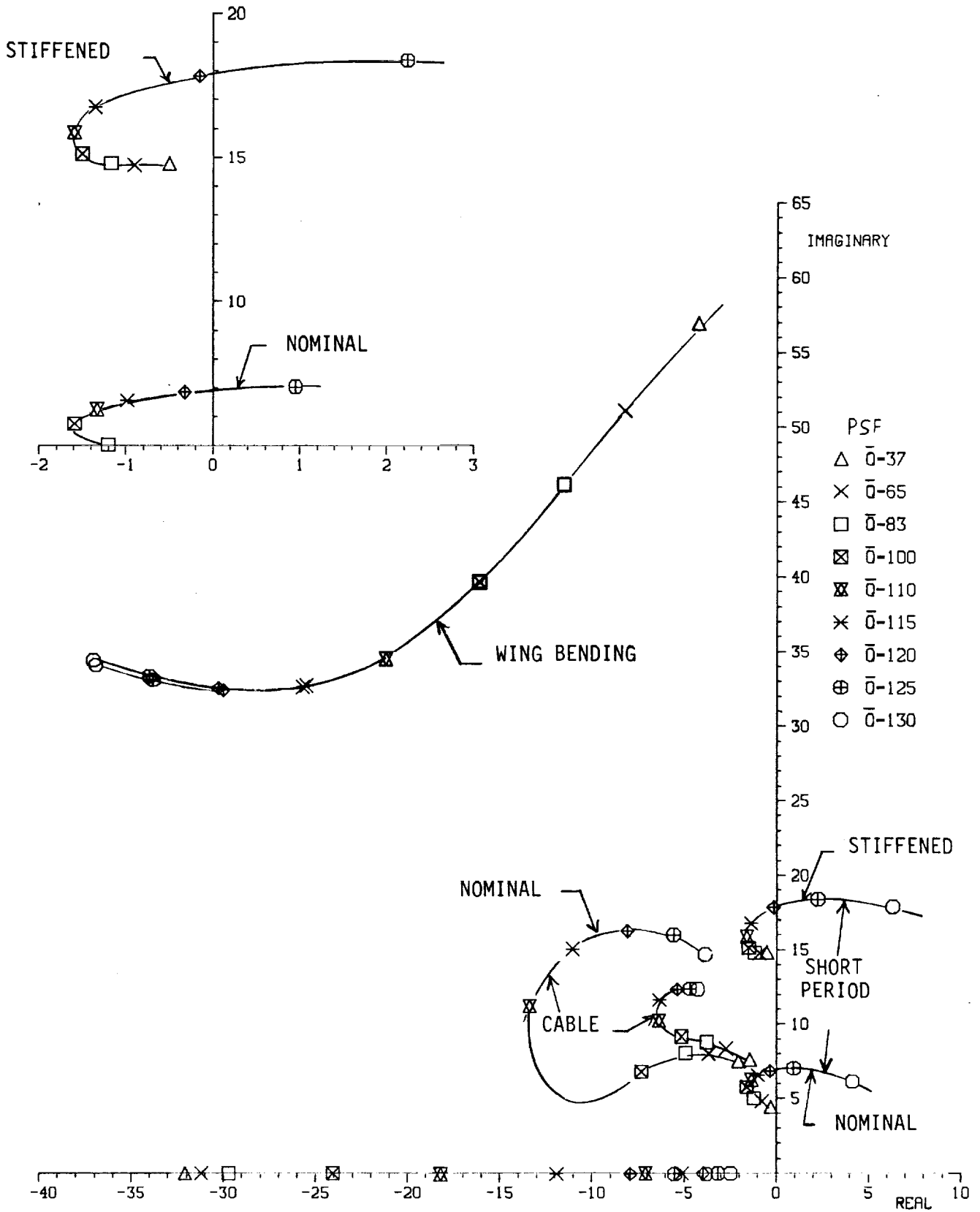
Figure 114.   Effect of Variation of Cable Spring Term a_{14}.
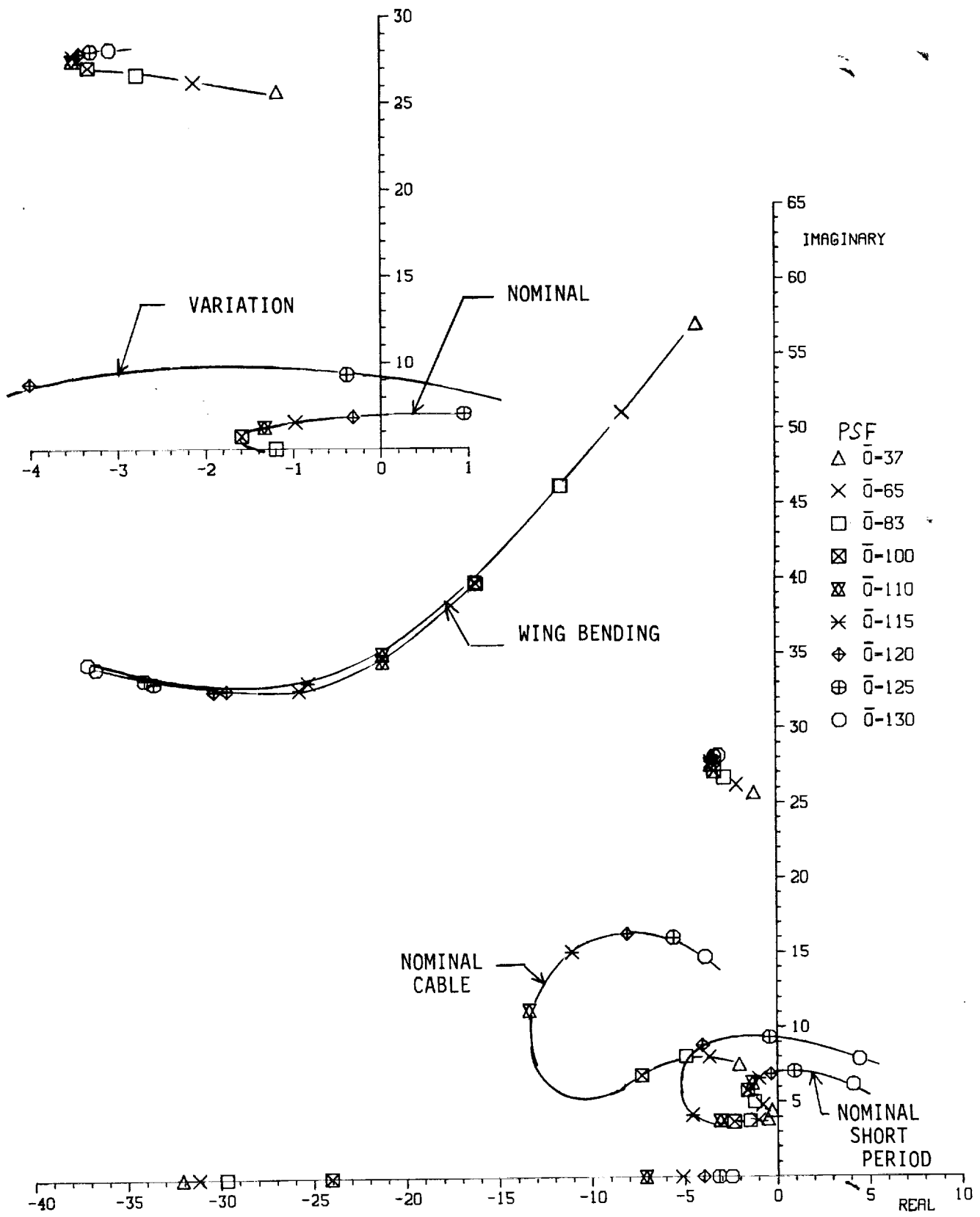
Figure 115. Effect of Variation of Cable Spring Term a_{25}.

Figure 116. Effect of Simulated Snubber Cable Spring.
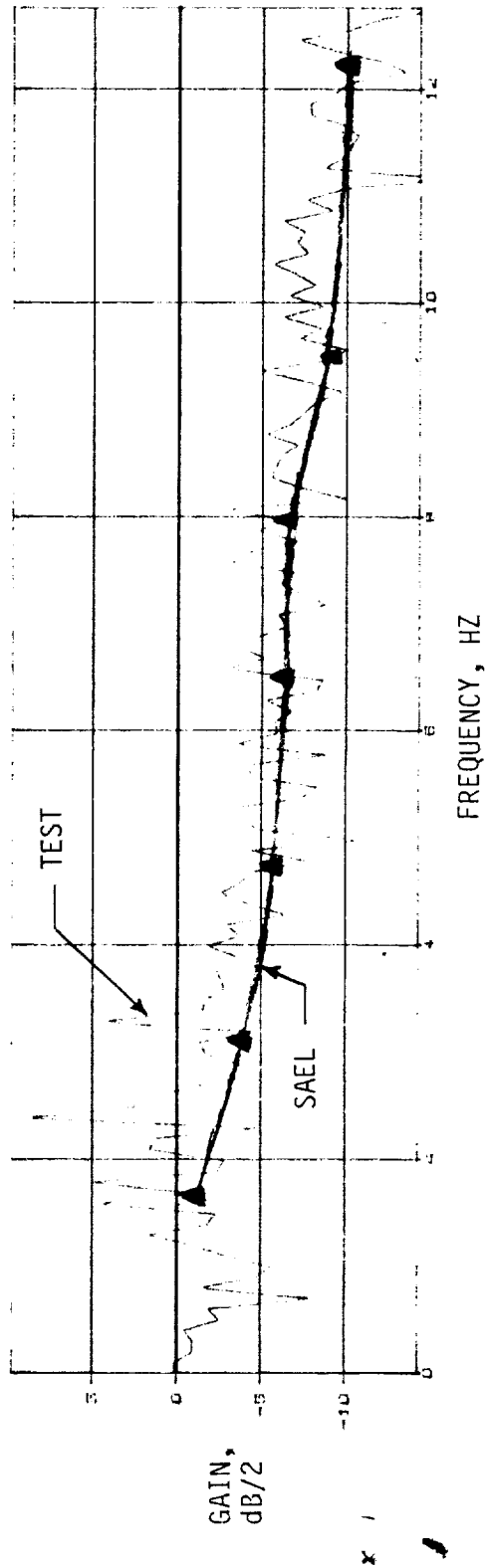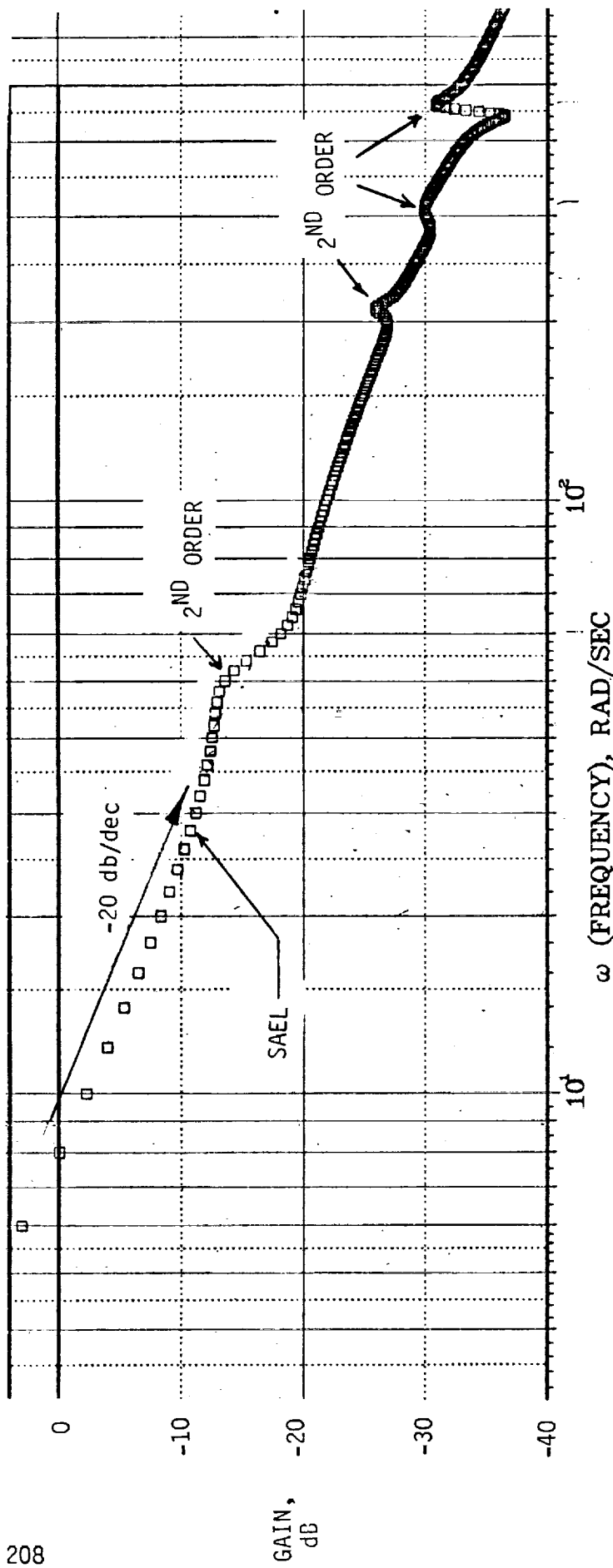
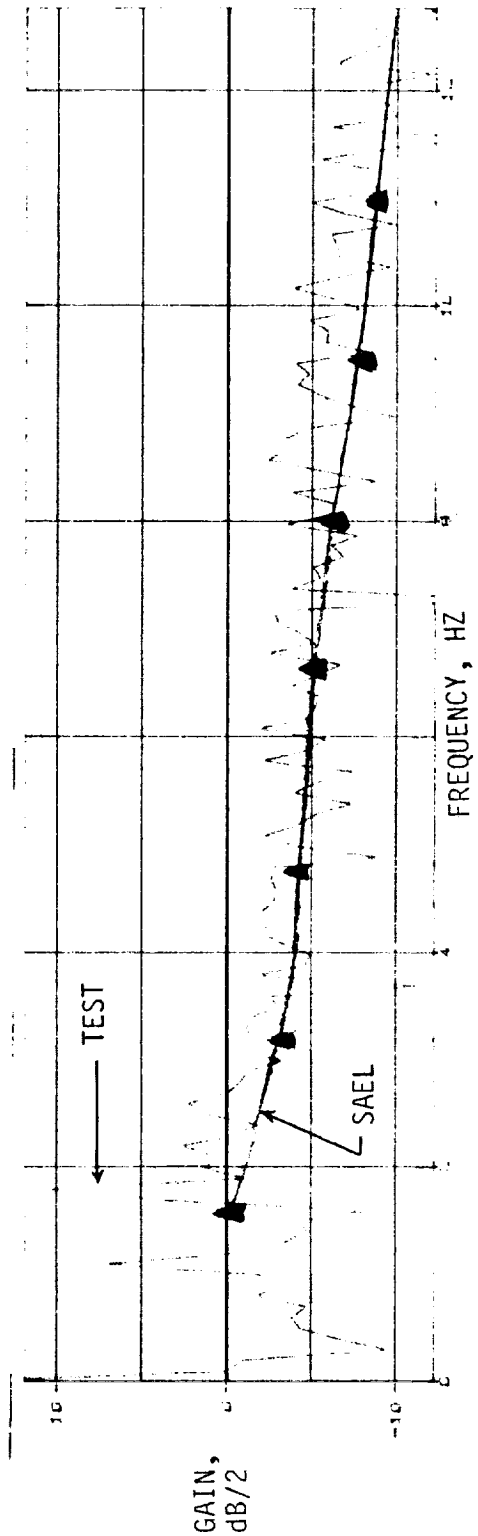Figure 117. Comparison Of Measured And SAEL Bode Plots : CG 225, C1-1, M = 0.80, $\overline{Q}$ = 65 psf.
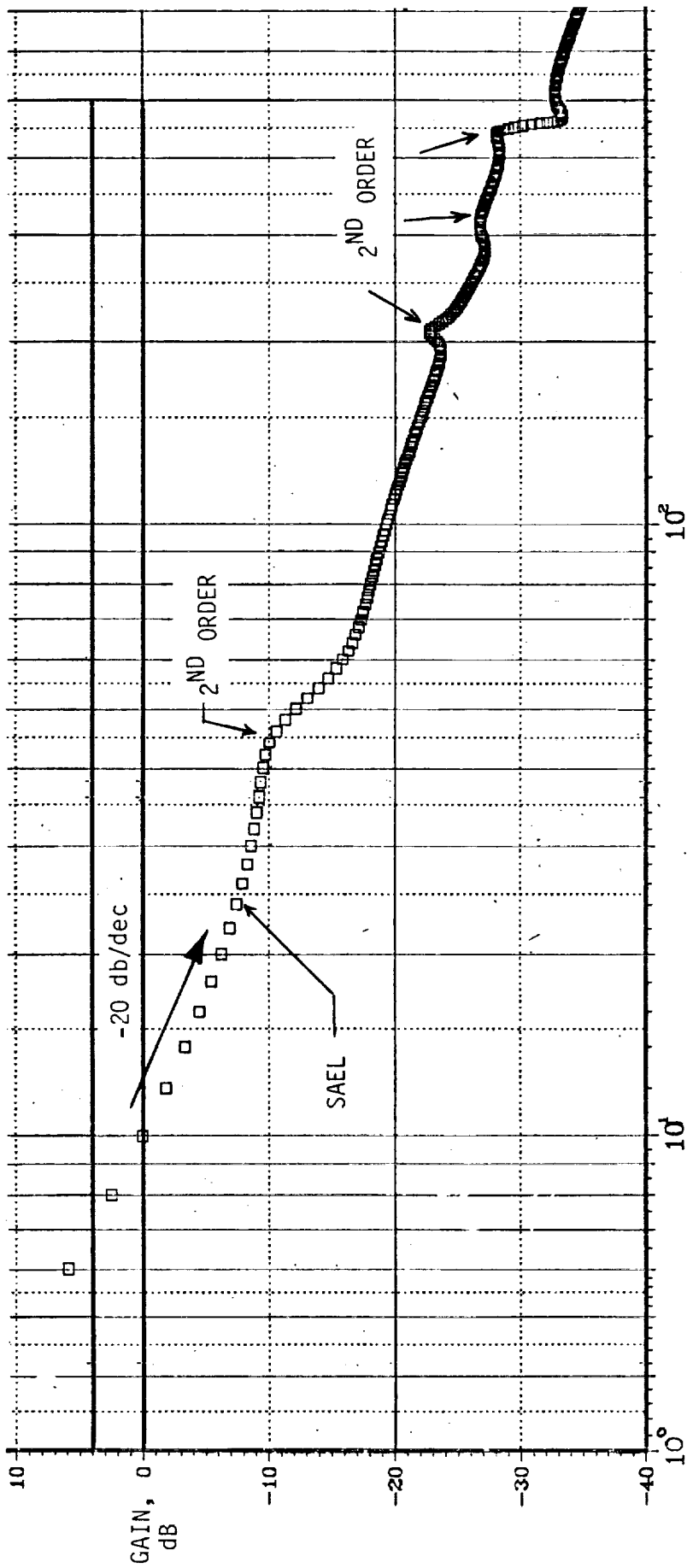
208

Figure 118. Comparison Of Measured And SAEL Bode Plots : CG 225, C1-1, M = 0.80, $\bar{Q}$ = 85 psf.

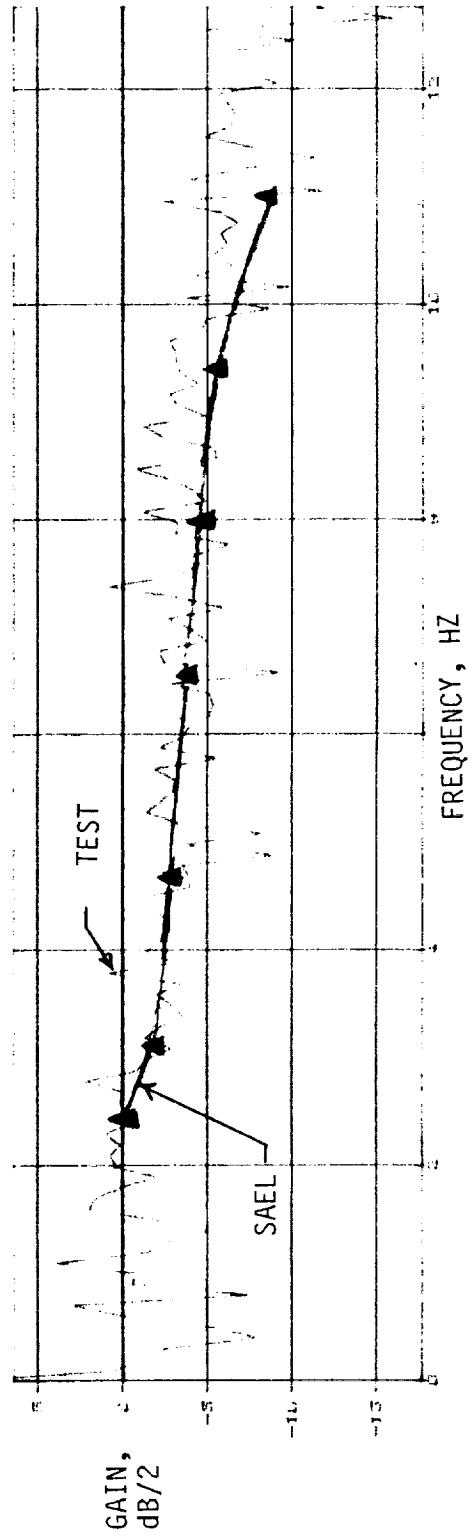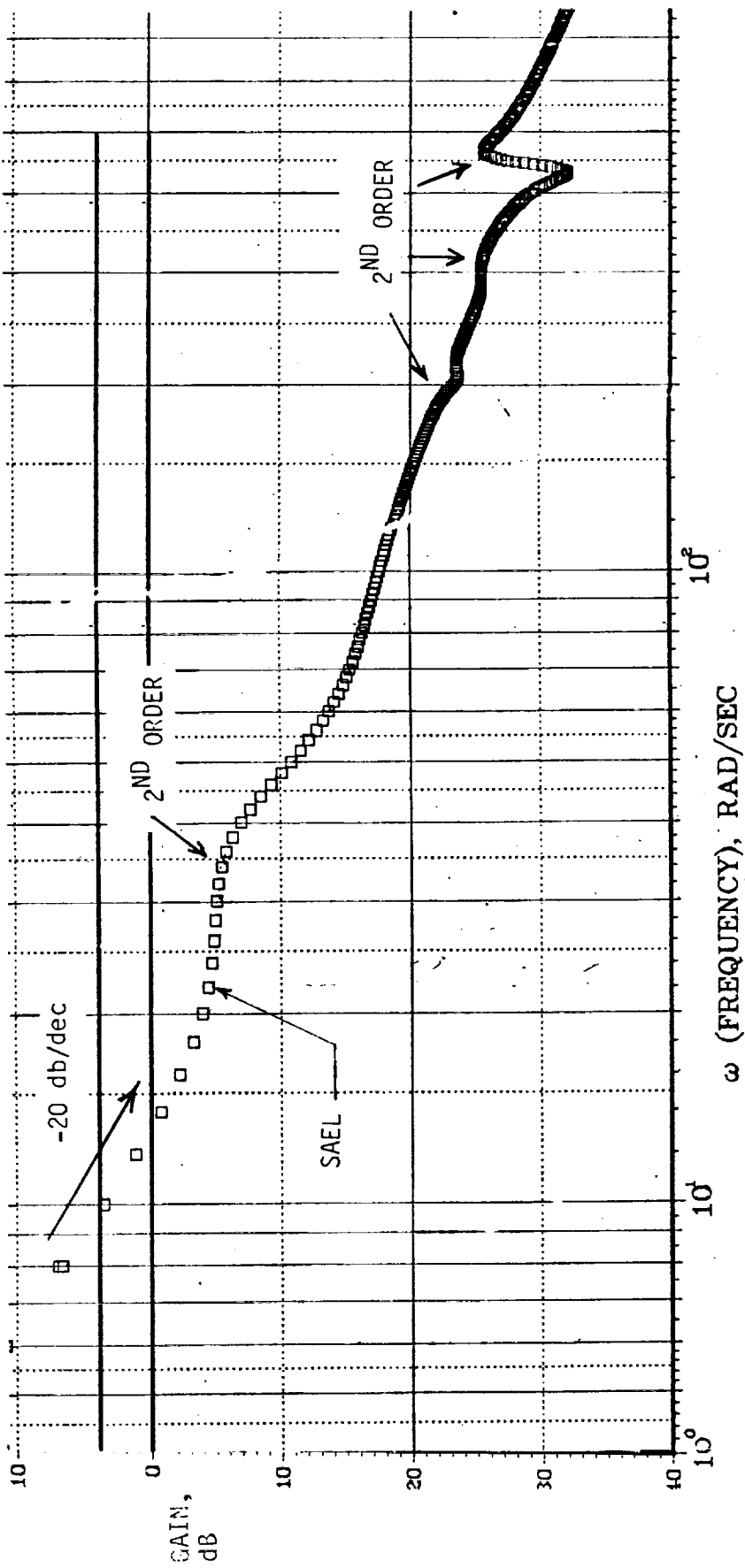Figure 119. Comparison Of Measured And SAEL Bode Plots CG 225, C1-1, M = 0.80, $\bar{Q}$ = 110 psf.

APPENDIX A

GVT FLUTTER MODEL RESULTS

This appendix presents the data obtained in the ground vibration testing of the model. As discussed in Section 6.2.4, the model was suspended by the roll-rod assembly and lift cable for the test. Ballast was added such that the fuselage reference line was level with ground. Figure A1 is comprised of a sketch and table that show the locations of the grid points at which modal displacements were measured. The origin of the axis system implicit in the tabulated coordinates is shown in the sketch to be the intersection of the wing trailing edge (projected) with the model center line. Figure A2 shows plots of the four measured flexible wing modes. Also the frequency and structural damping of each mode are given. Figure A3 is a matrix tabulating the modal displacements. The rows correspond to the nodes given in Figure A-1. Columns 3 to 6 correspond to the four flexible wing modes plotted in Figure A2. Note that the deflections on the fuselage and canard are zero for these modes, indicating that no appreciable motion was measured on them while the wing was being excited. Columns 1, 2, and 7 are the rigid heave, pitch (about CG 213) and canard rotation modes. The modal displacements in pitch equal the fore-aft distances between the nodes and the pitch axis (CG). Similarly, the modal displacements in the canard-rotation mode equal the fore-aft distances between the nodes and the canard pivot axis (which was unswept, that is parallel to the model fuselage
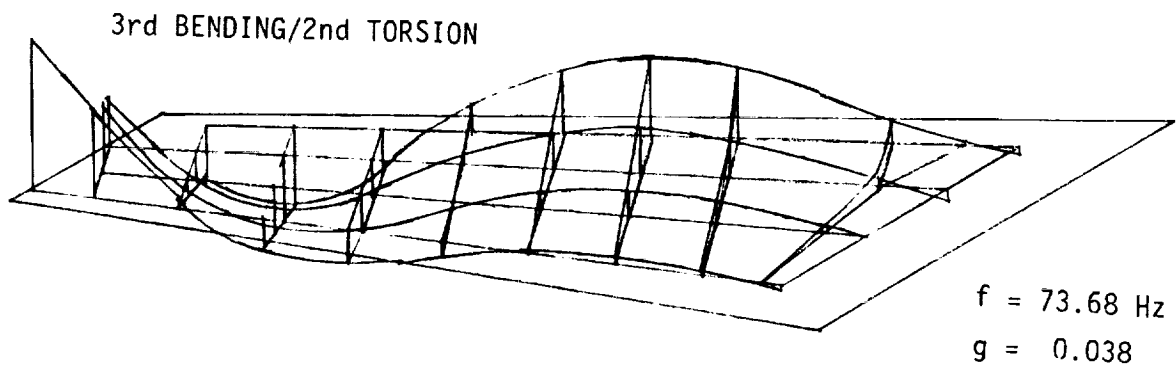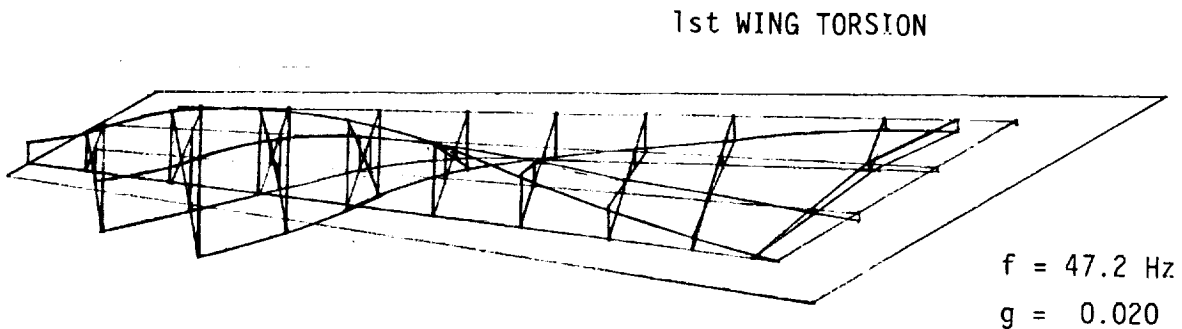
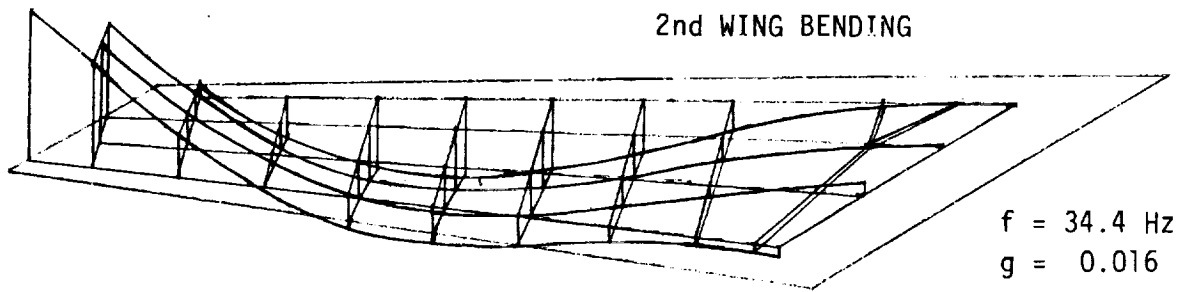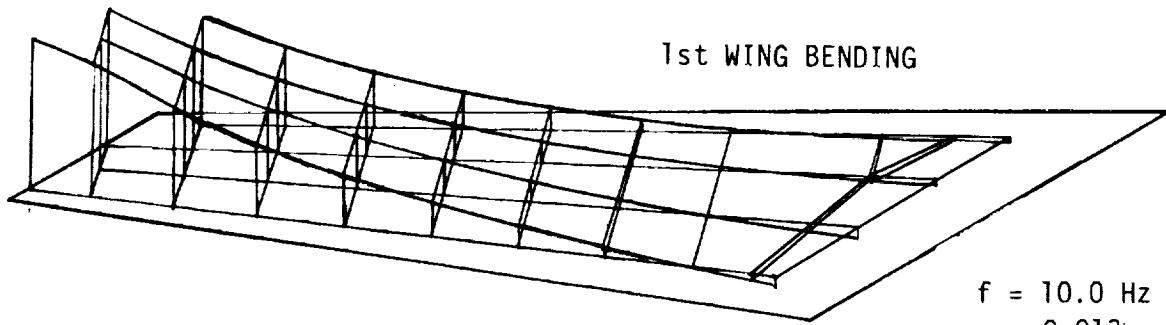stations). The zero displacements on the wing and fuselage indicate that only the canard rotates in this mode. Figure A4 presents a matrix tabulating the generalized weights in the seven afore-mentioned modes. The matrix has been diagonalized (i.e., minute amounts of coupling calculated from the measured data have been neglected) with the exception of the mass coupling between canard-rotation, and model heave and pitch.
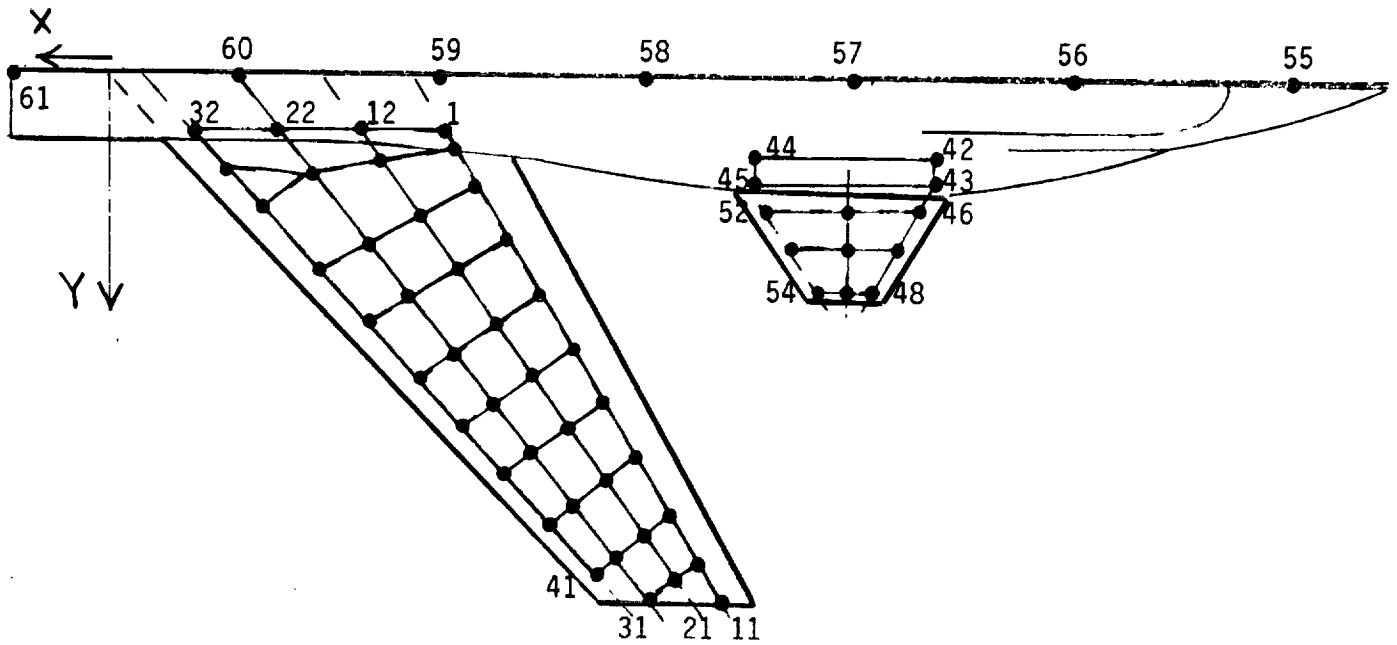
Coordinates of Grid Points

Node No.	X	Y	Node No.	X	Y
1	-55.91	8.50	32	-15.0	8.5
2	-57.61	11.30	33	-19.84	13.75
3	-61.02	16.91	34	-25.67	20.08
4	-66.12	25.31	35	-37.33	32.72
5	-71.22	33.72	36	-44.07	40.03
6	-76.33	42.13	37	-50.81	47.34
7	-81.43	50.53	38	-57.55	54.65
8	-86.54	58.94	39	-64.29	61.96
9	-91.65	67.35	40	-71.03	69.27
10	-96.75	75.75	41	-77.77	76.58
11	-100.30	81.60	42	-132.62	12.625
12	-43.84	8.50	43	-133.62	15.625
13	-47.15	13.23	44	-102.62	12.625
14	-53.90	22.87	45	-102.62	15.625
15	-59.50	30.86	46	-131.93	18.5
16	-65.10	38.86	47	-126.08	25.43
17	-70.70	46.85	48	-119.69	33.0
18	-76.29	54.84	49	-117.40	18.5
19	-81.89	62.83	50	-115.94	25.43
20	-87.49	70.83	51	-114.33	33.0
21	-93.08	78.82	52	-102.13	18.5
22	-30.42	8.50	53	-105.27	25.43
23	-35.72	15.09	54	-108.70	33.0
24	-46.31	28.27	55	-183.065	0.0
25	-52.44	35.89	56	-149.315	0.0
26	-58.56	43.51	57	-117.615	0.0
27	-64.69	51.13	58	-82.815	0.0
28	-70.81	58.75	59	-52.045	0.0
29	-76.93	66.36	60	-19.315	0.0
30	-83.05	73.98	61	+14.685	0.0
31	-89.18	81.60			

213

MODE SHAPES

1st WING BENDING

f = 10.0 Hz
g = 0.013

2nd WING BENDING

f = 34.4 Hz
g = 0.016

1st WING TORSION

f = 47.2 Hz
g = 0.020

3rd BENDING/2nd TORSION

f = 73.68 Hz
g = 0.038

MODAL DISPLACEMENTS

NODE NO.	HEAVE (1)	PITCH (2)	WING MODE 1 (3)	WING MODE 2 (4)	WING MODE 3 (5)	WING MODE 4 (6)	CANARD ROTATION (7)

(Large numerical table of modal displacement values for nodes 1–50; individual values not legibly reproducible.)

Bottom rows of the CANARD ROTATION column:

-7.192785E+00
-7.055549E-01
-1.724930E-01
1.758179E-02
1.395777E-01

MODAL DISPLACEMENTS CONTINUED

NODE NO.	HEAVE 1	PITCH 2	WING MODE 1 3	WING MODE 2 4	WING MODE 3 5	WING MODE 4 6	CANARD ROTATION 7
51	1.0000000E+00	-1.876256E+00	0.0	0.0	0.0	0.0	2.736564E-01
52	1.0000000E+00	-8.591320E-01	0.0	0.0	0.0	0.0	1.290781E+00
53	1.0000000E+00	-1.120788E+00	0.0	0.0	0.0	0.0	1.029124E+00
54	1.0000000E+00	-1.406943E+00	0.0	0.0	0.0	0.0	7.429692E-01
55	1.0000000E+00	-7.603860E+00	0.0	0.0	0.0	0.0	0.0
56	1.0000000E+00	-4.791473E+00	0.0	0.0	0.0	0.0	0.0
57	1.0000000E+00	-2.149916E-01	0.0	0.0	0.0	0.0	0.0
58	1.0000000E+00	7.499696E-01	0.0	0.0	0.0	0.0	0.0
59	1.0000000E+00	3.314033E+00	0.0	0.0	0.0	0.0	0.0
60	1.0000000E+00	6.041423E+00	0.0	0.0	0.0	0.0	0.0
61	1.0000000E+00	8.874642E+00	0.0	0.0	0.0	0.0	0.0

GENERALIZED WEIGHTS

MODE NO.	1	2	3	4	5	6	7
1	3.231990E+02	0.0	0.0	0.0	0.0	0.0	1.732899E+00
2	0.0	1.230240E+04	0.0	0.0	0.0	0.0	9.426029E-01
3	0.0	0.0	1.771964E+00	0.0	0.0	0.0	0.0
4	0.0	0.0	0.0	1.259333E+00	0.0	0.0	0.0
5	0.0	0.0	0.0	0.0	1.559507E+00	0.0	0.0
6	0.0	9.426029E-01	0.0	0.0	0.0	1.016756E+00	0.0
7	1.732899E+00	9.426029E-01	0.0	0.0	0.0	0.0	4.668138E+00

216

SAEL REPRESENTATION OF WIND-TUNNEL MODEL

The rigid and flexible modal equations of motion are written:

$$
\begin{bmatrix} m & 0 & 0 & 0 \\ 0 & I_{yy} & 0 & 0 \\ 0 & 0 & I & 0 \\ 0 & 0 & 0 & M_{\xi\xi} \end{bmatrix} \cdot \begin{bmatrix} \dot{W} \\ \dot{Q} \\ \dot{\xi} \\ \dot{\underline{\xi}} \end{bmatrix} + \begin{bmatrix} 0 & -Vm & 0 & 0 \\ 0 & 0 & 0 & 0 \\ 0 & 0 & 0 & I \\ 0 & 0 & K_{\xi\xi} & 0 \end{bmatrix} \cdot \begin{bmatrix} W \\ Q \\ \xi \\ \underline{\dot{\xi}} \end{bmatrix} = \bar{q} \begin{bmatrix} F_W \\ F_Q \\ 0 \\ F_\xi \end{bmatrix} + \bar{q} \begin{bmatrix} G_W \\ G_Q \\ 0 \\ G_\xi \end{bmatrix} \tag{B1}
$$

The aerodynamic forces due to motion are given by:

$$
\begin{bmatrix} F_W \\ F_Q \\ 0 \\ F_\xi \end{bmatrix} = \begin{bmatrix} \frac{1}{v} \cdot AO_{WW} & \overline{A1}_{WQ} & AO_{W\xi} & \overline{A1}_{W\xi} \\ \frac{1}{v} \cdot AO_{QW} & \overline{A1}_{QQ} & AO_{Q\xi} & \overline{A1}_{Q\xi} \\ 0 & 0 & 0 & 0 \\ \frac{1}{v} \cdot AO_{\xi W} & \overline{A1}_{\xi Q} & AO_{\xi\xi} & \overline{A1}_{\xi\xi} \end{bmatrix} \cdot \begin{bmatrix} W \\ Q \\ \xi \\ \cdot \\ \underline{\xi} \end{bmatrix}
$$

$$
+ \begin{bmatrix} \frac{1}{v} \cdot \overline{A1}_{WW} & \overline{A2}_{WQ} & 0 & \overline{A2}_{W\xi} \\ \frac{1}{v} \cdot \overline{A1}_{QW} & \overline{A2}_{QQ} & 0 & \overline{A2}_{Q\xi} \\ 0 & 0 & 0 & 0 \\ \frac{1}{v} \cdot \overline{A1}_{\xi W} & \overline{A2}_{\xi Q} & 0 & \overline{A2}_{\xi\xi} \end{bmatrix} \cdot \begin{bmatrix} W \\ Q \\ \xi \\ \dot{\underline{\xi}} \end{bmatrix}
$$

$$
+ \sum_{\ell=3}^{L} \begin{bmatrix} \frac{1}{v} \cdot A\ell_{WW} & A\ell_{WQ} & A\ell_{W\xi} \\ \frac{1}{v} \cdot A\ell_{QW} & A\ell_{QQ} & A\ell_{Q\xi} \\ 0 & 0 & 0 \\ \frac{1}{v} \cdot A\ell_{\xi W} & A\ell_{\xi Q} & A\ell_{\xi\xi} \end{bmatrix} \cdot \begin{bmatrix} W_\ell \\ Q_\ell \\ \xi_{\ell,} \end{bmatrix} \tag{B2}
$$

where $\overline{Ai} = (\frac{b}{v})^i Ai$, for $i = 1, 2.$

The aerodynamic lag states obey the equations:

$$
\begin{bmatrix} \dot{W}_\ell \\ \dot{Q}_\ell \\ \dot{\xi}_\ell \end{bmatrix} = \begin{bmatrix} -P_\ell & 0 & 0 \\ 0 & -P_\ell & 0 \\ 0 & 0 & -P_\ell \end{bmatrix} \cdot \begin{bmatrix} W_\ell \\ Q_\ell \\ \xi_\ell \end{bmatrix} + \begin{bmatrix} 0 & 0 & 0 \\ 0 & 1 & 0 \\ 0 & 0 & 0 \end{bmatrix} \cdot \begin{bmatrix} W \\ Q \\ \underline{\xi} \end{bmatrix} + \begin{bmatrix} 1 & 0 & 0 \\ 0 & 0 & 0 \\ 0 & 0 & I \end{bmatrix} \cdot \begin{bmatrix} \dot{W} \\ \dot{Q} \\ \underline{\dot{\xi}} \end{bmatrix}
$$

(B3)

for $\ell = 3$, L. (In this study, L=4.)

The aerodynamic forces due to canard displacement are given by:

$$
\begin{bmatrix} G_W \\ G_Q \\ 0 \\ G_\xi \end{bmatrix} = \begin{bmatrix} AO_{W\delta} \\ AO_{Q\delta} \\ 0 \\ AO_{\xi\delta} \end{bmatrix} \cdot \delta + \begin{bmatrix} \overline{AI}_{W\delta} \\ \overline{AI}_{Q\delta} \\ 0 \\ \overline{AI}_{\xi\delta} \end{bmatrix} \cdot \dot{\delta} + \sum_{\ell=3}^{L} \begin{bmatrix} A\ell_{W\delta} \\ A\ell_{Q\delta} \\ 0 \\ A\ell_{\xi\delta} \end{bmatrix} \cdot \delta_\ell
$$

(B4)

and the associated aerodynamic lags obey:

$$
\dot{\delta}_\ell = -P_\ell \, \delta_\ell + \dot{\delta},
$$

(B5)

for $\ell = 3$, L. Equations (B1) to (B4) are combined to form:

$$
[M_a] \, \underline{\dot{x}}_a = [\overline{A}_a] \, \underline{x}_a + \{\overline{G}\} \, \delta + [\overline{G}_\ell] \, \{\delta_\ell\},
$$

(B6)

where $\underline{x}_a$ includes W, Q, $\underline{\xi}$, $\underline{\dot{\xi}}$, $\underline{W}_\ell$, $\underline{Q}_\ell$ and $\underline{\xi}_\ell$. Inverting the M_a matrix yields:

$$
\underline{\dot{x}}_a = [A_a] \, \underline{x}_a + \{G\}\delta + [G_\ell] \, \{\delta_\ell\}.
$$

(B7)

To these equations, the actuator/control-system equations that will now be developed must be added. Referring to the block diagram in Figure 33,

$$
\dot{\delta} = -\frac{1}{\tau} \, \delta + \frac{1}{\tau} \, \delta_c \qquad e = K_L \, U - K_\alpha \, \delta_c
$$

$$
\delta_c = \delta_I + K_F e \qquad \dot{\delta}_I = K_I e
$$

(B8)

Performing some algebra, these equations together with Equation (B5) give:

$$\dot{\delta} = -\frac{1}{\tau} \delta + \frac{1}{\tau K_C} \delta_I + \frac{K_F K_L}{\tau K_C} U$$

$$\dot{\delta}_I = -\frac{K_I K_\alpha}{K_C} \delta_I + \frac{K_I K_L}{K_C} U$$

$$\dot{\delta}_\ell = -P_\ell \delta_\ell - \frac{1}{\tau} \delta + \frac{1}{\tau K_C} \delta_I + \frac{K_F K_L}{\tau K_C} U, \quad \ell = 2, L. \tag{B9}$$

These equations are now appended to Equations (B7); the state vector is expanded to include δ, $\underline{\delta}_\ell$ and δ_I ; and G and G_ℓ are brought into the state matrix to yield standard state variable format

$$\underline{\dot{x}} = [A] \underline{x} + [B] U. \tag{B10}$$

To close the loop, U is first expressed in terms of gains and measurements.

$$U = [D_Z] \underline{Z} = [K_{NZ} \ K_Q] \cdot \begin{bmatrix} NZ \\ Q \end{bmatrix} \tag{B11}$$

Then the measurements are related to the state variables by

$$Z_1 = NZ = \frac{1}{g} (-\dot{W} + VQ) = \frac{1}{g} [-A_W + [0 \ V \ 0 \ \ldots]] \underline{x}$$

$$Z_2 = Q = [0 \ 1 \ 0 \ \ldots] \underline{x},$$

i.e., $\underline{Z} = [E] \underline{x}.$ \hfill (B12)

Thus, the closed-loop equations become

$$\underline{\dot{x}} = [A + BD_Z E] \underline{x}. \tag{B13}$$

As explained in Section 6.4.2.3, the CABSAEL formulation is obtained by appending two states, z and θ, to the state vector and adding the following two equations to Equation (B10)

$$\dot{z} = W - V\theta$$
$$\dot{\theta} = Q. \tag{B14}$$

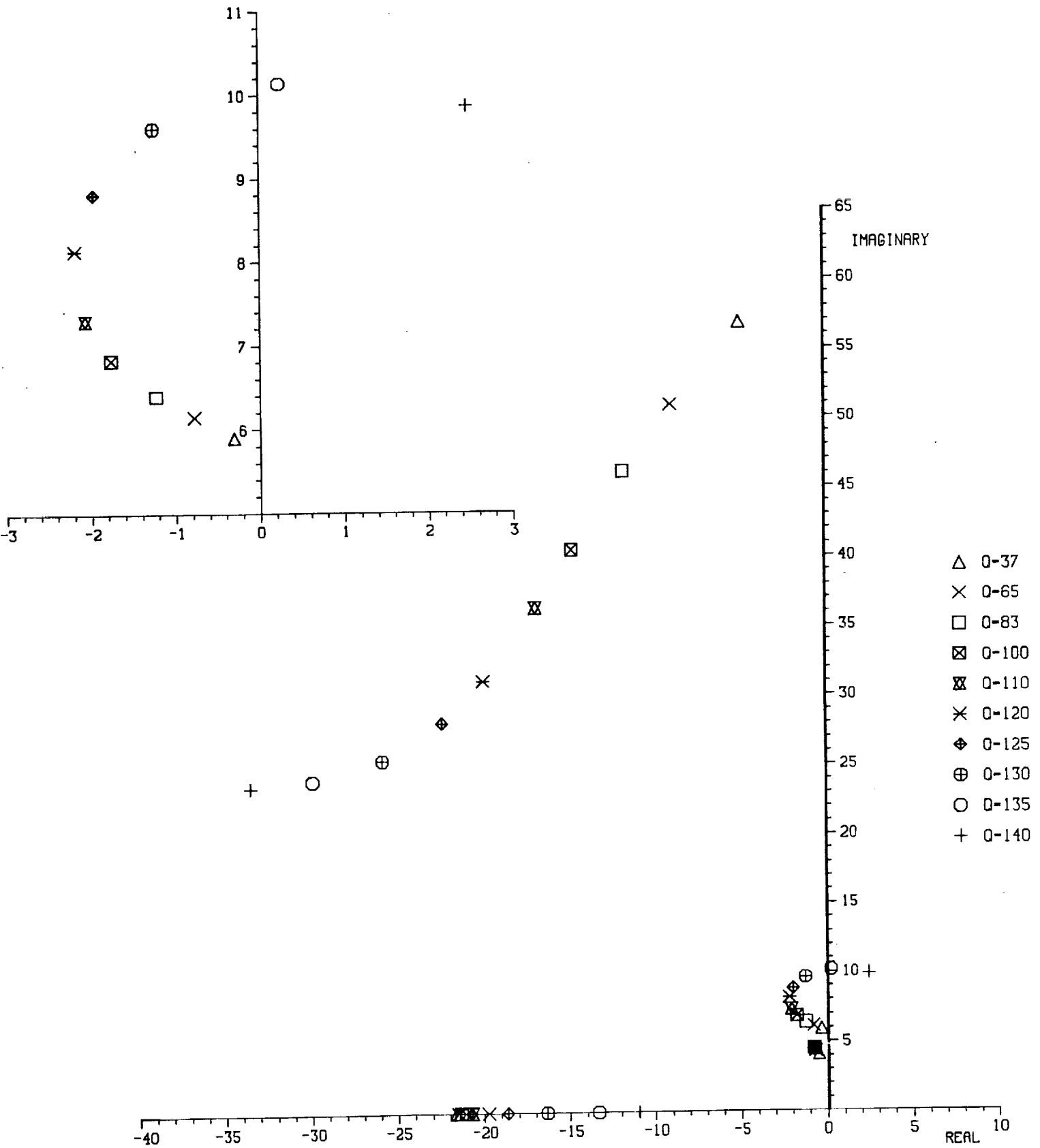As discussed in that section, the additional states cause additional spring terms to appear in the W, Q, W_ℓ, δ, δ_ℓ and δ_I equations.

PAGES

This appendix presents root loci generated by CABSAEL for the configurations tested. The control law gains are those given in Table 20 and the aerodynamic (aero) correction procedure is that described in Section 6.4.2.4. Each figure is in three parts, (a) M = 0.6, (b) M = 0.8, and (c) M = 0.9, appearing on three consecutive pages. In each figure, there are two plots. Each shows the loci of system roots as dynamic pressure is varied over a nominal range of 37 to 140 psf. The larger (main) plot shows each root for which the imaginary part is less than 65 rad/sec and the real part is greater than -40 rad/sec. The smaller plot is presented on a magnified scale and shows only the root that goes unstable as dynamic pressure is increased.

1/2 scale FSW CABSAEL CG 213 M=0.6
open loop response
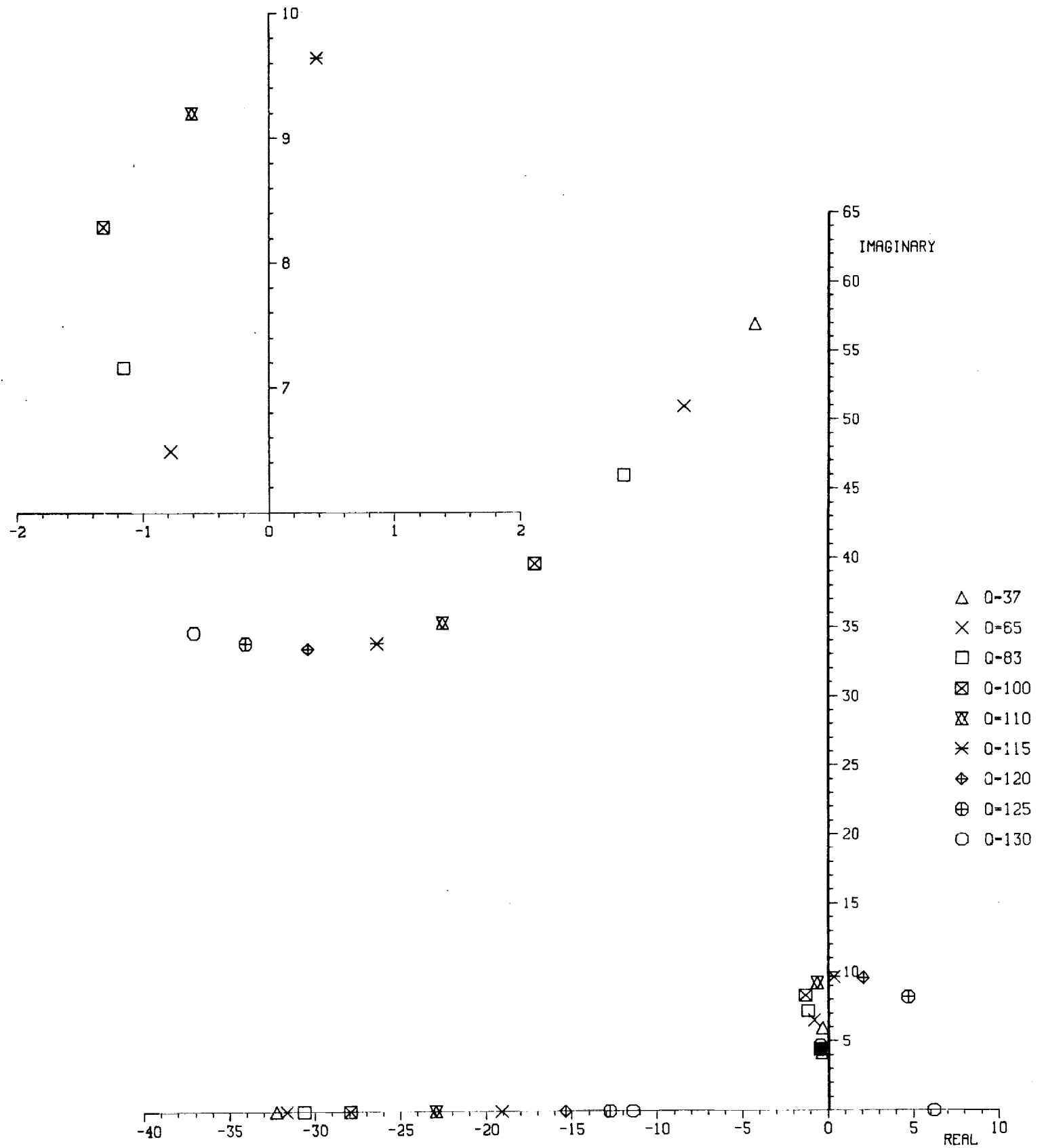## Q̄-matched aero corrections

Legend:
- △ Q-37
- ✕ Q-65
- □ Q-83
- ⊠ Q-100
- ⊠ Q-110
- ✳ Q-120
- ✦ Q-125
- ⊕ Q-130
- ○ Q-135
- + Q-140

1/2 scale FSW CABSAEL CG 213 M=0.8
open loop response
$\bar{Q}$-matched aero corrections

△ 0-37
✕ 0-65
□ 0-83
⊠ 0-1 00
▨ 0-110
✳ 0-115
✪ 0-120
⊕ 0-125
○ 0-130
+ 0-135

IMAGINARY

REAL

223
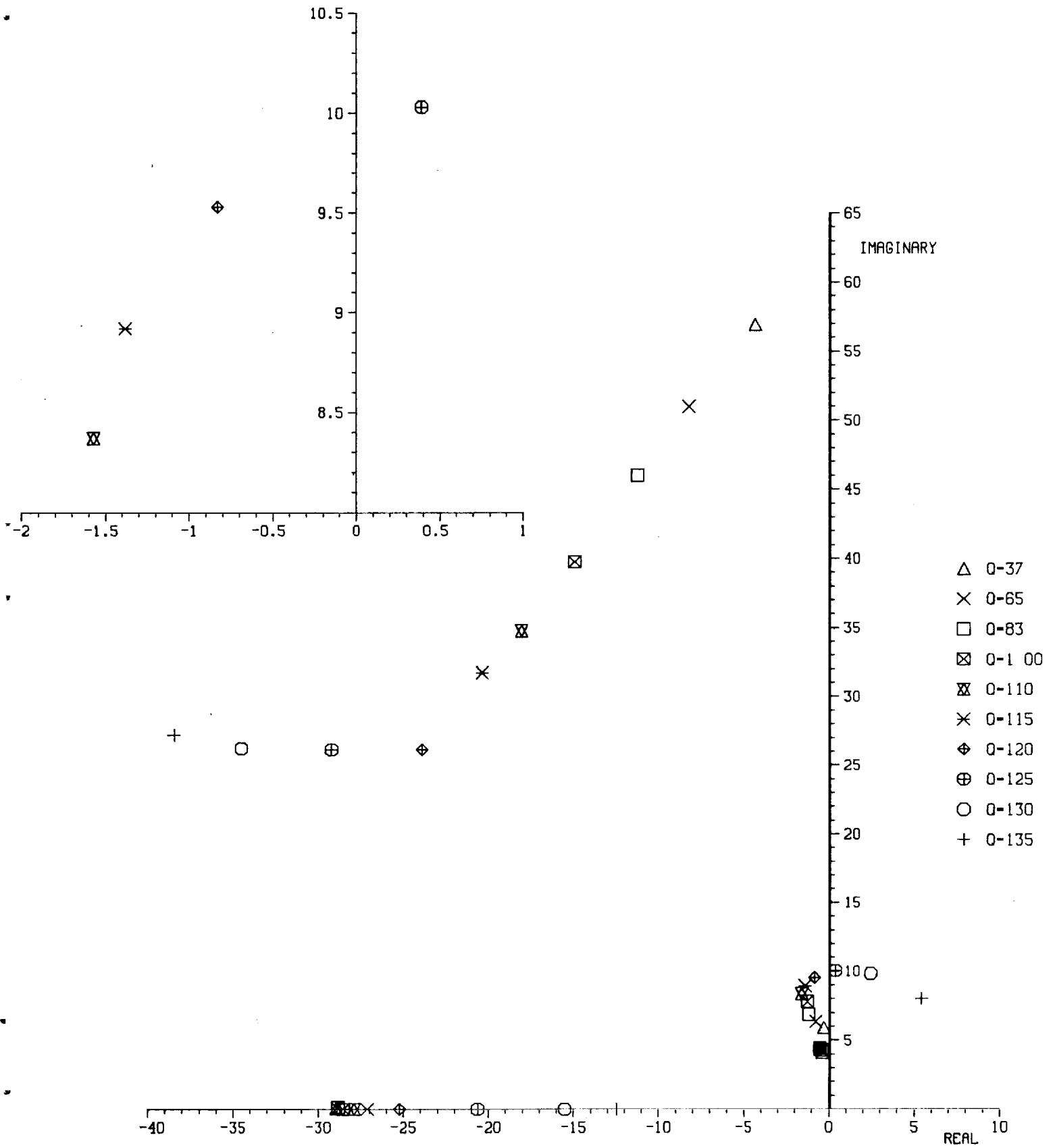
1/2 scale FSW CABSAEL CG213 M=0.9
open loop response
Q-matched aero corrections

Legend:
△ Q-37
✕ Q-65
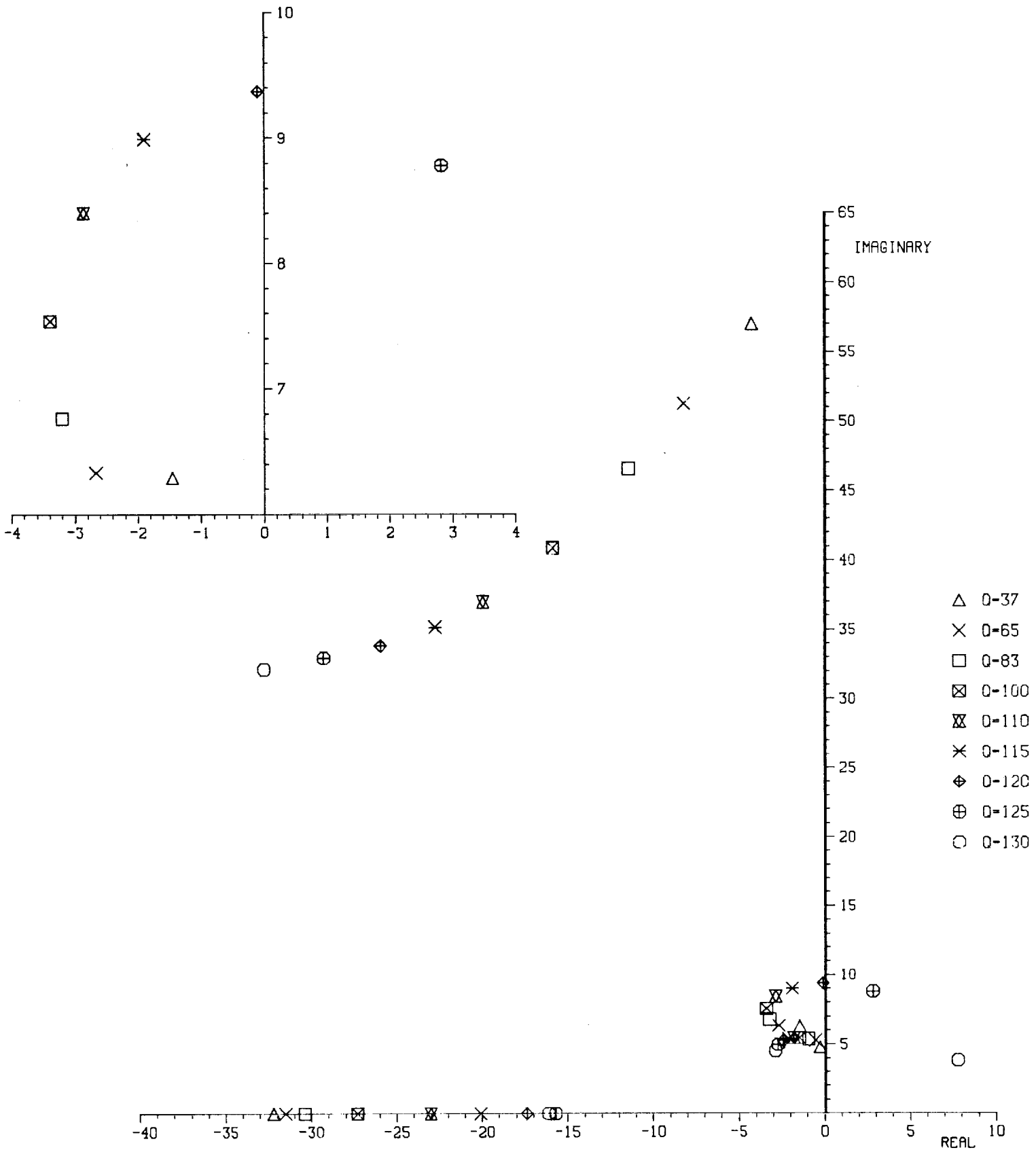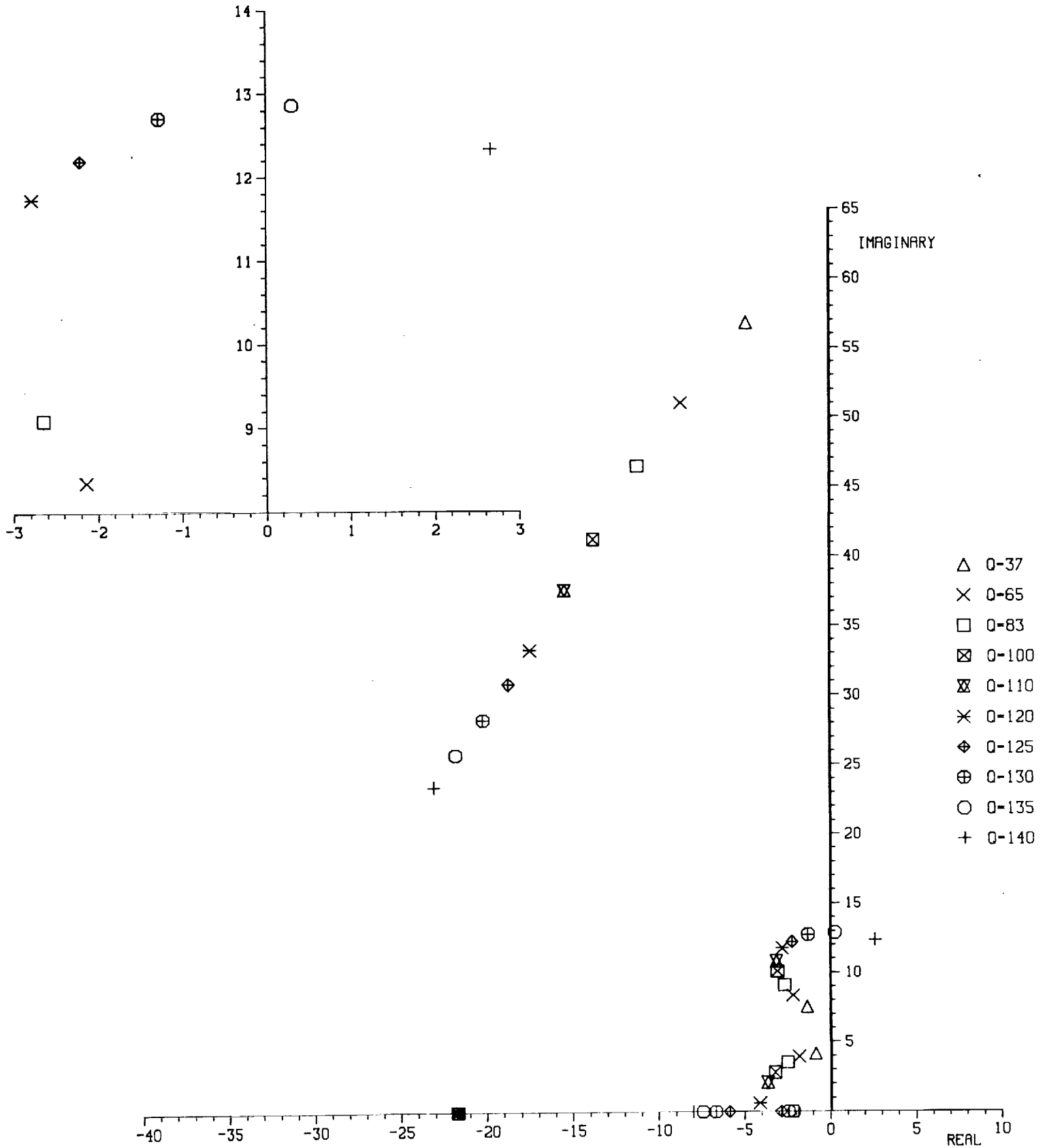□ Q-83
⊠ Q-100
⊠ Q-110
✳ Q-115
⊕ Q-120
⊕ Q-125
○ Q-130

1/2 scale FSW CABSAEL C1-1 M=0.6
_ control law as tested
Q-matched aero corrections
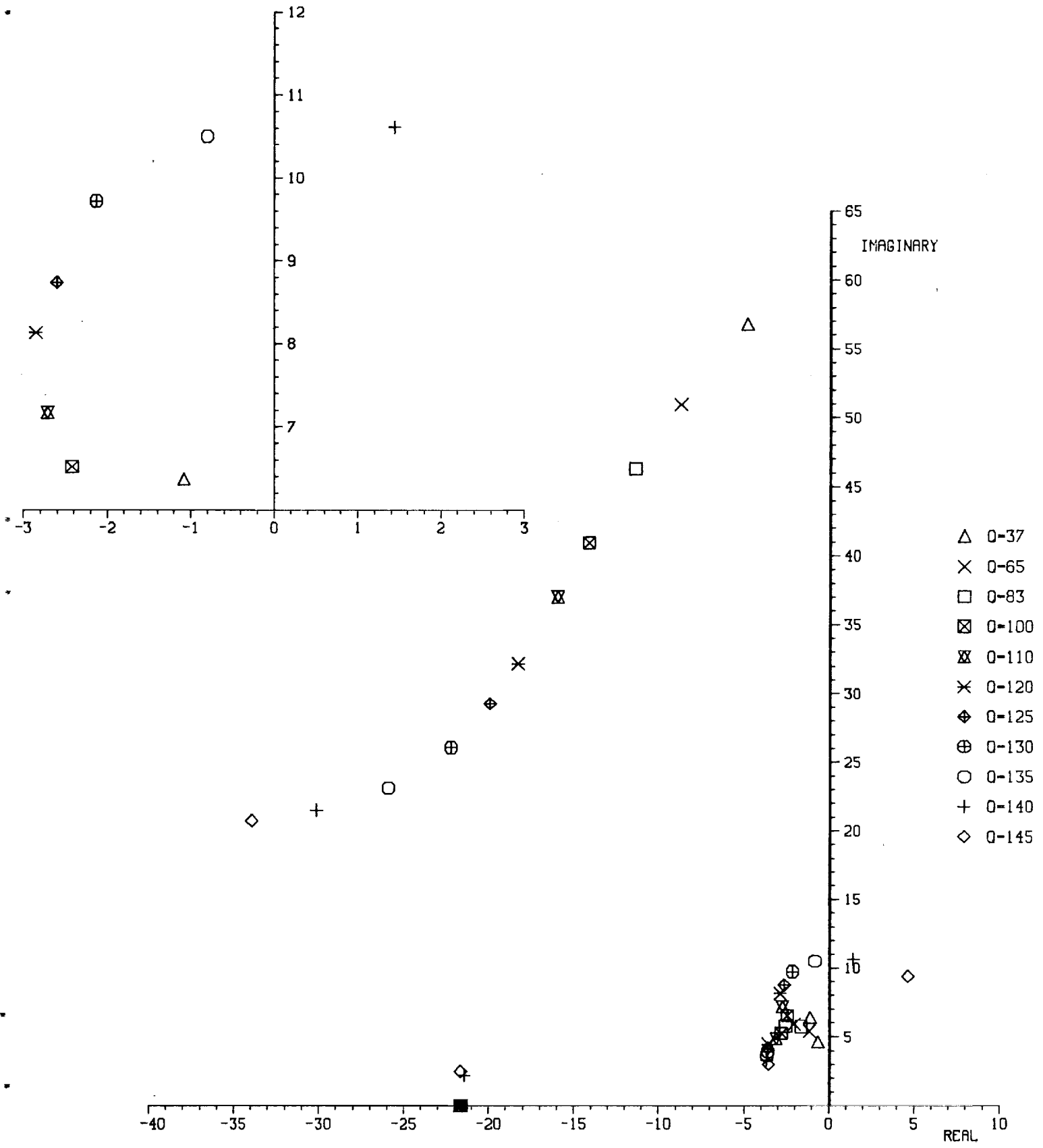
1/2 scale FSW CABSAEL C1-1 M=0.8
control law as tested
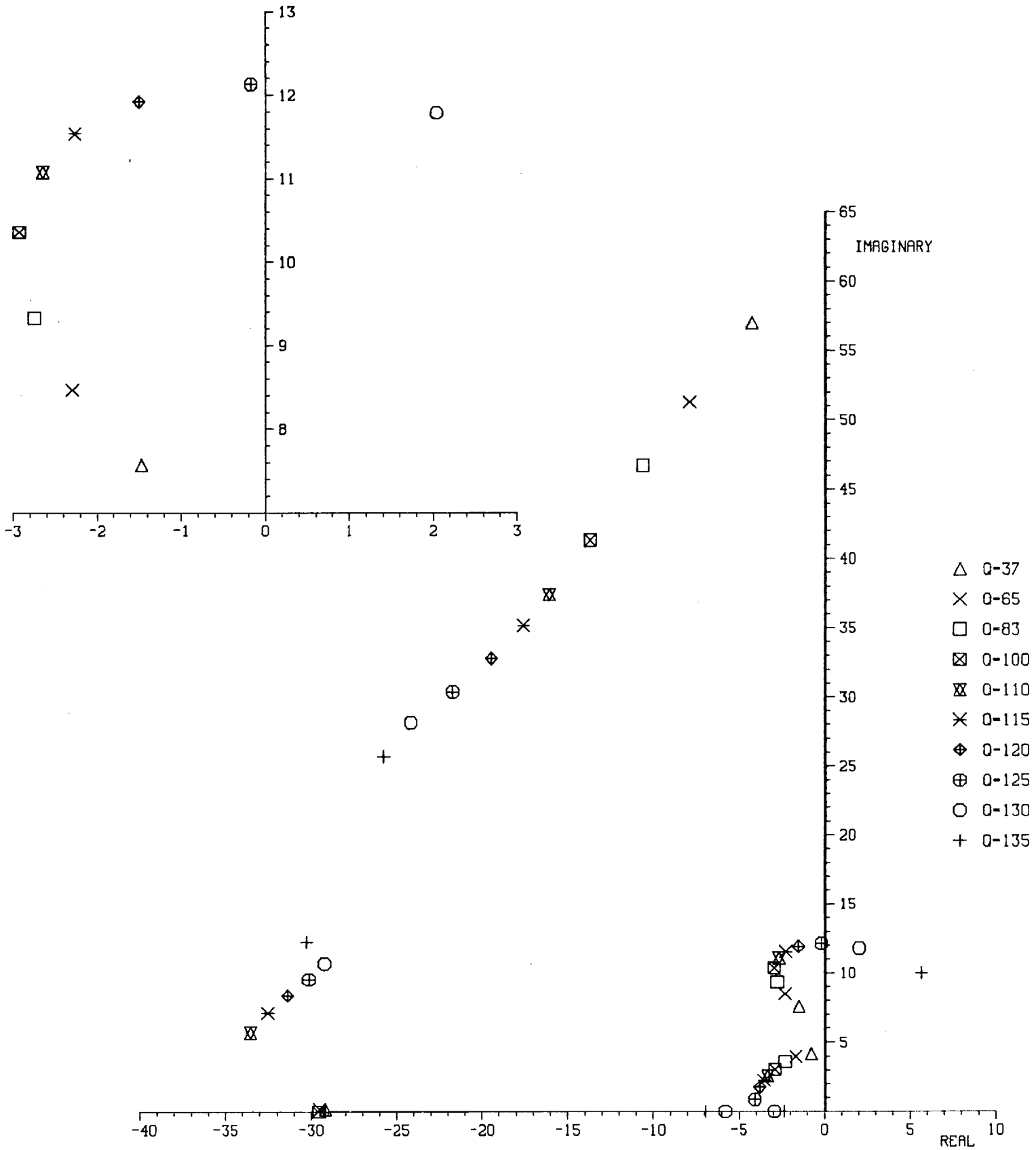Q̄-matched aero corrections

IMAGINARY

REAL

△ Q-37
✕ Q-65
□ Q-83
⊠ Q-100
⊠ Q-110
✶ Q-115
⊕ Q-120
⊕ Q-125
○ Q-130
+ Q-135
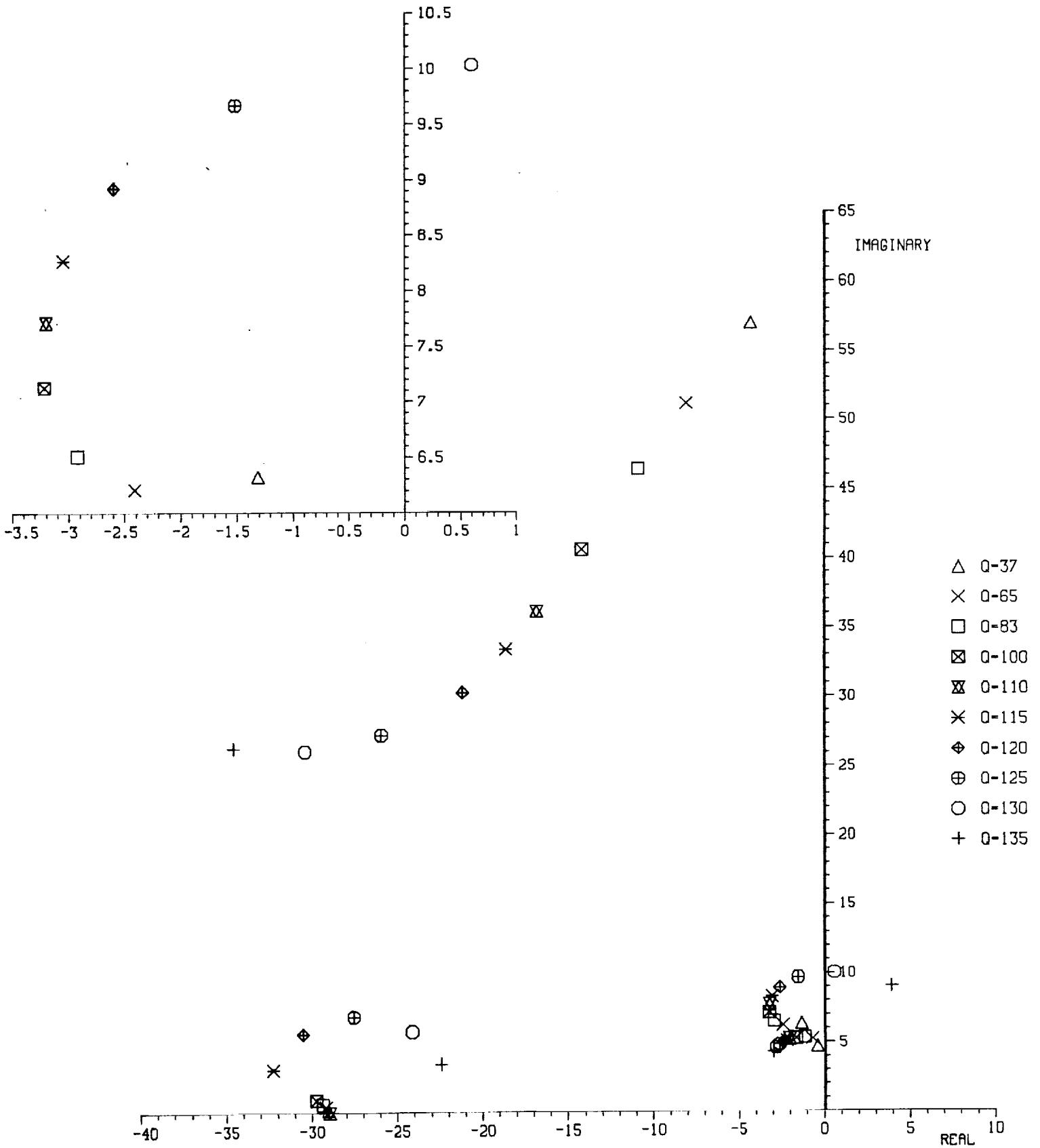
1/2 scale FSW CABSAEL C1-1 M=0.9
control law as tested
Q̄-matched aero corrections

227

1/2 scale FSW CABSAEL C1-2 M=0.6
control law as tested
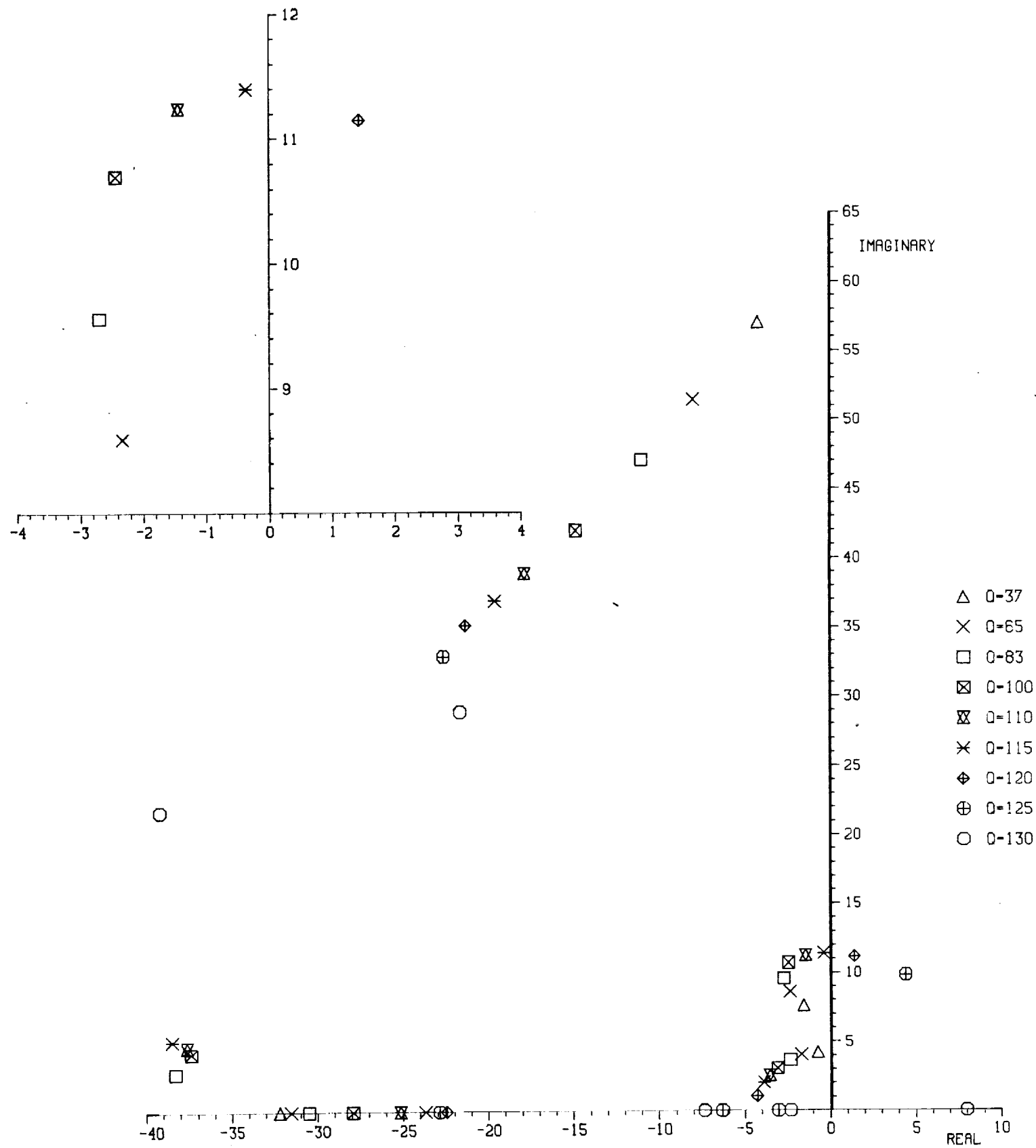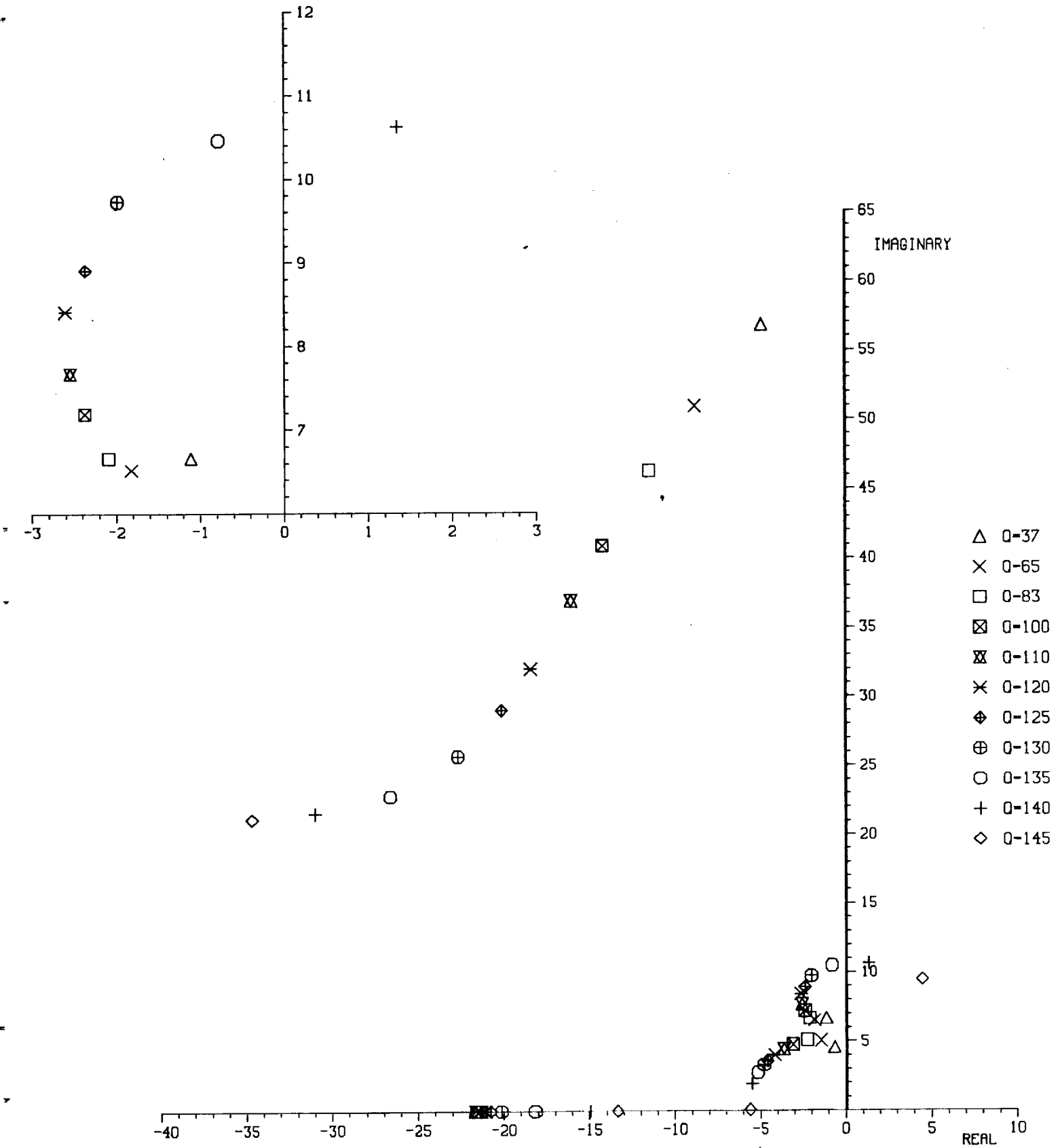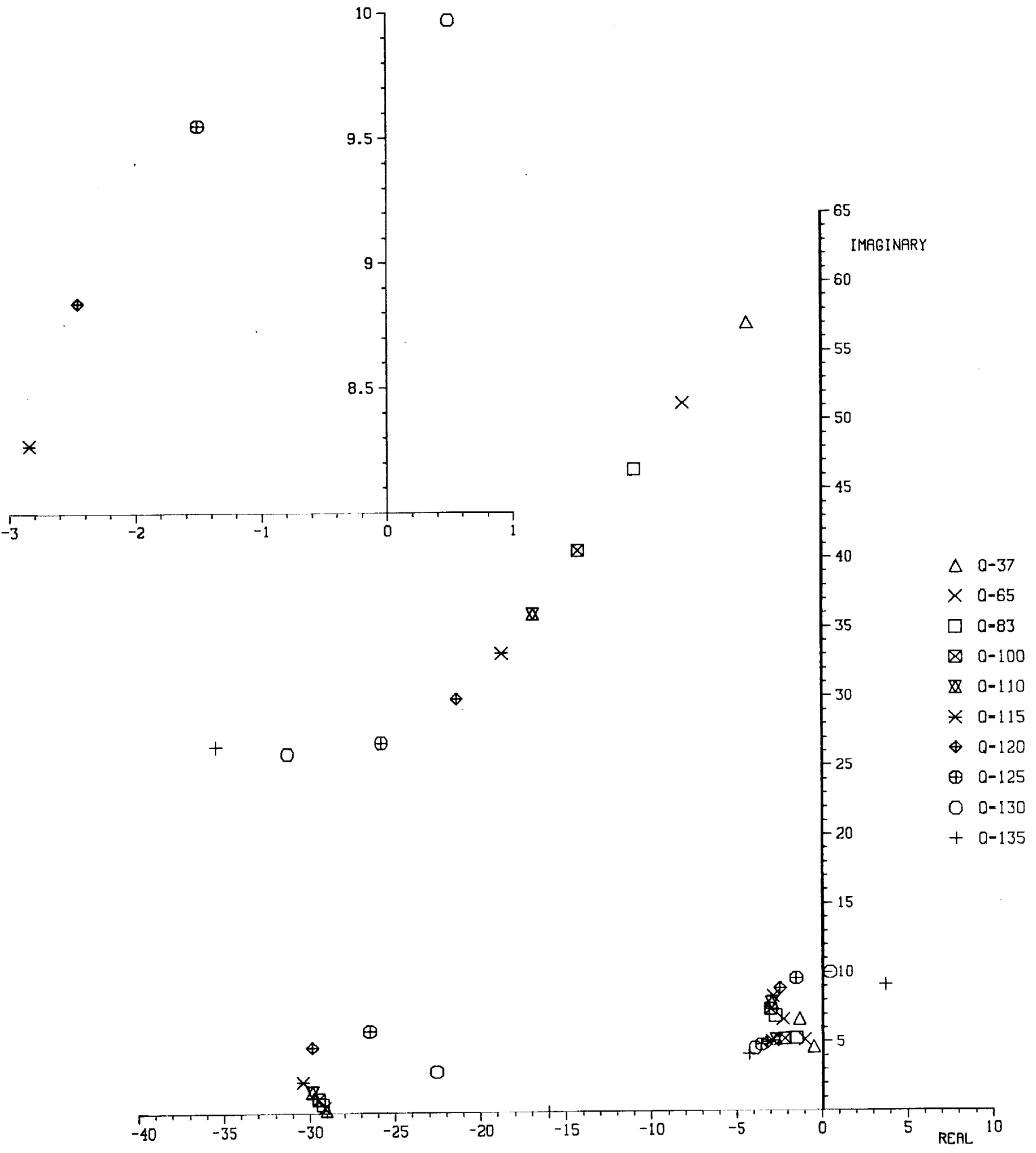## Q-matched aero corrections

IMAGINARY

△	Q-37
✕	Q-65
☐	Q-83
⊠	Q-100
⊠	Q-110
✱	Q-120
⊕	Q-125
⊕	Q-130
○	Q-135
+	Q-140

REAL

1/2 scale FSW CABSAEL C1-2 M=0.8
control law as tested
$\bar{Q}$-matched aero corrections

Legend:
- △ Q-37
- × Q-65
- □ Q-83
- ⊠ Q-100
- ⧆ Q-110
- ✳ Q-115
- ✦ Q-120
- ⊕ Q-125
- ○ Q-130
- + Q-135

IMAGINARY

REAL

1/2 scale FSW CABSAEL C1-2 M=0.9
_ control law as tested
Q-matched aero corrections

Legend:
△ Q-37
✕ Q-65
□ Q-83
⊠ Q-100
⊠ Q-110
✳ Q-115
⊕ Q-120
⊕ Q-125
○ Q-130

IMAGINARY

REAL

1/2 scale FSW CABSAEL C1-3 M=0.6
control law as tested
Q-matched aero corrections

IMAGINARY

△	Q-37
×	Q-65
□	Q-83
⊠	Q-100
⊠	Q-110
✳	Q-120
⊕	Q-125
⊕	Q-130
○	Q-135
+	Q-140
◇	Q-145

REAL

231

1/2 scale FSW CABSAEL C1-3 M=0.8
control law as tested
Q-matched aero corrections

Legend:
△ Q-37
✕ Q-65
☐ Q-83
⊠ Q-100
⊠ Q-110
✳ Q-115
✦ Q-120
⊕ Q-125
○ Q-130
+ Q-135

IMAGINARY

REAL

1/2 scale FSW CABSAEL C1-3 M=0.9
control law as tested
Q-matched aero corrections

Legend:
- △ Q-37
- ✕ Q=65
- ☐ Q-83
- ⊠ Q-100
- ⊠ Q-110
- ✳ Q-115
- ⊕ Q-120
- ⊕ Q-125
- ○ Q-130

1/2 scale FSW CABSAEL C1-4 M=0.6
control law as tested
Q̄-matched aero corrections

Legend:
△ Q-37
✕ Q-65
□ Q-83
⊠ Q-100
⊠ Q-110
✷ Q-120
⊕ Q-125
⊕ Q-130
○ Q-135
+ Q-140
◇ Q-145
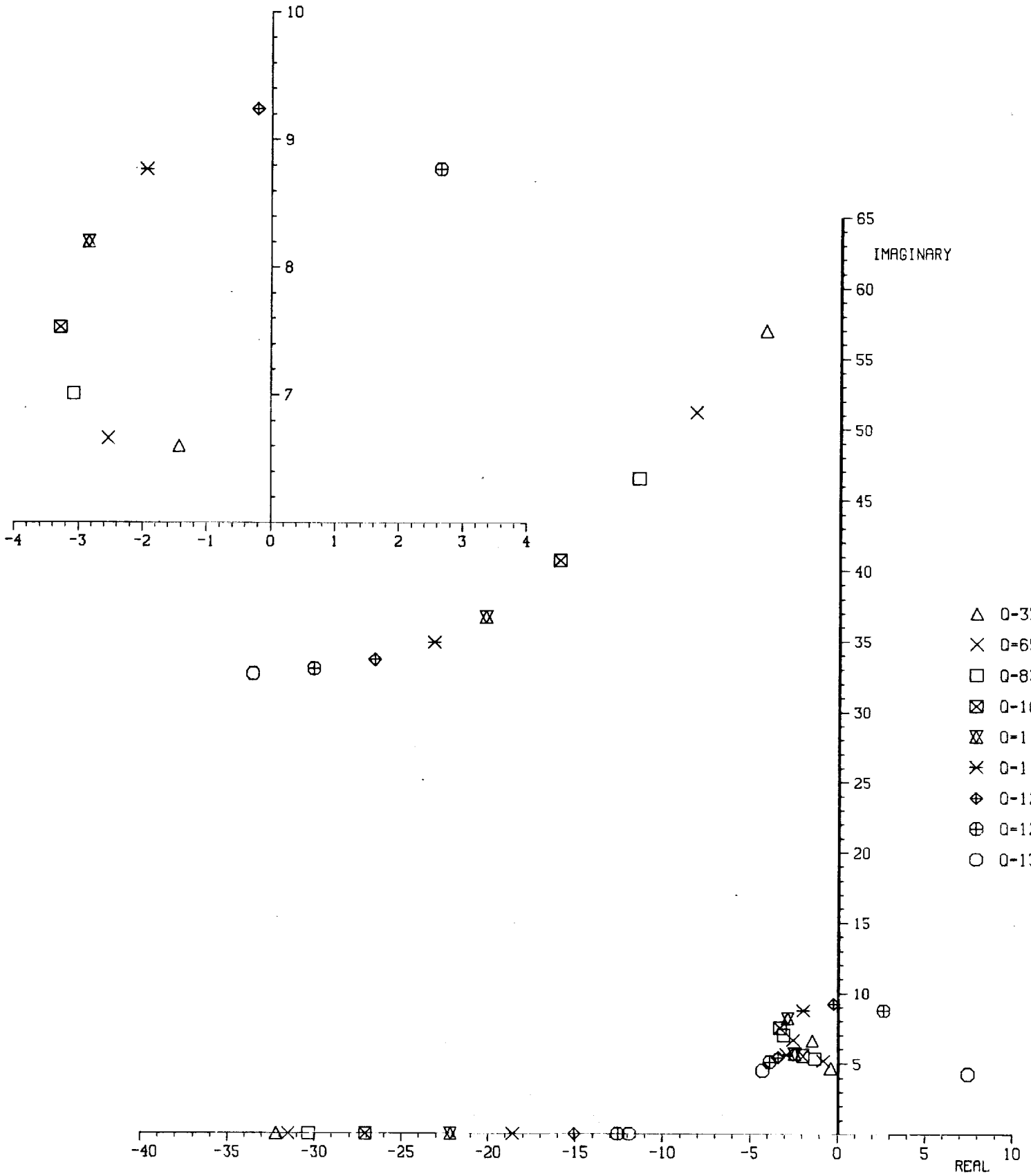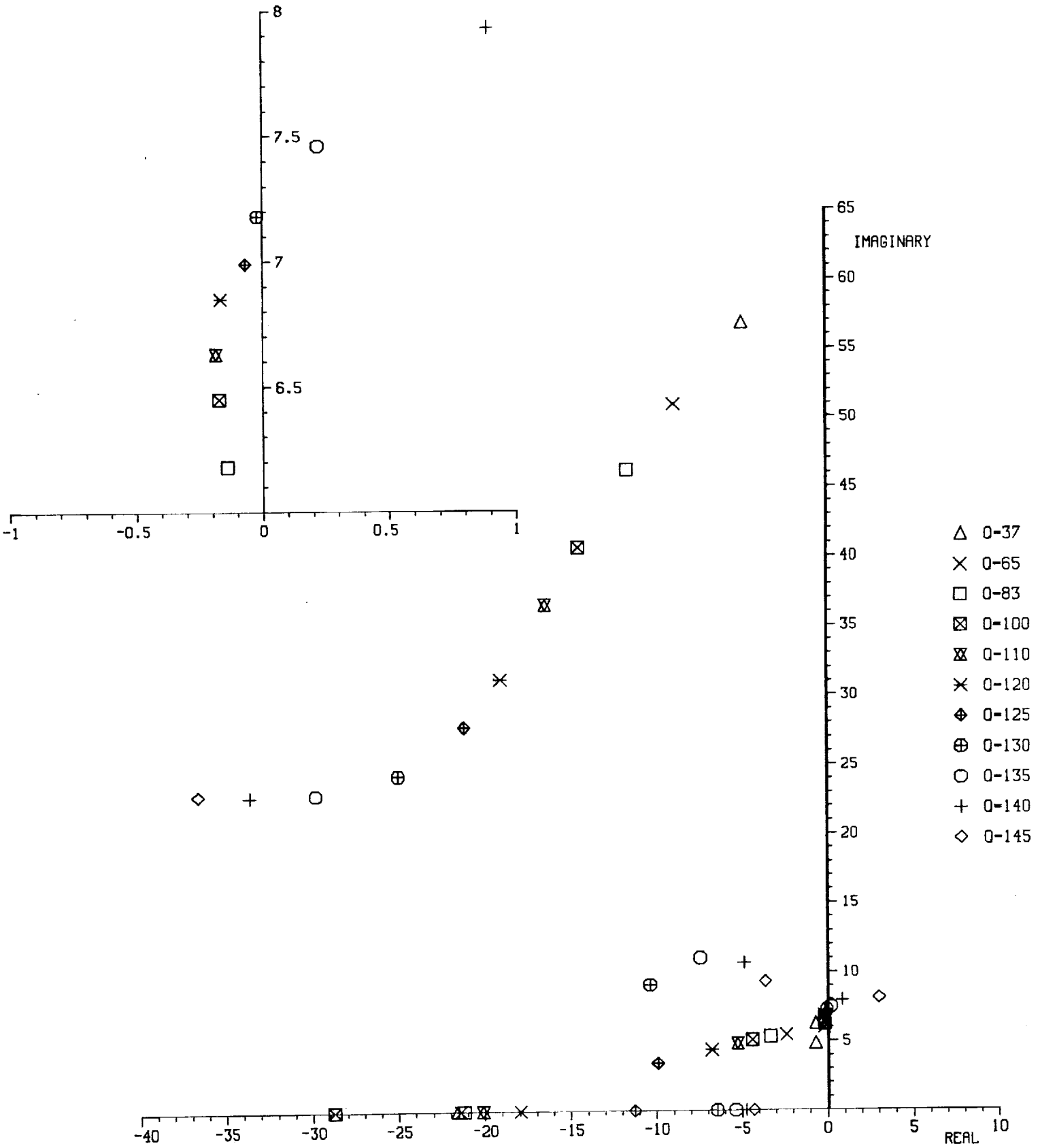
1/2 scale FSW CABSAEL C1-4 M=0.8
control law as tested
Q-matched aero corrections
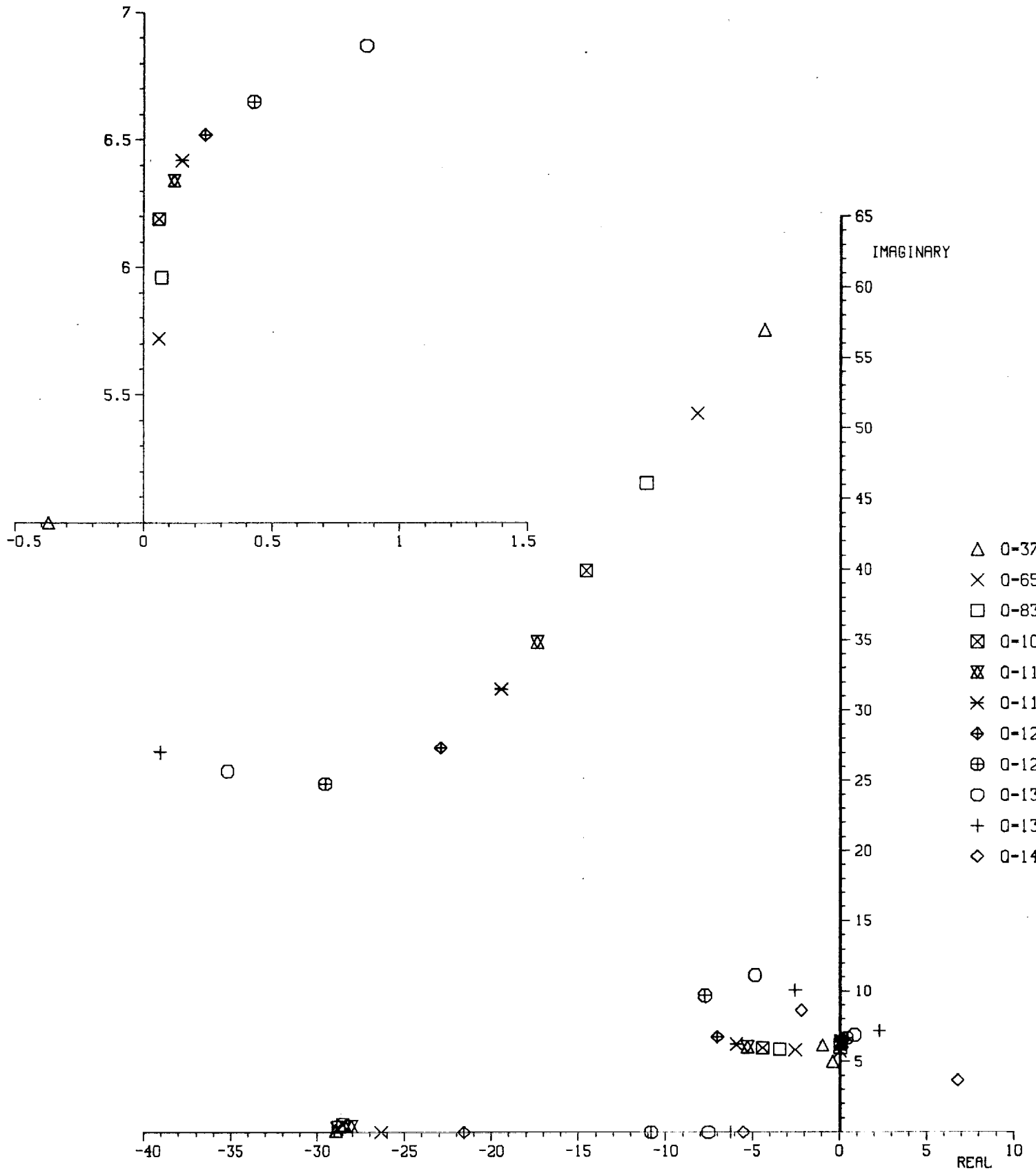
Legend:
- △ Q-37
- ✕ Q-65
- □ Q-83
- ⊠ Q-100
- ⊠ Q-110
- ✳ Q-115
- ⬥ Q-120
- ⊕ Q-125
- ○ Q-130
- + Q-135
- ◇ Q-140

1/2 scale FSW CABSAEL C1-4 M=0.9
control law as tested
Q-matched aero corrections

Legend:
△ Q-37
✕ Q-65
☐ Q-83
⊠ Q-100
⊠ Q-110
✳ Q-115
✦ Q-120
⊕ Q-125
○ Q-130

IMAGINARY

REAL
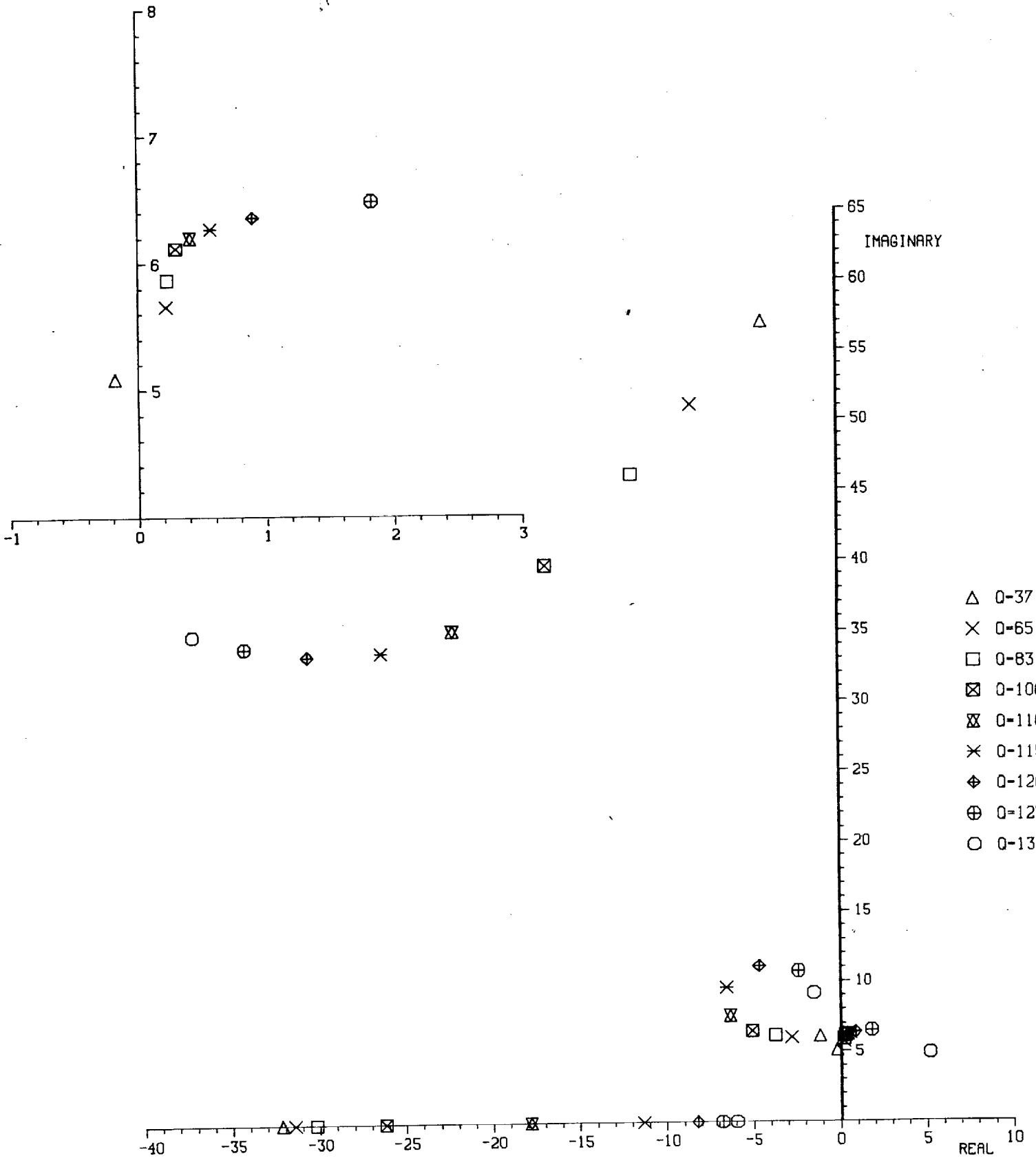
1/2 scale FSW CABSAEL C1-4A M=0.6
control law as tested
$\bar{Q}$-matched aero corrections

1/2 scale FSW CABSAEL C1-4A M=0.8
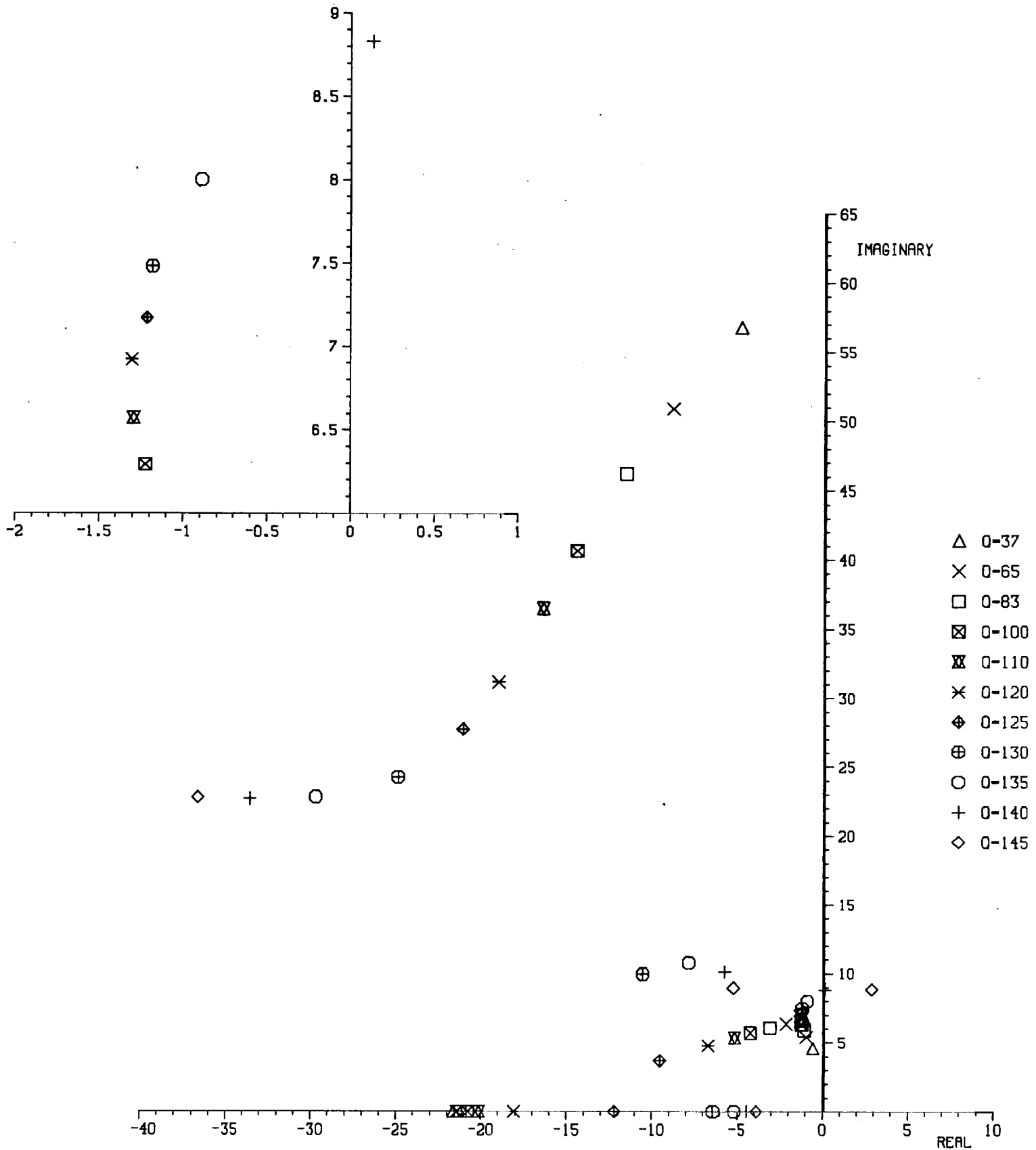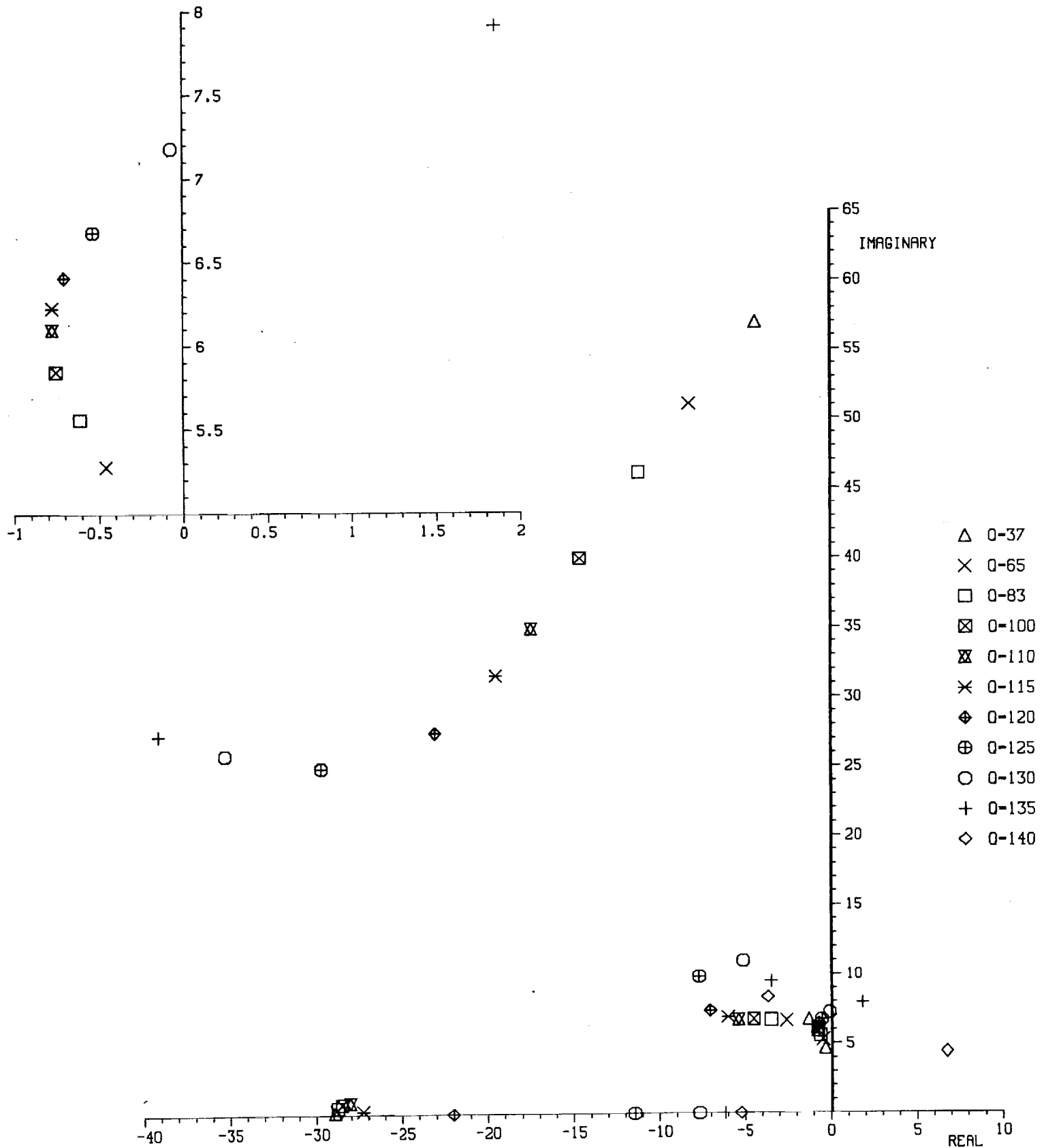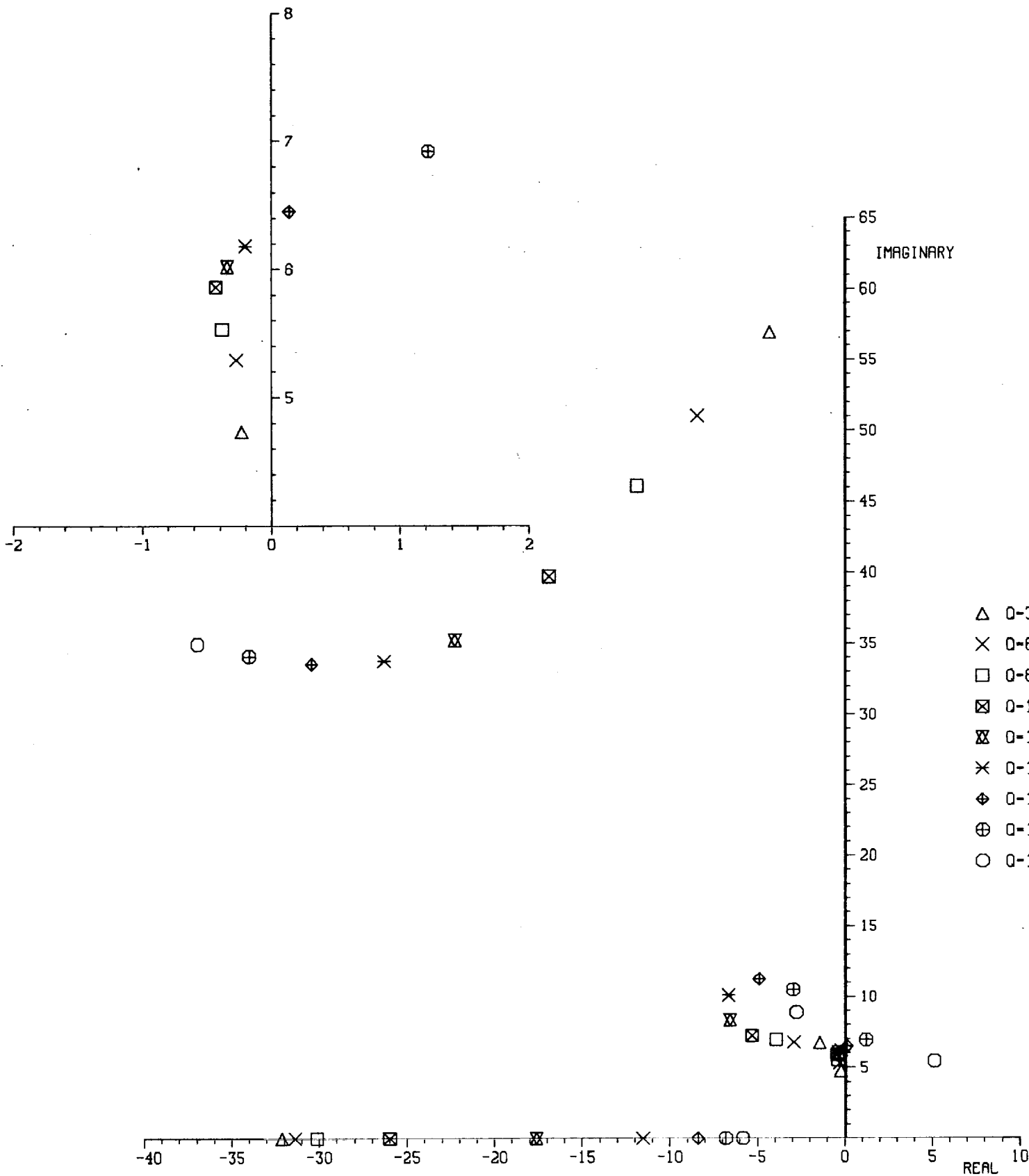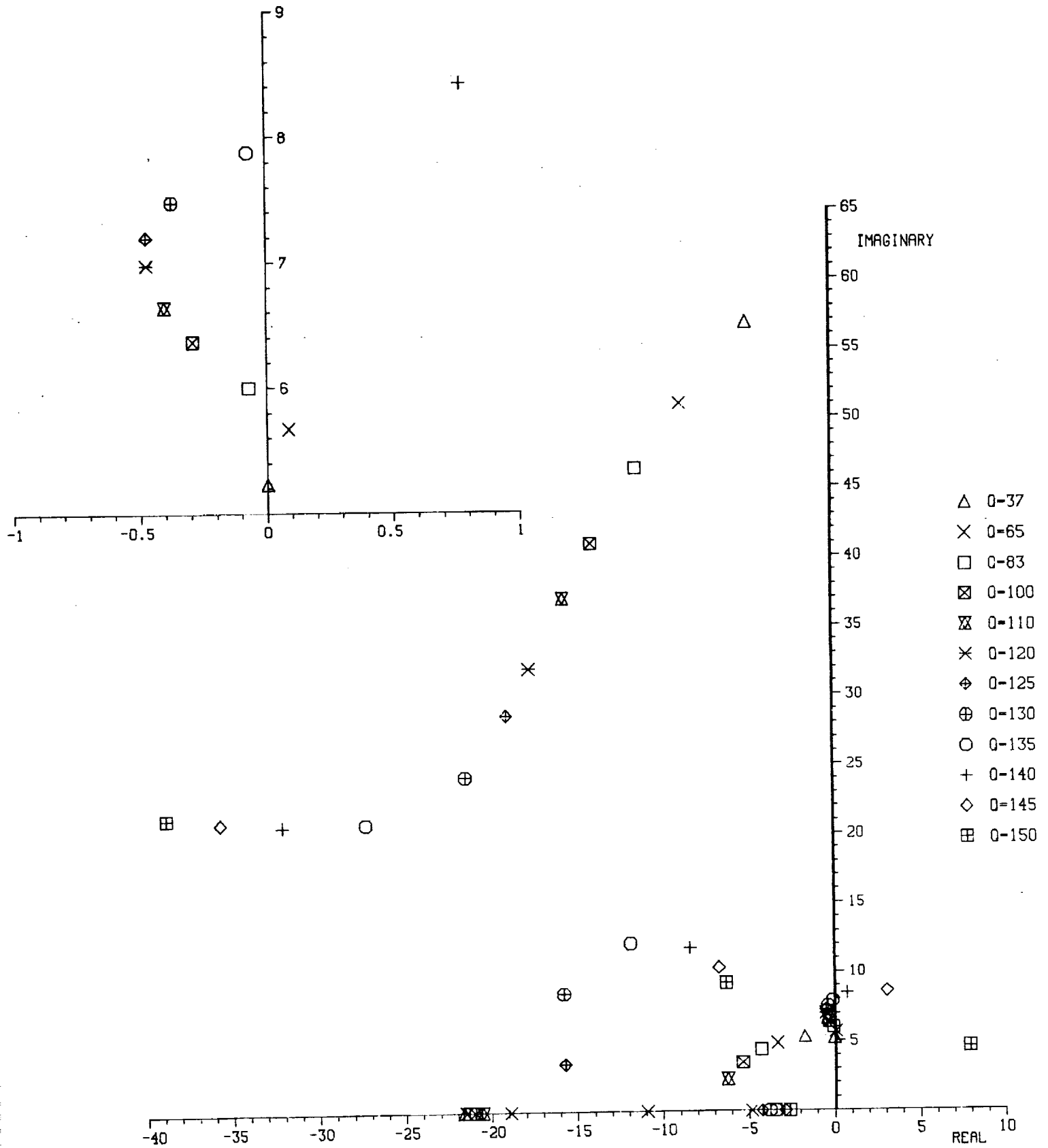control law as tested
Q-matched aero corrections

Legend:
△ Q-37
✕ Q-65
□ Q-83
⊠ Q-100
⧅ Q-110
✱ Q-115
⊕ Q-120
⊕ Q-125
○ Q-130
+ Q-135
◇ Q-140

IMAGINARY

REAL

238

1/2 scale FSW CABSAEL C1-4A M=0.9
control law as tested
Q̄-matched aero corrections

IMAGINARY

REAL

△ Q-37
✕ Q-65
☐ Q-83
⊠ Q-100
⊠ Q-110
✳ Q-115
✦ Q-120
⊕ Q-125
○ Q-130

239

1/2 scale FSW   CABSAEL   C2-1   M=0.6
control law as tested
Q̄-matched aero corrections

Legend:

Symbol	Value
△	Q-37
✕	Q-65
□	Q-83
⊠	Q-100
⊠	Q-110
✶	Q-120
✛	Q-125
⊕	Q-130
○	Q-135
+	Q-140
◇	Q-145
⊞	Q-150

1/2 scale FSW CABSAEL C2-1 M=0.8
control law as tested
Q̄-matched aero corrections

Legend:
△ 0-37
✕ 0-65
□ 0-83
⊠ 0-110
⊠ 0-110
✳ 0-115
⊕ 0-120
⊕ 0-125
○ 0-130
+ 0-135
◇ 0-140

241
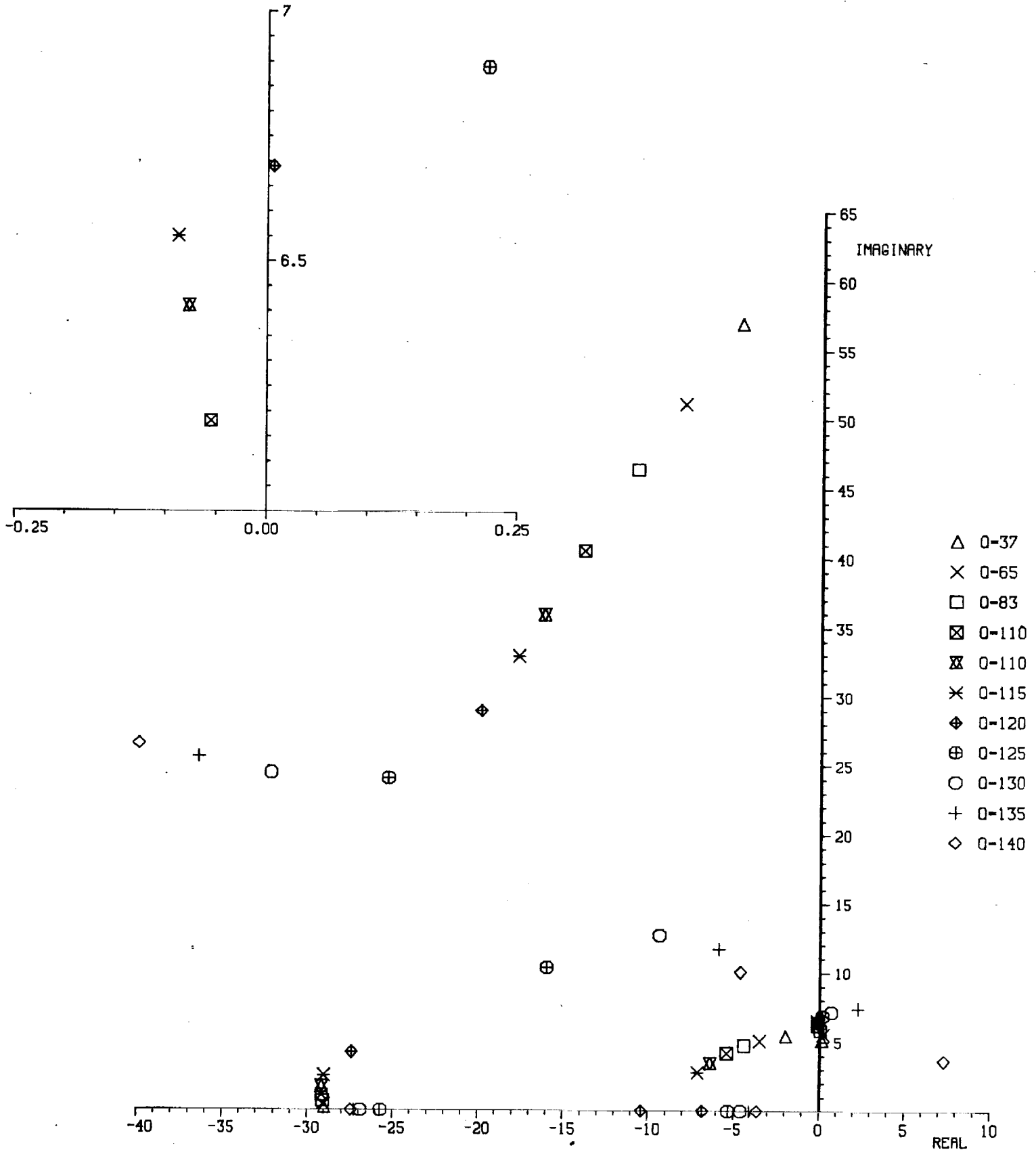
1/2 scale FSW CABSAEL C2-1   M=0.9
control law as tested
Q̄-matched aero corrections

Legend:
- △ Q-37
- ✕ Q-65
- □ Q-83
- ⊠ Q-100
- ⊠ Q-110
- ✳ Q-115
- ✦ Q-120
- ⊕ Q-125
- ○ Q-130
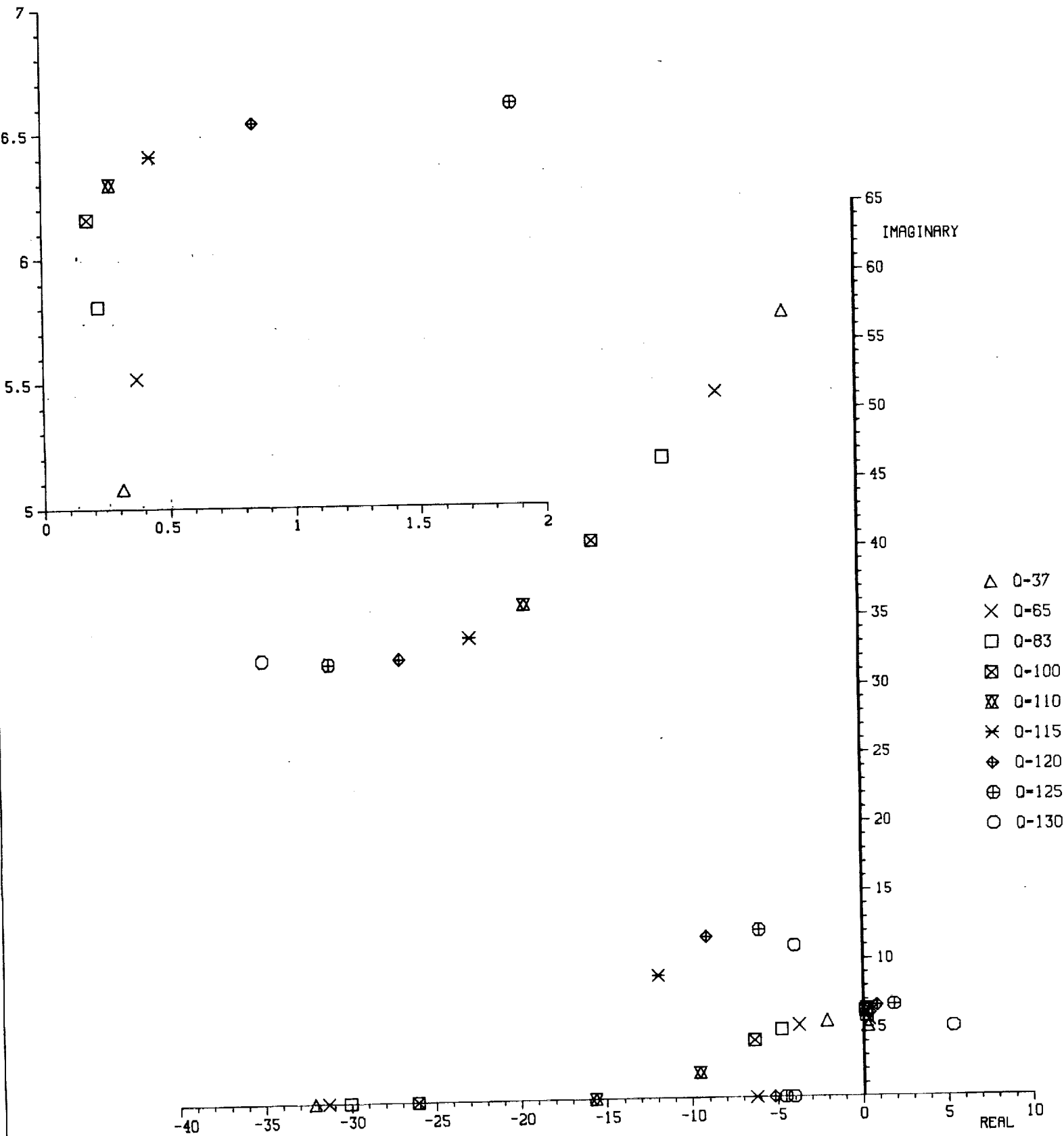
1/2 scale FSW CABSAEL C2-2 M=0.6
control law as tested
Q̄-matched aero corrections

Legend:

Symbol	
△	Q-37
✕	Q-65
□	Q-83
⊠	Q-100
🐾	Q-110
✳	Q-120
⊕	Q-125
⊕	Q-130
○	Q-135
+	Q-140
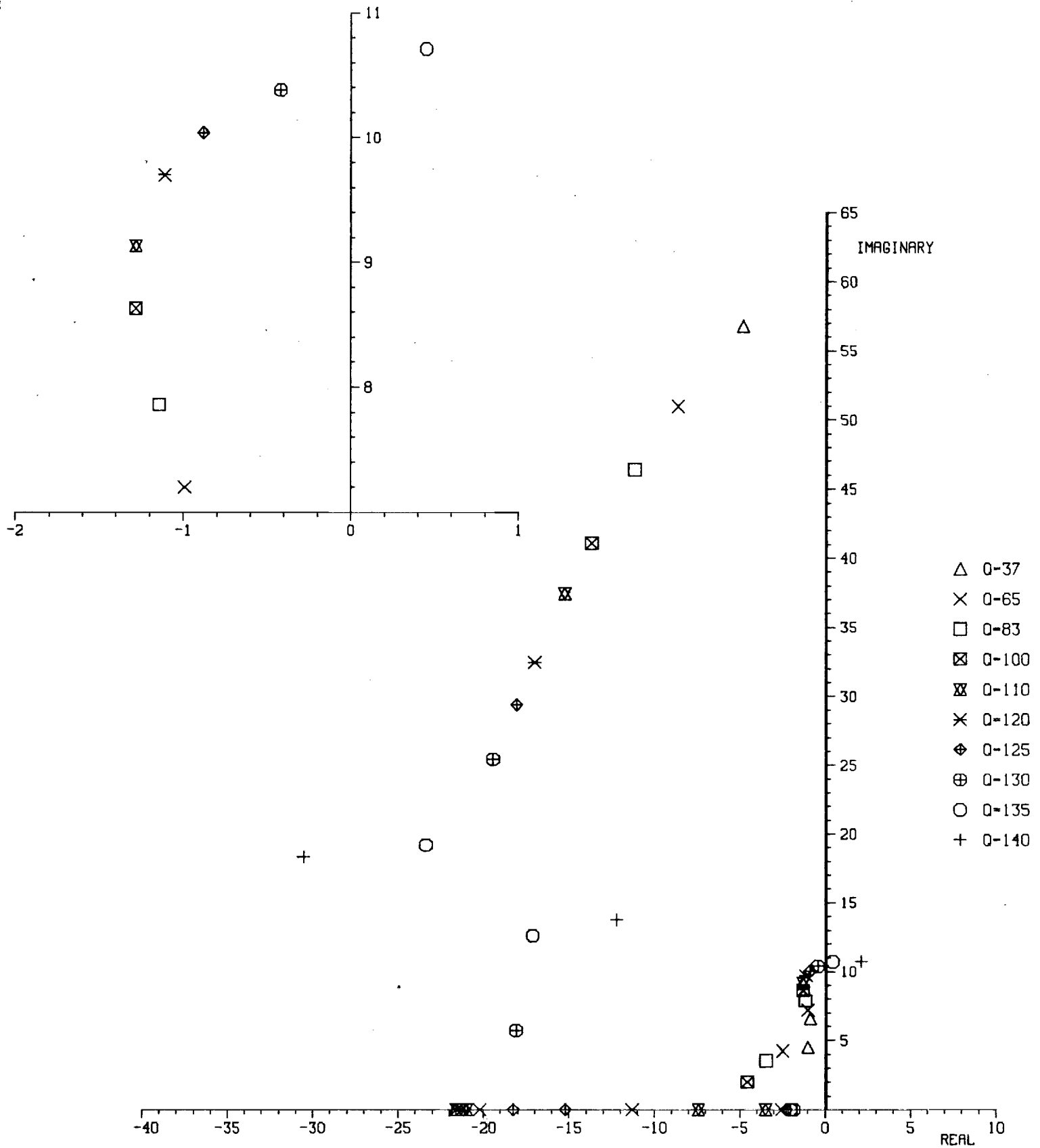
1/2 scale FSW CABSAEL C2-2 M=0.8
control law as tested
Q̄-matched aero corrections

Legend:
△ Q-37
✕ Q-65
□ Q-83
⊠ Q-100
✕ Q-110
✳ Q-115
✦ Q-120
⊕ Q-125
○ Q-130
+ Q-135

244
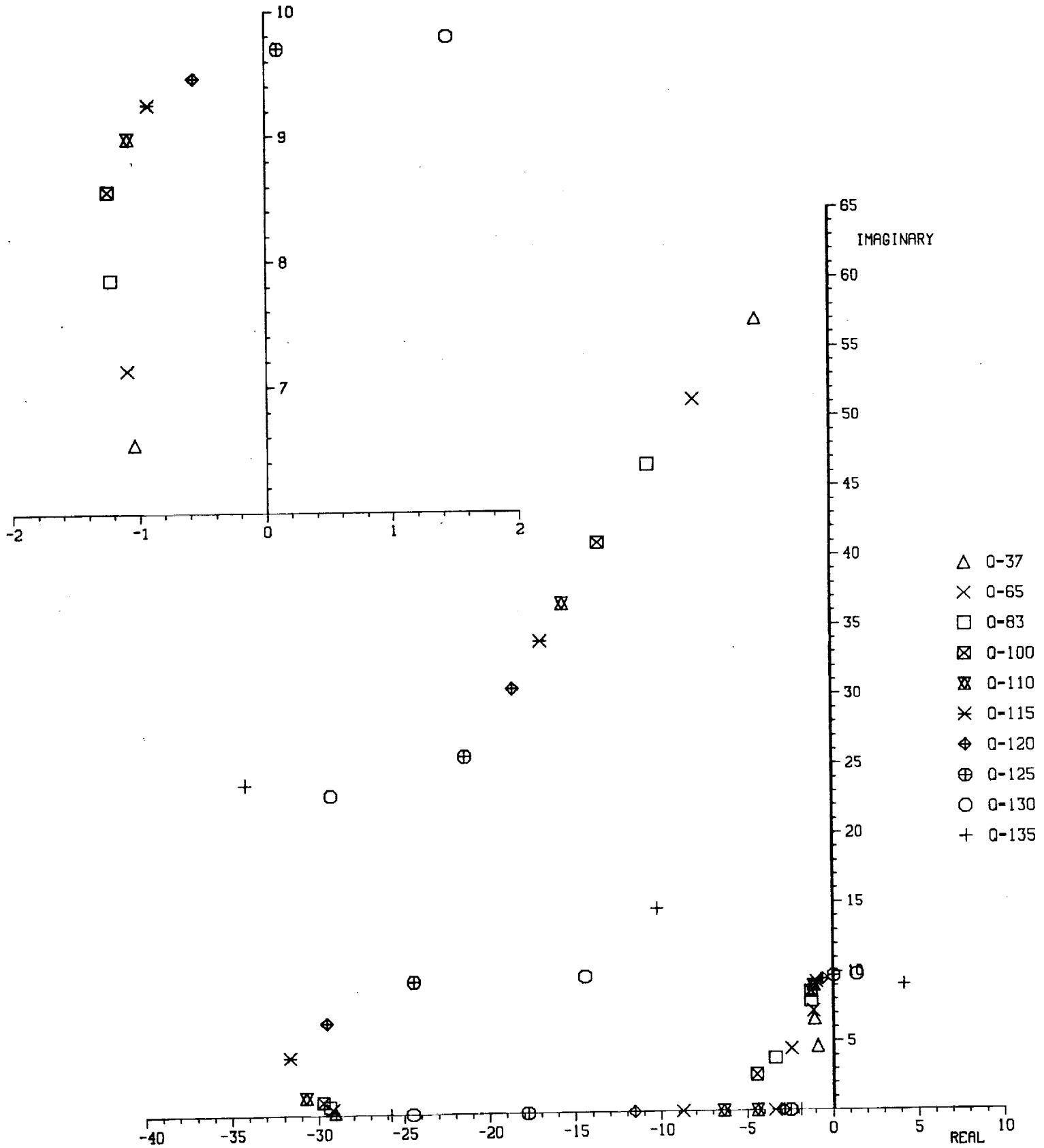
1/2 scale FSW CABSAEL C2-2 M=0.9
control law as tested
Q-matched aero corrections
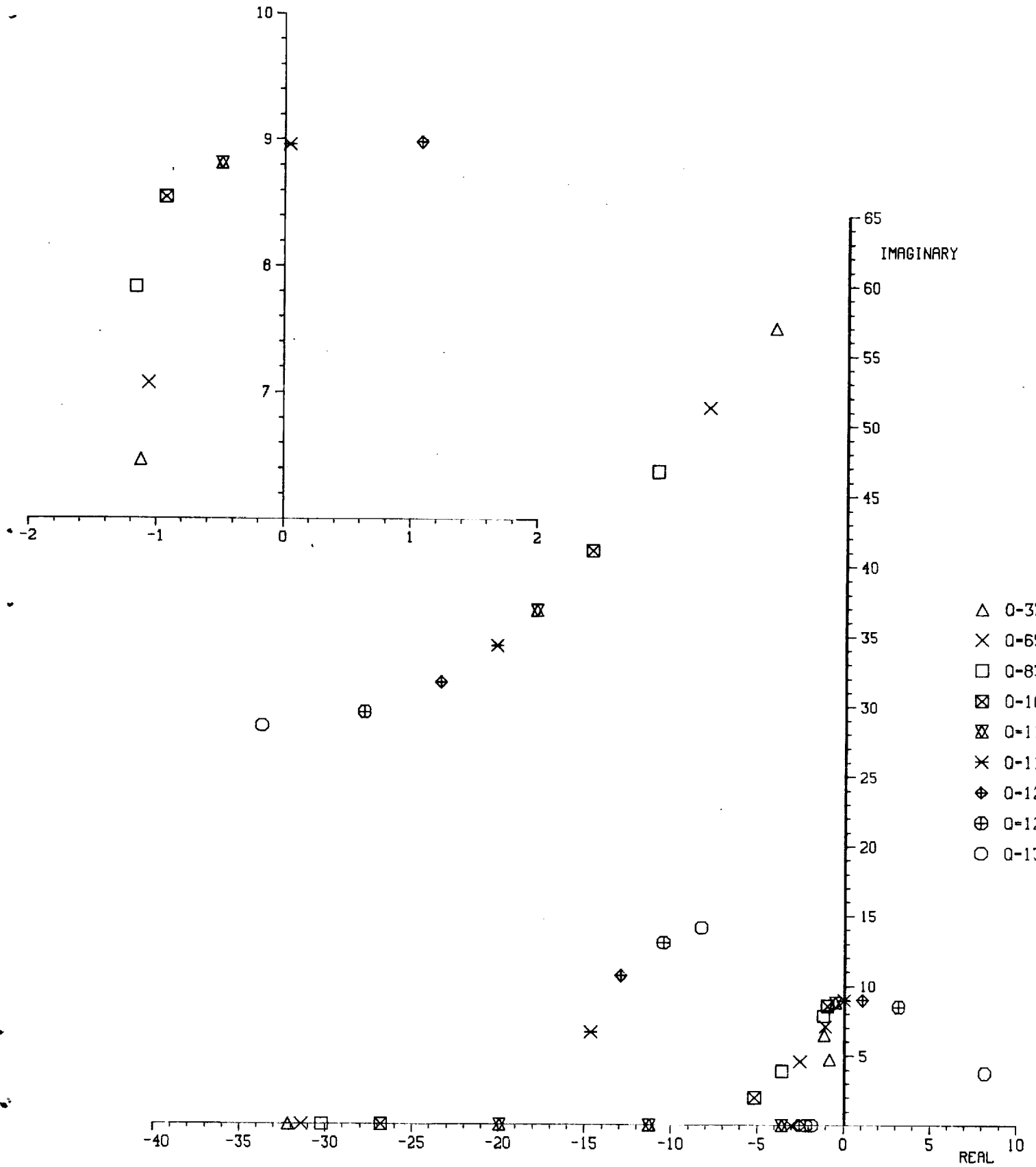
Legend:
△ Q-37
✕ Q-65
□ Q-83
⊠ Q-100
⊠ Q-110
✖ Q-115
✦ Q-120
⊕ Q-125
○ Q-130

IMAGINARY

REAL

1/2 scale FSW CABSAEL C2-3 M=0.6
control law as tested
Q̄-matched aero corrections

IMAGINARY

△	0-37
✕	0-65
□	0-83
⊠	0-100
⊠	0-110
✳	0-120
✦	0-125
⊕	0-130
○	0-135
+	0-140
◇	0-145

REAL

1/2 scale FSW CABSAEL C2-3 M=0.8
control law as tested
Q-matched aero corrections

Legend:
- △ Q-37
- ✕ Q-65
- □ Q-83
- ⊠ Q-100
- ⊠ Q-110
- ✳ Q-115
- ⬦ Q-120
- ⊕ Q-125
- ○ Q-130
- + Q-135

IMAGINARY

REAL
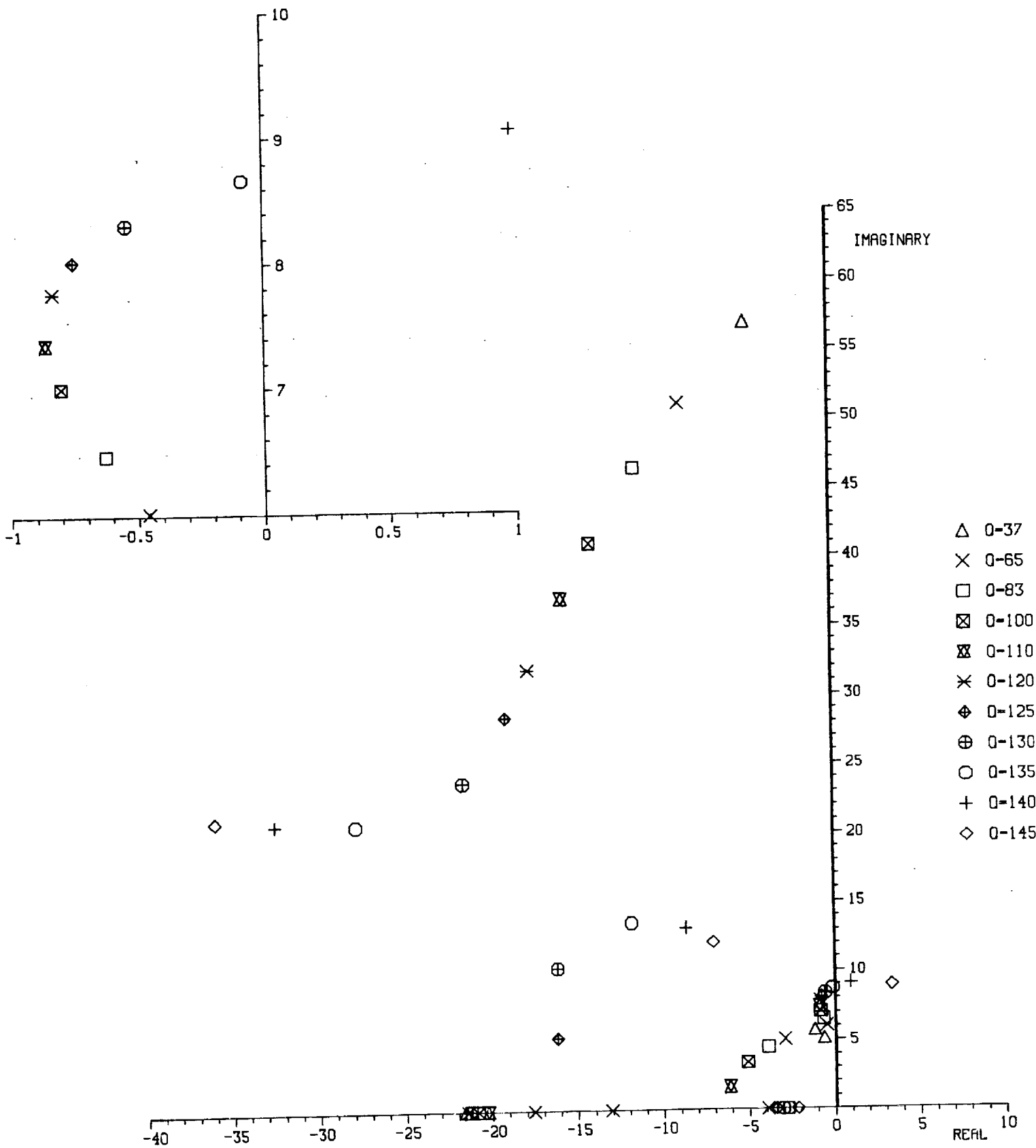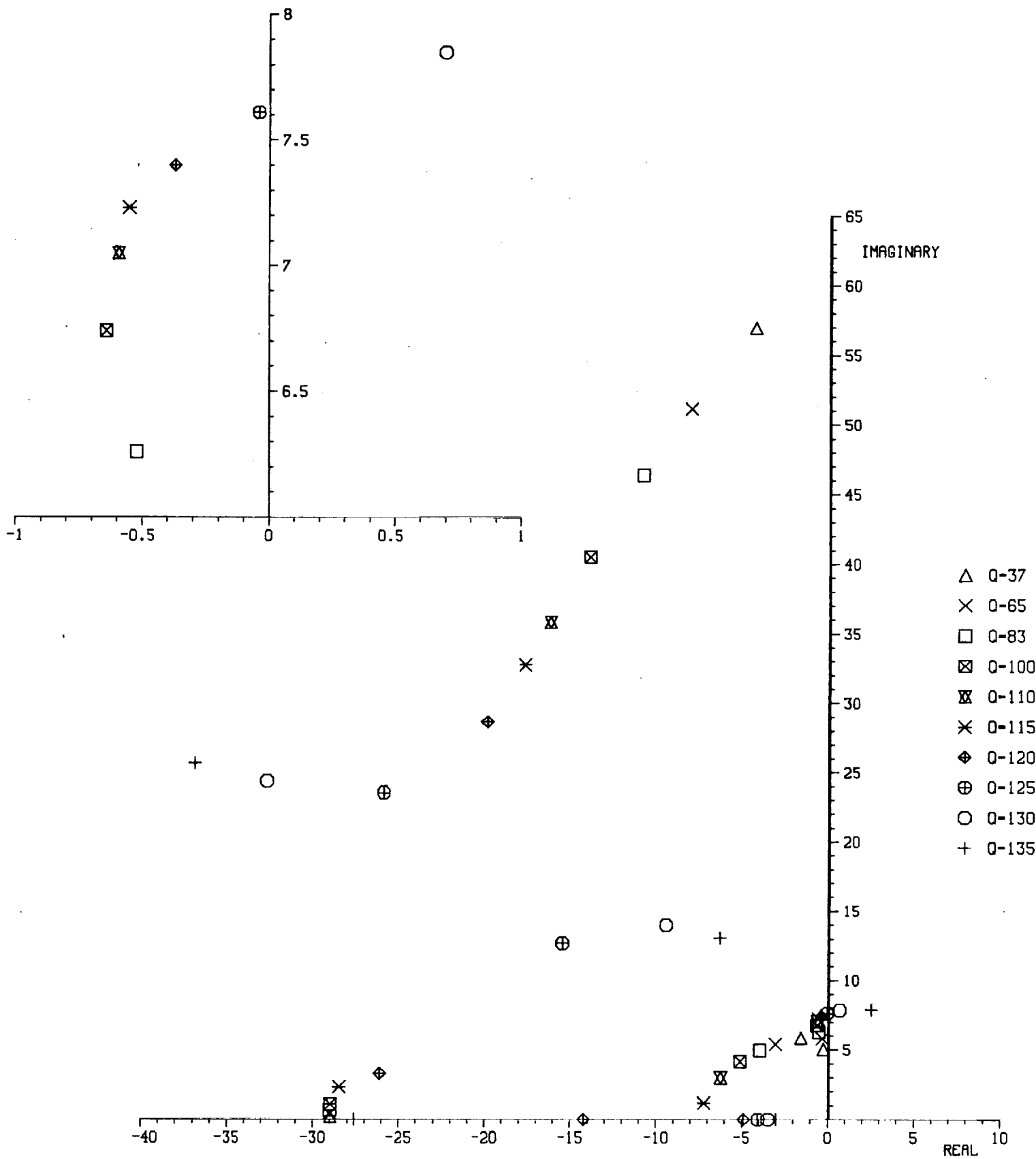
1/2 scale FSW CABSAEL C2-3 M=0.9
control law as tested
Q̄-matched aero corrections

Legend:
- △ Q-37
- ✕ Q-65
- □ Q-83
- ⊠ Q-100
- ⊠ Q-110
- ✖ Q-115
- ✦ Q-120
- ⊕ Q-125
- ○ Q-130
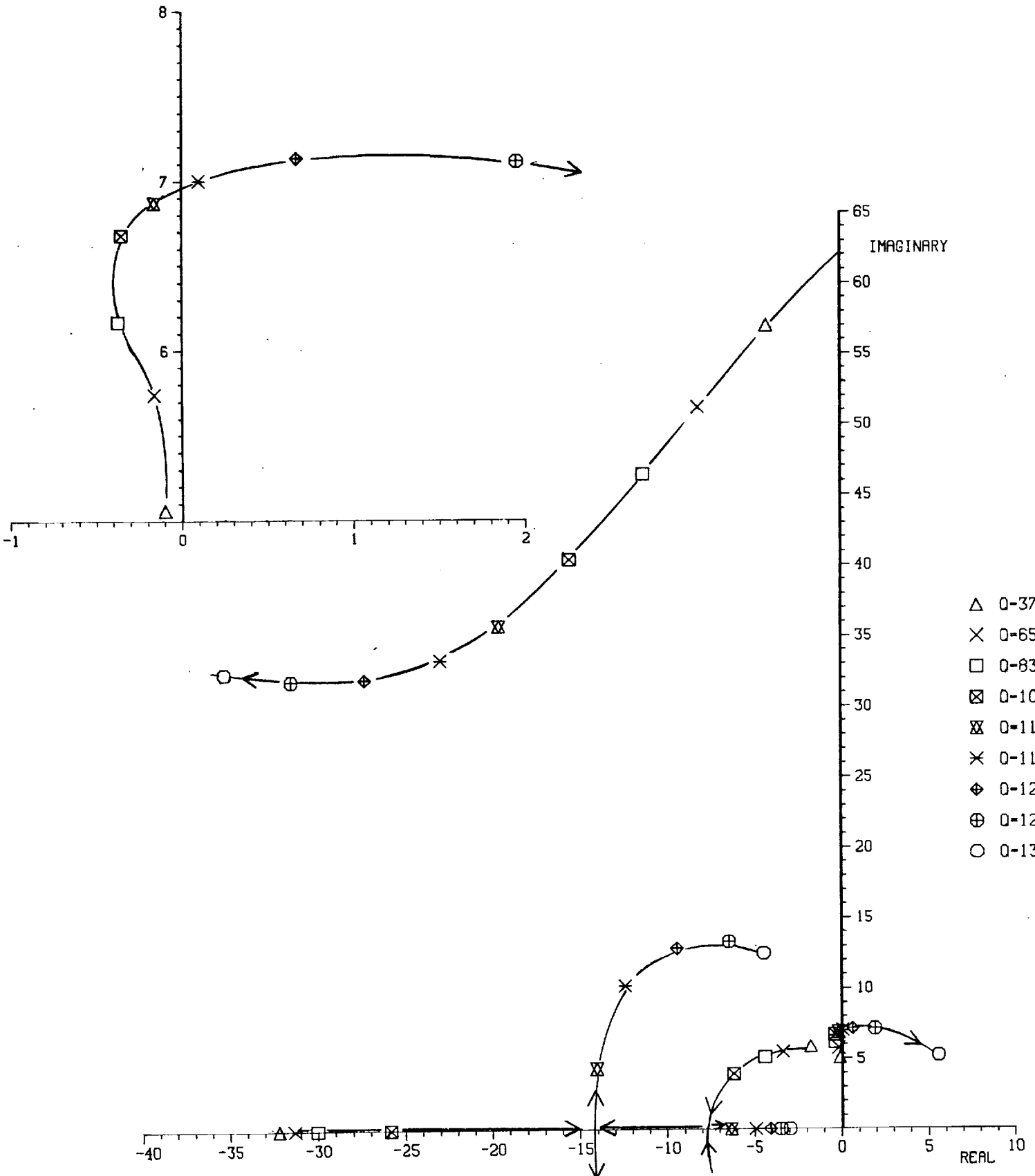
1/2 scale FSW CABSAEL C2-4 M=0.6
control law as tested
Q-matched aero corrections

Legend:
△ Q-37
× Q-65
□ Q-83
⊠ Q-100
⊠ Q-110
✱ Q-120
⊕ Q-125
⊕ Q-130
○ Q-135
+ Q-140
◇ Q-145

1/2 scale FSW CABSAEL C2-4 M=0.8
control law as tested
Q-matched aero corrections

Legend:
△ Q-37
✕ Q-65
☐ Q-83
⊠ Q-100
✕ Q-110
✳ Q-115
✦ Q-120
⊕ Q-125
○ Q-130
+ Q-135

IMAGINARY

REAL
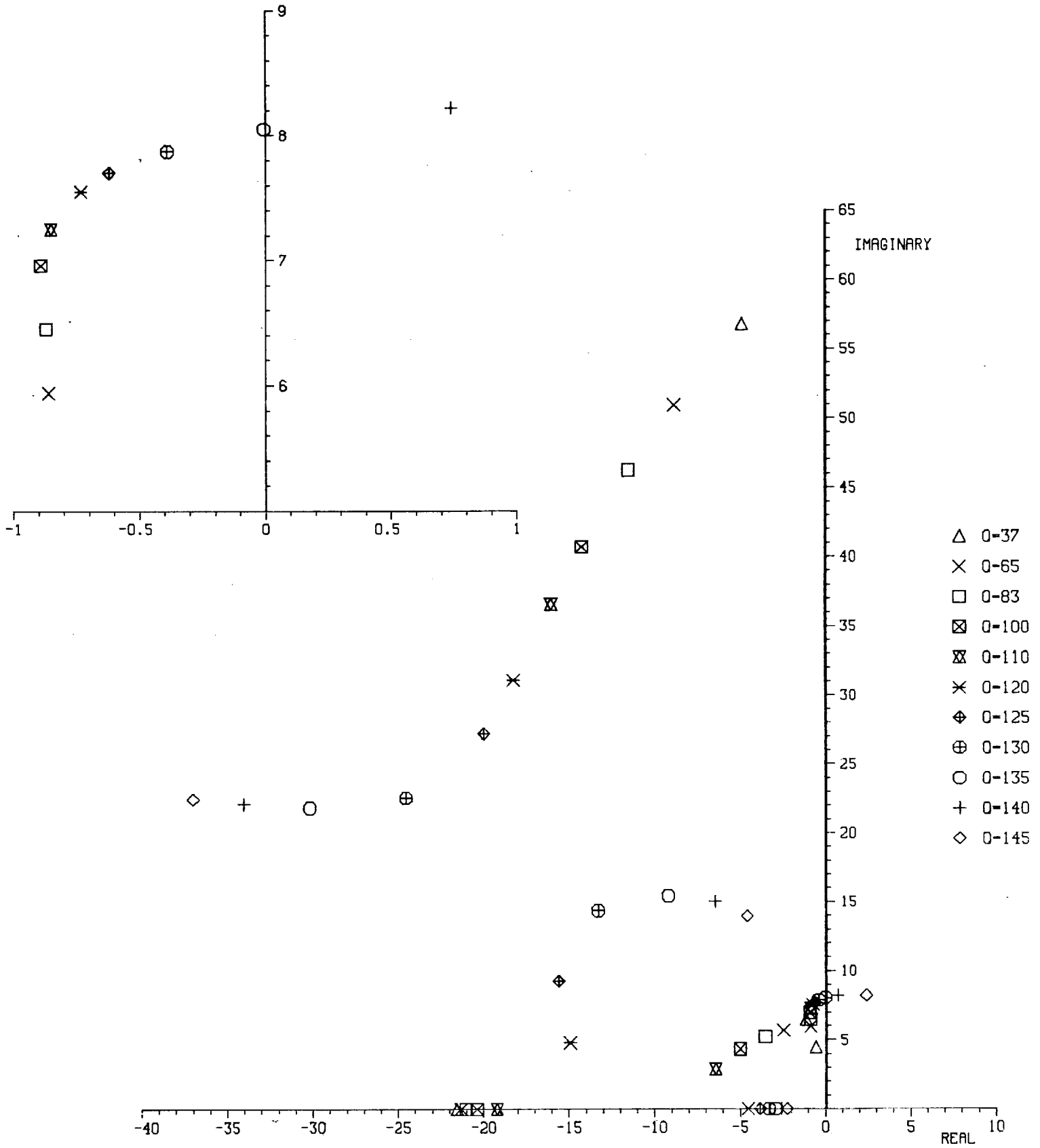
1/2 scale FSW CABSAEL C2-4 M=0.9
control law as tested
Q-matched aero corrections

Legend:
△ Q-37
✕ Q-65
□ Q-83
⊠ Q-100
⊠ Q-110
✻ Q-115
✧ Q-120
⊕ Q-125
○ Q-130

IMAGINARY
REAL
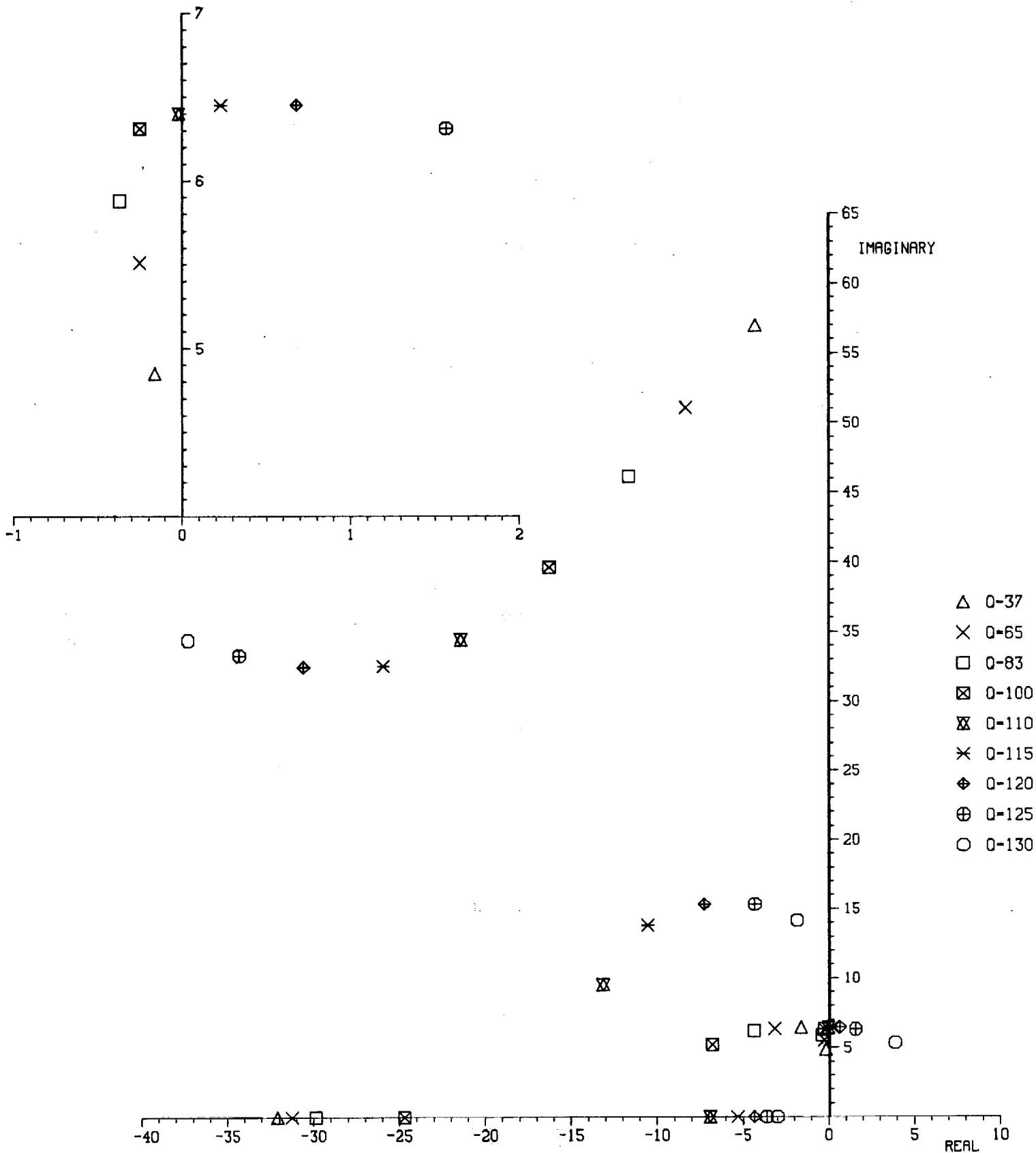
1/2 scale FSW   CABSAEL   C2-4A   M=0.6
control law as tested
Q̄-matched aero corrections

Legend:
- △ 0-37
- ✕ 0-65
- ☐ 0-83
- ⊠ 0-100
- ⊠ 0-110
- ✳ 0-120
- ✦ 0-125
- ⊕ 0-130
- ◯ 0-135
- + 0-140
- ◇ 0-145
- ⊞ 0-150

IMAGINARY

REAL

1/2 scale FSW CABSAEL C2-4A M=0.8
control law as tested
Q-matched aero corrections

Legend:
△ O-37
✕ O-65
☐ O-83
⊠ O-100
⊠ O-110
✱ O-115
✦ O-120
⊕ O-125
○ O-130
+ O-135
◇ O-140

IMAGINARY

REAL

1/2 scale FSW CABSAEL C2-4A M=0.9
control law as tested
Q̄-matched aero corrections

1. Report No. NASA CR-172324	2. Government Accession No.	3. Recipient's Catalog No.
4. Title and Subtitle BODY-FREEDOM FLUTTER OF A 1/2-SCALE FORWARD-SWEPT-WING MODEL, AN EXPERIMENTAL AND ANALYTICAL STUDY		5. Report Date April 1984
		6. Performing Organization Code
7. Author(s) Richard Chipman, Frank Rauch, Melvyn Rimer, Benigno Muñiz		8. Performing Organization Report No. LD-10-901-164
		10. Work Unit No.
9. Performing Organization Name and Address Grumman Aerospace Corporation Bethpage, NY 11714		11. Contract or Grant No. NAS1-17102
		13. Type of Report and Period Covered Contract Report
12. Sponsoring Agency Name and Address National Aeronautics and Space Administration Washington, D.C. 20546		14. Sponsoring Agency Code

15. Supplementary Notes

Langley Technical Monitor: Rodney H. Ricketts
Final Report

16. Abstract

A flutter model test program was undertaken to investigate the aeroelastic phenomenon known as Body-Freedom Flutter. BFF is a dynamic instability involving aircraft-pitch and wing-bending motions which, though rarely experienced on conventional vehicles, is characteristic of Forward-Swept-Wing (FSW) aircraft. Testing was conducted in the Langley Transonic Dynamics Tunnel on a flying, cable-mounted, ½-scale model of a FSW configuration with and without relaxed static stability (RSS). BFF instability boundaries were found to occur at significantly lower airspeeds than those associated with aeroelastic wing divergence on the same model. For those cases with RSS, a canard-based Stability Augmentation System (SAS) was incorporated in the model. This SAS was designed using aerodynamic data measured during a preliminary tunnel test in which the model was attached to a force balance. Data from the subsequent flutter test indicated that BFF speed was not dependent on open-loop static margin but, rather, on the equivalent closed-loop dynamics provided by the SAS. Servo-aeroelastic stability analyses of the flying model were performed using a computer code known as SAEL and predicted the onset of BFF reasonably well.

17. Key Words (Suggested by Author(s)) Flutter Flutter Model Testing RSS Bend-Pitch Coupling SAS Body-Freedom Flutter FSW		18. Distribution Statement Unclassified - Unlimited	
19. Security Classif. (of this report) Unclassified	20. Security Classif. (of this page) Unclassified	21. No. of Pages 256	22. Price